Prediction of Antisymmetric Buffet Loads on Horizontal Stabilizers in Massively Separated Flows, Phase II

May 1999

Final Report

19990630 069

This document is available to the U.S. public through the National Technical Information Service (NTIS), Springfield, Virginia 22161.

U.S. Department of Transportation
Federal Aviation Administration

NOTICE

1. Report No. DOT/FAA/AR-99/27	2. Government Accession No.	3. Recipient's Catalog No.	
4. Title and Subtitle PREDICTION OF ANTISYMMETRIC BUFFET LOADS ON HORIZONTAL STABILIZERS IN MASSIVELY SEPARATED FLOWS, PHASE II		5. Report Date May 1999	
		6. Performing Organization Code	
7. Author(s) Saeed Farokhi, Saeid Mirsafian, Tom Sherwood, and Mark Ewing*		8. Performing Organization Report No.	
9. Performing Organization Name and Address Aerotech Engineering & Research Corporation *University of Kansas 3115 W 6th Street, Suite I Lawrence, KS Lawrence, KS 66049		10. Work Unit No. (TRAIS) RPD-510	
		11. Contract or Grant No. DTRS-57-95-C-00091	
12. Sponsoring Agency Name and Address U.S. Department of Transportation Federal Aviation Administration Office of Aviation Research Washington, DC 20591		13. Type of Report and Period Covered Final Report	
		14. Sponsoring Agency Code ANM-100	

15. Supplementary Notes

16. Abstract

The Federal Aviation Administration (FAA) has a continuing program to collect data and develop predictive methods for aircraft flight loads. Some of the most severe and potentially catastrophic flight loads are produced by separated flows. Structural response to the aerodynamic excitation produced by separated flows is defined as buffeting.

A low-cost technique for the prediction of full-scale buffet loads on horizontal stabilizers of aircraft is described. A 1/13-scale rigid generic wind tunnel model with a t-tail configuration (based on the Beech Super King Air 200) was constructed and tested at the Wichita State University 7- x 10-ft. subsonic wind tunnel. The test matrix included a dynamic pressure range of 25 to 45 psf, an angle-of-attack range of −5 to 20 degrees, and a sideslip range of 0 to 20 degrees. The stabilizer was instrumented with differential pressure transducers and strain gages. The measured pressure power spectra and cross-spectral densities were scaled and used to excite a full-scale aeroelastic finite element model which included the tail structure and aft tail cone. The computed horizontal stabilizer rolling moment power spectra are used to determine the number of exceedences (within a known probability) of a specified rolling moment level per a given maneuver (e.g., stall). Representative pressure, strain gage, and rolling moment power spectra are discussed as is a selected exceedence estimate.

17. Key Words Antisymmetric buffet loads, Horizontal stabilizer, T-tail airplane, Wind tunnel test, Rolling moment	18. Distribution Statement This document is available to the public through the National Technical Information Service (NTIS), Springfield, Virginia 22161.		
19. Security Classif. (of this report) Unclassified	20. Security Classif. (of this page) Unclassified	21. No. of Pages 145	22. Price

Form DOT F1700.7 (8-72)   Reproduction of completed page authorized

TABLE OF CONTENTS

LIST OF FIGURES

LIST OF TABLES

ACRONYMS

ASTROS	Automated STRuctural Optimization System
CSD	Cross Spectral Density
PSD	Power Spectral Density
PSF	Pounds per Square Foot
FAA	Federal Aviation Administration
FEM	Finite Element Method
FAR	Federal Aviation Regulation
NIAR	National Institute of Aviation Research
PSID	Pounds per Square Inch, Differential
DC	Direct Current
AC	Alternating Current
A/D	Analog to Digital
MAPOL	Matrix Analysis Problem Oriented Language

GLOSSARY OF TERMS

G_{xx}	Single Sided Power Spectral Density
G_{xy}	Single Sided Cross Spectral Density
n_d	Number of records, number of averages
T	Record length, period
$w(t)$	Window Function, time history record
$W(f)$	Spectral Window, frequency history record
$w_h(t)$	Hanning window function, time history record
$W_h(f)$	Hanning window function, frequency history record
ρ_a	Density, full scale
l_a	Length, full scale
l_m	Length, model
ρ_m	Length, model
V_a	Velocity, full scale
V_m	Velocity, model
f_a	Force, full scale
f_m	Force, model
S_x	Modal buffet force matrix
S	Modal response PSD matrix
S_y	Structural response matrix
N_y	Structural responses due to unit modal displacements
$H(\omega)$	Modal complex frequency response matrix
α	Angle of attack
ψ	Side Slip Angle
R.M.	Rolling moment
rms	Root mean square

EXECUTIVE SUMMARY

A low-cost technique for the prediction of full-scale buffet loads on horizontal stabilizers of aircraft is described. A 1/13-scale rigid generic wind tunnel model with a t-tail configuration (based on the Beech Super King Air 200) was constructed and tested at the Wichita State University 7- x 10-ft. subsonic wind tunnel. The test matrix included a dynamic pressure range of 25-45 psf, an angle-of-attack range of -5 to 20 degrees, and a sideslip range of 0 to 20 degrees. The stabilizer was instrumented with differential pressure transducers and strain gages. The measured pressure power spectra and cross-spectral densities were scaled and used to excite a full-scale aeroelastic finite element model which included the tail structure and aft tail cone. The computed horizontal stabilizer rolling moment power spectra are used to determine the number of exceedences (within a known probability) of a specified rolling moment level per a given maneuver (e.g., stall). Representative pressure, strain gage, and rolling moment power spectra are discussed as is a selected exceedence estimate.

1. INTRODUCTION.

The Federal Aviation Administration (FAA) has a continuing program to collect data and develop predictive methods for aircraft flight loads. Some of the most severe and potentially catastrophic flight loads are produced by separated flows. Structural response to the aerodynamic excitation produced by separated flows is defined as buffeting. [1] Buffeting can cause serious controllability problems and in severe cases produce structural failure. The result of control difficulties can be catastrophic if the aircraft is in a near-ground flight path such as landing or takeoff. Structural failure, in the extreme, is life threatening at any flight condition. The potential severity of tail buffet has persuaded the FAA to include buffet loading as a design load criterion for commercial transports. Under Federal Aviation Regulation (FAR) 25-305(e), aircraft manufacturers are required to demonstrate that the cumulative probability of an aircraft encountering dangerous levels of buffet-induced rolling moments is below the prescribed level. The current accepted method of meeting this requirement involves a great deal of full-scale flight testing. This method costs manufacturers a large amount of capital to meet the requirement and allows them no easy recourse should the aircraft not qualify. New methodologies are being considered that would allow the design rolling moment load to be estimated before the full-scale aircraft is constructed. A standardized method would expedite the certification process and enable consistent and repeatable results.

Two major classes of buffet prediction methods are currently in use. The first method is buffet prediction by computational fluid dynamics codes. This method is very computationally intensive, requires an expert user, and is still unproved. An alternate approach is to use experimental data in conjunction with a computational solution of the structural dynamics equations. Experimental/computational methods also have several subdivisions, most notably in the experimental methods employed. The wind tunnel model used for measurement of the unsteady surface pressure can be rigid or flexible. The merits of each type of buffet prediction methodology are summarized in references 2, 3, and 4. This study describes a combined experimental and computational method to predict antisymmetric buffeting loads of horizontal stabilizers in massively separated flows. The objective is to predict, within a known probability, the anti-symmetric response. The most obvious benefit is safety. If an aircraft has predictable characteristics in critical flight scenarios, precautionary measures can be taken. If a prediction of undesirable behavior can be performed early in the design process, it can be remedied. Other important benefits of this methodology are reduced design costs and reduced design cycle time.

2. BUFFET PREDICTION METHOD.

Buffeting is governed by the dynamic equilibrium, equation 1, given in terms of the generalized coordinate q: [2]

$$M_n \ddot{q}(t) + D_n \dot{q}(t) + \omega_n^2 M_n q_n(t) + F_{D_n}(\dot{q}_1(t)...\dot{q}_N(t)) + +F_{K_n}(q_1(t)...q_N(t)) = P_n(t) \qquad (1)$$

where the first three terms represent the generalized mass, structural damping, and structural stiffness respectively. The following two terms are the motion-dependent aerodynamic damping

and the motion-dependent aerodynamic stiffness. The term on the right-hand side is the motion-independent aerodynamic force (buffet pressure excitation). [2]

Although there are several approaches to solving equation 1, a rigid body method for buffet prediction was chosen due to its relatively low cost and experimental simplicity. The prediction methodology can be divided into two distinct tasks: (1) experimental acquisition of unsteady pressures on the tail of a rigid model and (2) prediction of the aeroelastic results based on the buffet forcing function as defined by the first task. The prediction of tail buffet using this methodology can be best summarized in the flowchart illustrated in figure 1. [5]

```
                          ┌──────────────────┐
                          │   Structural     │
                          │  Modeling and    │
                          │  Modal Analysis  │
                          │    [ASTROS]      │
                          └────────┬─────────┘
                                   │
┌──────────────┐   ┌───────────────┴──┐              ┌──────────────────┐
│    Wind      │   │  Postprocessing  │              │    Unsteady      │
│   Tunnel     │──▶│  Buffet Pressure │◀────────────│  Aerodynamics    │
│   Testing    │   │   [PSDs/CSDs]    │──▶          │    [ASTROS]      │
│ [Rigid Model]│   └──────────────────┘              └──────────────────┘
└──────────────┘            │
                            ▼
                   ┌──────────────────┐
                   │     Modal        │
                   │    Response      │
                   │    Analysis      │
                   │    [ASTROS]      │
                   └────────┬─────────┘
                            │
                            ▼
                   ┌──────────────────┐
                   │   Structural     │
                   │    Response      │
                   │    [ASTROS]      │
                   └────────┬─────────┘
                            │
                            ▼
                   ┌──────────────────┐
                   │   Calculate      │
                   │   Probability    │
                   │  of Exceedence   │
                   └──────────────────┘
```
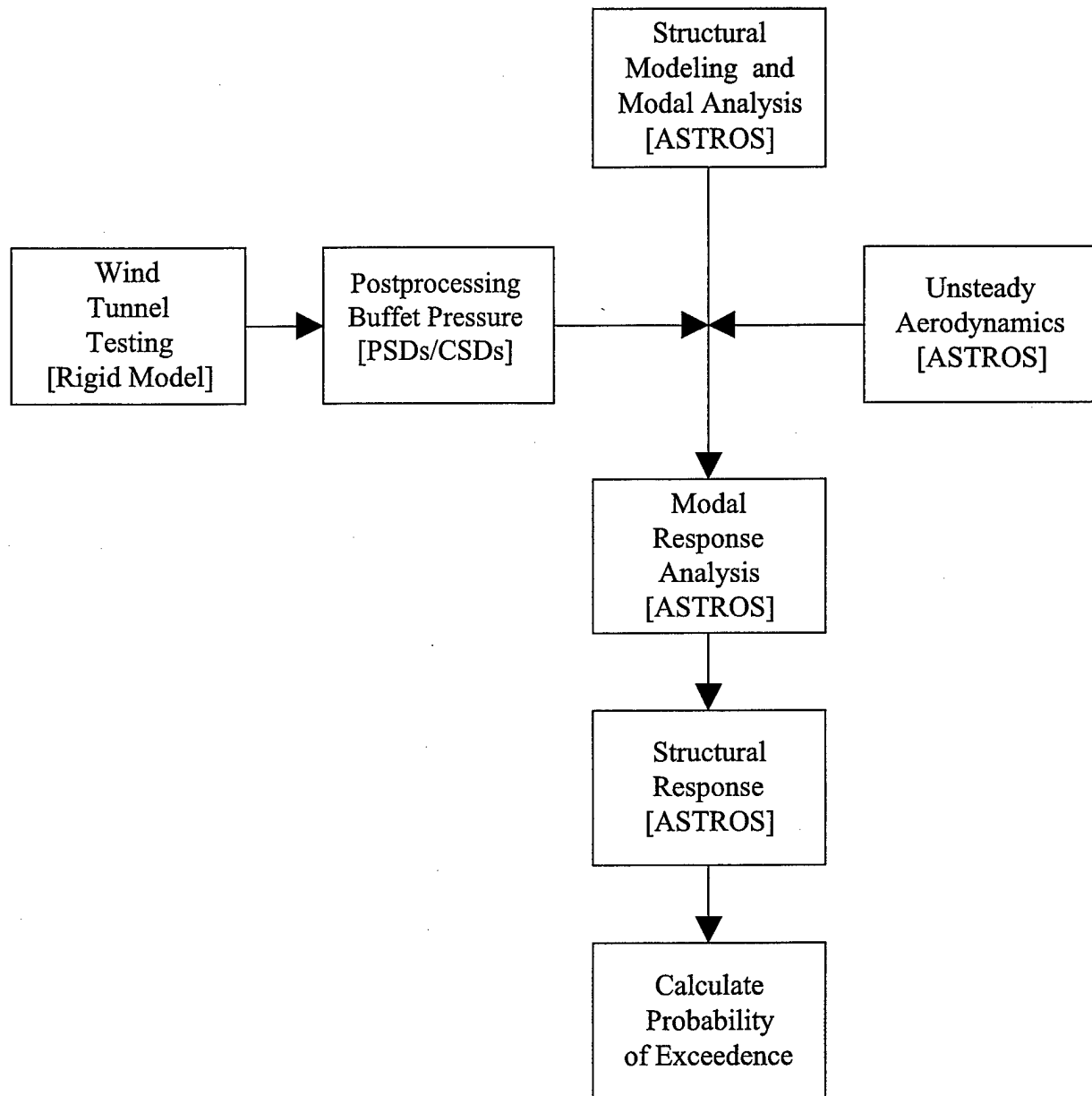
FIGURE 1. SCHEMATIC REPRESENTATION OF BUFFET PREDICTION

2.1 EXPERIMENTAL METHODS.

2.1.1 Test Facility.

The experimental testing was performed at the National Institute for Aviation Research (NIAR) facilities in Wichita, Kansas. The Walter H. Beech Memorial Wind Tunnel which has a 7- by 10-foot test section was used. The model was supported by a sting that could be used to vary the model angle of attack from -5 to 20 degrees. The sting was mounted on a rotary table, which allowed the sideslip angle to be adjusted.

The test matrix is given in table 1. These dynamic pressures represent a Reynolds number range of 9.2×10^5/ft to 1.2×10^6/ft. Appendix A contains the entire test matrix.

TABLE 1. TEST MATRIX

Dynamic Pressure (psf): 25, 35, 45
Angle of Attack (degrees): -5, 0, 5, 10, 15, 20
Heading Angle (degrees): 0, -10, -20

2.1.2 Model Design.

The model used for the tests was a rigid 1/13-scale generic t-tail model based on the Beech Super King Air 200 and it can be seen in figures 2 through 4. The model consists of three major sections: the wing, fuselage, and tail. The dimensions for the model were primarily driven by the load limitations of the sting mount.
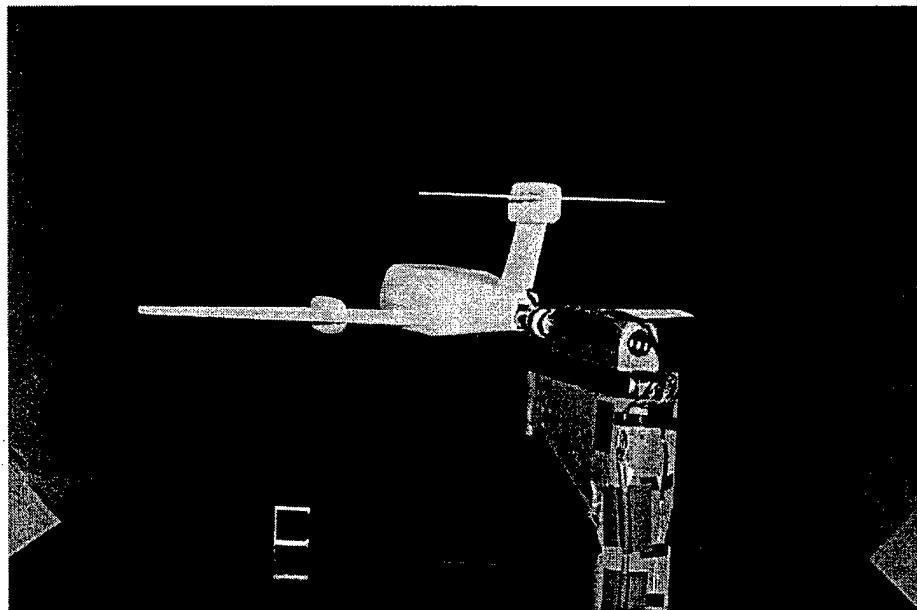
FIGURE 2. WIND TUNNEL MODEL OF BEECH SUPER KING AIR 200

3
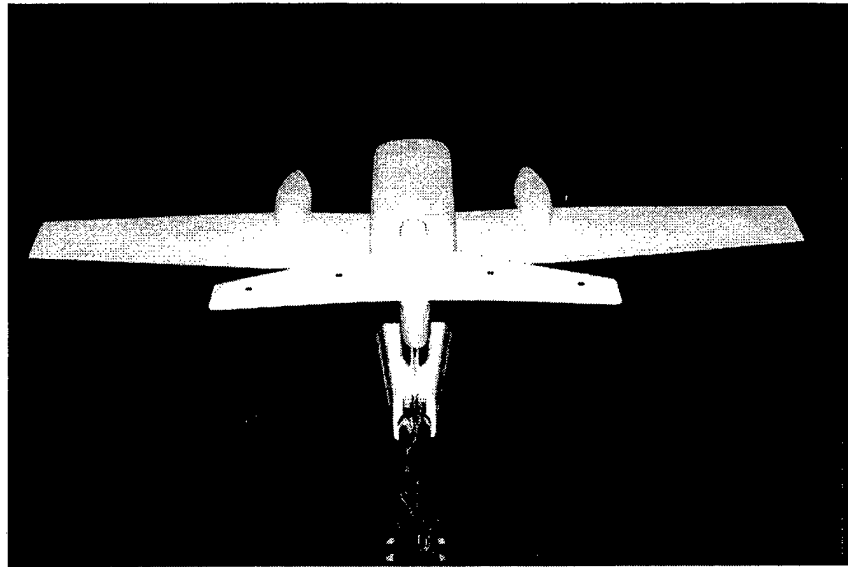
FIGURE 3. TOP VIEW OF AEROTECH WIND TUNNEL MODEL
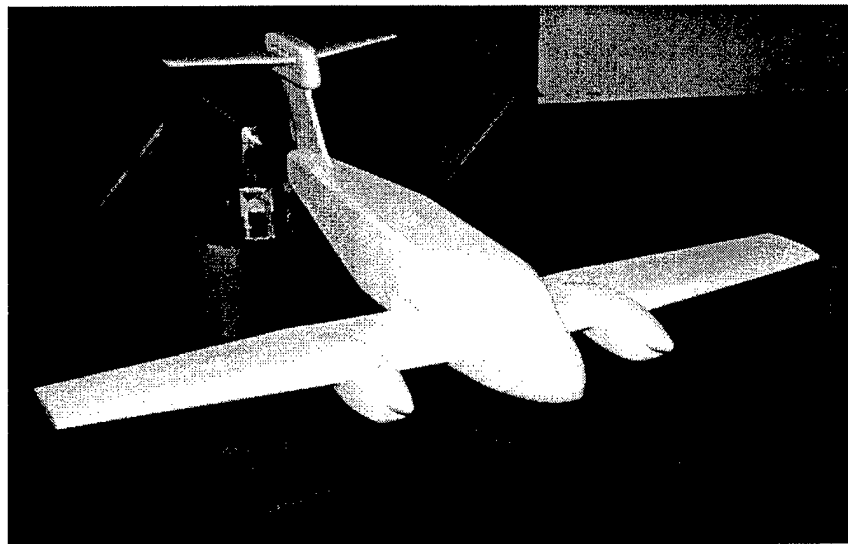
FIGURE 4. FRONT VIEW OF AEROTECH WIND TUNNEL MODEL

The fuselage of the model was cut from a wooden mandrel, which was made from several 1-inch-thick pieces of basswood which were epoxied together under vacuum. Basswood was used for its workability. The wooden mandrel was then cut longitudinally into two sections. One section about one-third of the height of the mandrel formed the bottom section of the fuselage while the remaining piece was used to make the top fuselage section. The top section was then hollowed out to attach the sting mount/model backbone to the model. This can be seen in figure 5. A detailed drawing of the model mounting apparatus can be seen in figure 6.
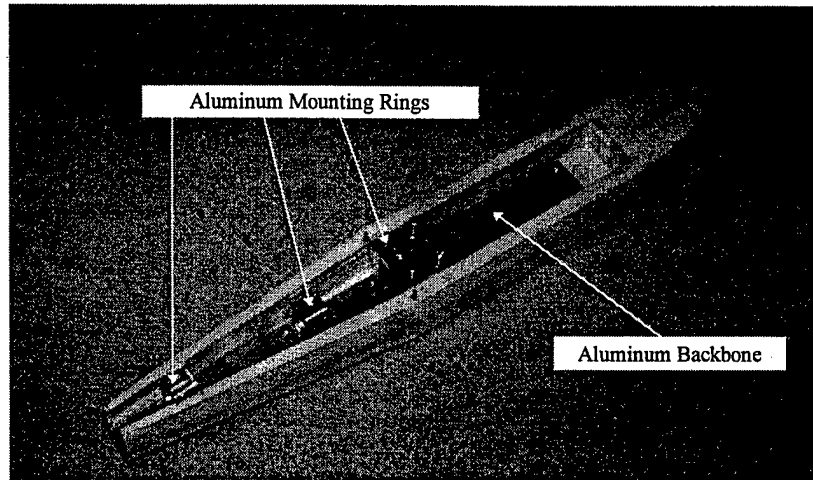
FIGURE 5. TOP OF FUSELAGE WITH STING MOUNT/ALUMINUM BACKBONE
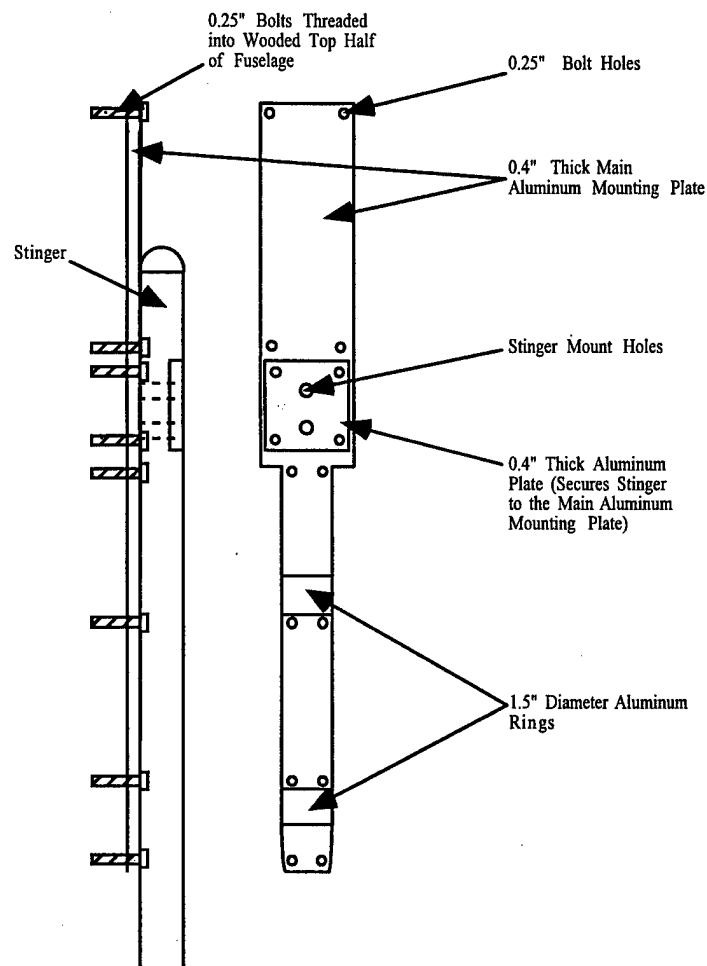
FIGURE 6. DETAILED DRAWING OF WIND TUNNEL MODEL MOUNT

5

The core of the wing was shaped from styrofoam with a thin aluminum spar for added rigidity. This aluminum spar/styrofoam core was then wrapped in a thin plywood sheet. This structure, along with a wooden center body for attachment of the wing to the model fuselage, can be seen in figure 7. The wing as seen in figure 7 was completed by adding a layer of fiberglass for increased strength before being sanded smooth and painted. After a section was carved out of the bottom of the fuselage section, the wing was fitted into this section and the entire assembly was bolted to the top portion of the fuselage.

Wooden Center Body
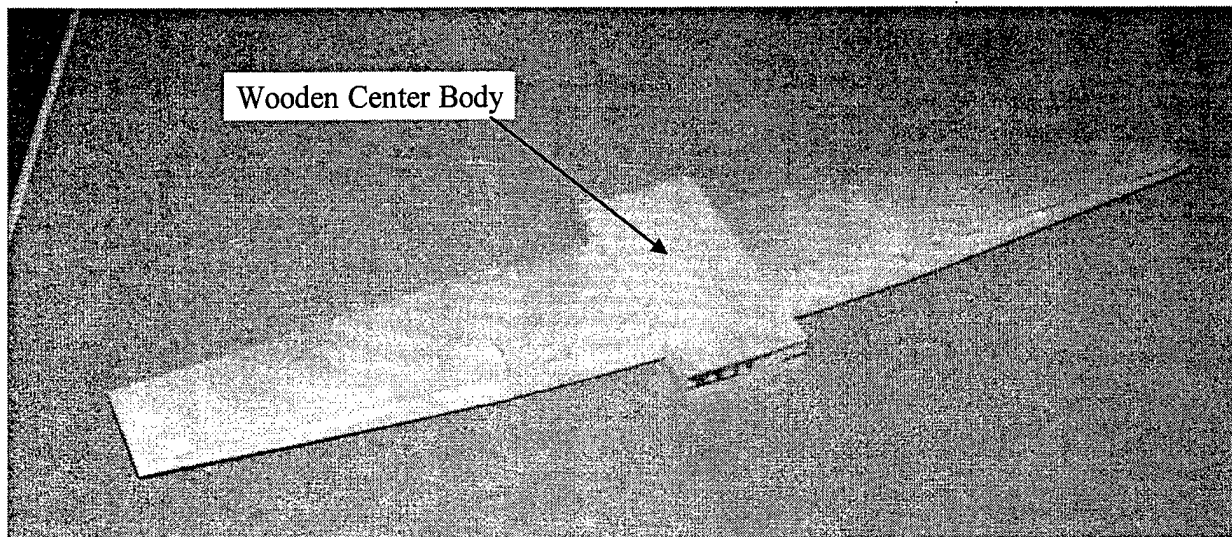
FIGURE 7. MODEL WING BEFORE FIBERGLASS LAYER WAS APPLIED

The vertical tail was machined out of a solid piece of aluminum. The leading and trailing edges were filed smooth, and this piece was bolted to the aluminum backbone of the model.

The horizontal stabilizer was made by first milling out a solid aluminum core as shown in figure 8. This served to create an extremely stiff (rigid) structure. It also provided a structure for mounting the pressure transducers. Small indentations into the aluminum core surface were made to allow the pressure transducers to be secured. The transducers where then fully secured by a press fit between the two-piece aluminum skin. Once the aluminum skin was finished, small holes were drilled to allow the differential pressure transducers to be vented to the upper and lower surfaces of the horizontal tail. The skin for the horizontal tail was then filed smooth to a symmetric airfoil shape. The tail was made about 6 percent thicker than on the actual aircraft. This construction technique was deemed sufficient because extreme accuracy in the shape and thickness of the horizontal tail does not play a significant role in the flow of interest for this study.
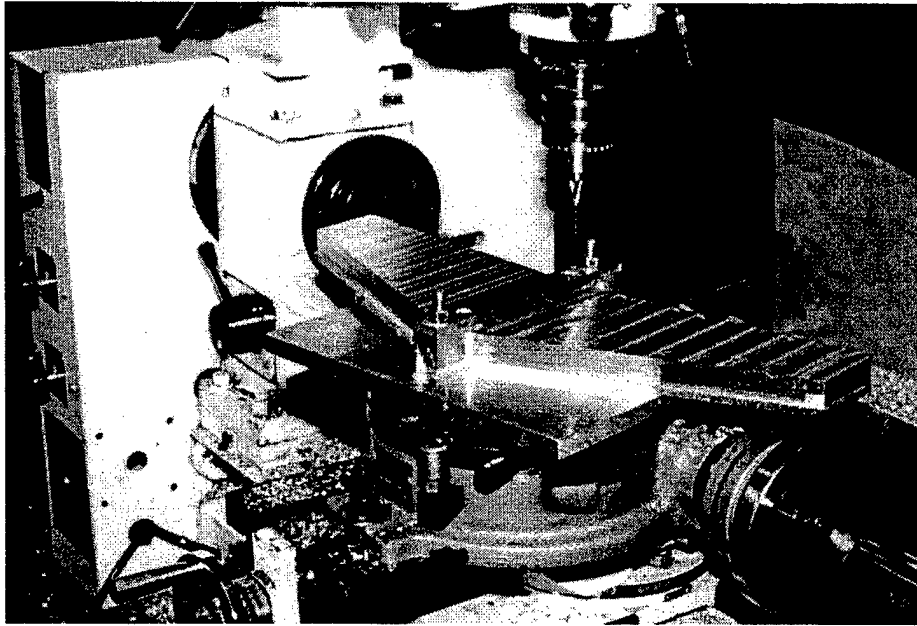
FIGURE 8. HORIZONTAL STABILIZER ALUMINUM CORE ON
MILLING MACHINE

2.1.3 Instrumentation.

The pressure transducers used for measuring the horizontal tail pressures were Kulite LQ-1-200-5D (range: 5 pounds per square inch differential (psid)). These transducers have a high natural frequency of over 70 kHz and have a linear response in the region of interest for the present tests. Twelve transducers were mounted in the center of the stabilizer at the locations shown in figure 9. Small holes were drilled in the stabilizer skin to vent the transducers to the upper and lower surfaces. The numbers in figure 9 represent the channel numbers referred to later in this report.
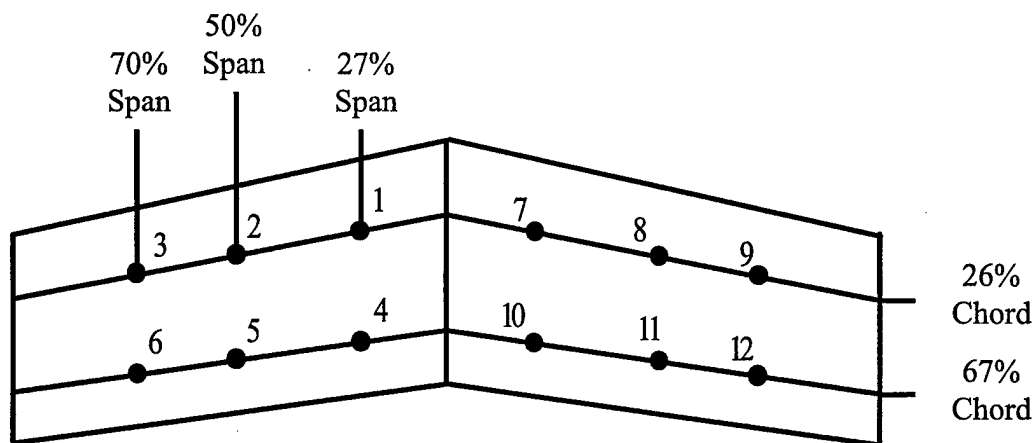
FIGURE 9. PRESSURE TRANSDUCER LOCATIONS

To remove the signal that is attributable to the free stream signal, the free stream pressure had to be recorded. A Kulite LQ-125-5SG pressure transducer with a 0-5 psi measuring range, a nonlinearity and hysteresis of ± 0.5%, and a natural frequency of 70-350 kHz was used for this purpose. It was mounted at the forward end of the test section out of the tunnel boundary layer and out of the range of influence of the model and can be seen in figure 10.
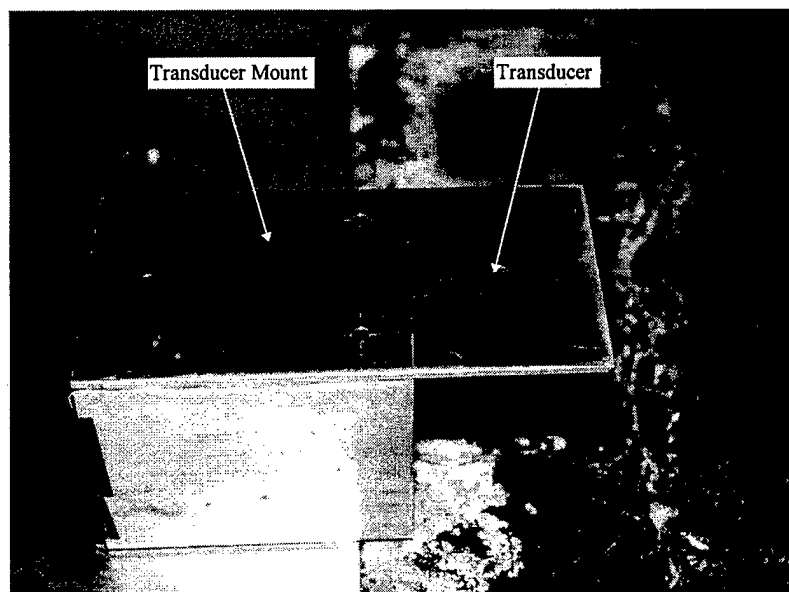
FIGURE 10. FREE STREAM TRANSDUCER AND MOUNT

The strain gages used were Omega KFG-10-120-C1-11L1M2R prewired gages. They were mounted as close to the root of the horizontal tail as possible in the configuration shown in figure 11. The 1/2-bridge configuration, unlike the full bridge, allows for the resolution of both bending and torsional loads. The 1/2-bridge configuration also eliminates the need for temperature compensation and has a larger output signal than a 1/4-bridge setup. The strain gage configuration, as shown in figure 11, has the following characteristics (for bending strain): 10 $\mu V/\mu\varepsilon$ output given a 10V excitation with a sensitivity of 1.0 mV/V at 1000 $\mu\varepsilon$.[6]

(a) Strain Gage Locations

(b) Half-Bridge Circuit
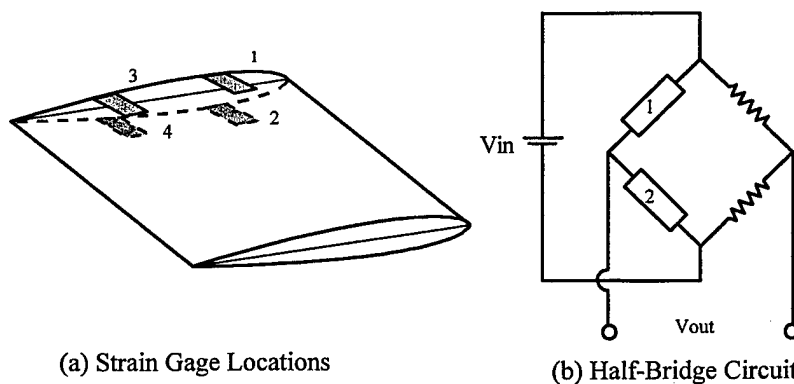
FIGURE 11. STRAIN GAGE LOCATIONS AND CIRCUITRY

2.1.4 Data Acquisition.

A schematic of the data acquisition procedure can be seen in figure 12. An alternating current (AC) coupling was enabled during data acquisition to remove the direct current (DC) component of the signal. The AC was coupled using a 2200 System from Vishay. In total, seventeen 2210 signal conditioning amplifier units were used for the pressure transducer and strain gage channels. This unit also provided the signal amplification and low-pass filtering functions. The low-pass filter used was a four-pole Bessel with a cutoff frequency of 1000 Hz. Low-pass filtering is required to prevent aliasing (the process of high-frequency data folding over into the lower frequency range) in the data. [6,7]

Pressure Transducer Signal/Strain Gage Signal	
↓	
High-Pass Filter (1 Hz)	Eliminates DC Offset
↓	
Amplifier (x1000-3000)	Provides Maximum A/D Resolution
↓	
Low-Pass Filter (~1000 Hz)	Prevents Aliasing
↓	
Simultaneous Sample and Hold Card	Prevents Time Skew
↓	
A/D Conversion (Rate ~4 kS/sec)	Record Time History
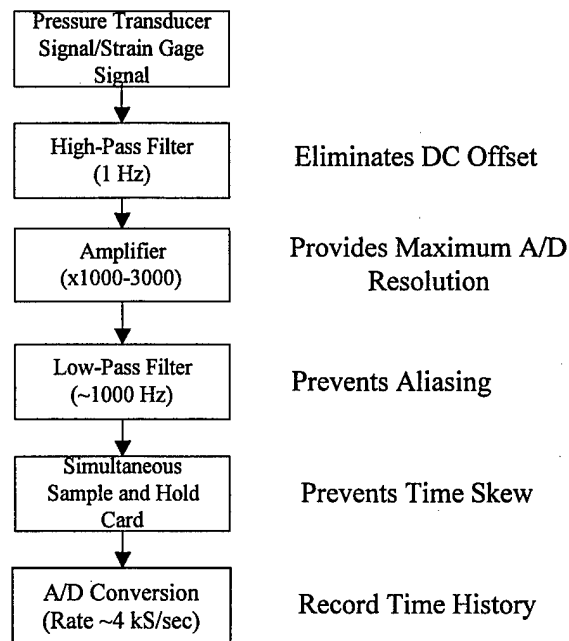
FIGURE 12. SCHEMATIC OF SIGNAL CONDITIONING
AND RAW DATA RECORDING

HP-44730A (4-channels/card) simultaneous track-and-hold cards were used in this experiment. Although there is only one analog-to-digital converter in the HP-3835, these cards allowed the simultaneous acquisition of all of the transducers by providing a buffer. This prevents a lag between data points which, in turn, prevents the data from being time skewed (accurately preserving the phase data).

To set the amplification for both pressure transducer and strain gage data, a representative signal was recorded using no amplification, and then the amplification was set to a value to ensure the maximum amount of resolution of the signal without exceeding the input range of the analog-to-digital (A/D) board.

At each point in the test matrix, 51,200 data points per channel (51,200 x 17 = 870,400 total) were recorded at a sampling frequency of 4,000 Hz.

9

2.2 DATA POSTPROCESSING AND ANALYSIS.

The data postprocessing begins where the last box in figure 12 ends. There were two goals of the postprocessing data analysis. The first was to convert the time series pressure data obtained from the wind tunnel to a format compatible with the computational tail buffet prediction, and the second was to convert the time series strain gage data into a format compatible with the estimation of the power spectra of the horizontal tail root bending moment as a check of the validity of the pressure measurements. Appendices B and C contain power spectral density (PSD) plots of the pressure and strain, respectively.

2.2.1 Pressure Data.

The most efficient and popular method for estimating the power spectral densities of time data is the Fast Fourier Transform. Among other important qualities, it allows for the elimination of the noise floor due to the data acquisition system [7]. For uncorrelated noise, this can be represented by

$$Y(f) \; = \; X(f) \; + \; N(f) \tag{2}$$

where $Y(f)$ = measured signal
   $X(f)$ = desired signal
   $N(f)$ = uncorrelated noise

The one-sided power spectral density is given by

$$\hat{G}_{xx}(f) = \frac{2}{\eta_d T} \sum_{k=1}^{\eta_d} \left| X_k(f,T) \right|^2 \tag{3}$$

$$\hat{G}_{xy}(f) = \frac{2}{\eta_d T} \sum_{k=1}^{\eta_d} X_k^*(f,T) Y_k(f,T) \tag{4}$$

If the one-sided power and cross-spectral densities are estimated using equations 2 and 3, significant errors may be introduced into the estimation due to the inherent windowing of the data. If those two equations are used, it is the same as applying a rectangular or boxcar window to the data. This windowing function is given by the following equation:

$$w(t) = 1, 0 \le t \le T$$

$$w(t) = 0, otherwise \tag{5}$$

and plots of $w(t)$ and $\left| W(f) \right|$ are shown in figure 13.
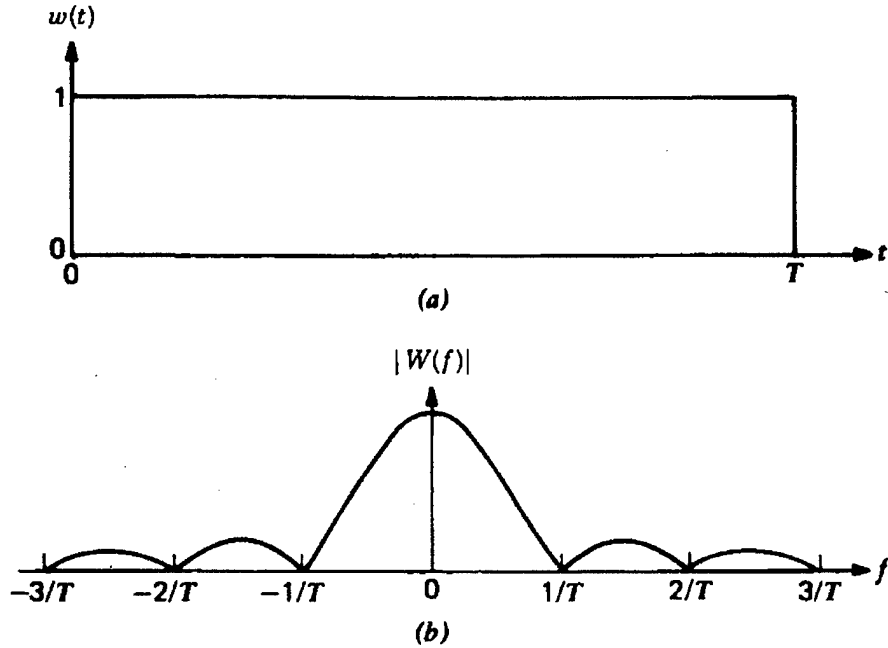
FIGURE 13. RECTANGULAR ANALYSIS WINDOW (a) TIME WINDOW,
(b) SPECTRAL WINDOW [7]

As can be seen in figure 13 this window allows large power leakage at frequencies far away from the main lobe of the power spectral window. This can be a source of error in spectra estimation. To avoid this problem another windowing function was used. The Hanning window is a full cosine tapering window and it is described by

$$w_h(t) = \frac{1}{2}\left(1 - cos\frac{2\pi t}{T}\right), 0 \le t \le T$$
$$w_h(t) = 0, otherwise$$

(6)

Plots of $w_h(t)$ and $|W_h(f)|$ can be seen in figure 14. It is clear from this figure that the power leakage seen in figure 14 has been largely reduced. Use of the Hanning window results in a loss of the estimation of the magnitude of the spectral density of $\sqrt{\frac{8}{3}}$. The solution is to multiply the Hanning window estimation by this scale factor.
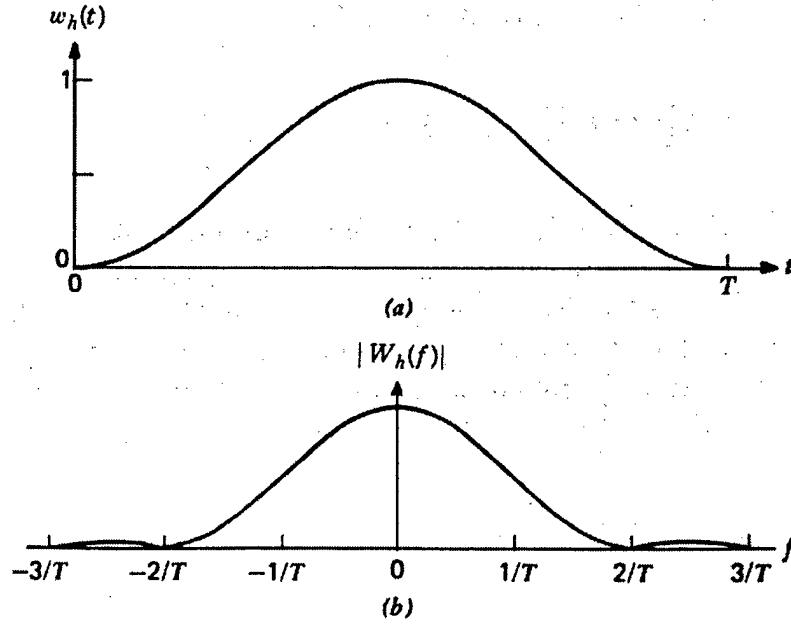
**FIGURE 14. HANNING ANALYSIS WINDOW (a) TIME WINDOW,
(b) SPECTRAL WINDOW [7]**

In addition to the uncorrelated noise which was removed as previously described, the coherent noise in the free stream and tail pressures was removed using the following relationship.

$$\hat{G}_{xx}(f) = \left[1 - \hat{\gamma}_{xf}^{2}(f) \right] \hat{G}_{xx}^{*}(f) \tag{7}$$

where $\hat{\gamma}_{xf}^{2}(f)$ = coherence function between tail and free stream pressures given in equation 8

$\hat{G}_{xx}^{*}(f)$ = previously determined one-sided power spectral density

$$\hat{\gamma}_{xy}^{2}(f) = \frac{\left| \hat{G}_{xy}(f) \right|^{2}}{\hat{G}_{xx}(f)\,\hat{G}_{yy}(f)} \tag{8}$$

A sample set of graphs illustrating the effects of the signal techniques previously described follows. Figure 15 shows the noise floor PSD for channel 7. As can be seen, the highest peak in the noise floor is approximately 0.00001 psi^2/Hz while most of the signal is an order of

12

magnitude below this value. The only peak in the data of note is the one occurring at 60 Hz. This signal is due to the power supply and could not be reduced further with the available equipment (although it was reduced to an acceptable level).
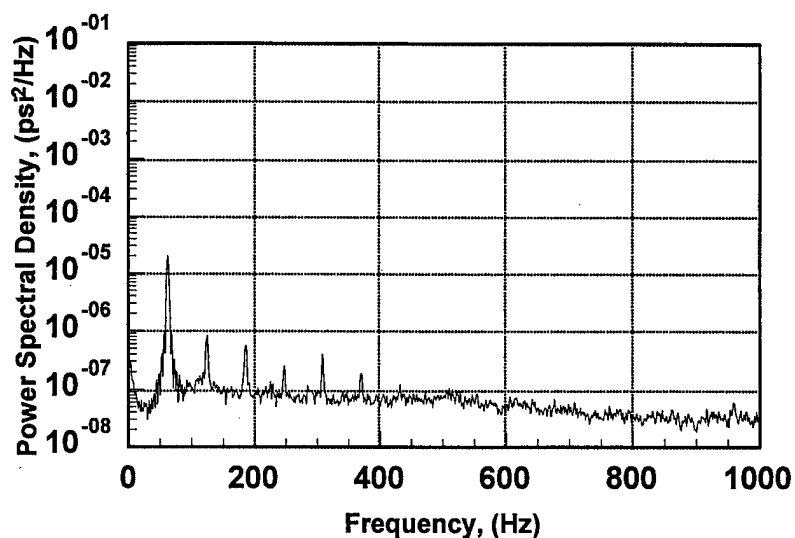
FIGURE 15. POWER SPECTRAL DENSITY OF PRESSURE TRANSDUCER
NOISE FLOOR (Run 10, Point 0, Channel 7)

Figure 16 shows the free stream transducer signal for a dynamic pressure of 45 psf, an angle of attack of 20 degrees, and a heading angle of -10 degrees. This graph shows several peaks within the free stream signal. Most notable are the peaks near 80, 160, and 240 Hz. These peaks correspond to the wind tunnel blade passage frequency (80 Hz) and its higher harmonics (160 and 240 Hz). Again, these signals are inevitably present in these types of measurements.
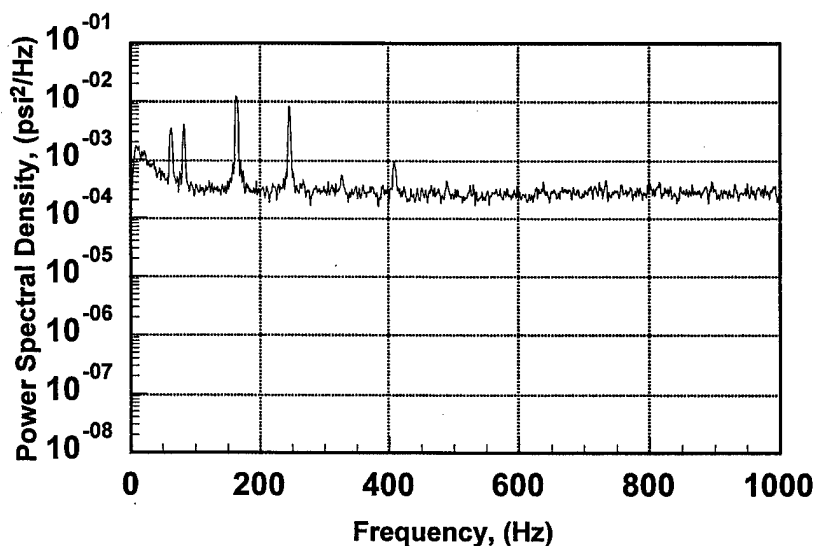
FIGURE 16. POWER SPECTRAL DENSITY OF FREE STREAM PRESSURE
(Run 10, Point 6, Channel 13)

13

Figure 17 shows the PSD of channel 7 without any of the noise and free stream coherence removed. A peak near 80 Hz can be seen in this graph.
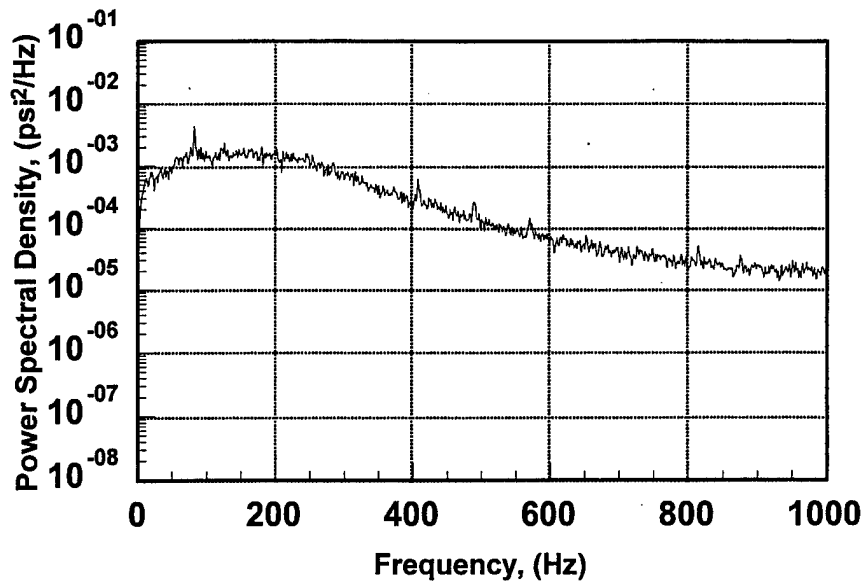
FIGURE 17. POWER SPECTRAL DENSITY OF BUFFET
PRESSURE (Run 10, Point 6, Channel 7)

Figure 18 shows the same data as in figure 17 with the noise floor removed. As expected (in this case), the peak at 80 Hz was not affected by removing the noise floor data because the noise floor was several orders of magnitude lower than the data in figure 18, and the peak at 80 Hz was caused by the wind tunnel propeller blade which was not running during the noise floor data acquisition period.
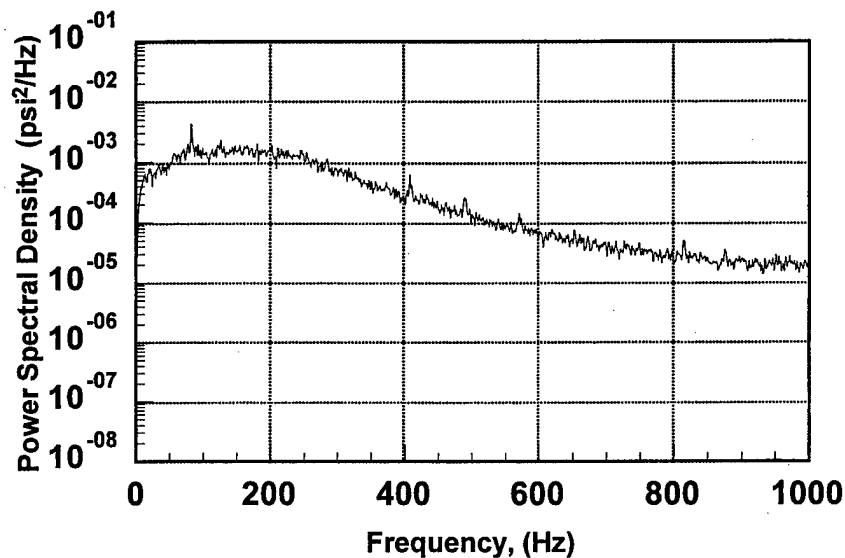
FIGURE 18. POWER SPECTRAL DENSITY OF BUFFET PRESSURE WITH NOISE
FLOOR REMOVED (Run 10, Point 6, Channel 7)

14

Figure 19 illustrates the effect of the removal of the coherence of the signal between the free stream transducer and the transducer of interest on the horizontal tail. The peak at 80 Hz is missing from this plot indicating that it is not due to wing separation (buffet pressure) impinging on the horizontal tail location.
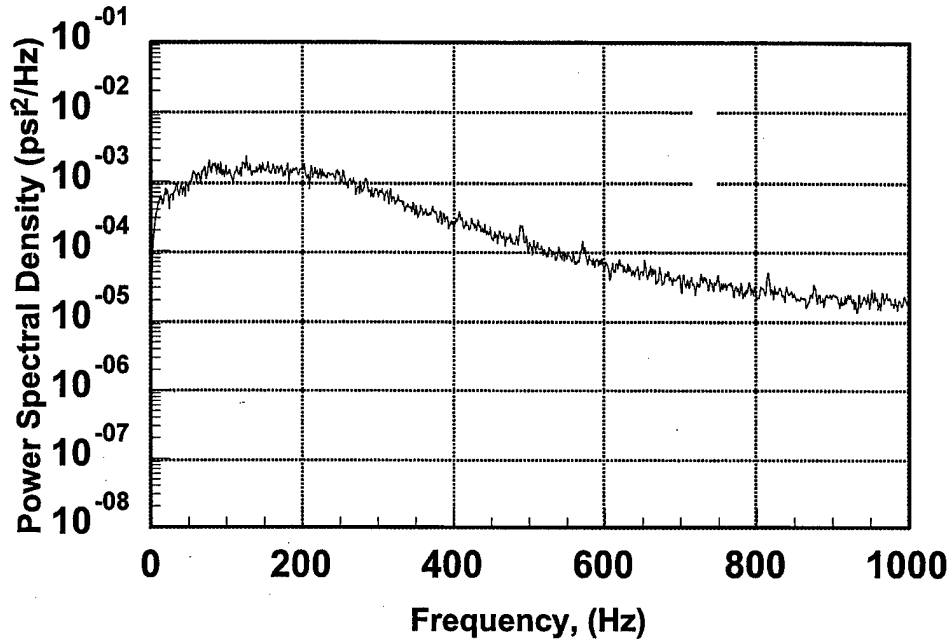
FIGURE 19. POWER SPECTRAL DENSITY OF BUFFET PRESSURE WITH NOISE FLOOR AND FREE STREAM COHERENCE REMOVED (Run 10, Point 6, Channel 7)

To apply the PSD and CSD pressure data to a full-scale finite element model, scaling laws needed to be applied. Equations 9 and 10 give the scaling laws used in this study (a refers to aircraft scale and m refers to model scale):

$$P_a = [(l_a/l_m)(\rho_a/\rho_m)^2(V_a/V_m)^3]P_m \tag{9}$$

$$f_a = [(V_a/V_m)/(l_a/l_m)]f_m \tag{10}$$

These scaling laws are taken directly from reference 3. To check the validity, similar validation plots to those found in reference 3 were prepared. These can be seen in figures 20 and 21. They are in agreement with the results given in reference 3 and the scaling laws are assumed to be valid. Figures 22a through 22c show typical variations of pressure PSD values with angle of attack. Since no significant flow separation exists for the conditions in figure 22a, it will not be compared with figures 22b and 22c. The frequency corresponding to the peak level of PSD shifts to a higher value with increasing angle of attack. Because this study only included two points within this highly separated range, it is difficult to draw any clear conclusions from this trend.

15
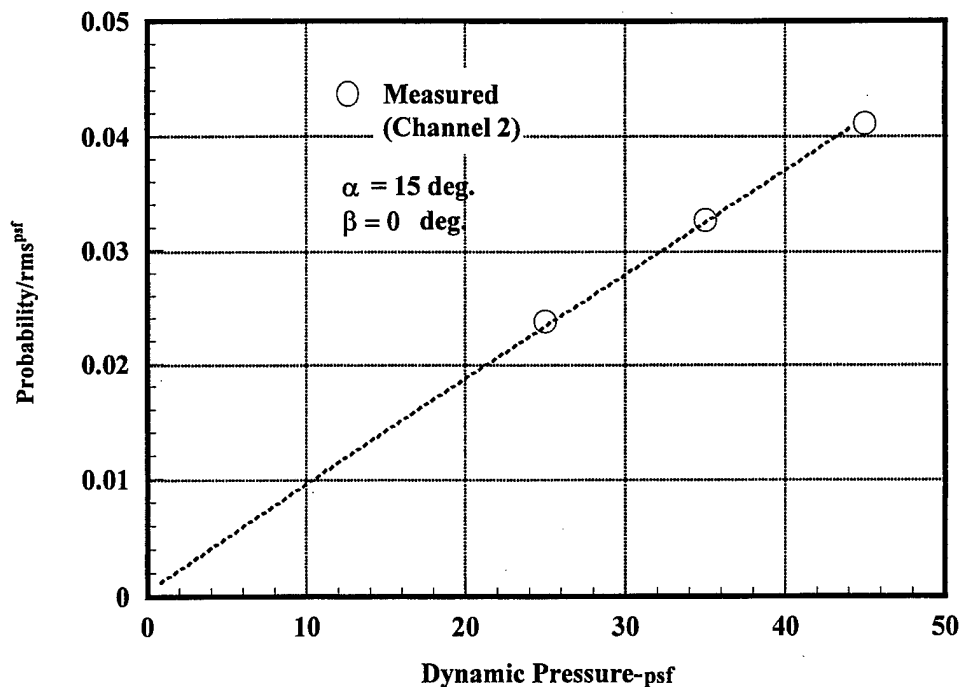
FIGURE 20. VALIDATION CHECK OF ROOT MEAN SQUARE BUFFET PRESSURE
SCALING (1/13-Scale Wind Tunnel Model)
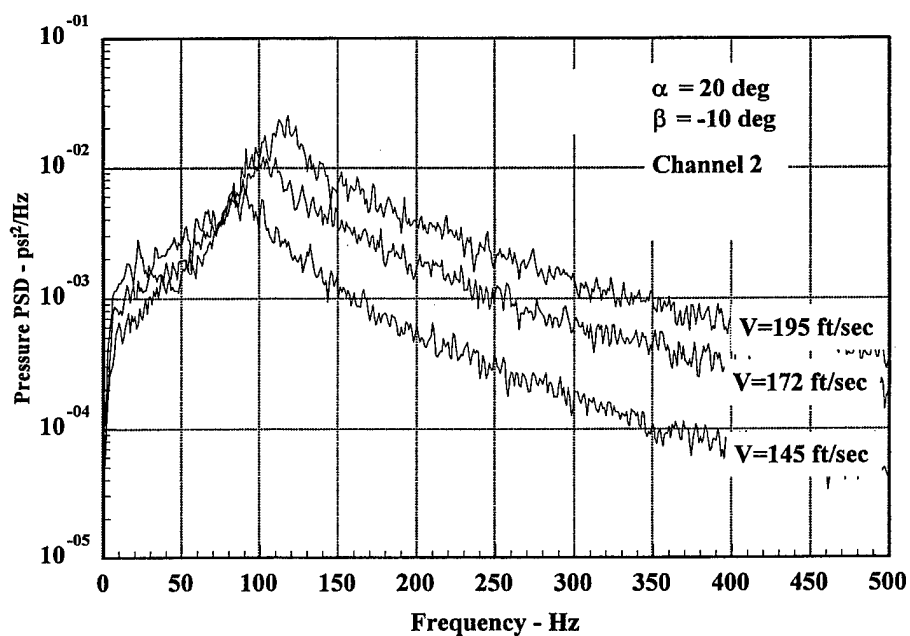
FIGURE 21. VALIDATION OF BUFFET PRESSURE SCALING CHARACTERISTICS
WITH AIRSPEED

16
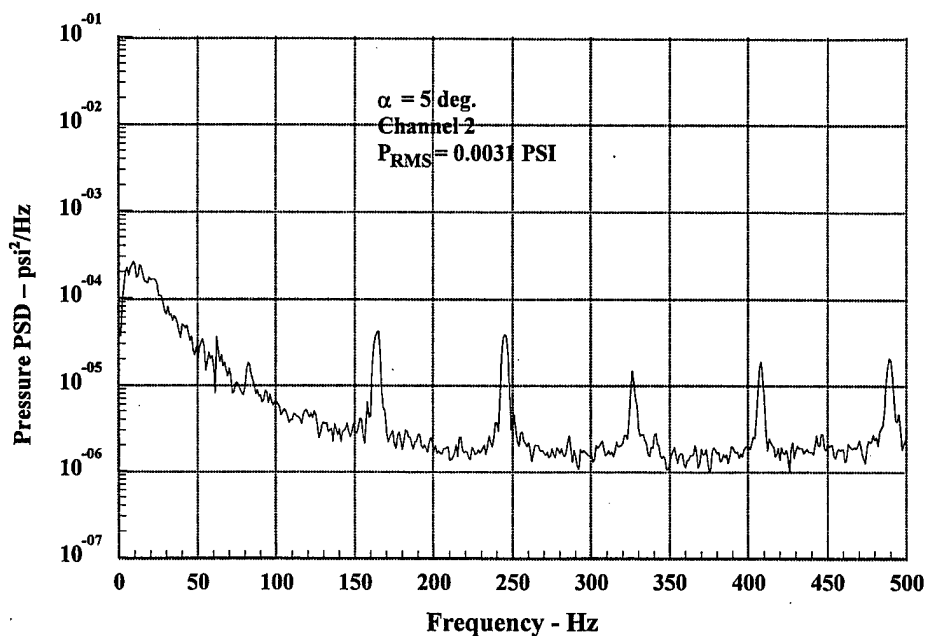
FIGURE 22a. PRESSURE CHARACTERISTIC VARIATION WITH ANGLE OF ATTACK (1/13-Scale Wind Tunnel Model, Q = 45 psf)
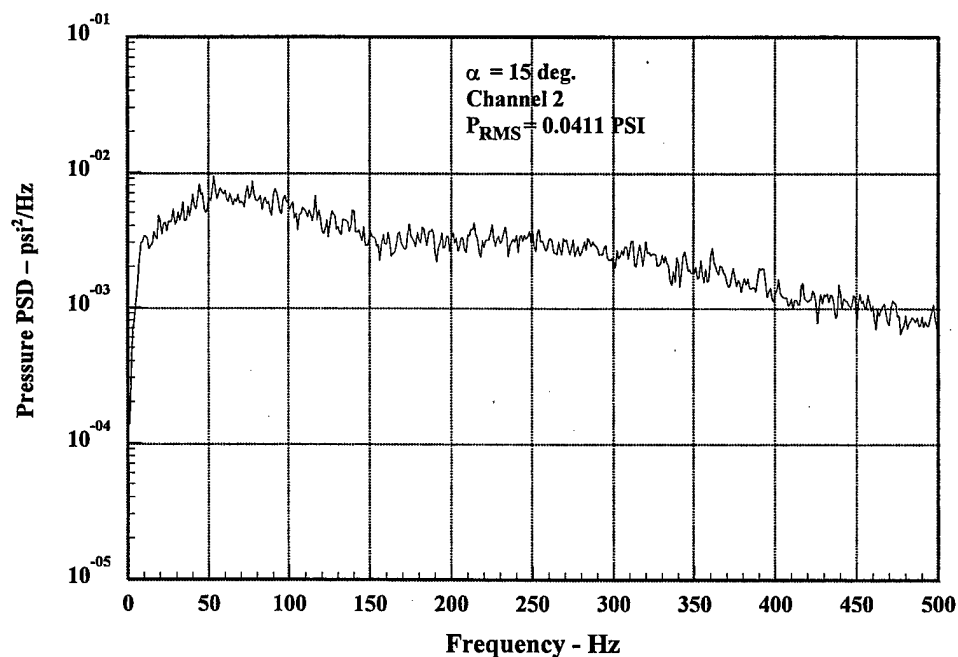
FIGURE 22b. PRESSURE CHARACTERISTIC VARIATION WITH ANGLE OF ATTACK (1/13-Scale Wind Tunnel Model, Q = 45 psf)

17
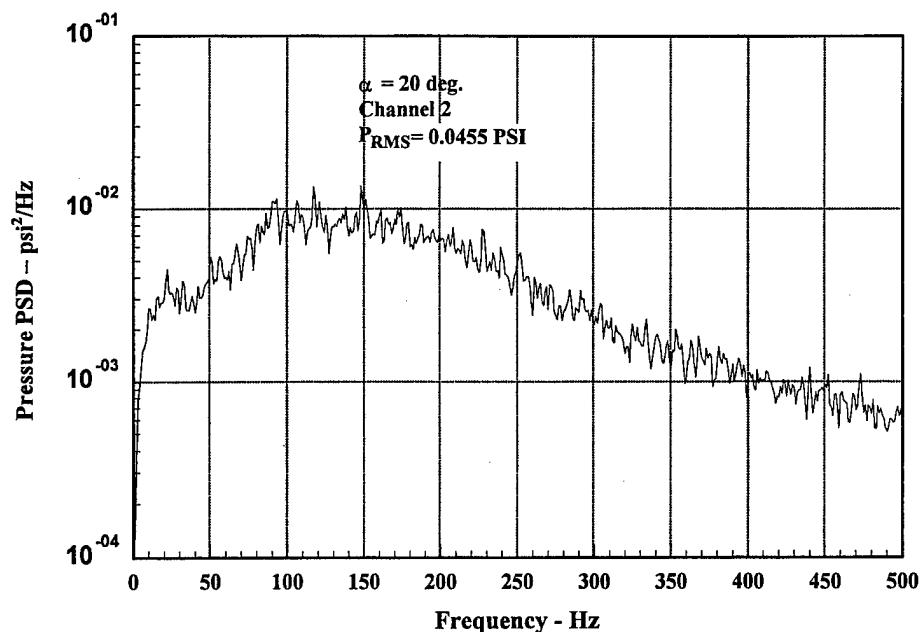
FIGURE 22c. PRESSURE CHARACTERISTIC VARIATION WITH ANGLE OF ATTACK
(1/13-Scale Wind Tunnel Model, Q = 45 psf)

2.2.2 Strain Gage Data.

The strain gage data were analyzed in a manner similar to the pressure data, except that the removal of the coherent data was eliminated. The strain gage data were used to provide a check on the accuracy of the pressure data. To determine this, the pressure data were used in conjunction with a simple finite element model of one side of the horizontal stabilizer. The PSD for the bending moment was calculated at the same locations as the strain gages. The results indicated reasonable agreement between the root bending moment measured by the strain gages and those predicted by the measured buffet pressures and finite element model.

2.3 FINITE ELEMENT ANALYSIS.

2.3.1 Finite Element Model.

Figure 1 schematically represents the overall approach used by Aerotech to predict the number of exceedences of a given rolling moment load. The four boxes in figure 1 which contain the term ASTROS represent the finite element procedure used for this analysis. The first step in the finite element analysis is to model the aircraft and determine its mode shapes and natural frequencies. The next step is to perform an unsteady aerodynamic analysis using the model made in the previous step. This analysis provides the aerodynamic stiffness and damping terms given in equation 1. The next step is to compute the modal complex frequency response matrix, while the final step in the finite element analysis is to calculate the structural response due to unit modal displacements.

18

The finite element model used in this study can be seen in figure 23. It was produced using the MSC/XL software package. Table 2 lists the major dimensions for the model shown in figure 23, while table 3 lists the separate element types used for the aircraft structure. The dimensions of the structural components were estimated using data and drawings from reference 8. The model is restrained in all 6 degrees of freedom at the grid points which define the forward ring frame. The aft fuselage (tail cone) structure was included in the model primarily for its torsional characteristics. Table 4 lists the first nine natural frequencies along with their associated mode shapes. Note that the frequencies referred to here are full-scale frequencies. The appropriate scaling laws are given in the following section. This analysis was limited to these nine frequencies due to the available computational resources. However, the first few modes play the dominant role in the horizontal stabilizer rolling moment due to buffet; therefore, this number of modes was deemed sufficient. Of these nine modes, five are localized in the forward bulkhead that lies inside the ring frame to which the front spar of the vertical tail attaches. Although these modes either will not exist in an actual aircraft, or if they do, they will be insignificant, they were included for computational ease. Figures 24-27 show the four most important modes in this analysis. Mode 1, the first bending mode, occurs at 12.7 Hz. Since the problem at hand is antisymmetrical in nature, this is an important mode. This mode causes the aft spar of the vertical tail to move in a lateral motion while the front spar remains relatively fixed. Mode 2 occurs at 15 Hz. This mode is similar to mode 6 which occurs at 26.2 Hz. They are both symmetrical flapping modes. During mode 2, the vertical moves forward and aft along with the horizontal stabilizer flapping motion. As the vertical tail structure reaches its furthest point forward, the tips of the horizontal stabilizer are at their highest point. The reverse is true for mode 6. As the vertical tail structure reaches its furthest point forward, the horizontal stabilizer tips bend downward and reach their lowest point. The final mode of interest is the secondary bending mode which occurs at a frequency of 24.2 Hz. In addition to its bending, it imparts a torsional load to the fuselage structure.
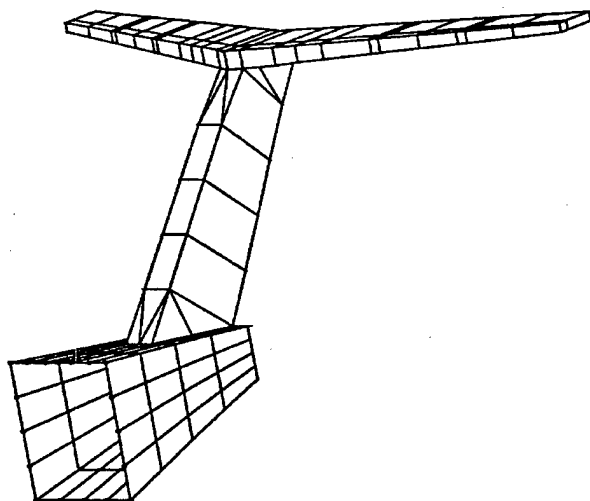
FIGURE 23. FINITE ELEMENT MODEL OF BEECH SUPER KING AIR 200 AFT TAIL CONE AND TAIL STRUCTURE

TABLE 2. GEOMETRIC VALUES USED FOR FINITE ELEMENT ANALYSIS

Characteristic	Value
Tail Span	121 inches
Root Chord	60 inches
Tip Chord	30 inches
Root Depth	6 inches
Tip Depth	3 inches
Front Spar	15% Chord
Rear Spar	Elevator Hinge Line

TABLE 3. FINITE ELEMENT TYPES USED IN THE ANALYSIS

Component	Element	Properties
Skin	CQUAD4/CTRIA3	0.032 in. thick
Longeron	CBAR	1.25-in. x 1/8-in. x 2-in. I-Beam
Ring Frame	CBAR	1.25-in. x 1/8-in. x 2-in. I-Beam
Ribs (web)	CSHEAR	0.1 in. thick
Spar (web)	CSHEAR	0.1 in. thick
Bulkheads	CQUAD4	0.1 in. thick
Rib (flange)	CROD	0.1 sq. in. area
Spar (flange)	CBAR	1.25-in. x 1/8-in. Beam

TABLE 4. NATURAL FREQUENCY AND MODES

Mode		Type
1	12.7 Hz	First Bending Mode
2	15.0 Hz	First Flapping Mode
3	23.1 Hz	Local Forward Bulkhead
4	24.2 Hz	Second Bending Mode
5	25.9 Hz	Local Forward Bulkhead
6	26.2 Hz	Second Flapping Mode
7	41.3 Hz	Local Forward Bulkhead
8	46.4 Hz	Local Forward Bulkhead
9	49.9 Hz	Local Forward Bulkhead
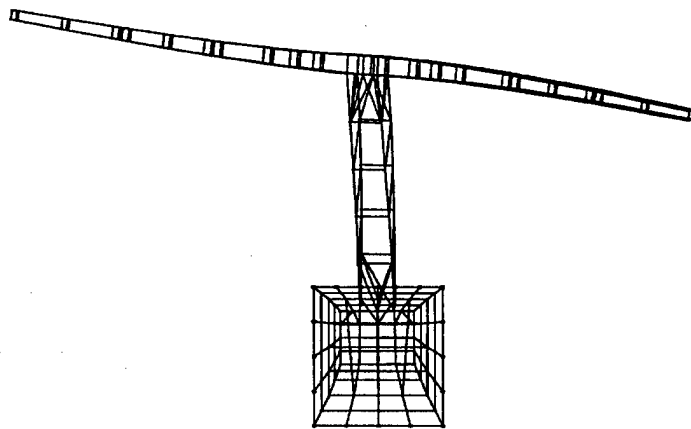
FIGURE 24. MODE 1 OF TAIL STRUCTURE (f_n = 12.7 Hz)
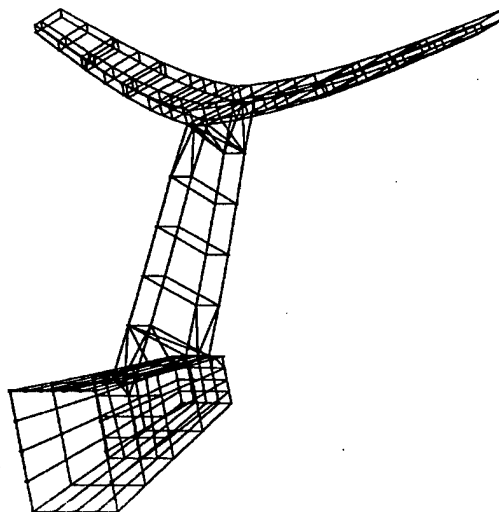
FIGURE 25. MODE 2 OF TAIL STRUCTURE (f_n = 15.0 Hz)
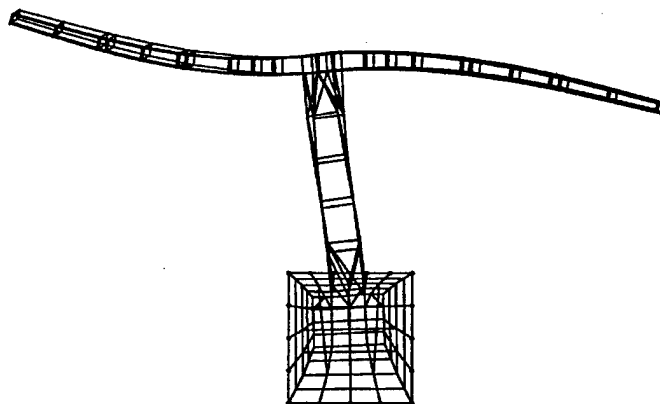
FIGURE 26. MODE 4 OF TAIL STRUCTURE (f_n = 24.2 Hz)
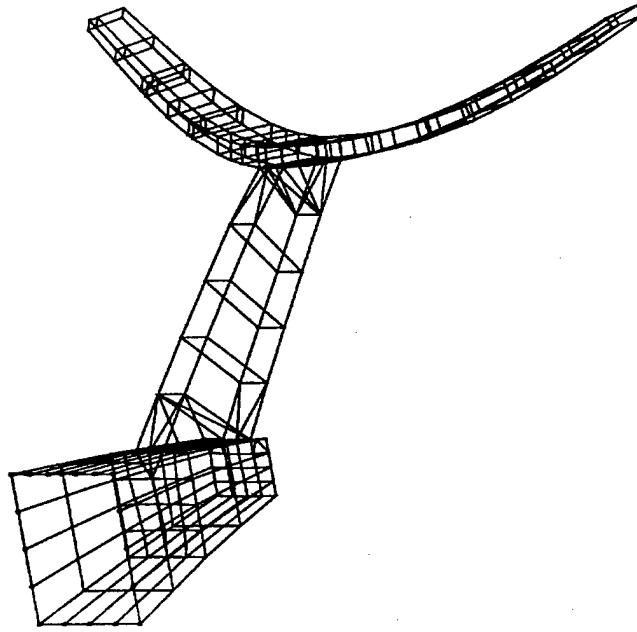
FIGURE 27. MODE 6 OF TAIL STRUCTURE ($f_n = 26.2$ Hz)

2.3.2 Finite Element Analysis Procedure.

ASTROS (Automated STRuctural Optimization System) finite element software was used for the finite element analysis. This program is a multidisciplinary finite element-based procedure for the design and analysis of aerospace structures.[9] It is a public domain program with proven capabilities paralleling those of the widely used NASTRAN. ASTROS is written in a flexible high-level language, MAPOL (Matrix Analysis Problem Oriented Language). Although the program does not directly support buffet analysis, ASTROS can be used for buffet analysis by modifying the standard MAPOL sequence. All of the terms on the left-hand side of equation 1 were calculated using ASTROS. As mentioned previously, linear modal analysis was performed to determine the natural frequencies and mode shapes of the system, and this determines the first three terms in equation 1. Since the buffet pressure excitation, P_n, was determined experimentally in the wind tunnel, only the motion-dependent aerodynamic and stiffness terms remain to be calculated.

The ASTROS flutter, gust, and blast analyses solution sequences include the aerodynamic stiffness and damping terms of equation 1. These terms are computed by use of the doublet lattice method which is recognized as a standard in the aerospace industry. The aerodynamic model was created using aerodynamic panel elements (CAERO1). For this study, only the horizontal stabilizer was modeled for these terms.

There are two differences between the present problem and the ASTROS gust analysis solution sequence: (1) the right-hand side of equation 1 is different and (2) a gust analysis in ASTROS is treated as a frequency response analysis, not a random response analysis. The present buffet problem was solved using a multistep approach.

22

The first step was to determine the modal complex frequency response matrix, [H(ω)]. This matrix can be computed at each frequency of interest by replacing the gust analysis right-hand side with the identity matrix. The resulting response matrix is [H(ω)]. Step two is to perform the following matrix multiplication to determine the modal buffet pressures

$$[S_x(\omega)]=[\phi]^T[S(\omega)][\phi]$$ (10)

where [S(ω)] is a matrix of forces corresponding to the pressures measured in the wind tunnel. To determine this matrix the pressures were first scaled to full-scale using the equations 9 and 10 and then multiplied by the area in which they act.

The third step is to compute the modal response PSD matrix, [S(ω)]. This matrix multiplication is given by equation 11.

$$[S(\omega)]=[H(-\omega)][S_x(\omega)][H(\omega)]^T$$ (11)

The fourth step involves using ASTROS to calculate the structural responses [N_y] due to unit modal displacements. This requires the MAPOL sequence to be modified in a similar manner to the first step in this process. The terms in the row matrix [N_y] are the structural responses due to unit modal displacements. For example, if the desired output is the PSD of the axial force in a bar element, N_{y11} represents the axial force due to $q_1=1$ and $q_2=q_3...q_{(\# modes)}=0$.

The fifth step is to solve for the structural responses [$S_y(\omega)$] using equation 12.

$$[S_y(\omega)]=[N_y][S(\omega)][N_y]^T$$ (12)

The complex structural responses found using equation 12 can be used to determine a variety of structural responses. What is of interest to this study is the rolling moment generated on the horizontal stabilizer. The rolling moment generated on the horizontal stabilizer was determined using equation 13 and the forces defined in figure 28. These are the axial forces in the CBAR elements which model the attachment of the vertical tail to the horizontal stabilizer. Since these values are complex, the phase information from the wind tunnel pressures are preserved and by taking the difference an overall rolling moment can be calculated.

$$M_R=[(F_1+F_2)-(F_3+F_4)]*d^2/2$$ (13)

Figures 29a through 29f show a representative series of horizontal stabilizer rolling moments generated in this manner. Although the data extends to nearly 80 Hz (full scale), little happened past 50 Hz therefore only 0-50 Hz was plotted. Figures 29a through 29d indicate very little buffet-induced rolling moments, as to be expected, from the combination of low dynamic pressure angle of attack and sideslip angle. Figures 29e through 29f indicate much higher rolling moments than the other four cases, as is expected, as the highly separated flow field at these conditions impinges on the stabilizer. In all cases, the first two modes have the highest response indicating their importance to the buffet-induced rolling moment phenomenon.
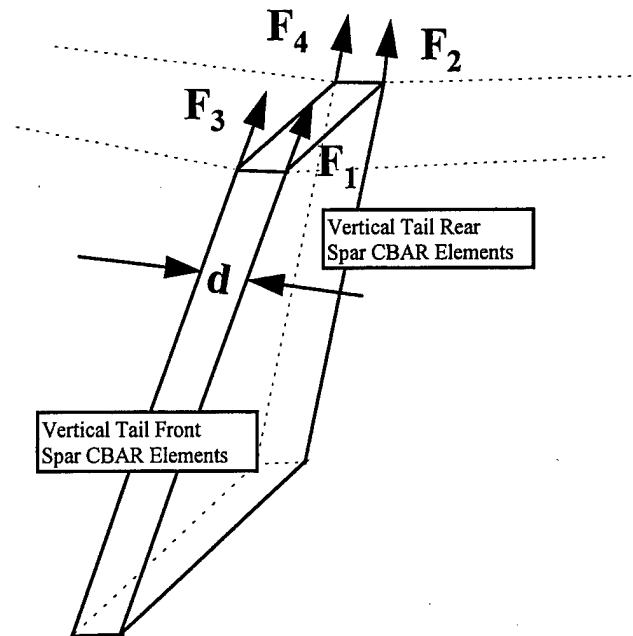
FIGURE 28. AXIAL FORCE COMPONENTS USED FOR ROLLING MOMENT
COMPUTATION
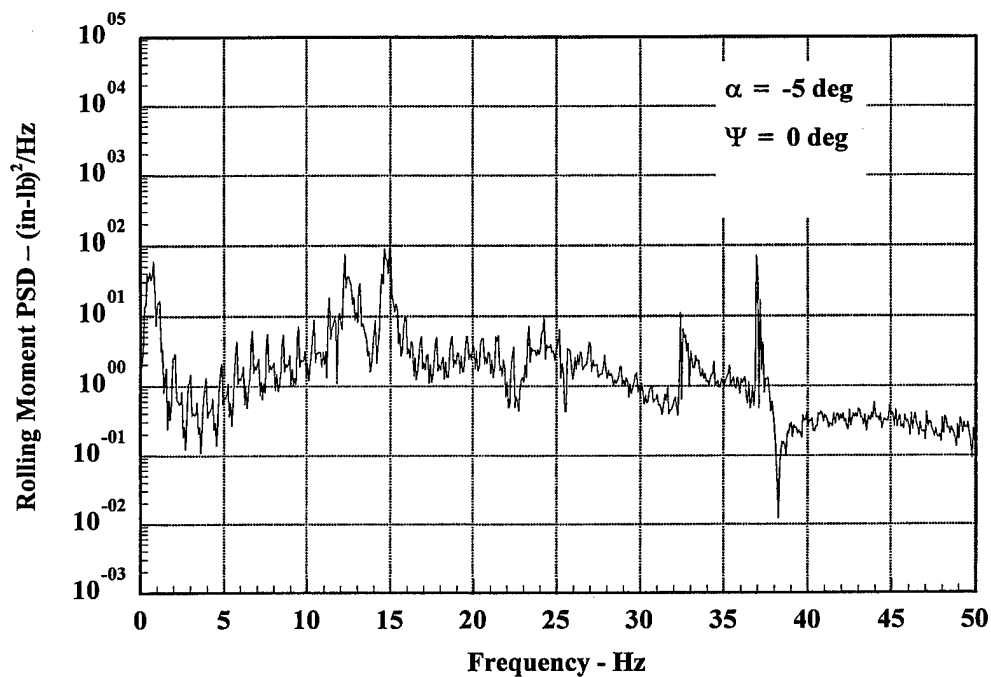
FIGURE 29a. POWER SPECTRAL DENSITY OF PREDICTED ROLLING MOMENT
(Q = 25 psf)
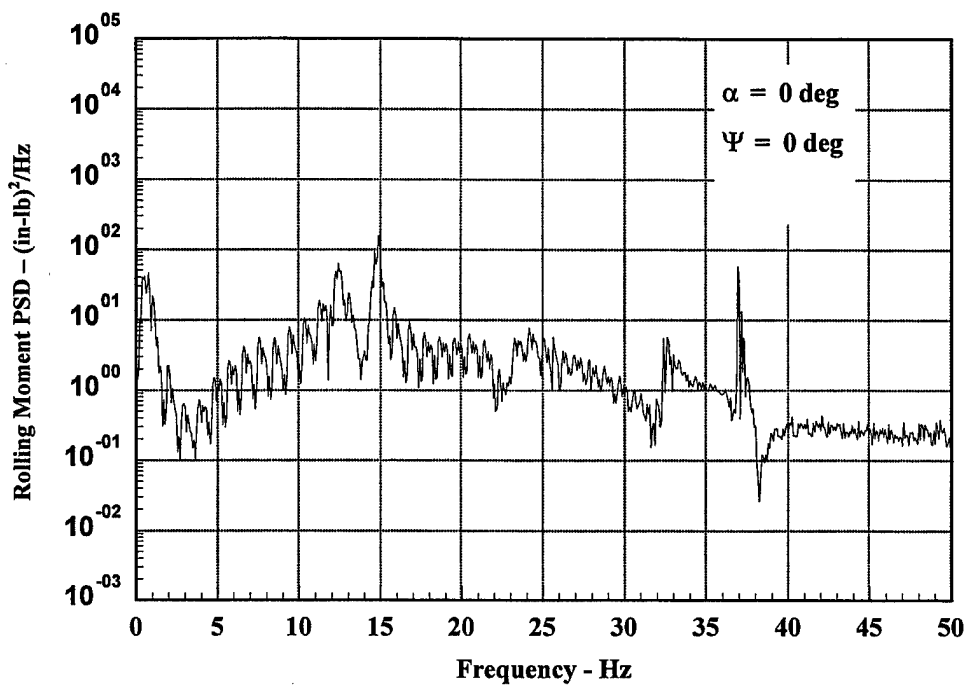
FIGURE 29b. POWER SPECTRAL DENSITY OF PREDICTED ROLLING MOMENT
(Q = 25 psf)
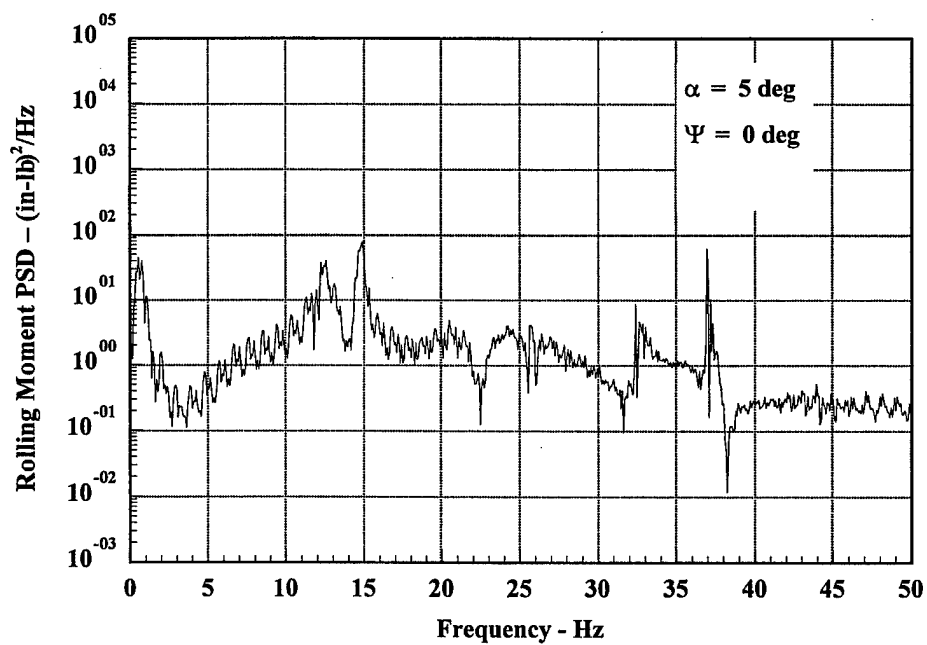
FIGURE 29c. POWER SPECTRAL DENSITY OF PREDICTED ROLLING MOMENT
(Q = 25 psf)
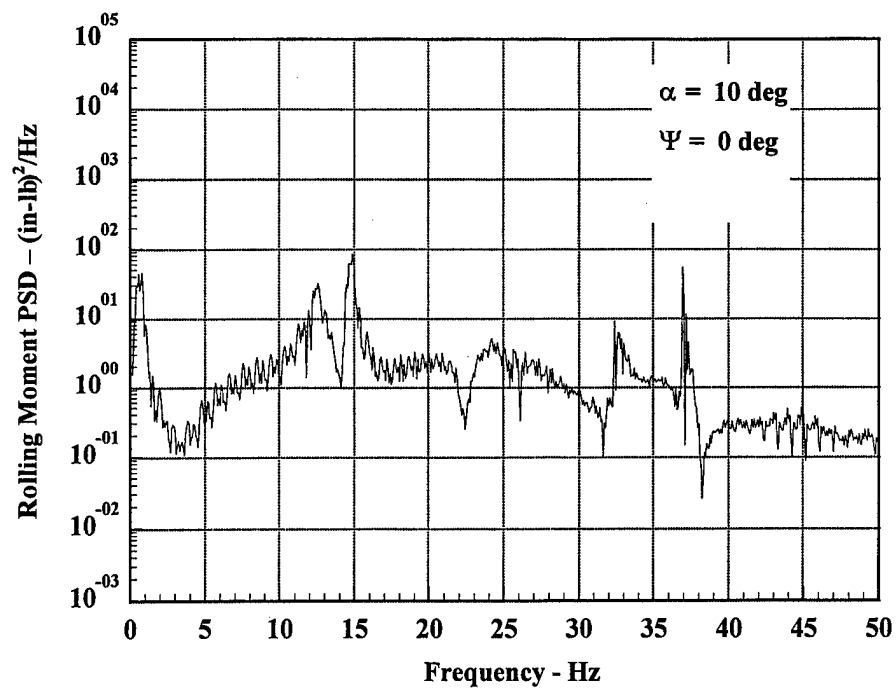
FIGURE 29d. POWER SPECTRAL DENSITY OF PREDICTED ROLLING MOMENT
(Q = 25 psf)
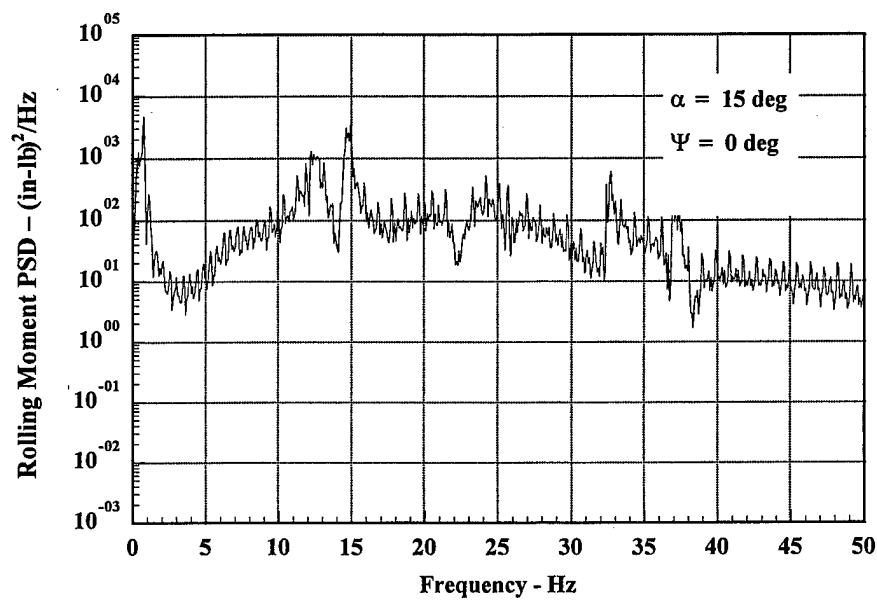
FIGURE 29e. POWER SPECTRAL DENSITY OF PREDICTED ROLLING MOMENT
(Q = 25 psf)

26
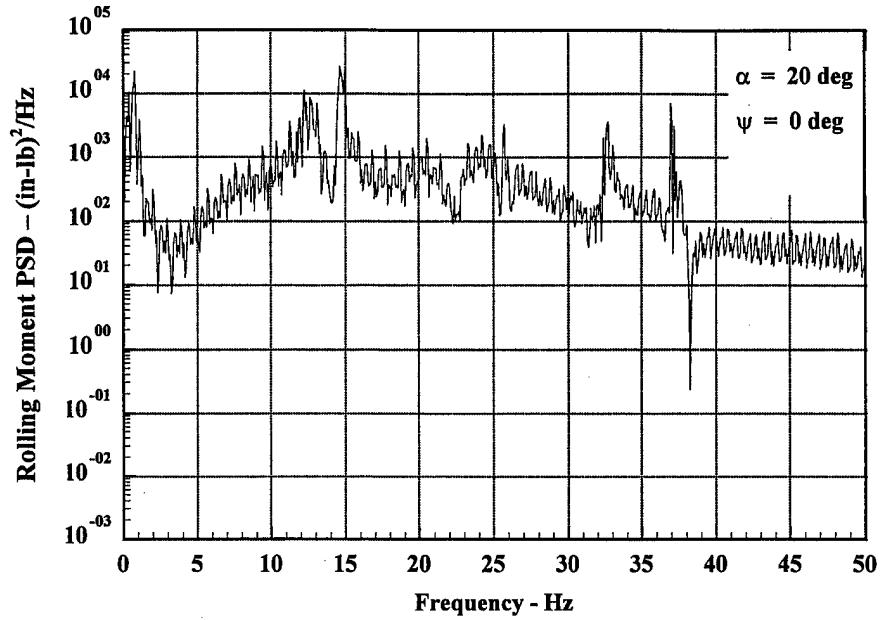
FIGURE 29f. POWER SPECTRAL DENSITY OF PREDICTED ROLLING MOMENT
(Q = 25 psf)

The final step in the design procedure is to determine the number of exceedences of a given loading level (in this case, a rolling moment on the horizontal stabilizer) that occur for a specific flight history as indicated in figure 30. Equation 14 shows the method used.

$$N(R.M.) = \sum_{k=1}^{X} f_k \sum_{i=1}^{I} P_{i,k}(R.M.) t_i \tag{14}$$

The $P_{i,k}$ term in equation 14 represents the probability that a given peak of the structural response PSD will exceed a given level. This is given by the relation shown in equation 15. This represents the Rayleigh distribution which applies to the peak values in the PSD of random responses.[10]

$$P_{i,k}(R.M.) = \int_{\frac{R.M.}{\sigma_{i,k}}}^{\infty} \frac{R.M.}{\sigma_{i,k}^2} e^{-R.M.^2 / 2\sigma_{i,k}^2} d(R.M.) \tag{15}$$

The variance in equation (15) is given by

$$\sigma^2_{i,k} = \frac{E_{j,j}(f_k) f_k \pi}{4 \xi_k} \tag{16}$$

27

$E_{j,j}(f_k)$ is the PSD of the rolling moment calculated using equation 13 and ξ_k is the structural damping which is assumed to be 0.03 for this study.

The final step is to calculate several values using equation 14 and plot the results.
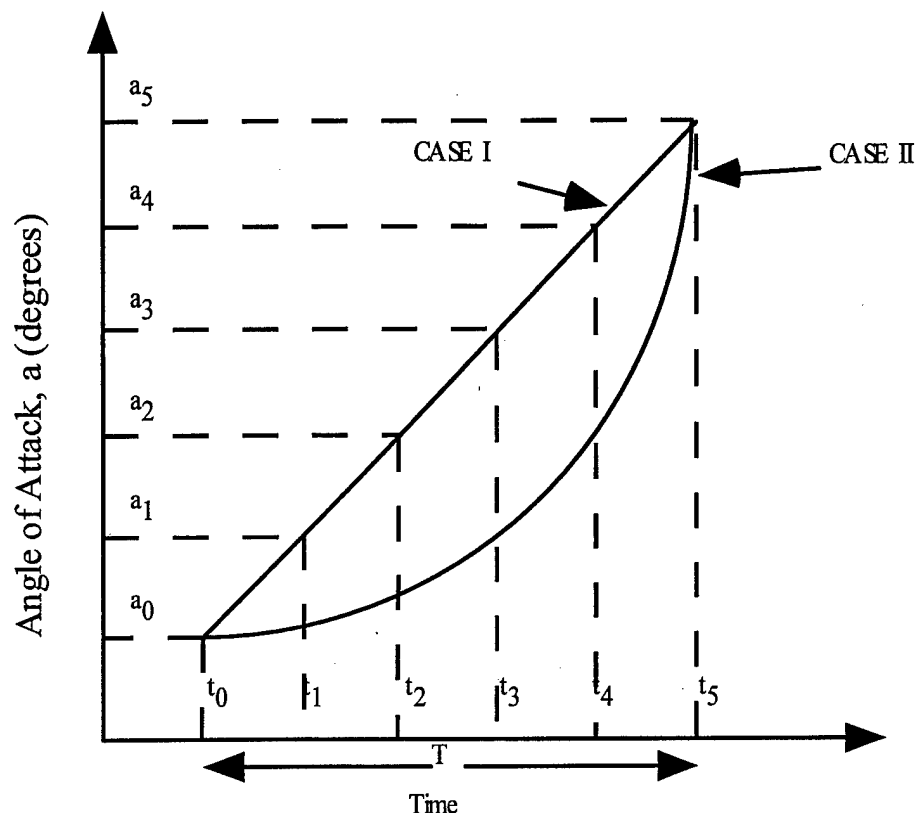
FIGURE 30. DEFINITION OF A STALL EVENT

The data given in figures 29a through 29f were used with equations 14-16 to determine a predicted design curve for the number of exceedences for a given stall event as shown in figure 31. Figure 31 was made for methodology demonstration only. The stall event was assumed to occur in a linear fashion with the aircraft holding each one of the six loading conditions (there are six angle-of-attack data points) for two seconds. As expected from equation 15, the curve drops rapidly with increasing specified rolling moment levels until it nearly reaches zero by a rolling moment of 5000 in-lbs.
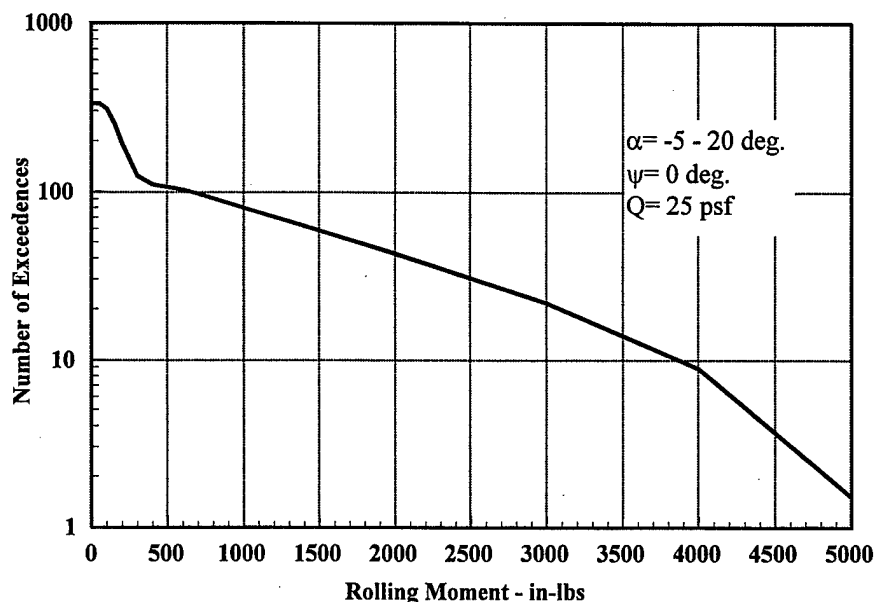
FIGURE 31. PREDICTION OF NUMBER OF EXCEEDENCES FOR A
GIVEN STALL EVENT

3. CONCLUSIONS.

Based on rigid model wind tunnel pressure measurements and an aeroelastic, full-scale finite element model, a design methodology for the rapid and low-cost assessment of the rolling moment loads due to asymmetric horizontal stabilizer buffeting has been demonstrated. Now that the feasibility of the process has been demonstrated, the validity of the approach needs to be determined. It is recommended that the methodology should be applied to an actual aircraft and predictions compared with flight tests to confirm the results.

4. REFERENCES.

1.   Triplett, W.E., "Pressure Measurements on Twin Vertical Tails in Buffeting Flow," *Journal of Aircraft*, Vol. 20, No. 11, November 1983, pp. 920-925.

2.   Mauk, C.S., "Methods of Stochastic Modeling of Antisymmetric Buffet Loads on Horizontal Stabilizers in Massively Separated Flows," Aerotech Technical Report AER TR93-052, May 5, 1993.

3.   Ferman, M.A., Patel, S.R., Zimmerman, N.H., and Gerstenkorn, G., "A Unified Approach to Buffet Response of Fighter Aircraft Empennage," AGARD CP-483, 1990.

4.   Butler, G.F. and Jones, J.G., "The Prediction of Buffeting Response in Flight from Wind-Tunnel Measurements on Models of Conventional Construction," *Aeronautical Journal*, Aug./Sept. 1984.

5. Farokhi, S., Mauk C.S., and Locke, J.E., "Stochastic Modeling of Antisymmetric Buffet Loads on Horizontal Stabilizers in Massively Separated Flows," DOT/FAA/AR-95/7, March 1996.

6. Bendat, J.S. and Piersol, A.G., <u>Random Data: Analysis and Measurement Procedures</u>, John Wiley & Sons, New York, 1986.

7. Bendat, J.S. and Piersol, A.G., <u>Engineering Applications of Correlation and Spectral Analysis</u>, John Wiley & Sons, New York, 1993.

8. Taylor, J.W.R., <u>Jane's All The World Aircraft</u>, Jane's Publishing Company, London.

9. Neill, D.J. and Herendeen, D.L., <u>ASTROS Enhancements: Volume I - ASTROS User's Manual</u>, WL-TR-93-3025, March 1993.

10. Wirsching, H.P., Paez, L.T., and Ortiz, K., <u>Random Vibrations: Theory and Practice</u>, John Wiley & Sons, New York, 1995.

APPENDIX A—TEST MATRIX

Run Number	Data Point	Dynamic Pressure (psf)	Alpha (deg.)	psi (deg.)
5	0 (Noise Floor)	0	N/A	N/A
	1	25	-5	0
	2	25	0	0
	3	25	5	0
	4	25	10	0
	5	25	15	0
	6	5	20	0
6	0 (Noise Floor)	0	N/A	N/A
	1	35	-5	0
	2	35	0	0
	3	35	5	0
	4	35	10	0
	5	35	15	0
	6	35	20	0
7	0 (Noise Floor)	0	N/A	N/A
	1	45	-5	0
	2	45	0	0
	3	45	5	0
	4	45	10	0
	5	45	15	0
	6	45	20	0
8	0 (Noise Floor)	0	N/A	N/A
	1	25	-5	-10
	2	25	0	-10
	3	25	5	-10
	4	25	10	-10
	5	25	15	-10
	6	25	20	-10
9	0 (Noise Floor)	0	N/A	N/A
	1	35	-5	-10
	2	35	0	-10
	3	35	5	-10
	4	35	10	-10
	5	35	15	-10
	6	35	20	-10
10	0 (Noise Floor)	0	N/A	N/A
	1	45	-5	-10
	2	45	0	-10
	3	45	5	-10
	4	45	10	-10
	5	45	15	-10
	6	45	20	-10

Run Number	Data Point	Dynamic Pressure (psf)	Alpha (deg.)	psi (deg.)
11	0 (Noise Floor)	0	N/A	N/A
	1	25	-5	-20
	2	25	0	-20
	3	25	5	-20
	4	25	10	-20
	5	25	15	-20
	6	25	20	-20
12	0 (Noise Floor)	0	N/A	N/A
	1	35	-5	-20
	2	35	0	-20
	3	35	5	-20
	4	35	10	-20
	5	35	15	-20
	6	35	20	-20
13	0 (Noise Floor)	0	N/A	N/A
	1	45	-5	-20
	2	45	0	-20
	3	45	5	-20
	4	45	10	-20
	5	45	15	-20
	6	45	20	-20
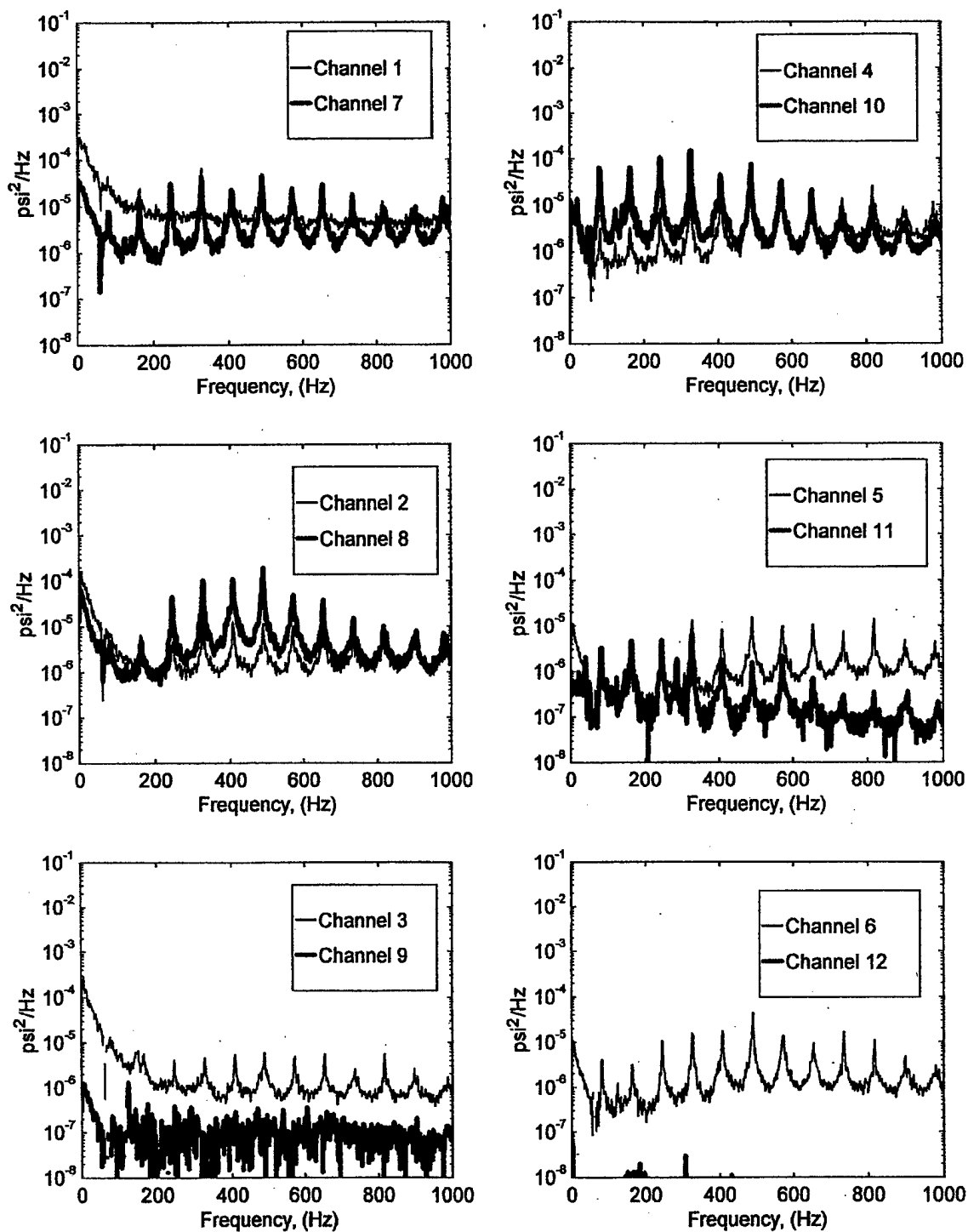
FIGURE B-1. PRESSURE POWER SPECTRAL DENSITY (RUN 5, POINT 1)
$(\overline{q} = 25 psf, \alpha = -5^{\circ}, \psi = 0^{\circ})$
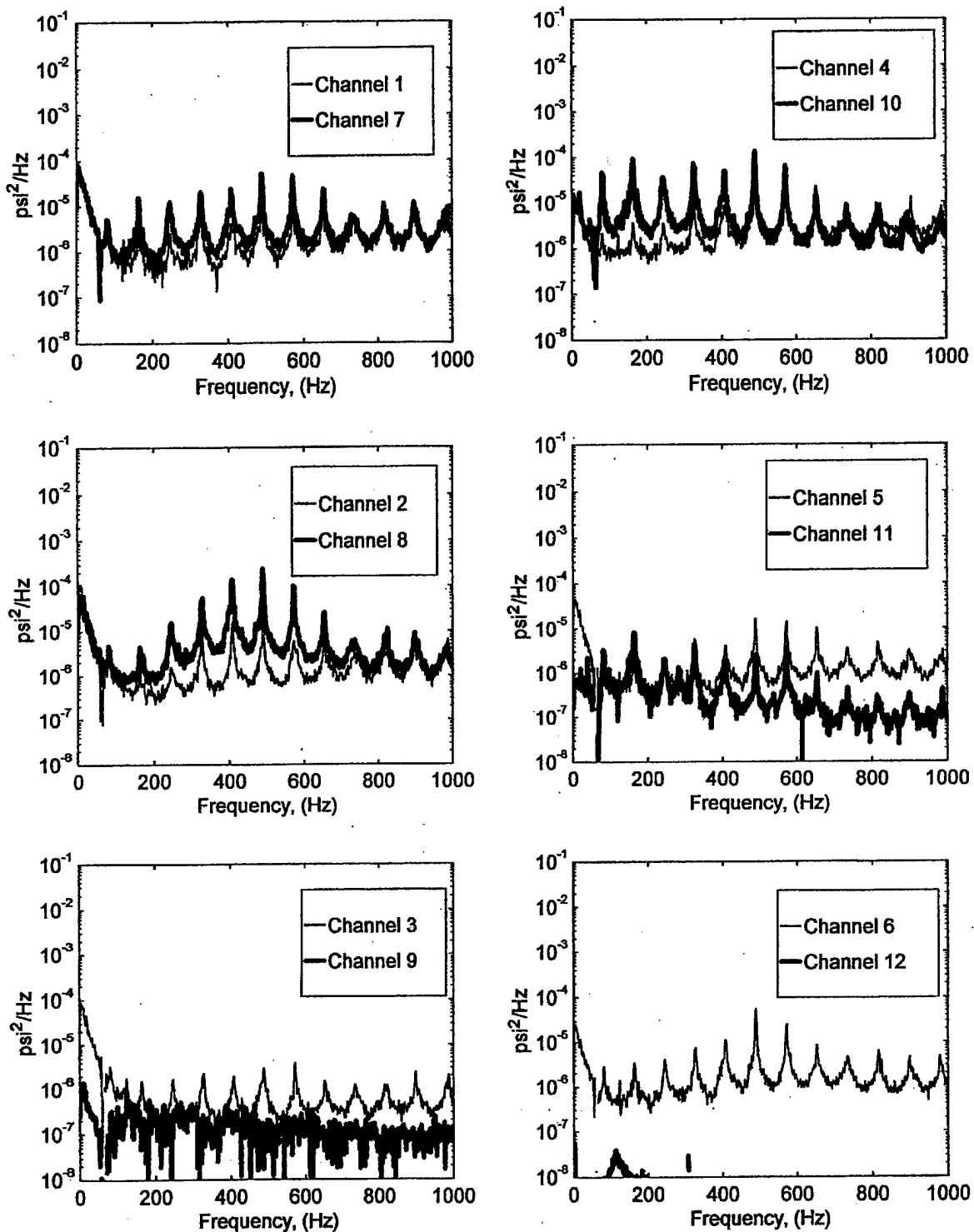
FIGURE B-2. PRESSURE POWER SPECTRAL DENSITY (RUN 5, POINT 2)
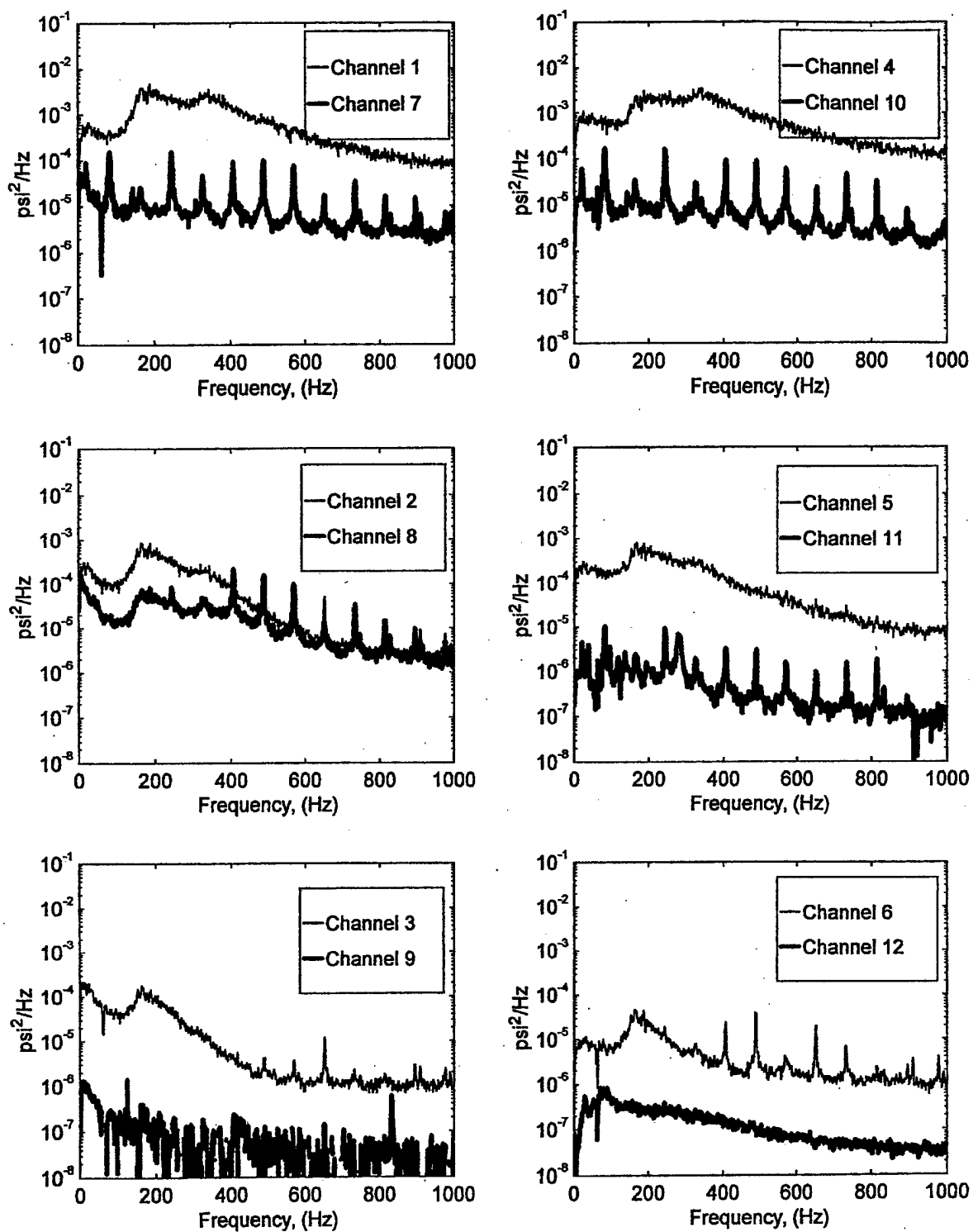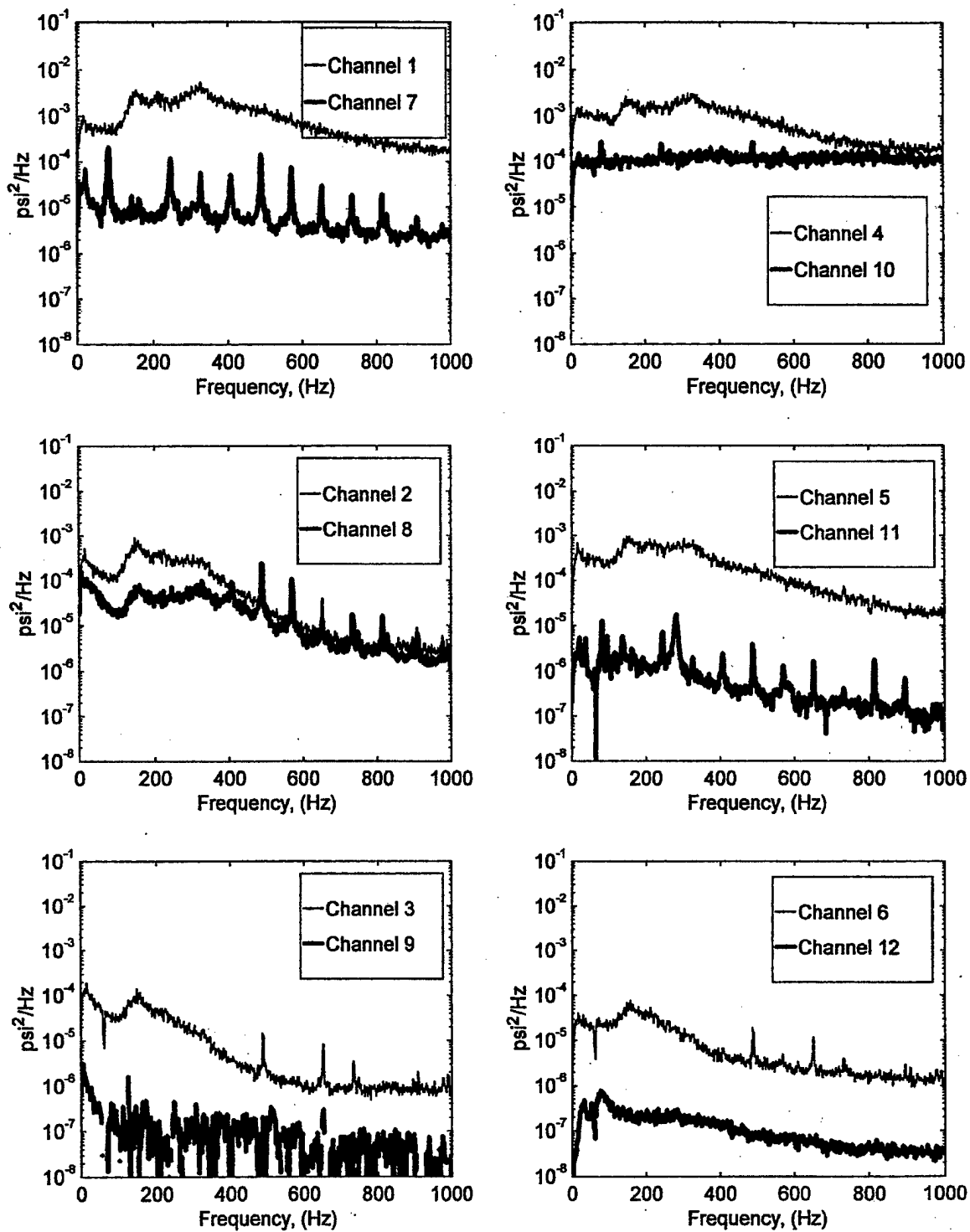$(\bar{q} = 25psf, \alpha = 0^{\circ}, \psi = 0^{\circ})$
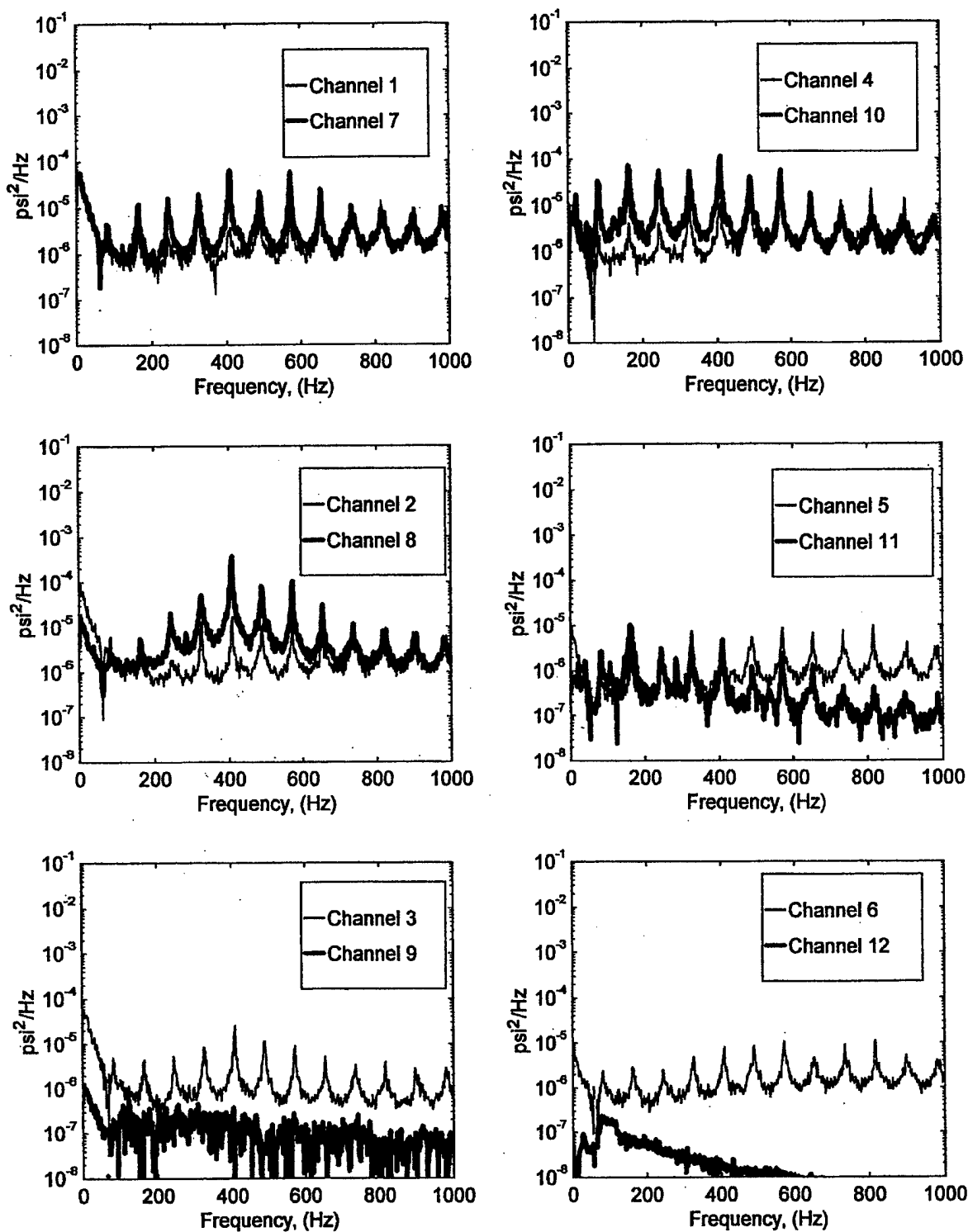
FIGURE B-3. PRESSURE POWER SPECTRAL DENSITY (RUN 5, POINT 3)
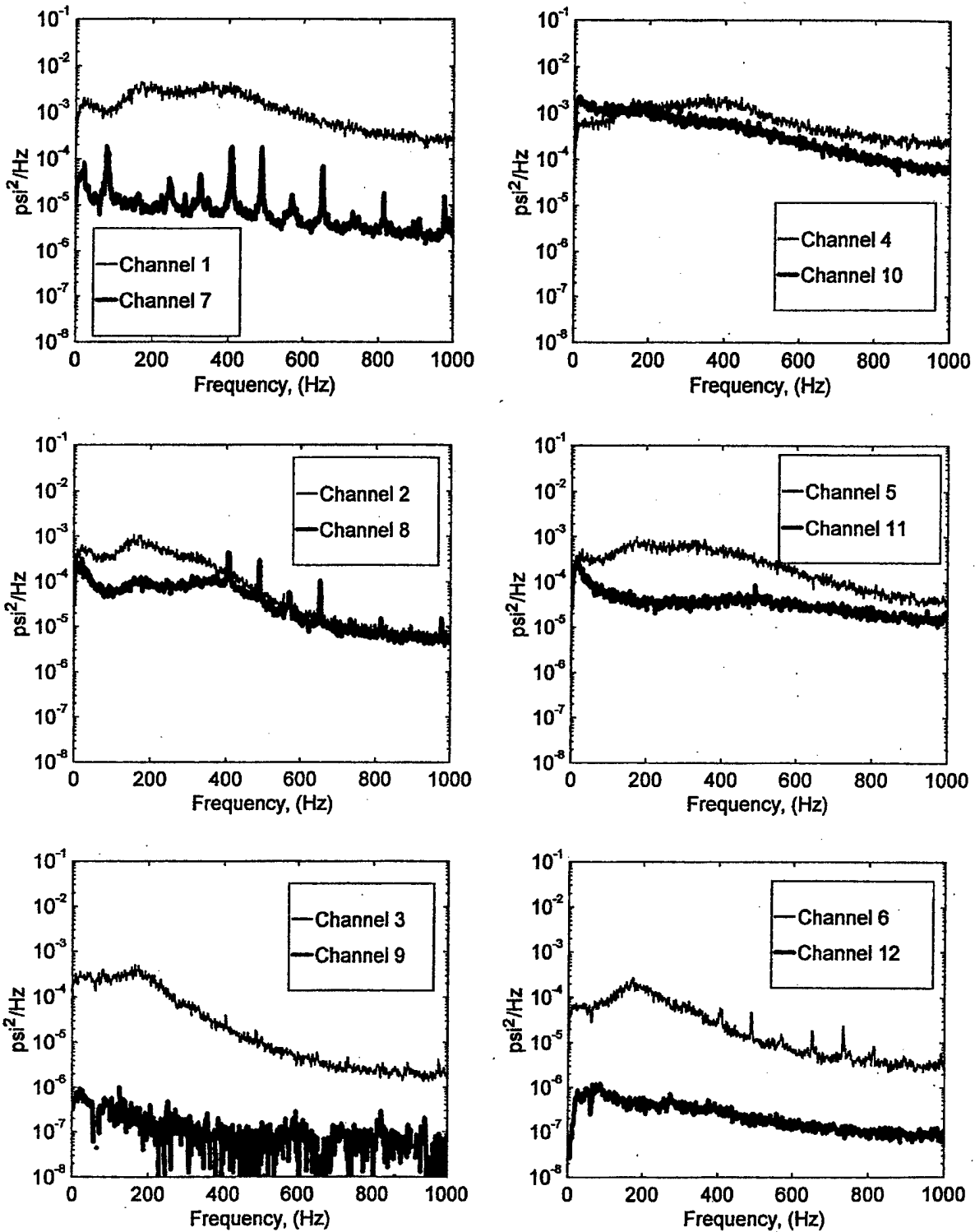$(\bar{q} = 25psf, \alpha = 5^\circ, \psi = 0^\circ)$
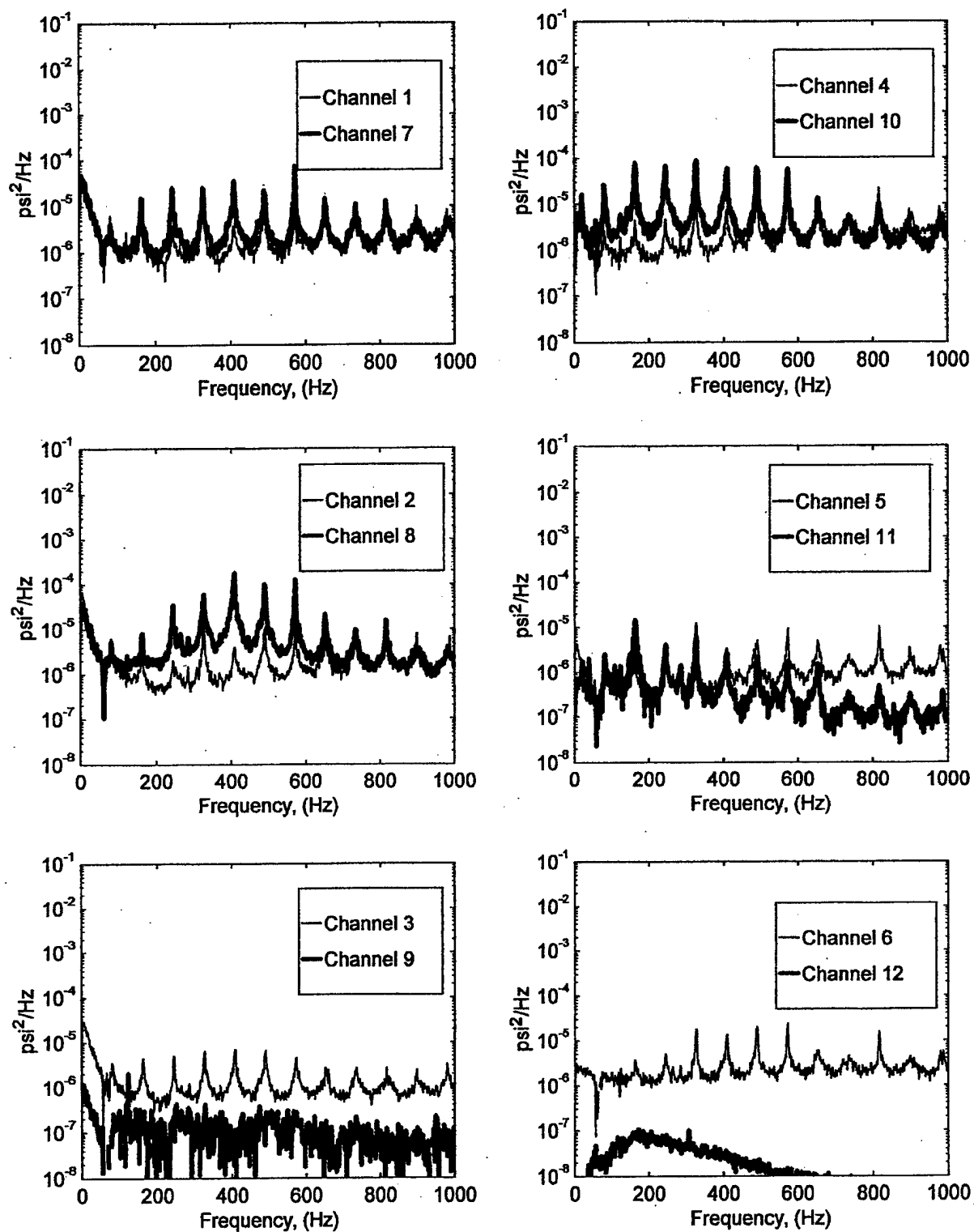
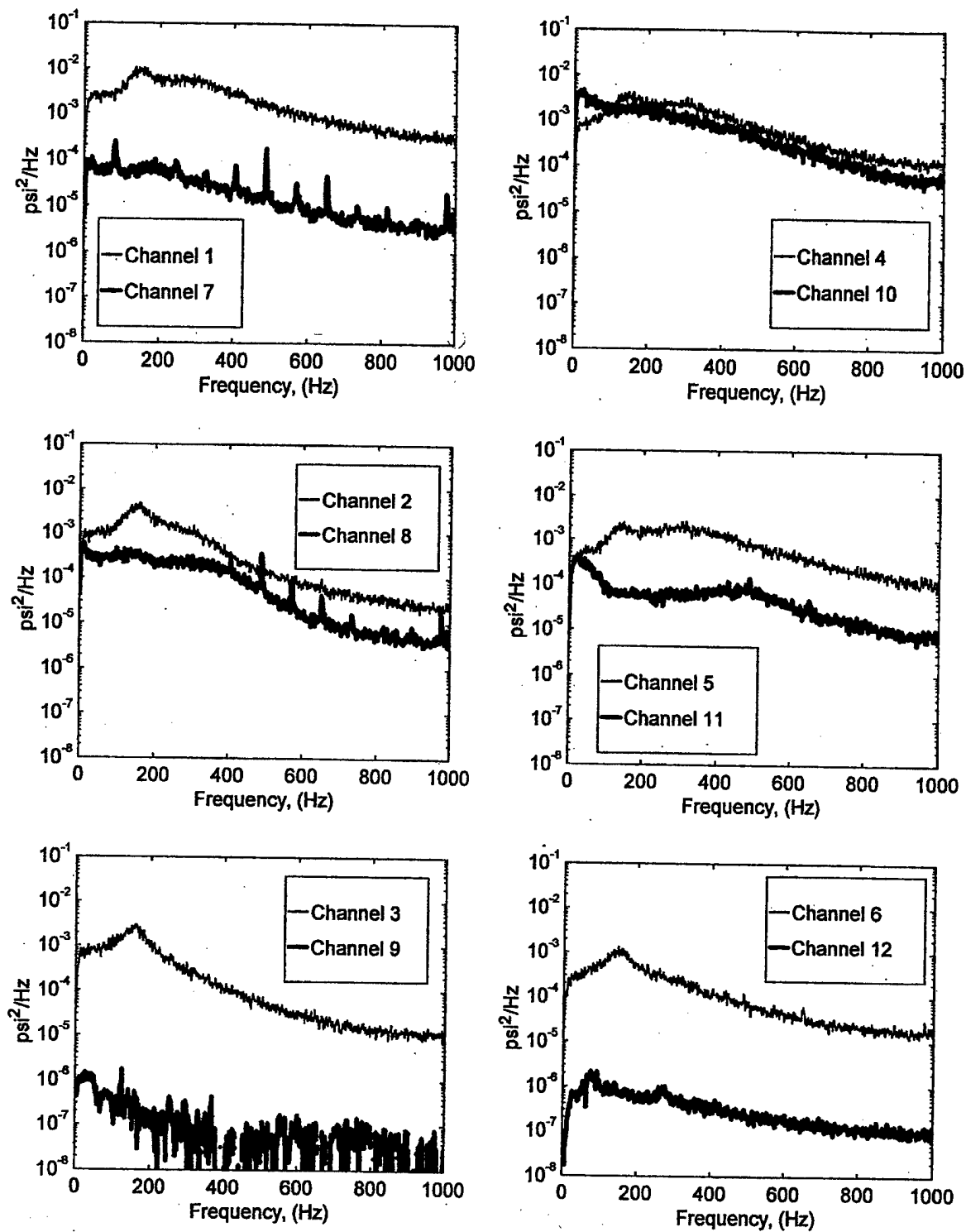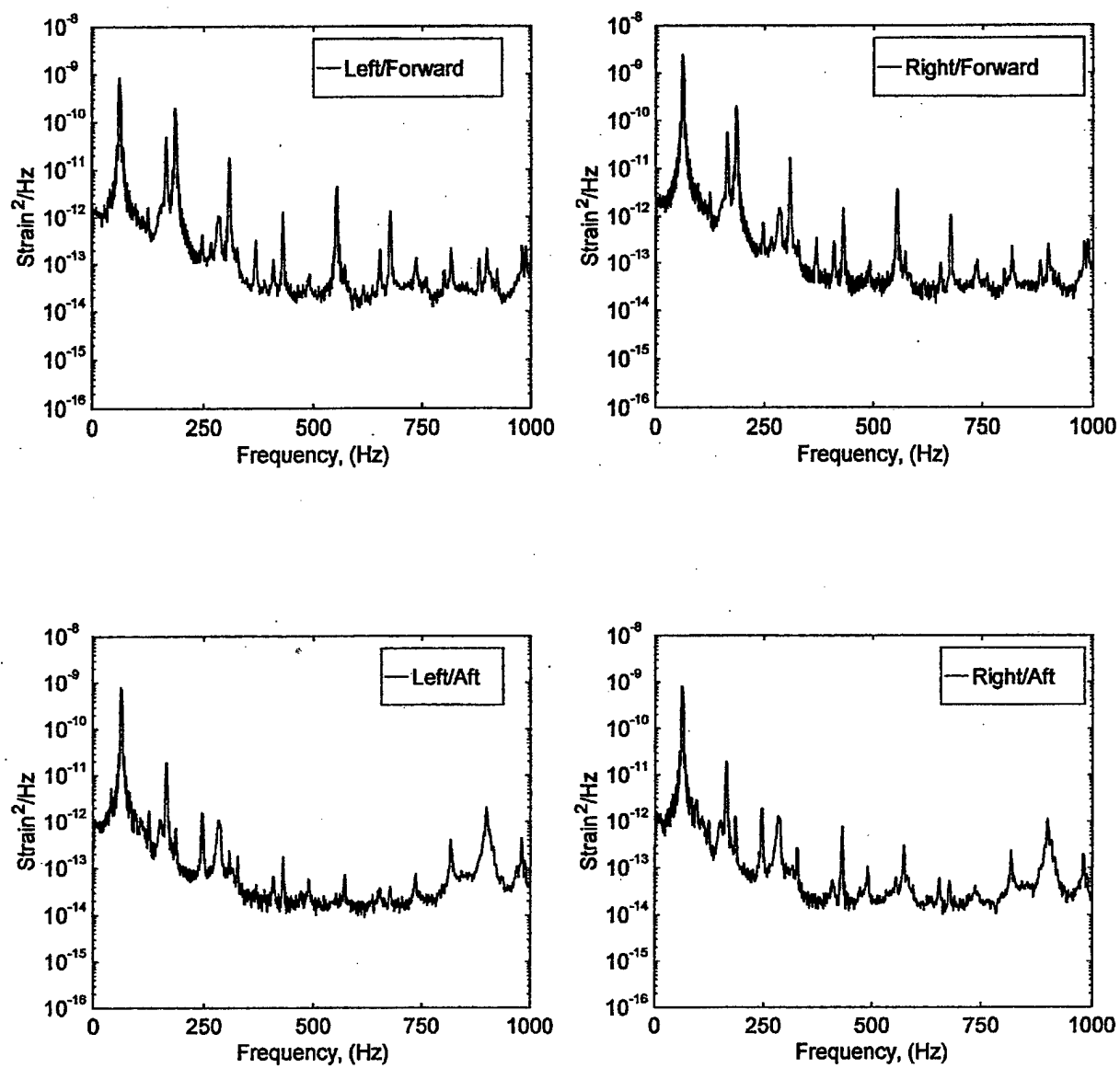FIGURE B-4. PRESSURE POWER SPECTRAL DENSITY (RUN 5, POINT 4)
($\bar{q} = 25\,psf, \alpha = 10°, \psi = 0°$)

B-4
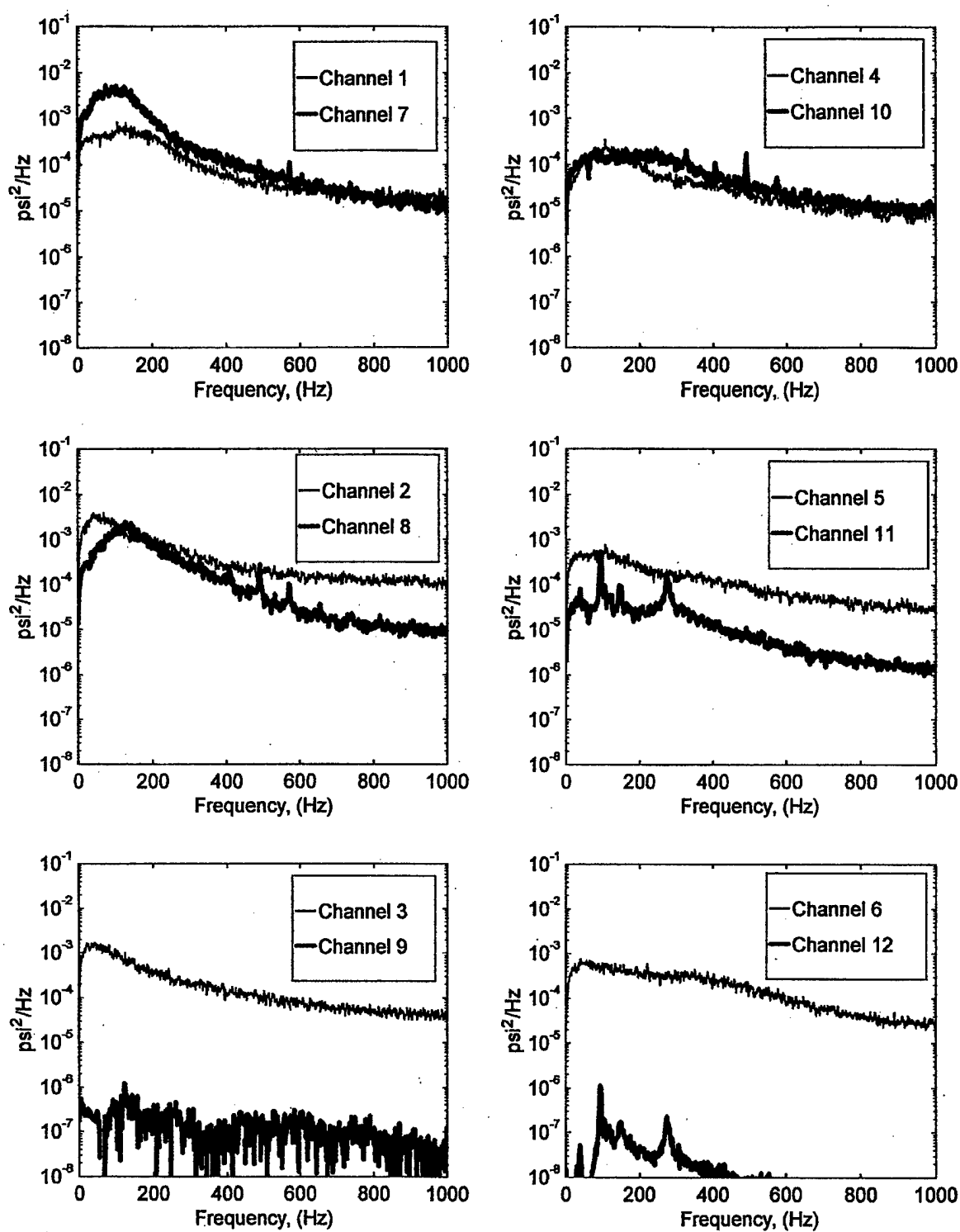
FIGURE B-5. PRESSURE POWER SPECTRAL DENSITY (RUN 5, POINT 5)
$(\bar{q} = 25 psf, \alpha = 15°, \psi = 0°)$
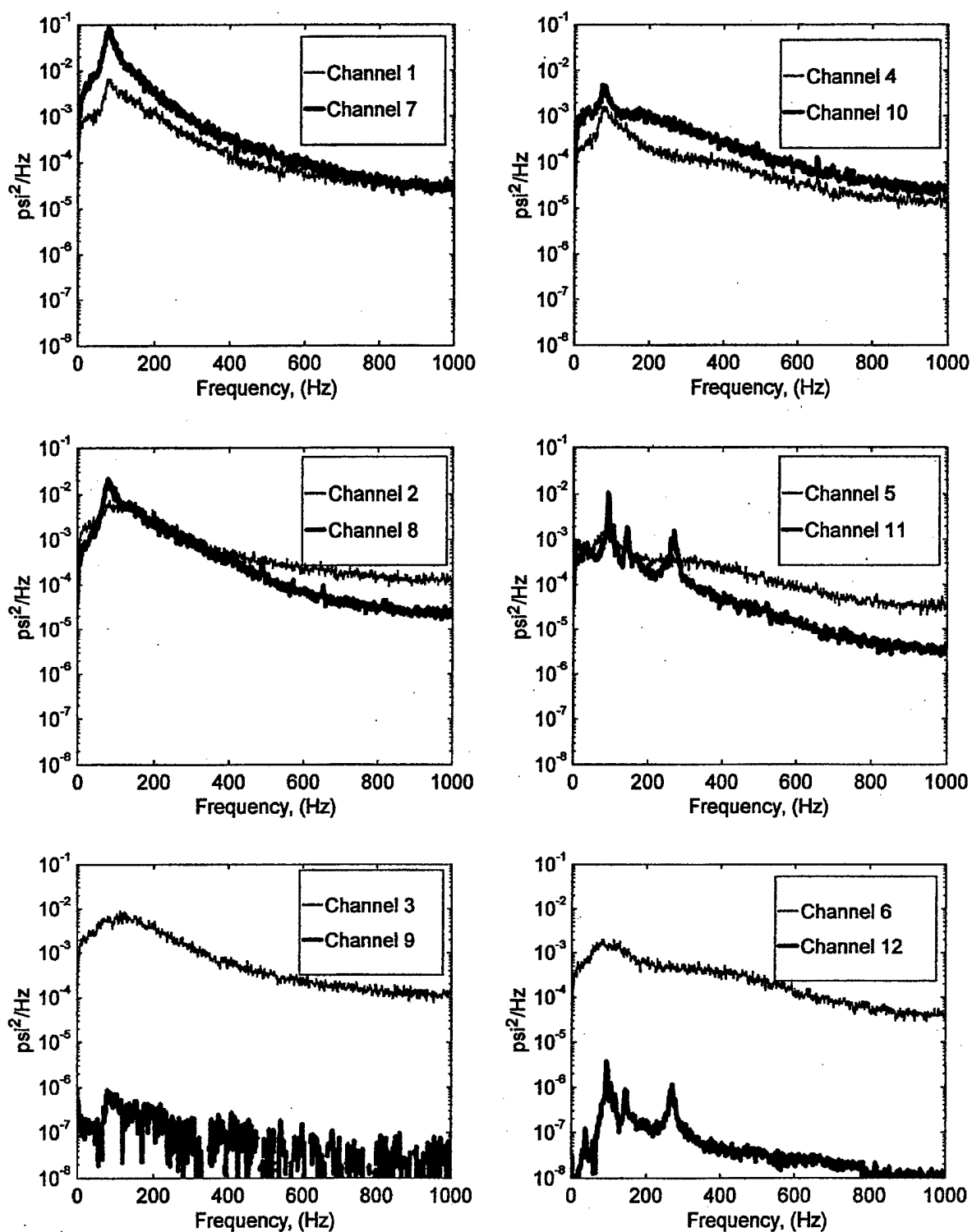
FIGURE B-6. PRESSURE POWER SPECTRAL DENSITY (RUN 5, POINT 6)
$$(\overline{q} = 25\,psf, \alpha = 20^{\circ}, \psi = 0^{\circ})$$
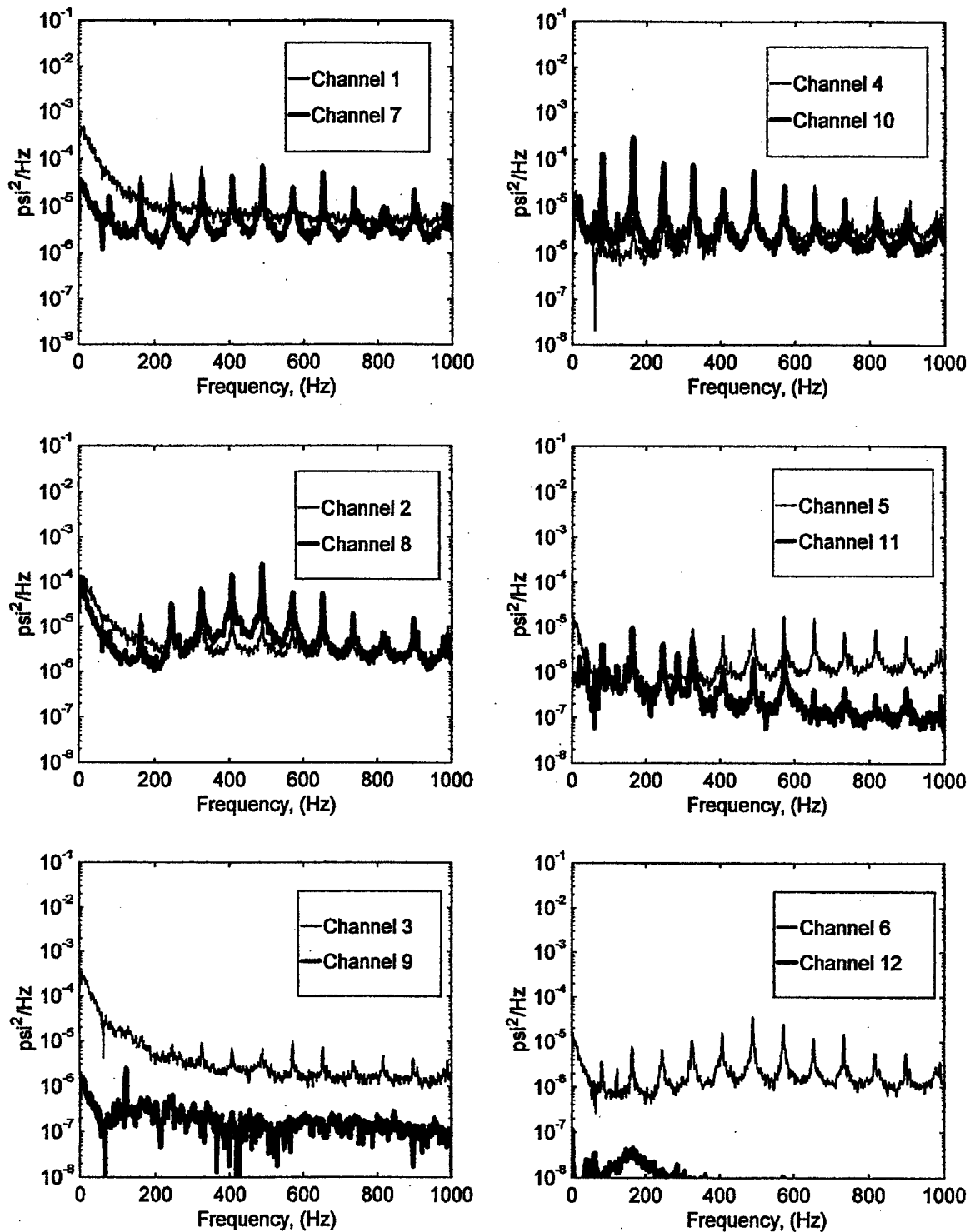
FIGURE B-7. PRESSURE POWER SPECTRAL DENSITY (RUN 6, POINT 1)

$$(\overline{q} = 35\,psf, \alpha = -5^{\circ}, \psi = 0^{\circ})$$
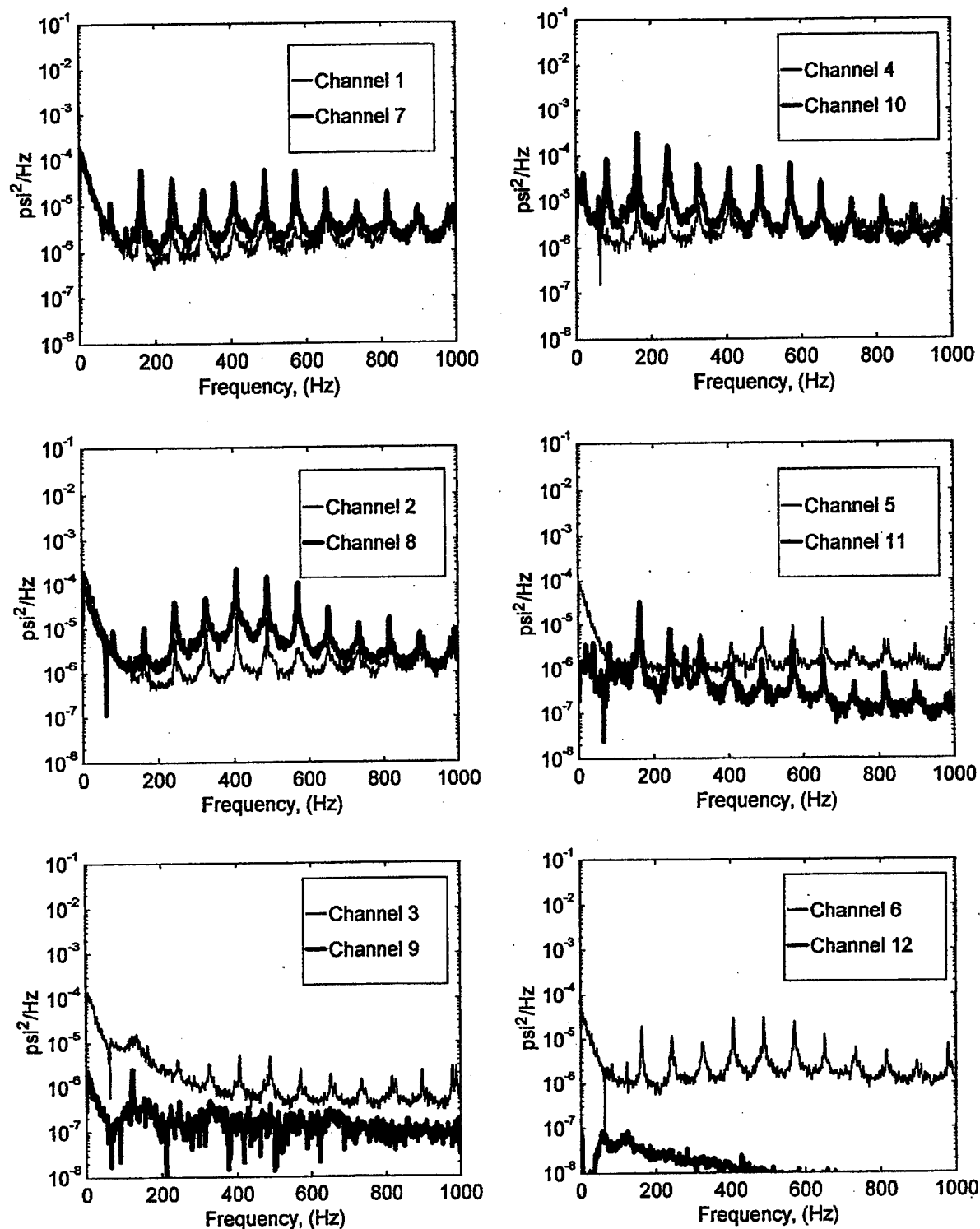
FIGURE B-8. PRESSURE POWER SPECTRAL DENSITY (RUN 6, POINT 2)
$(\overline{q} = 35\,psf, \alpha = 0^{\circ}, \psi = 0^{\circ})$
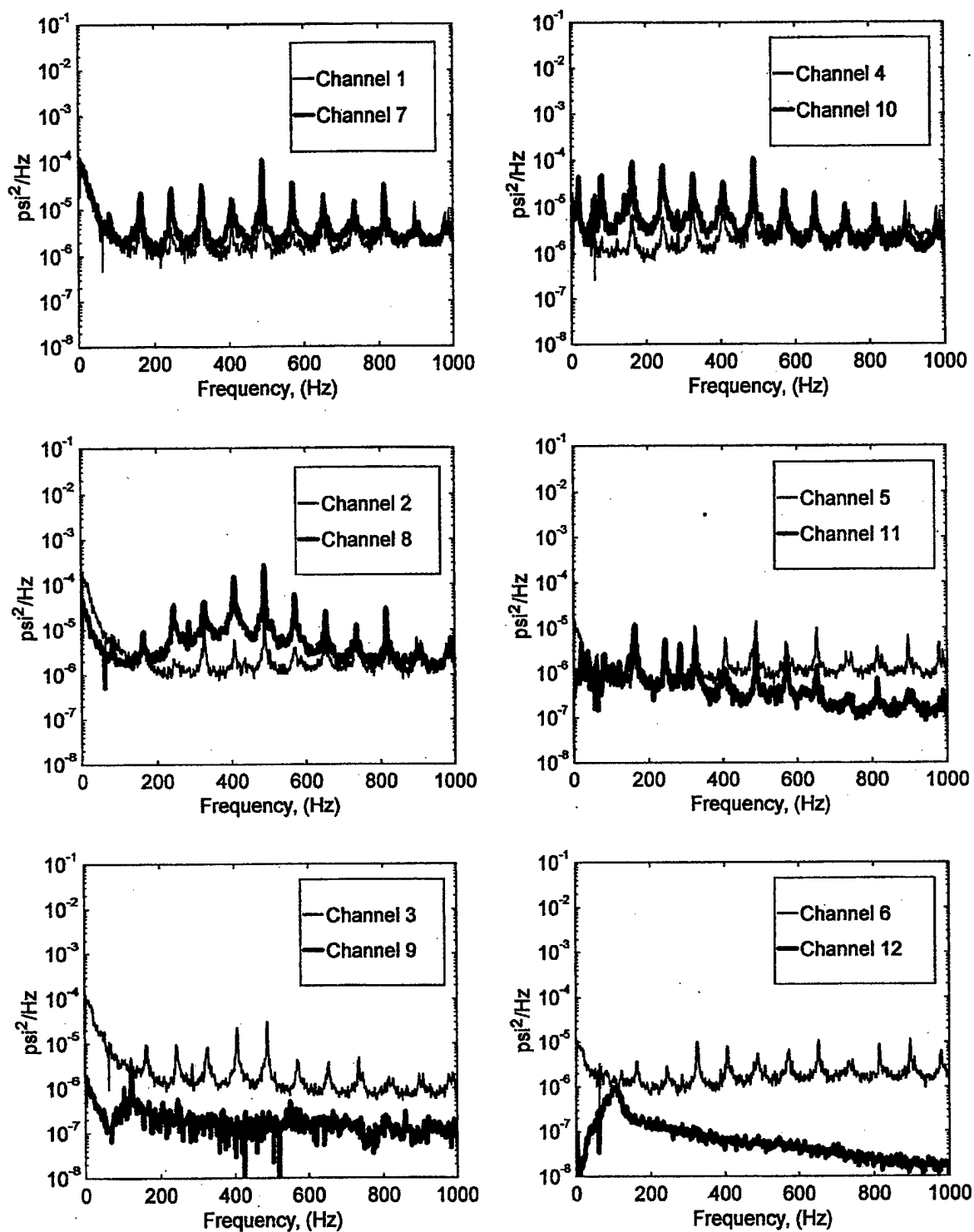
FIGURE B-9. PRESSURE POWER SPECTRAL DENSITY (RUN 6, POINT 3)
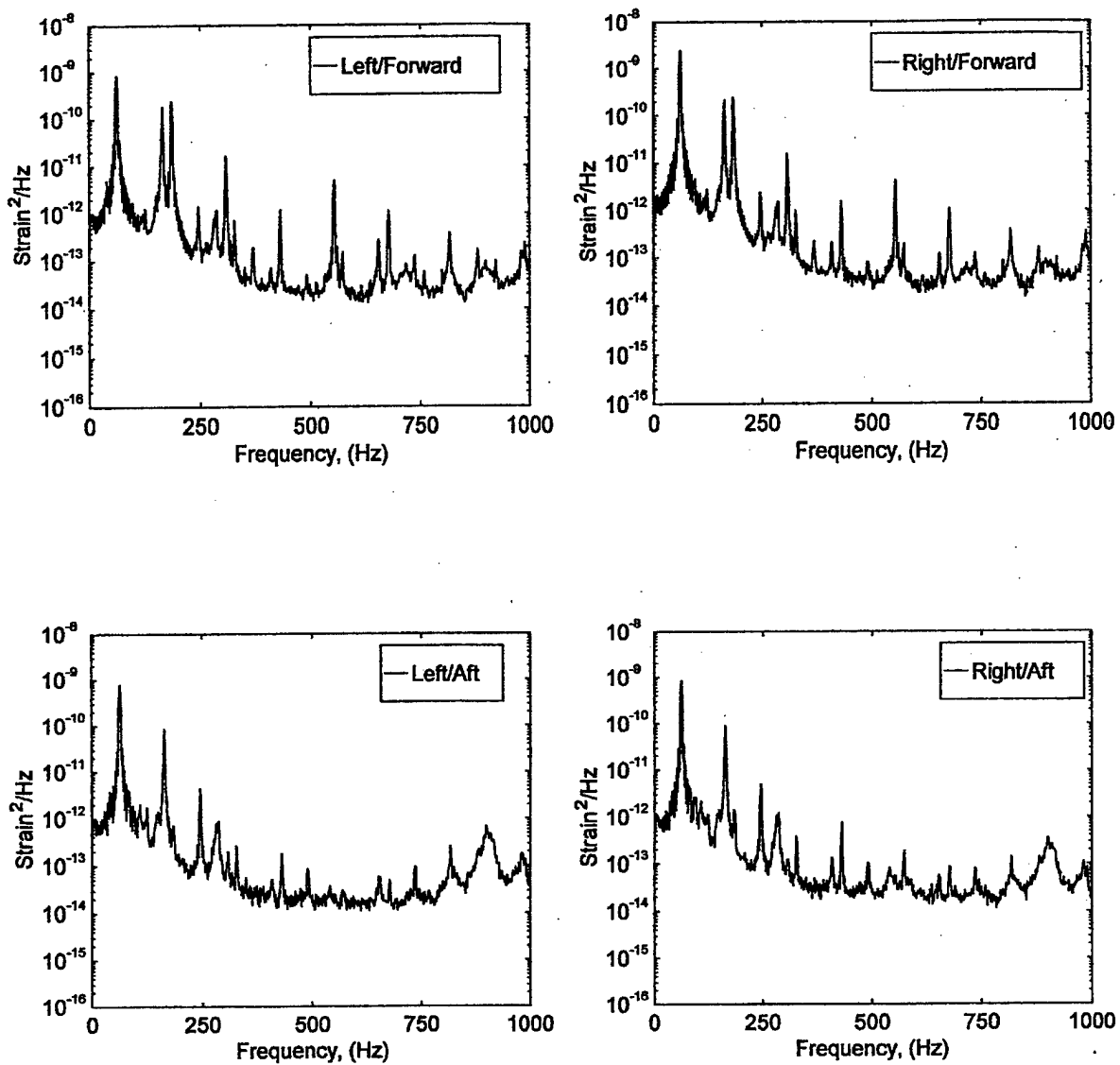$(\bar{q} = 35\,psf, \alpha = 5^{\circ}, \psi = 0^{\circ})$
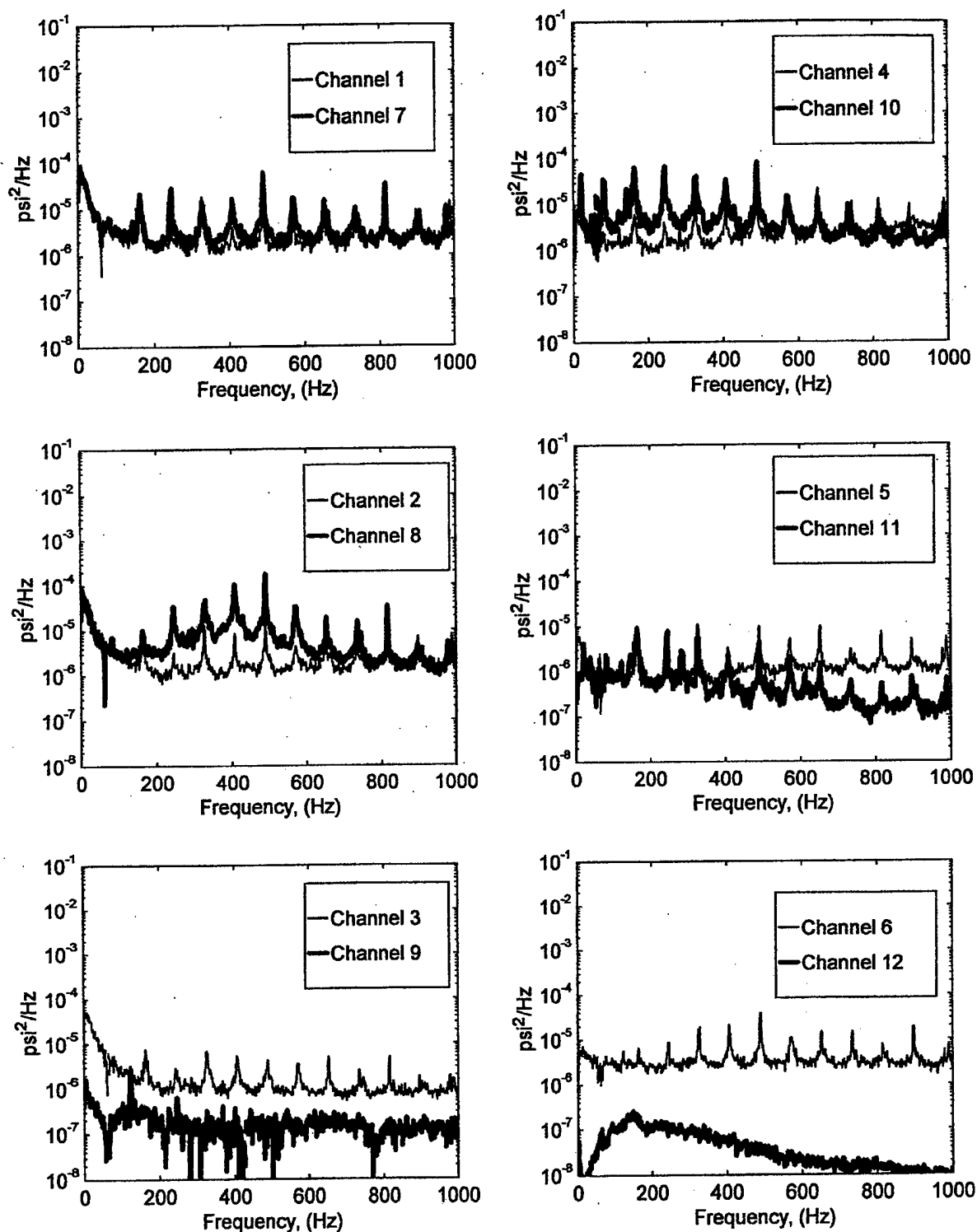
FIGURE B-10. PRESSURE POWER SPECTRAL DENSITY (RUN 6, POINT 4)
$$(\bar{q} = 35\,psf, \alpha = 10^{\circ}, \psi = 0^{\circ})$$
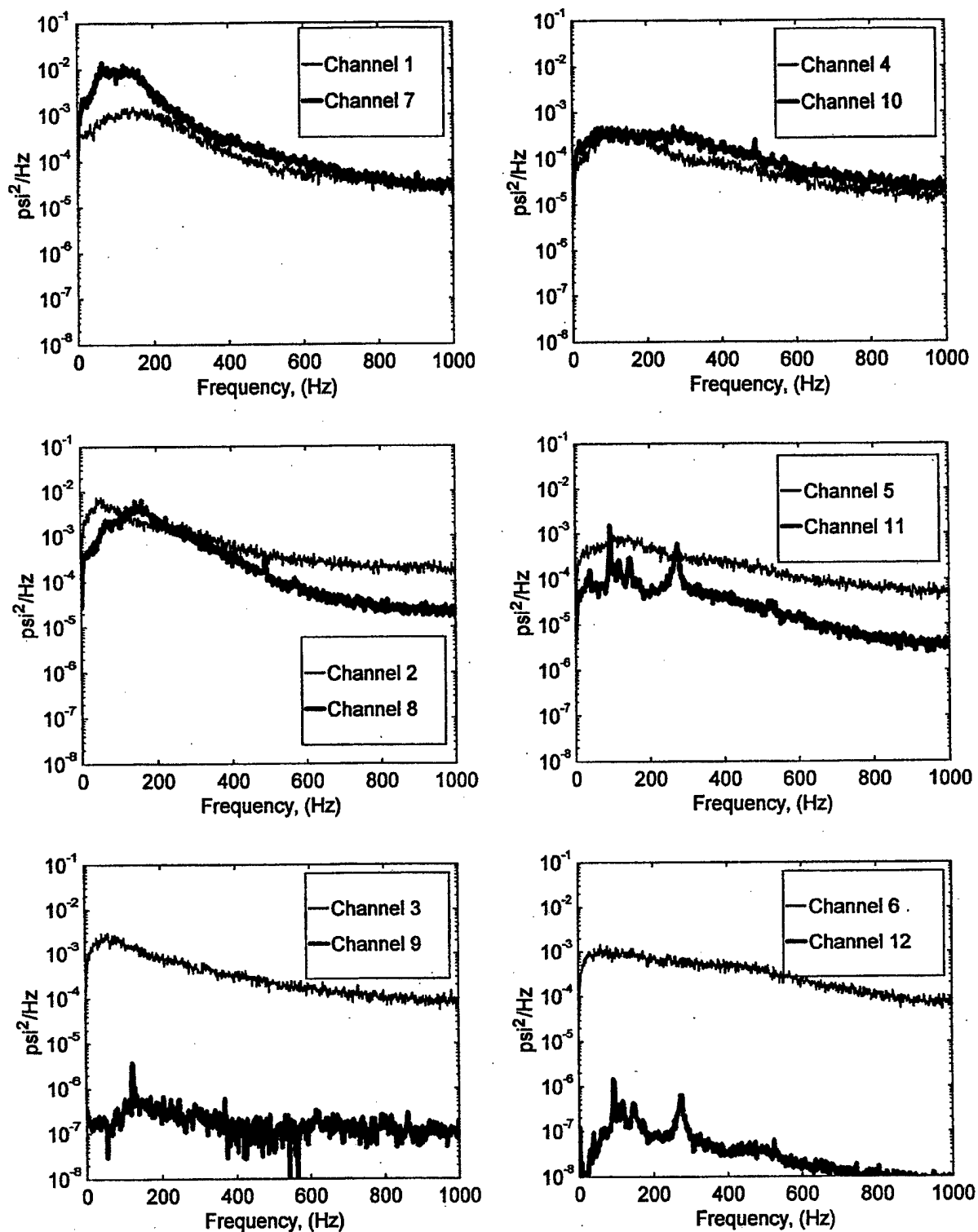
FIGURE B-11. PRESSURE POWER SPECTRAL DENSITY (RUN 6, POINT 5)
$(\overline{q} = 35\,psf, \alpha = 15^\circ, \psi = 0^\circ)$
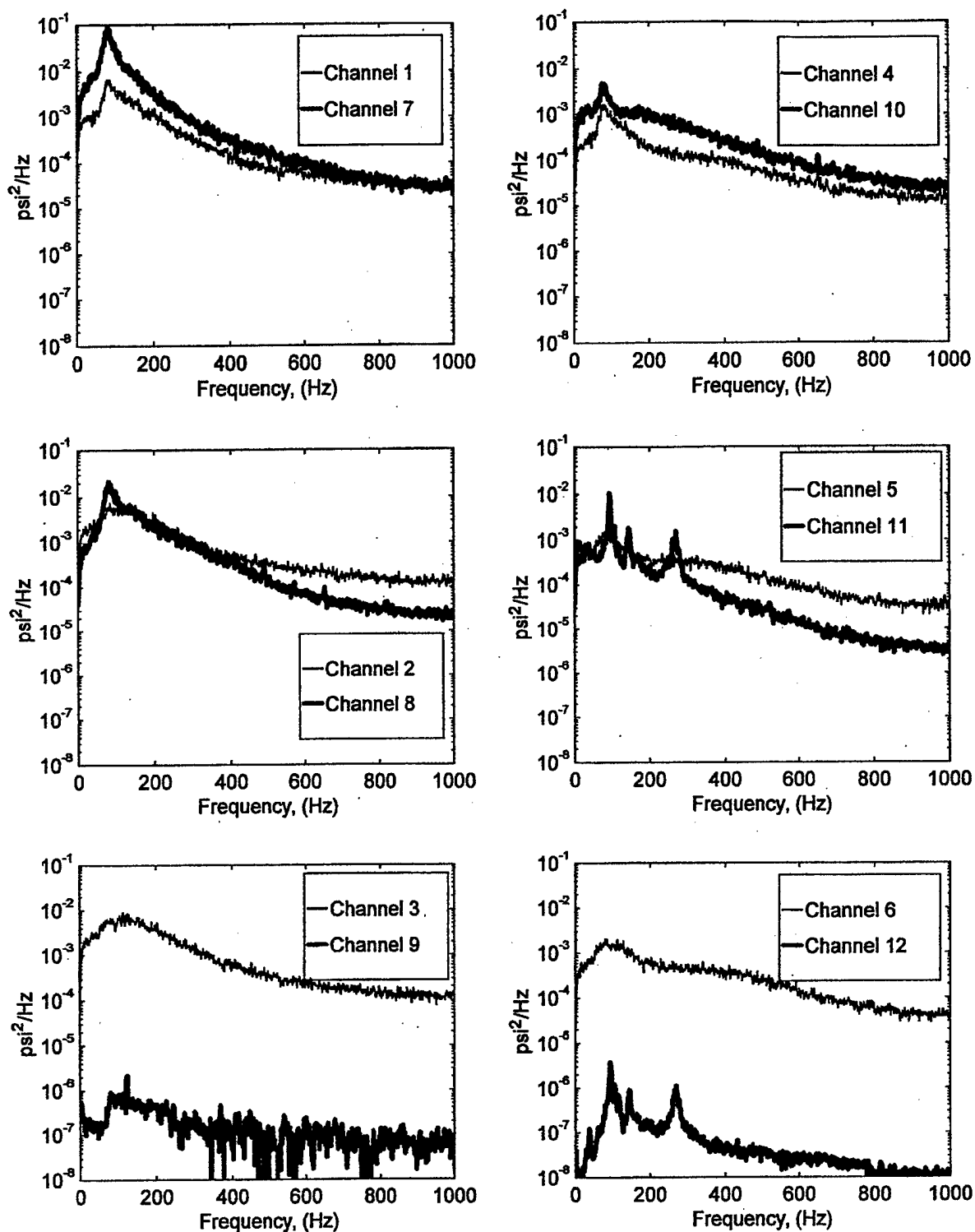
FIGURE B-12. PRESSURE POWER SPECTRAL DENSITY (RUN 6, POINT 6)
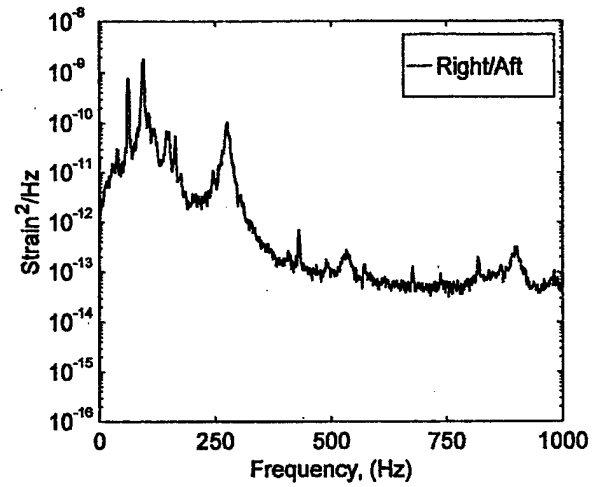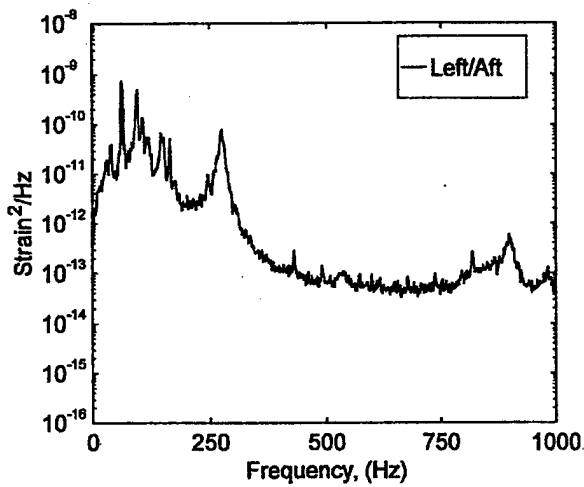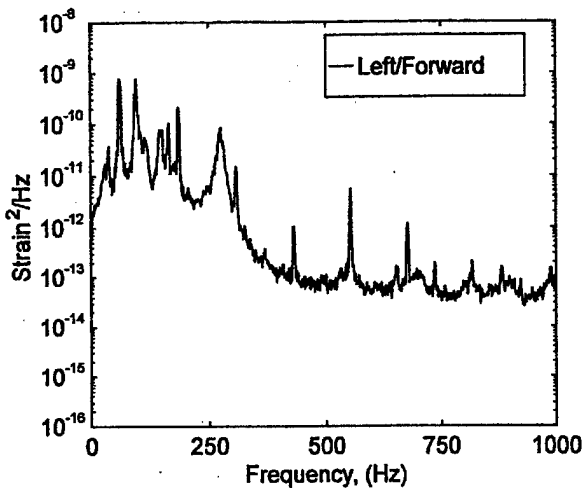$(\bar{q} = 35 psf, \alpha = 20^\circ, \psi = 0^\circ)$
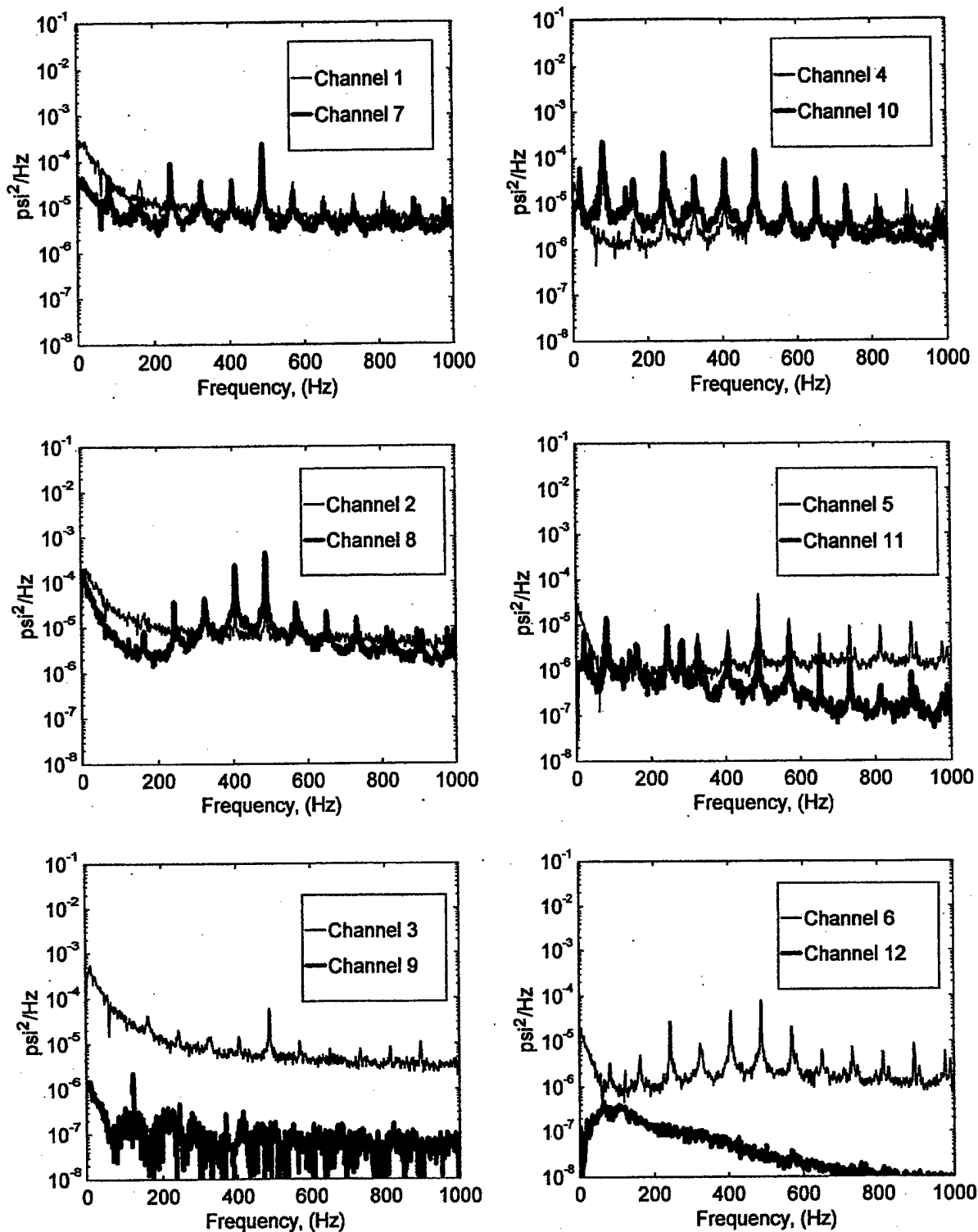
FIGURE B-13. PRESSURE POWER SPECTRAL DENSITY (RUN 7, POINT 1)
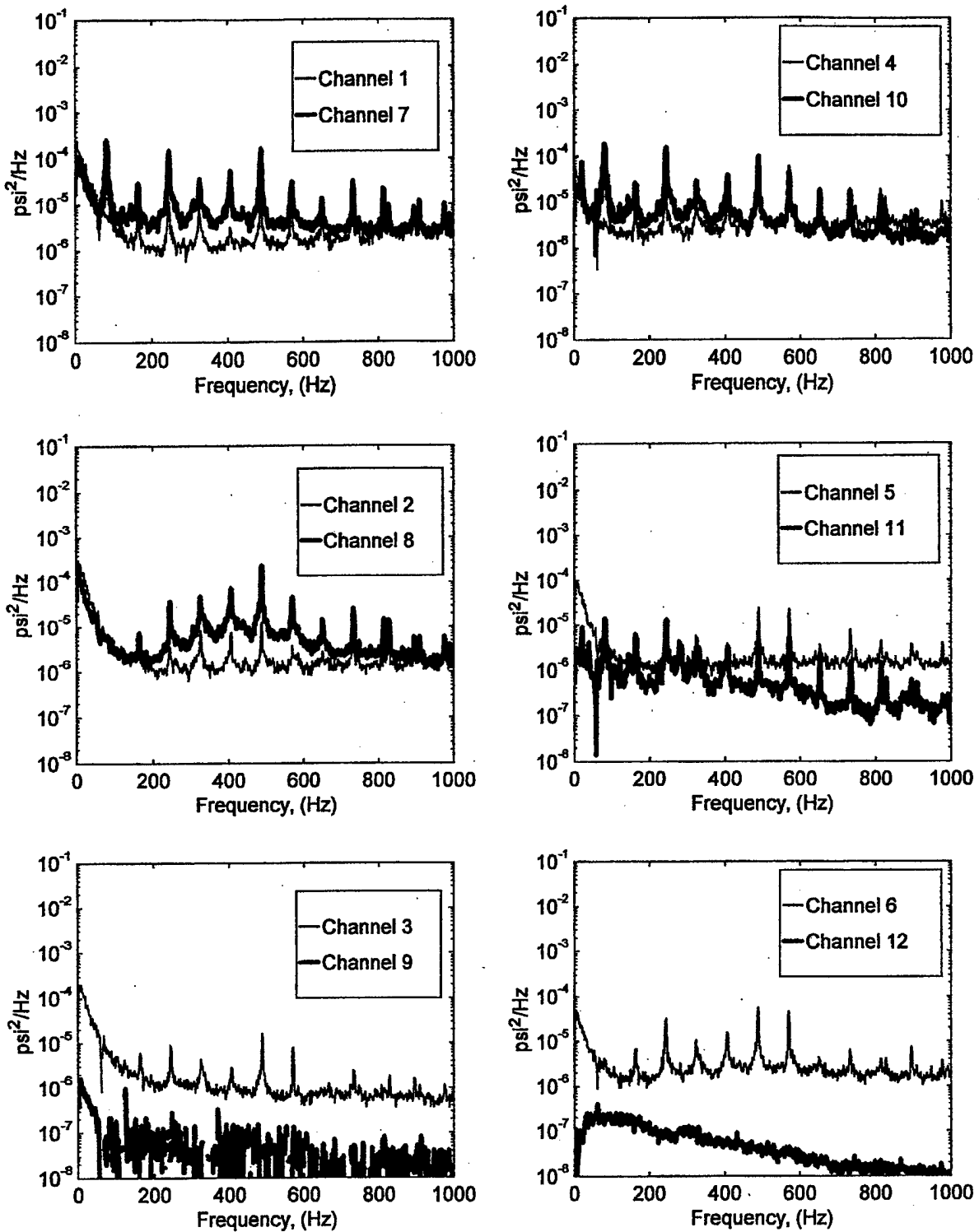
$(\overline{q} = 45 psf, \alpha = -5°, \psi = 0°)$

FIGURE B-14. PRESSURE POWER SPECTRAL DENSITY (RUN 7, POINT 2)
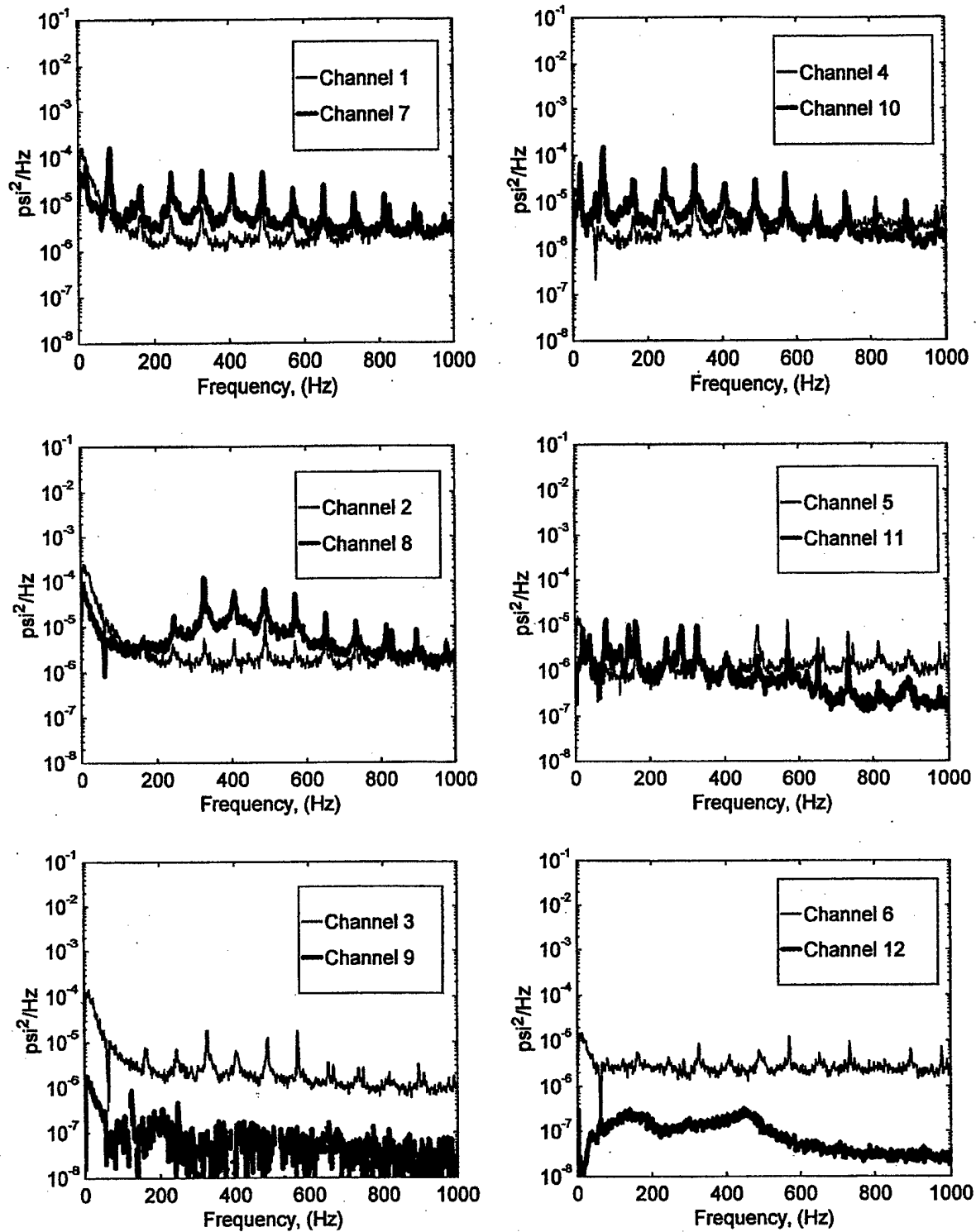
$$(\overline{q} = 45psf, \alpha = 0°, \psi = 0°)$$

FIGURE B-15. PRESSURE POWER SPECTRAL DENSITY (RUN 7, POINT 3)
$(\bar{q} = 45 psf, \alpha = 5°, \psi = 0°)$
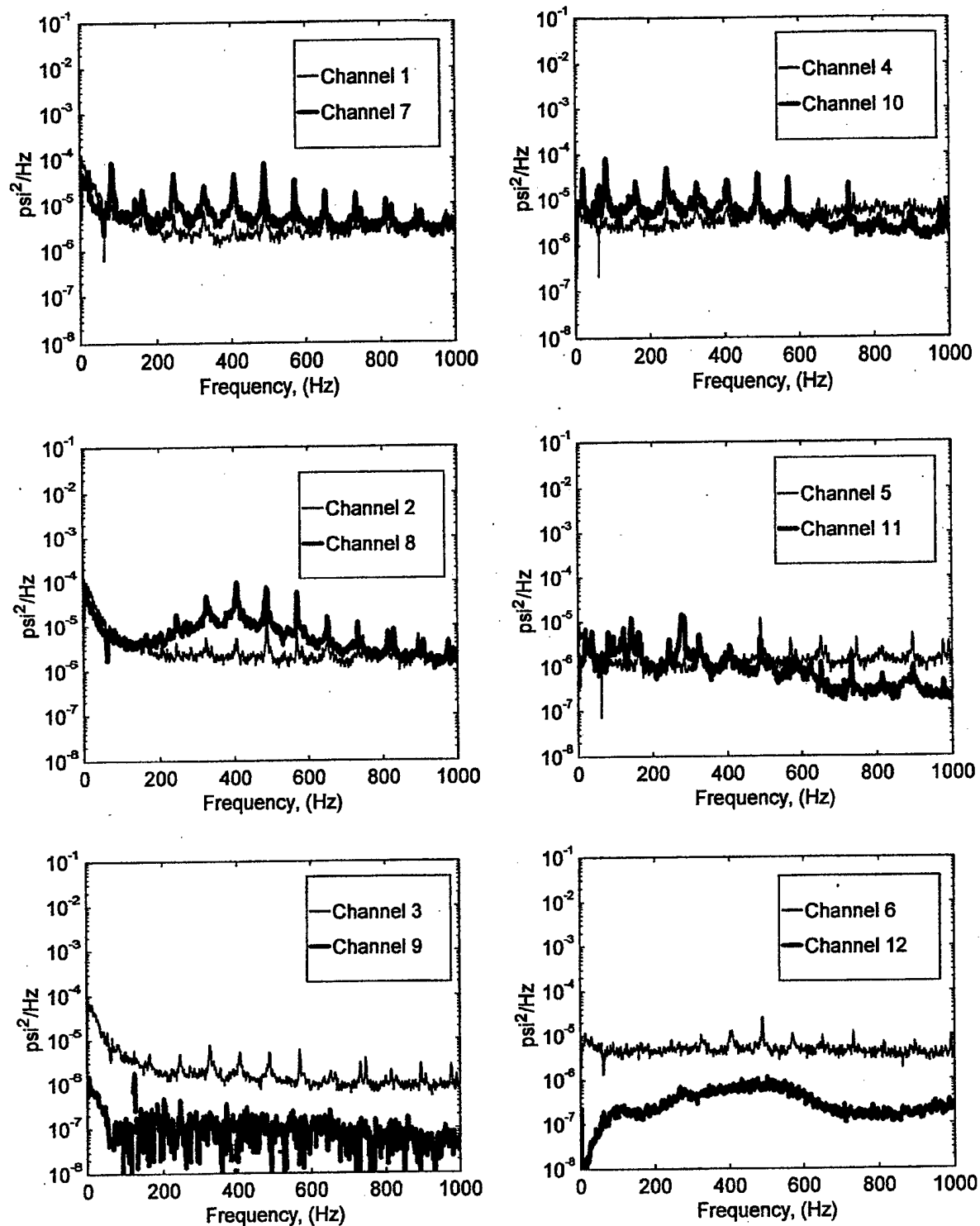
FIGURE B-16. PRESSURE POWER SPECTRAL DENSITY (RUN 7, POINT 4)
$(\overline{q} = 45 psf, \alpha = 10^{\circ}, \psi = 0^{\circ})$
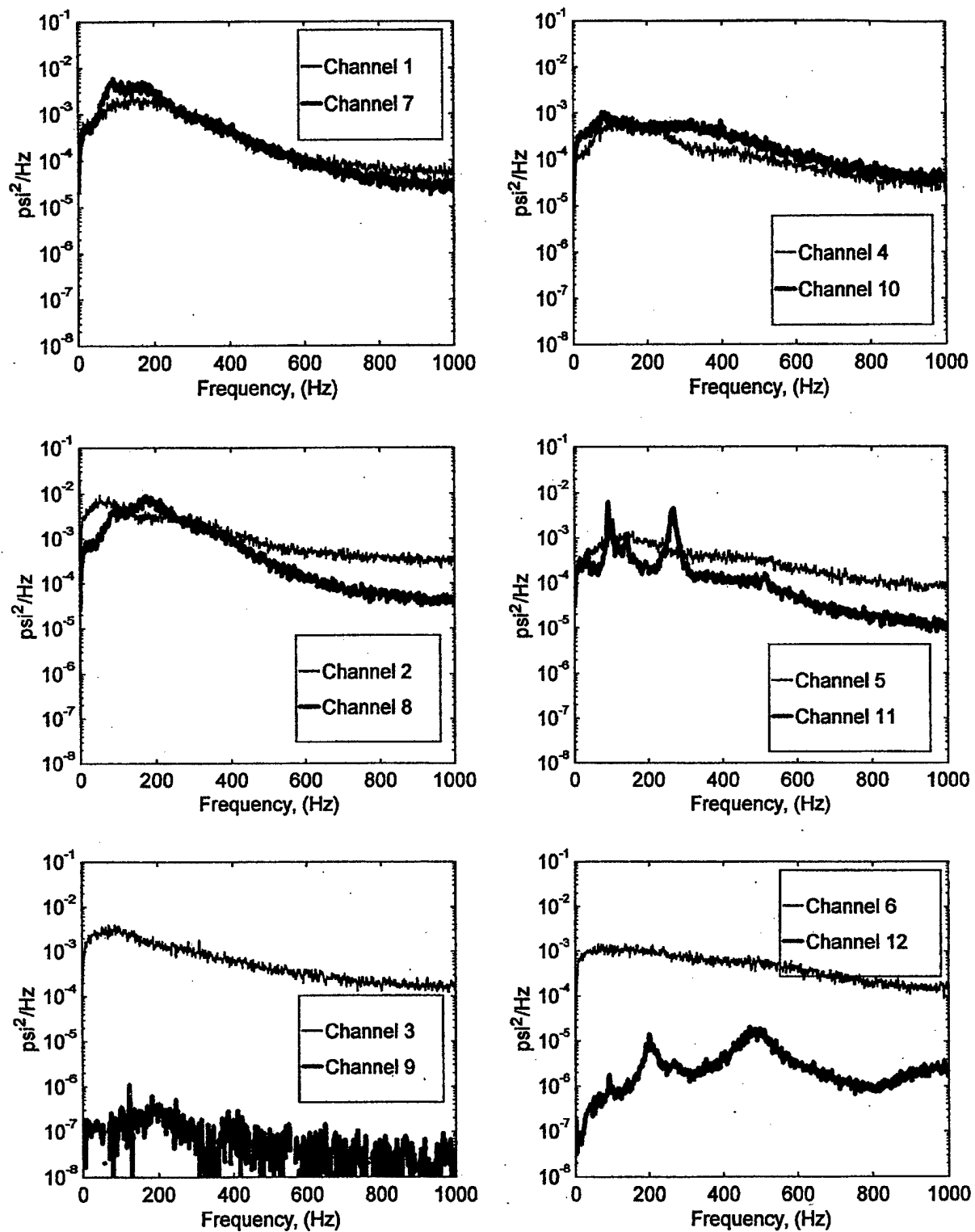
FIGURE B-17. PRESSURE POWER SPECTRAL DENSITY (RUN 7, POINT 5)
$(\bar{q} = 45 psf, \alpha = 15^{\circ}, \psi = 0^{\circ})$
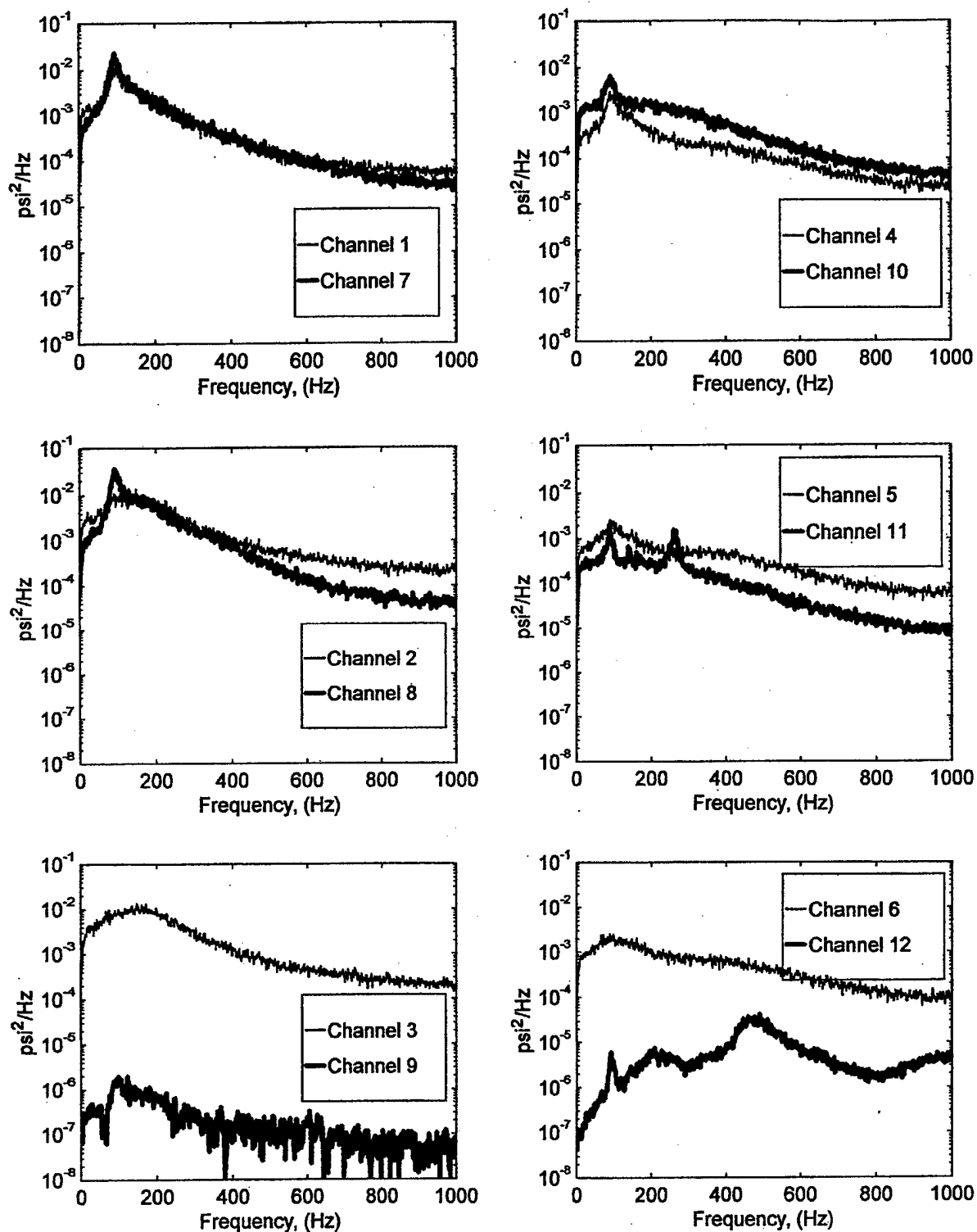
FIGURE B-18. PRESSURE POWER SPECTRAL DENSITY (RUN 7, POINT 6)
$(\overline{q} = 45 psf, \alpha = 20\degree, \psi = 0\degree)$
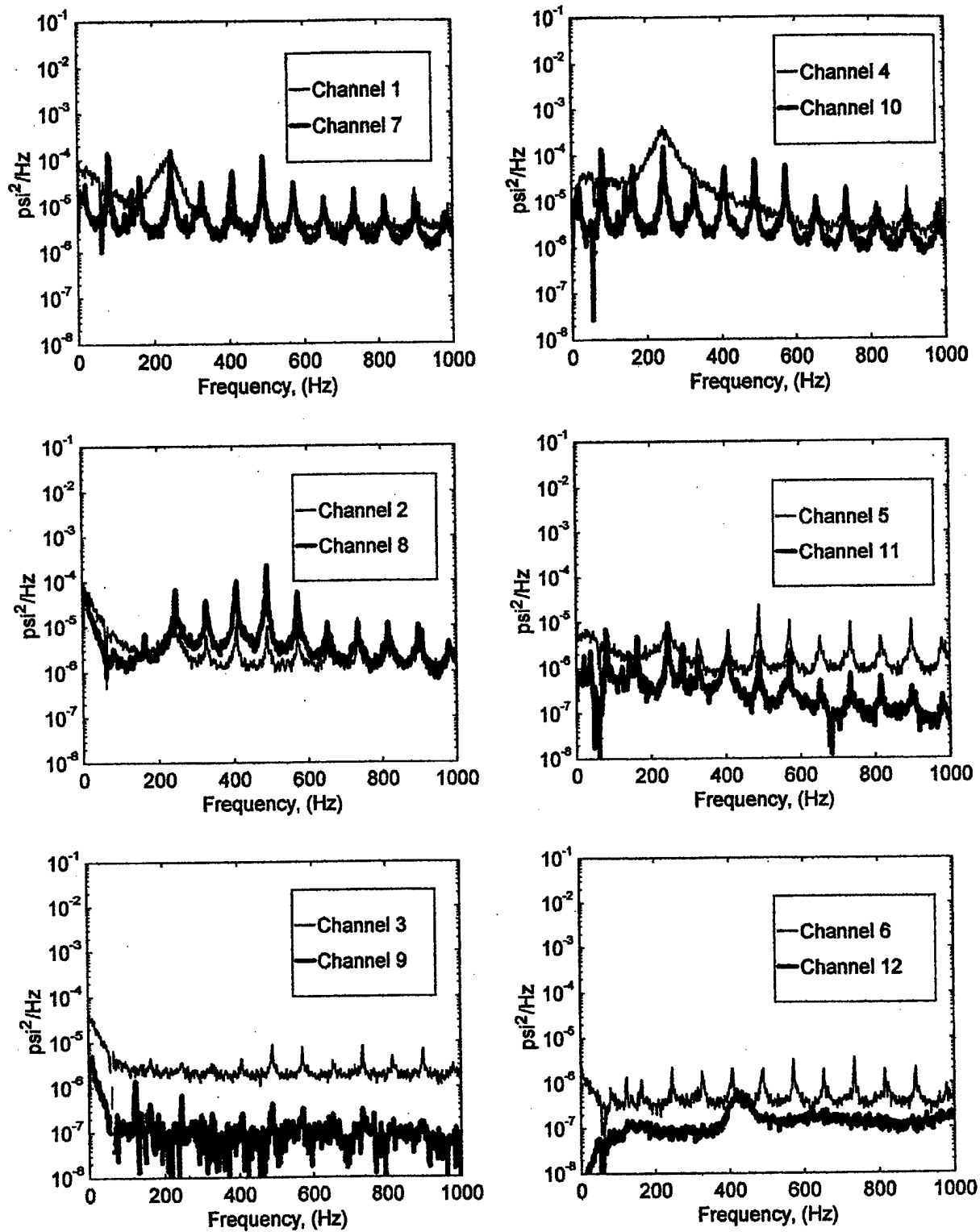
FIGURE B-19. PRESSURE POWER SPECTRAL DENSITY (RUN 8, POINT 1)
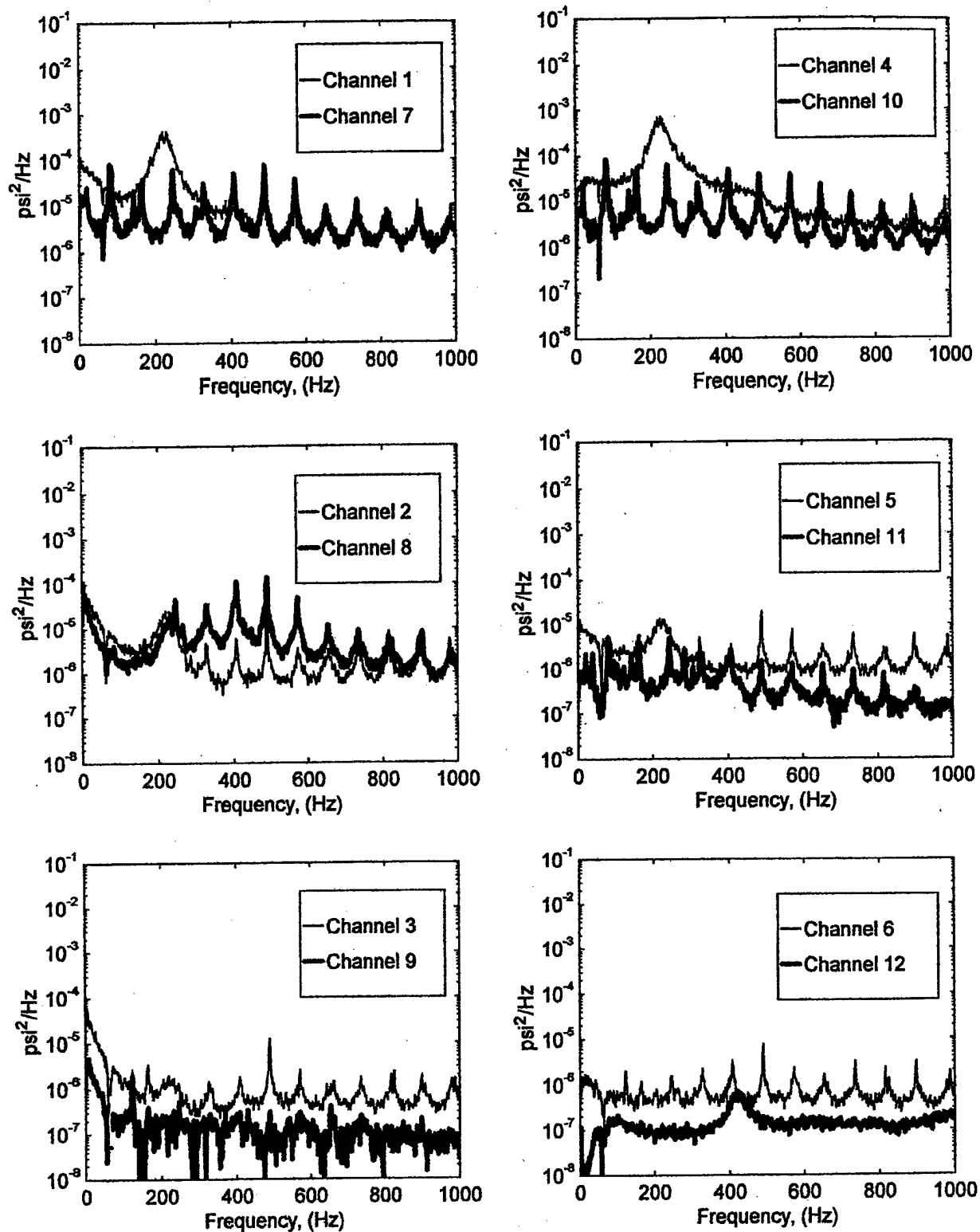
$$(\overline{q} = 25\,psf, \alpha = -5^{\circ}, \psi = -10^{\circ})$$

FIGURE B-20. PRESSURE POWER SPECTRAL DENSITY (RUN 8, POINT 2)
$(\bar{q} = 25\,psf, \alpha = 0^{\circ}, \psi = -10^{\circ})$
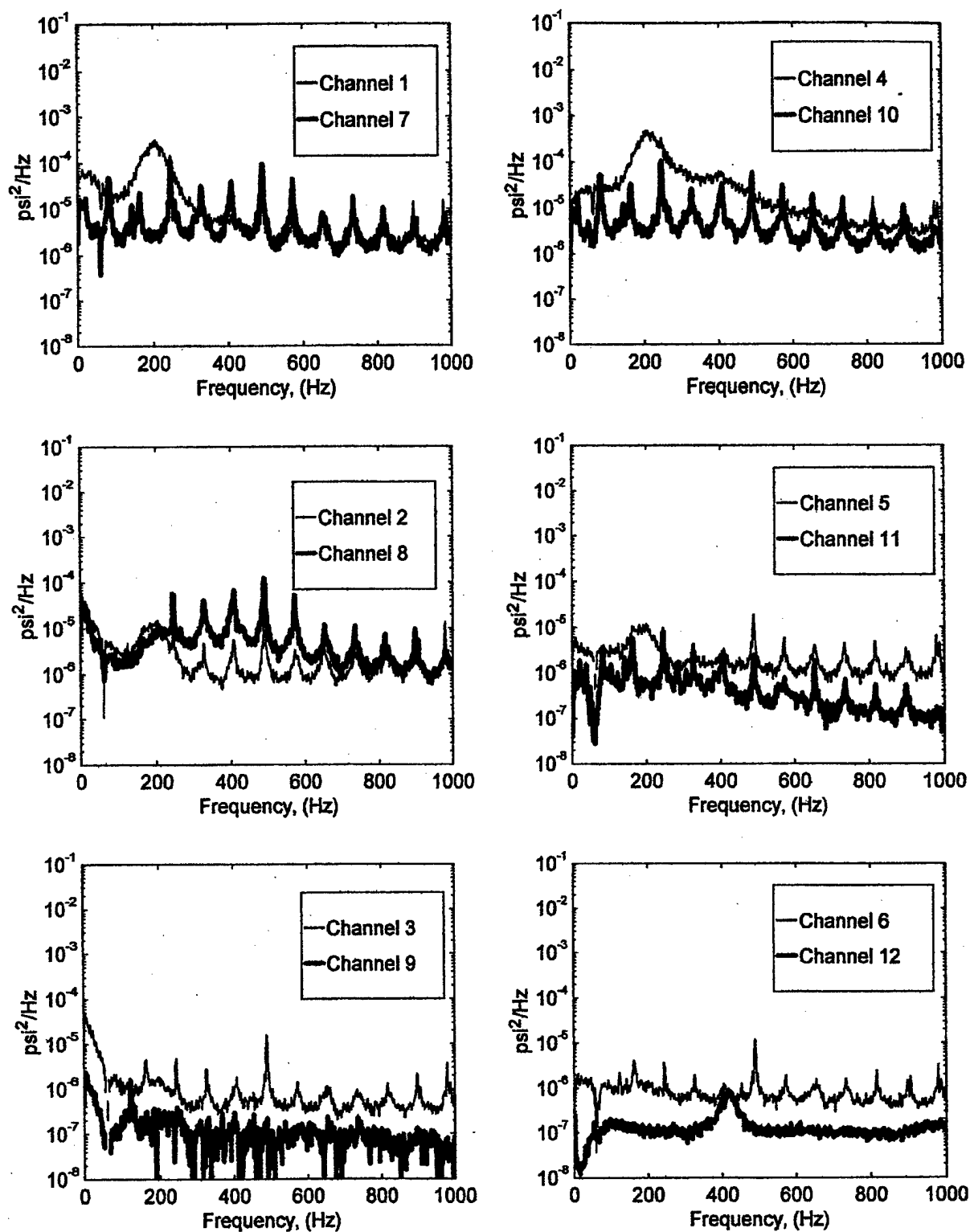
FIGURE B-21. PRESSURE POWER SPECTRAL DENSITY (RUN 8, POINT 3)
$(\overline{q} = 25\,psf, \alpha = 5^\circ, \psi = -10^\circ)$
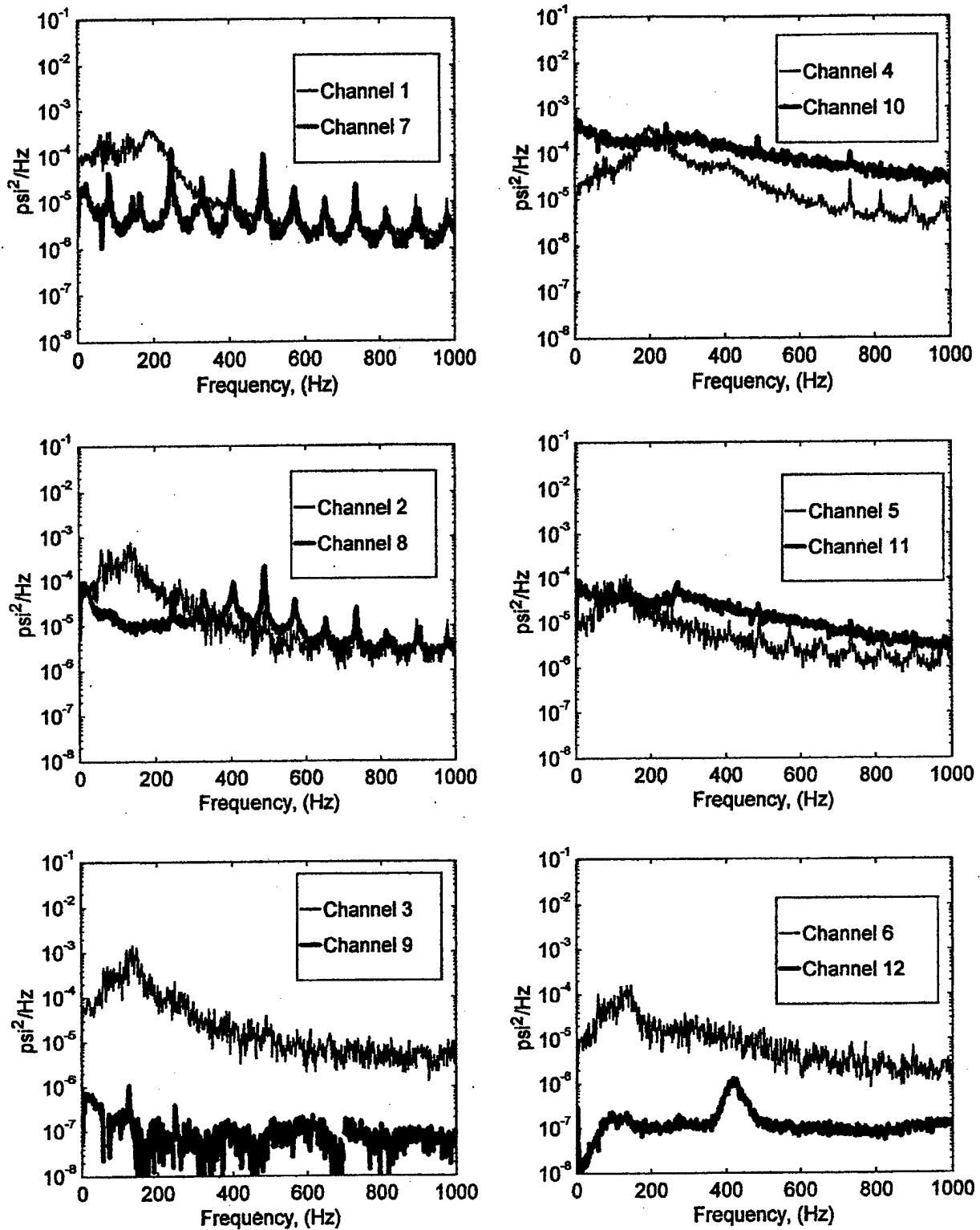
FIGURE B-22. PRESSURE POWER SPECTRAL DENSITY (RUN 8, POINT 4)

$(\bar{q} = 25 psf, \alpha = 10^{\circ}, \psi = -10^{\circ})$
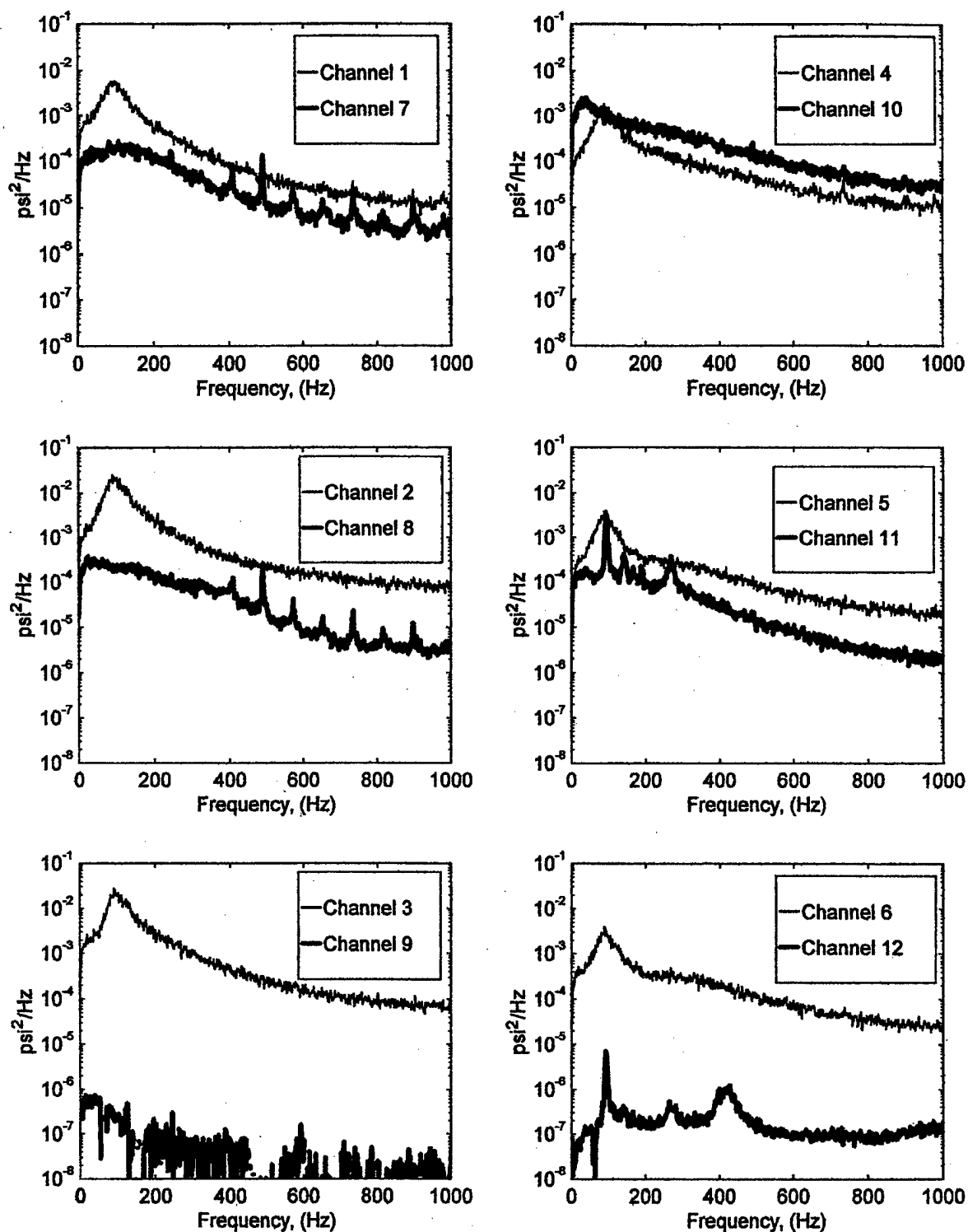
FIGURE B-23. PRESSURE POWER SPECTRAL DENSITY (RUN 8, POINT 5)
$(\overline{q} = 25psf, \alpha = 15^{\circ}, \psi = -10^{\circ})$
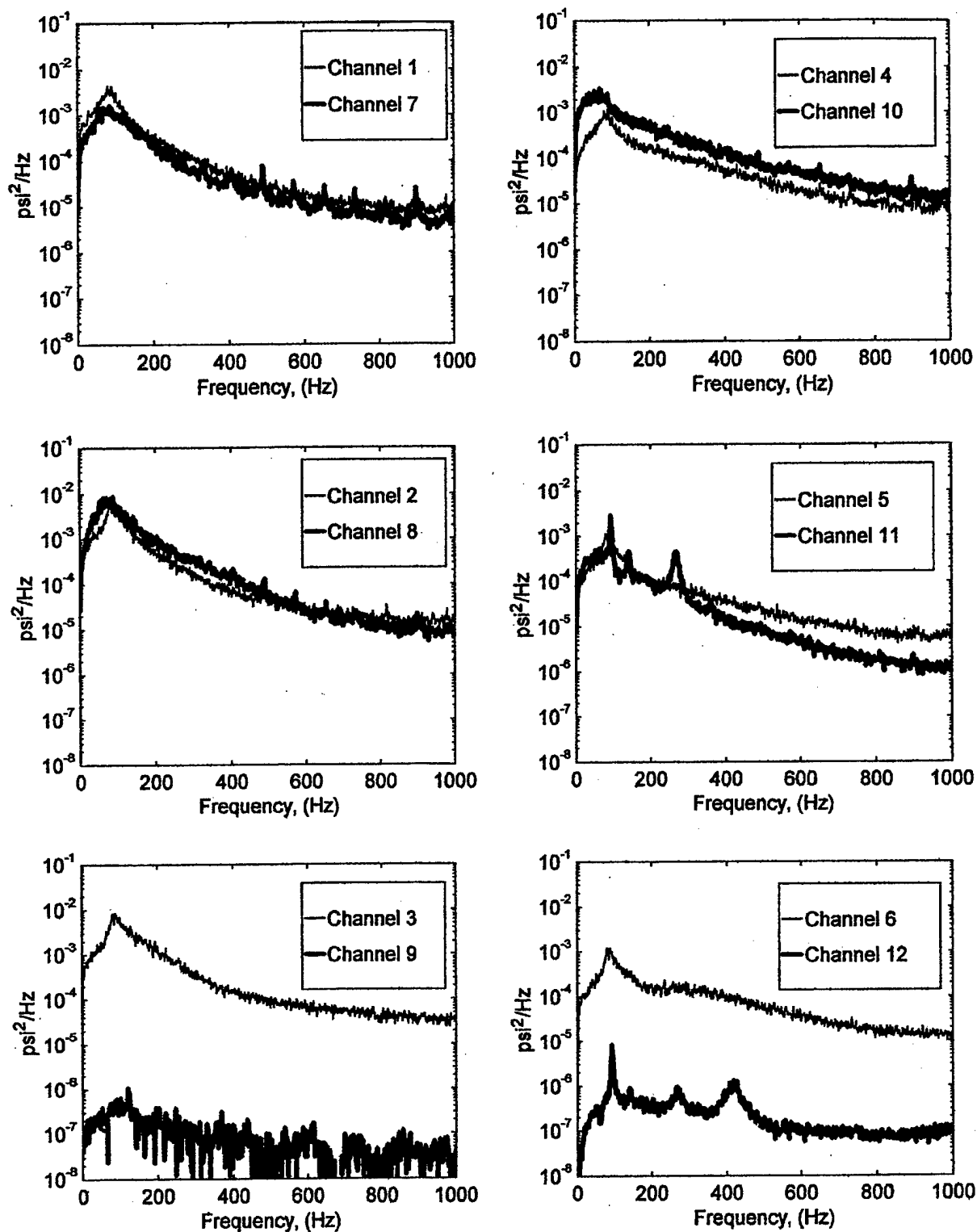
FIGURE B-24. PRESSURE POWER SPECTRAL DENSITY (RUN 8, POINT 6)

$$(\overline{q} = 25\,psf, \alpha = 20°, \psi = -10°)$$
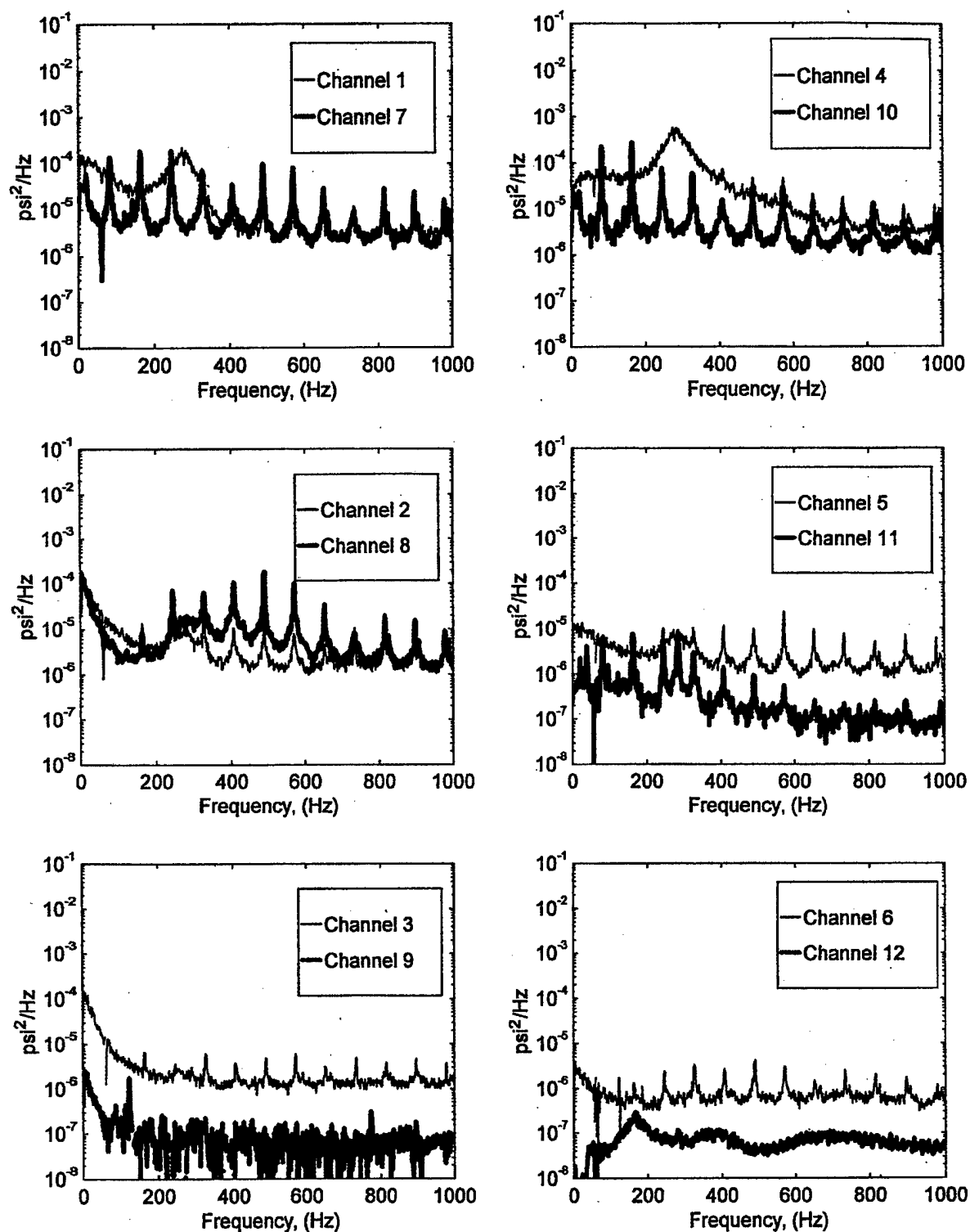
FIGURE B-25. PRESSURE POWER SPECTRAL DENSITY (RUN 9, POINT 1)
$(\overline{q} = 35psf, \alpha = -5^{\circ}, \psi = -10^{\circ})$
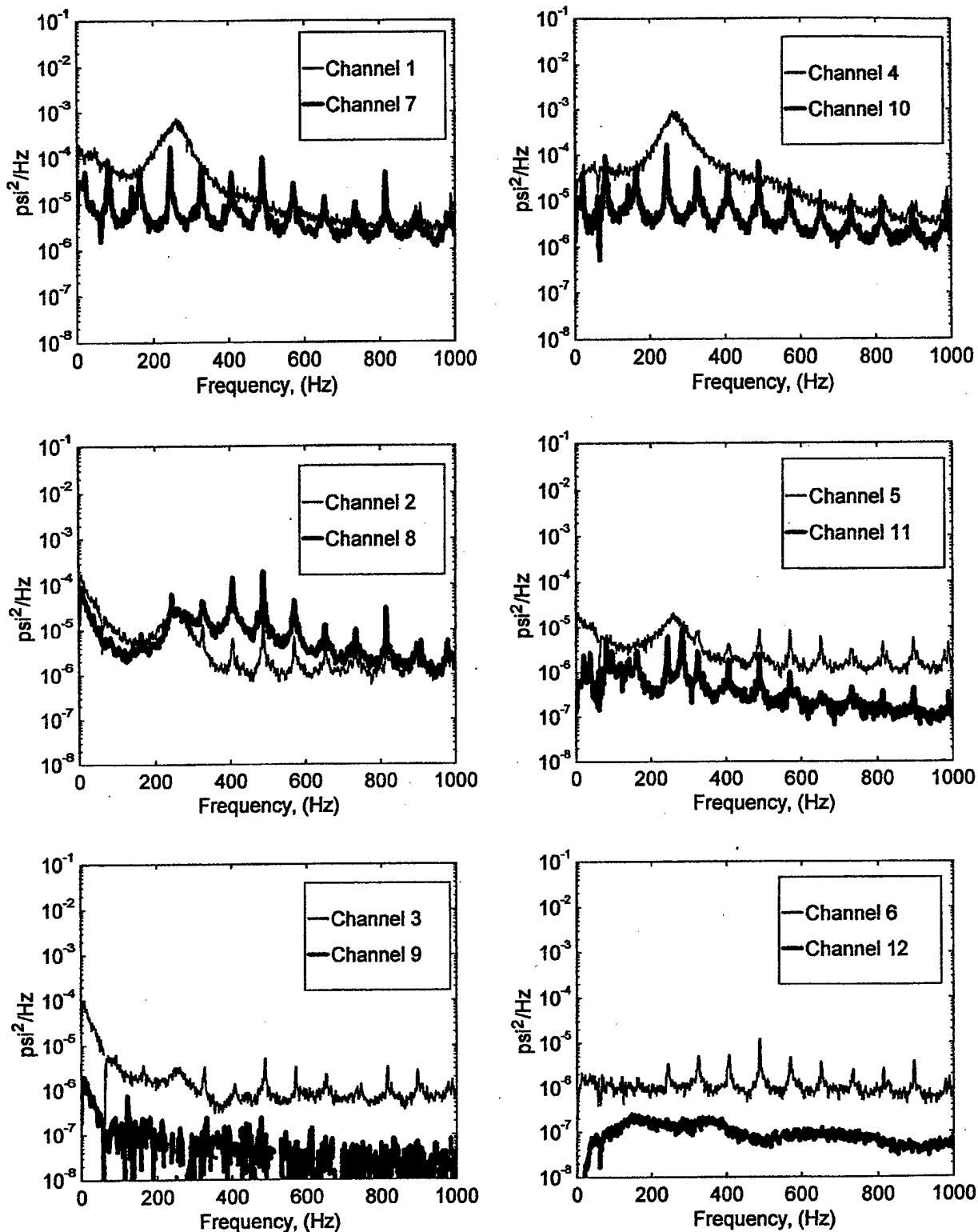
FIGURE B-26. PRESSURE POWER SPECTRAL DENSITY (RUN 9, POINT 2)

$$(\overline{q} = 35\,psf, \alpha = 0^{\circ}, \psi = -10^{\circ})$$
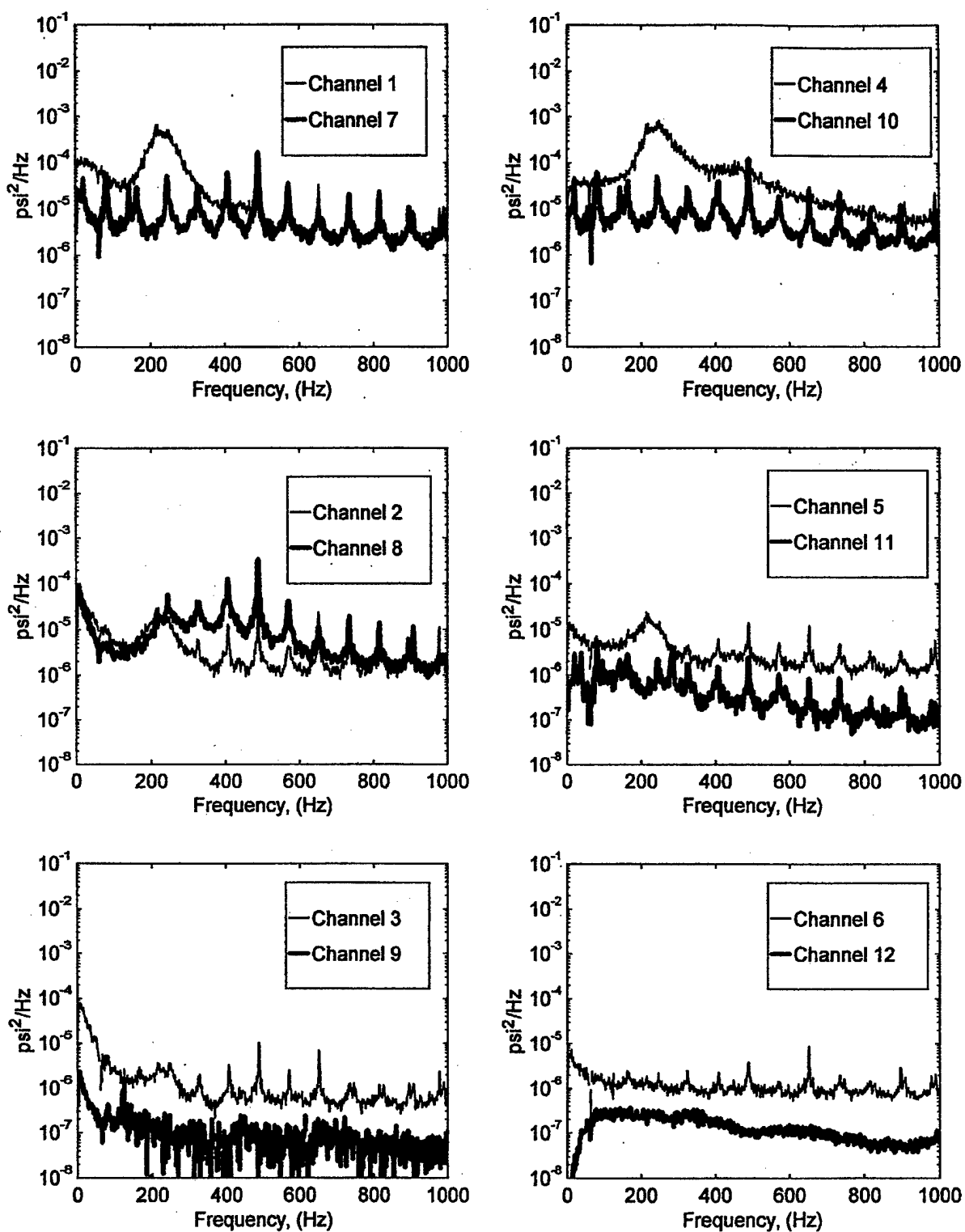
FIGURE B-27. PRESSURE POWER SPECTRAL DENSITY (RUN 9, POINT 3)

$$(\overline{q} = 35psf, \alpha = 5^{\circ}, \psi = -10^{\circ})$$
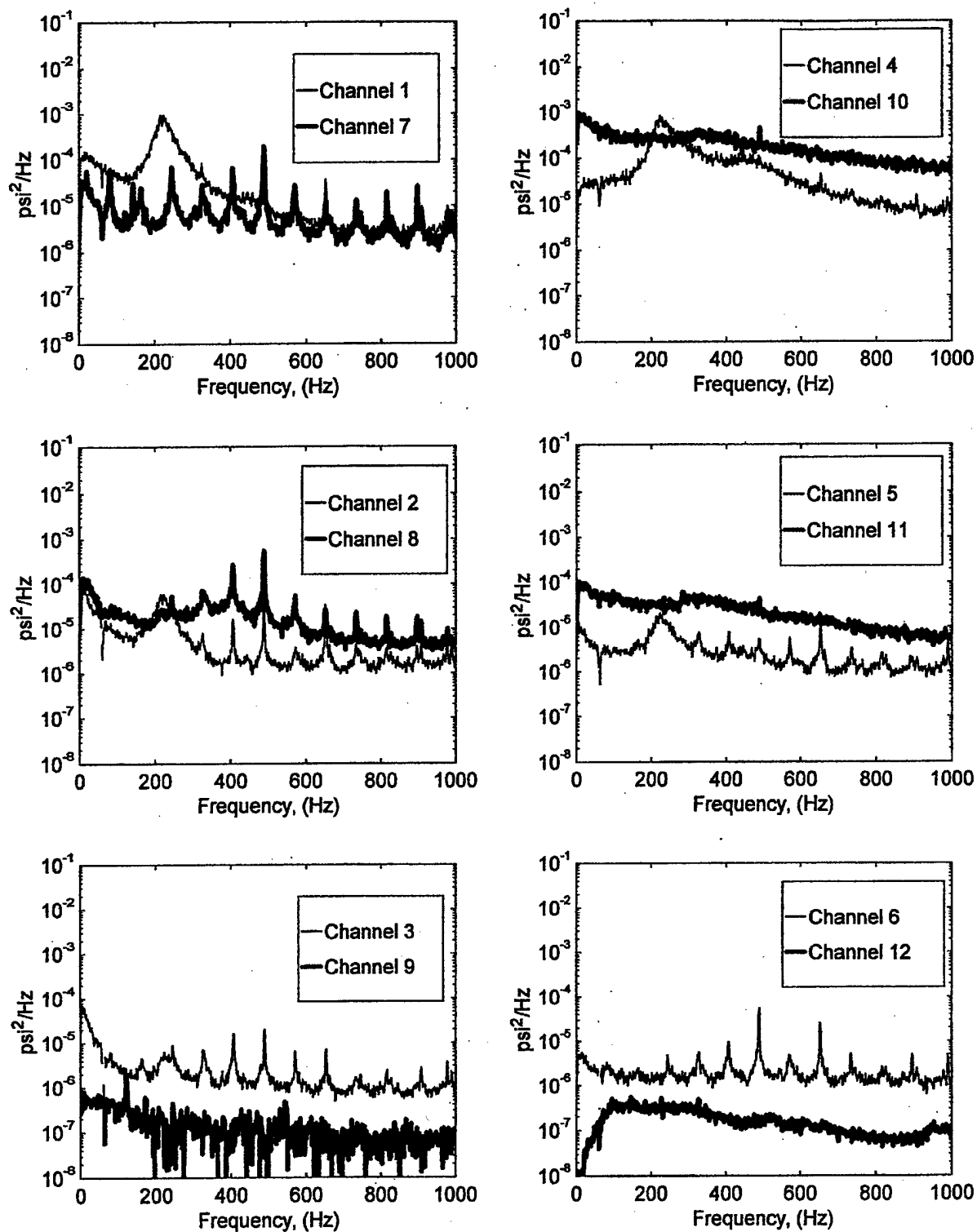
FIGURE B-28. PRESSURE POWER SPECTRAL DENSITY (RUN 9, POINT 4)
$(\overline{q} = 35psf, \alpha = 10^\circ, \psi = -10^\circ)$

B-28
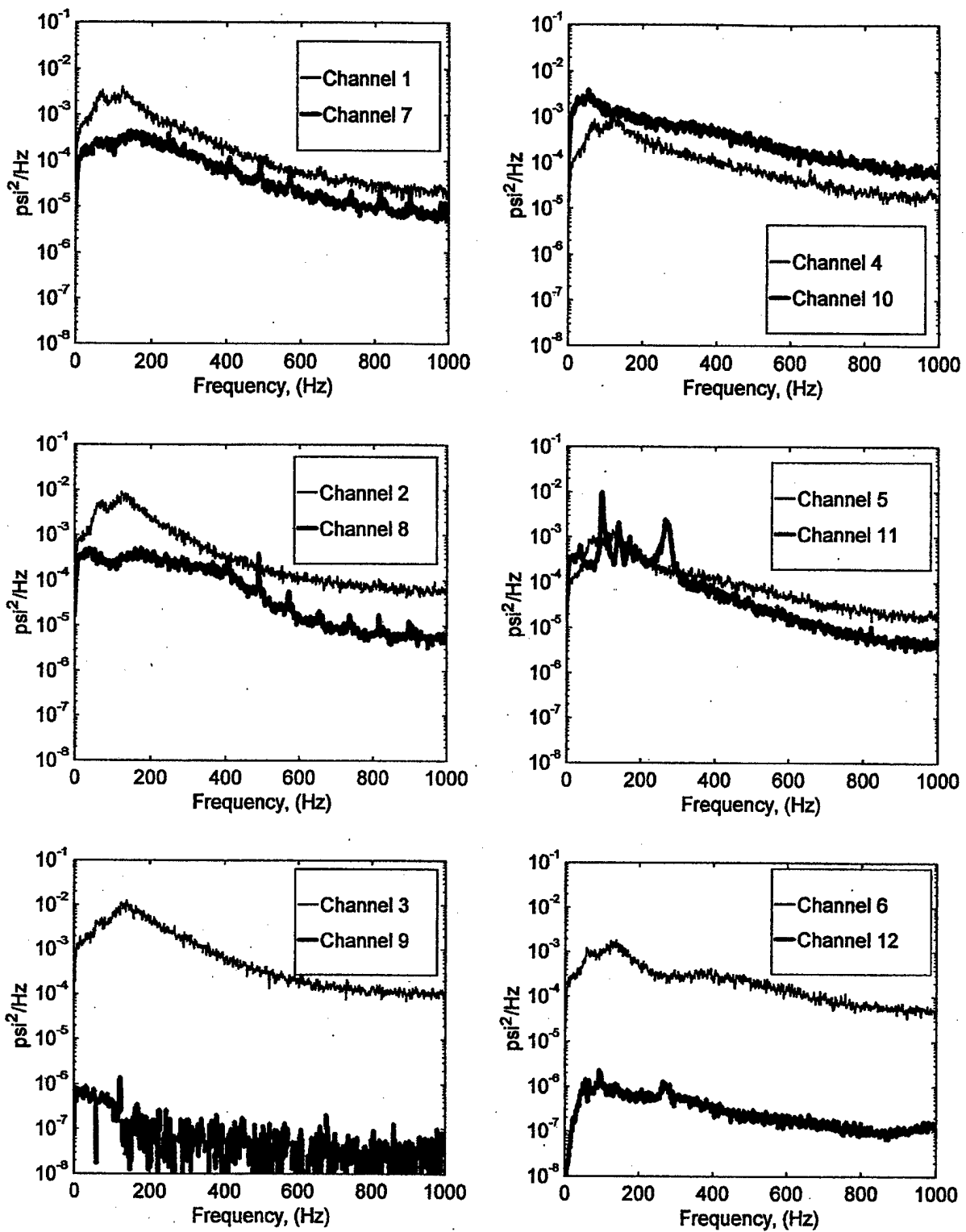
FIGURE B-29. PRESSURE POWER SPECTRAL DENSITY (RUN 9, POINT 5)

$(\overline{q} = 35psf, \alpha = 15°, \psi = -10°)$
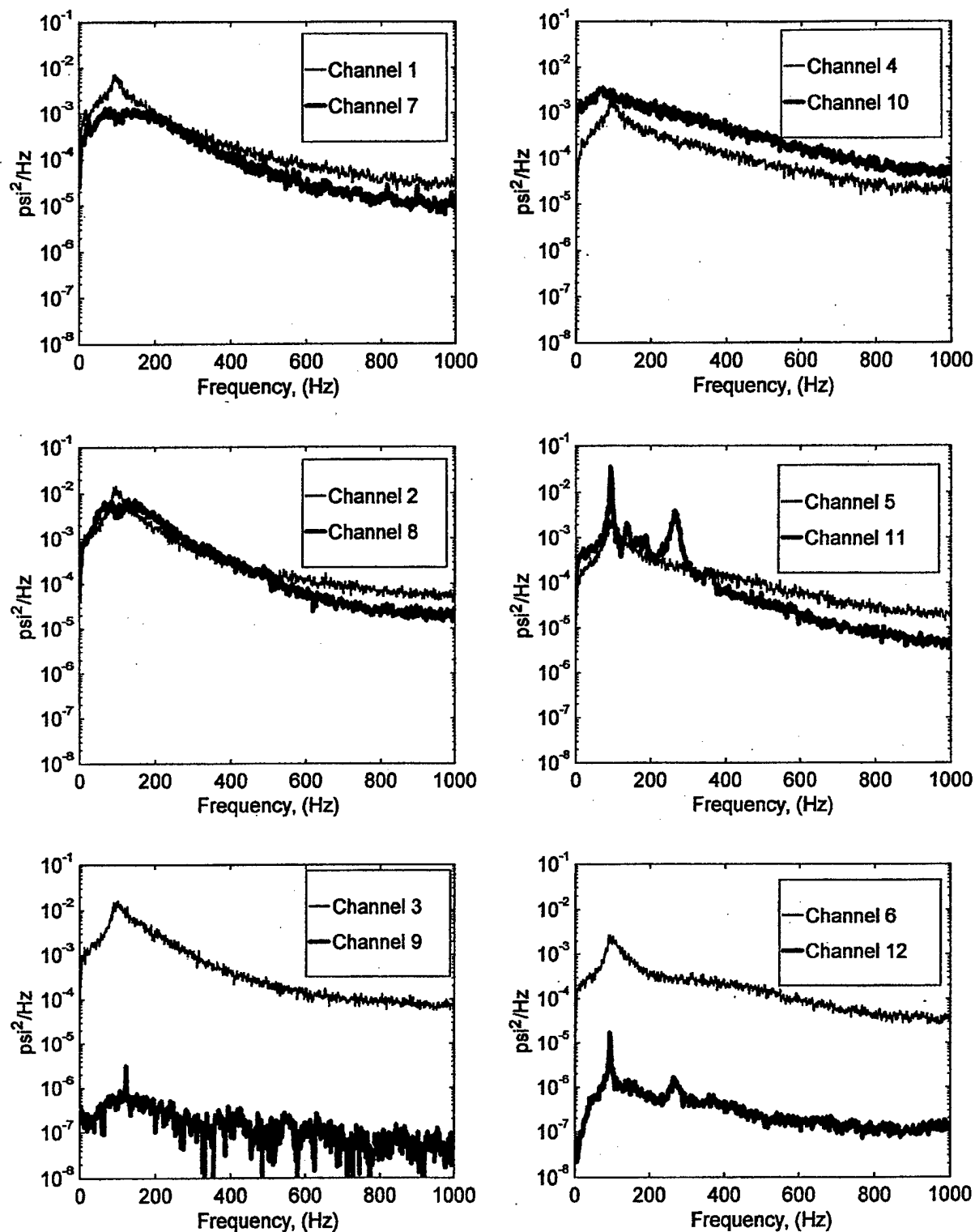
FIGURE B-30. PRESSURE POWER SPECTRAL DENSITY (RUN 9, POINT 6)
$$(\overline{q} = 35\,psf, \alpha = 20^{\circ}, \psi = -10^{\circ})$$
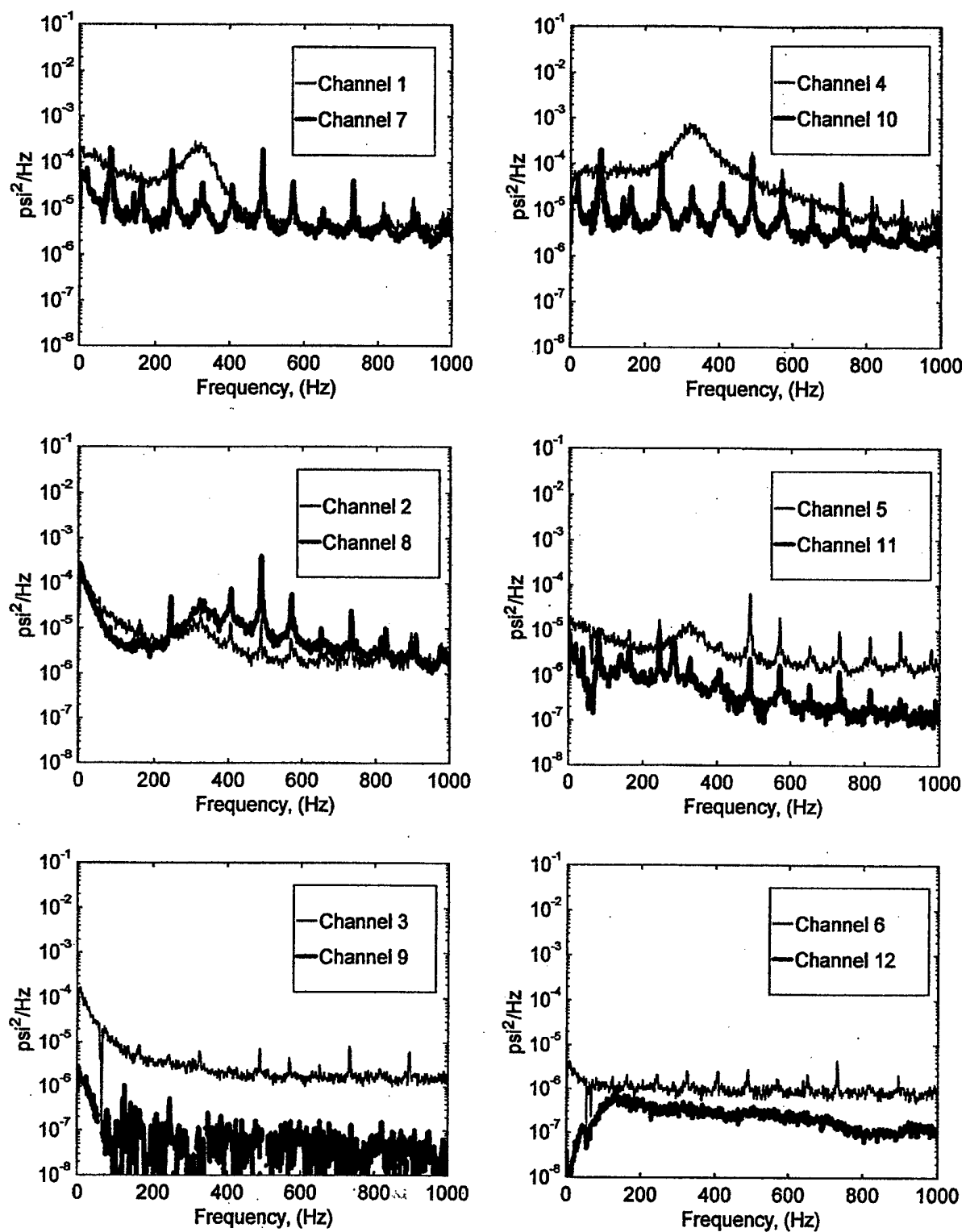
FIGURE B-31. PRESSURE POWER SPECTRAL DENSITY (RUN 10, POINT 1)
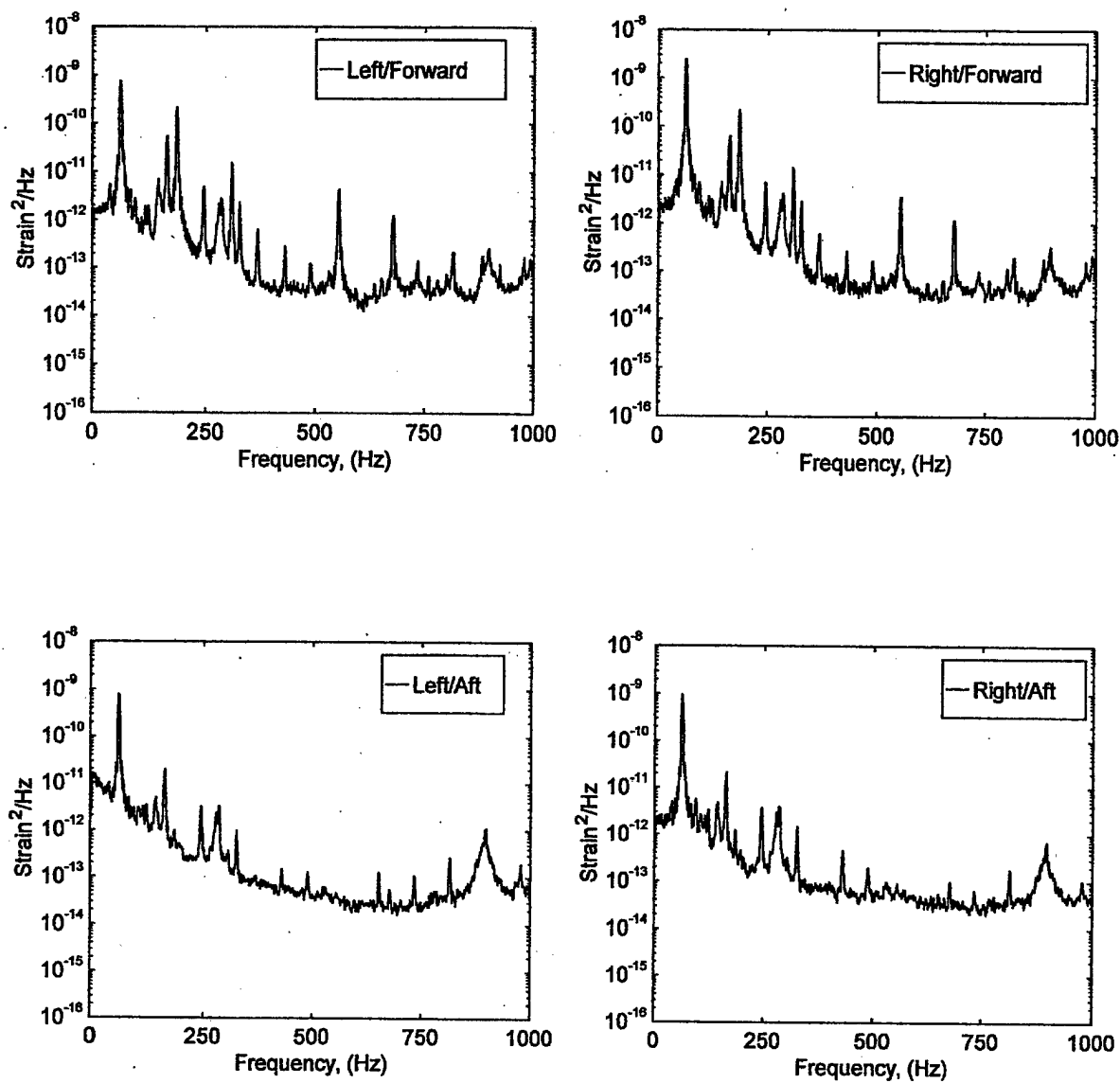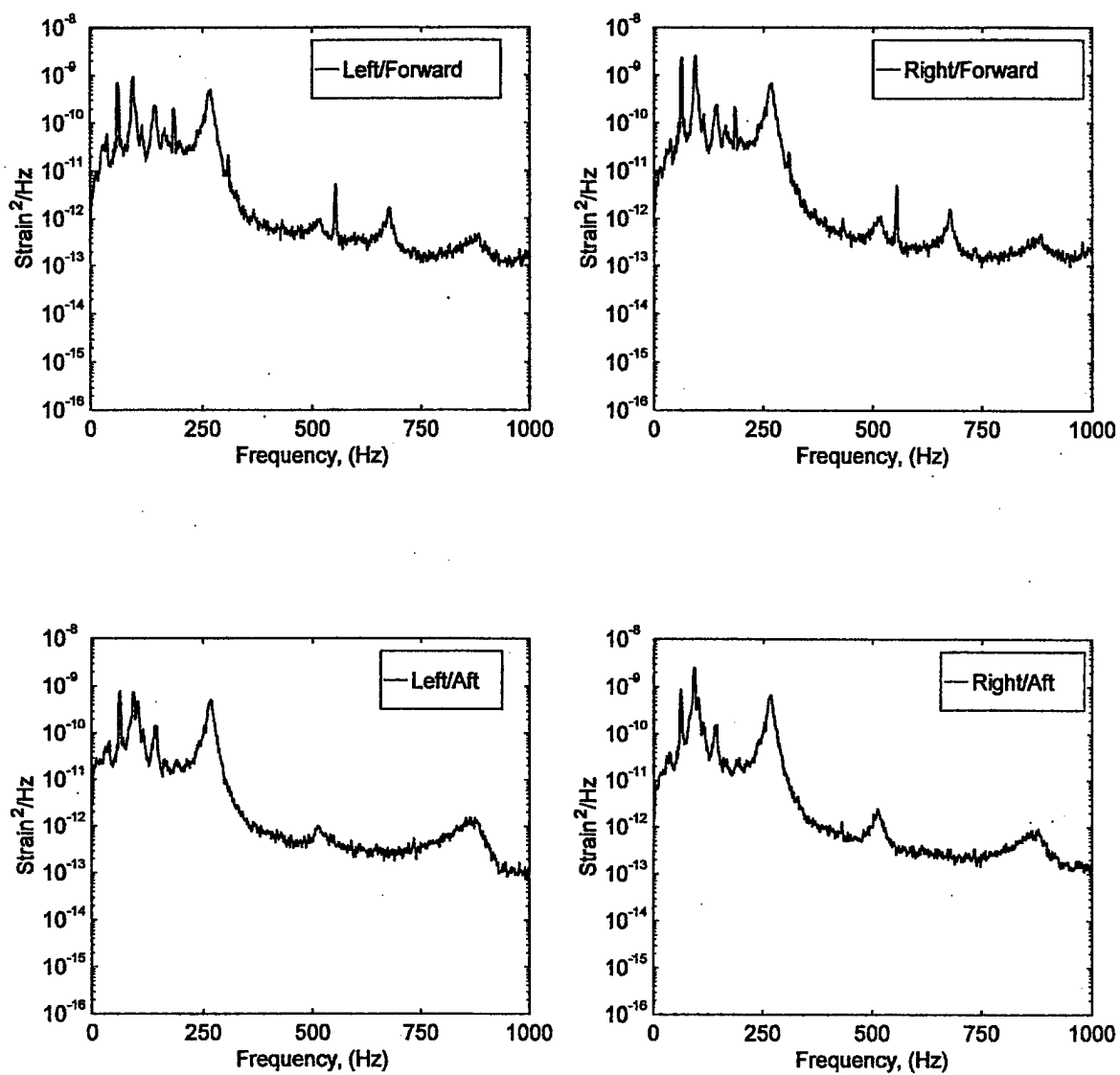$(\bar{q} = 45psf, \alpha = -5^\circ, \psi = -10^\circ)$
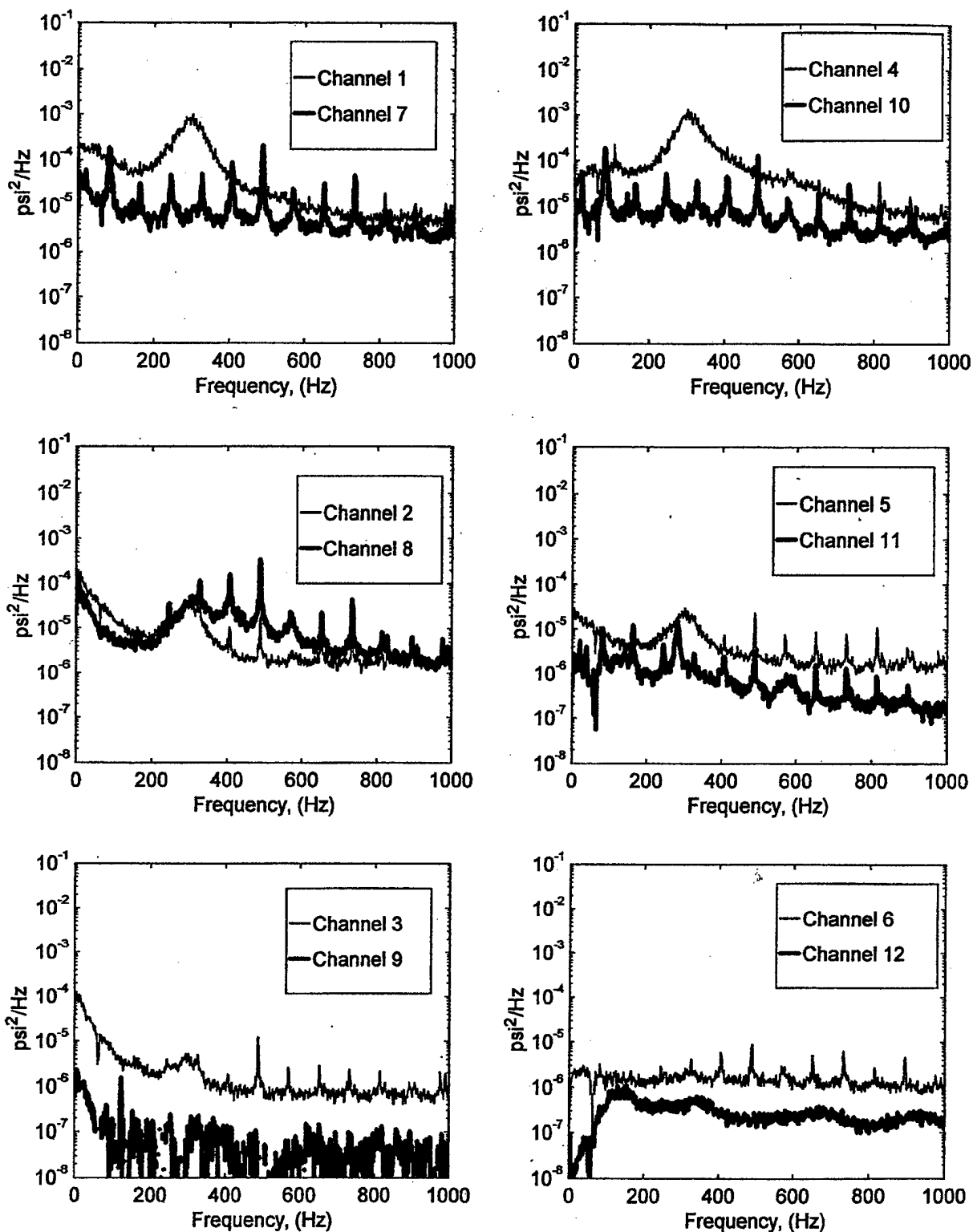
FIGURE B-32. PRESSURE POWER SPECTRAL DENSITY (RUN 10, POINT 2)
$(\overline{q} = 45 psf, \alpha = 0^{\circ}, \psi = -10^{\circ})$
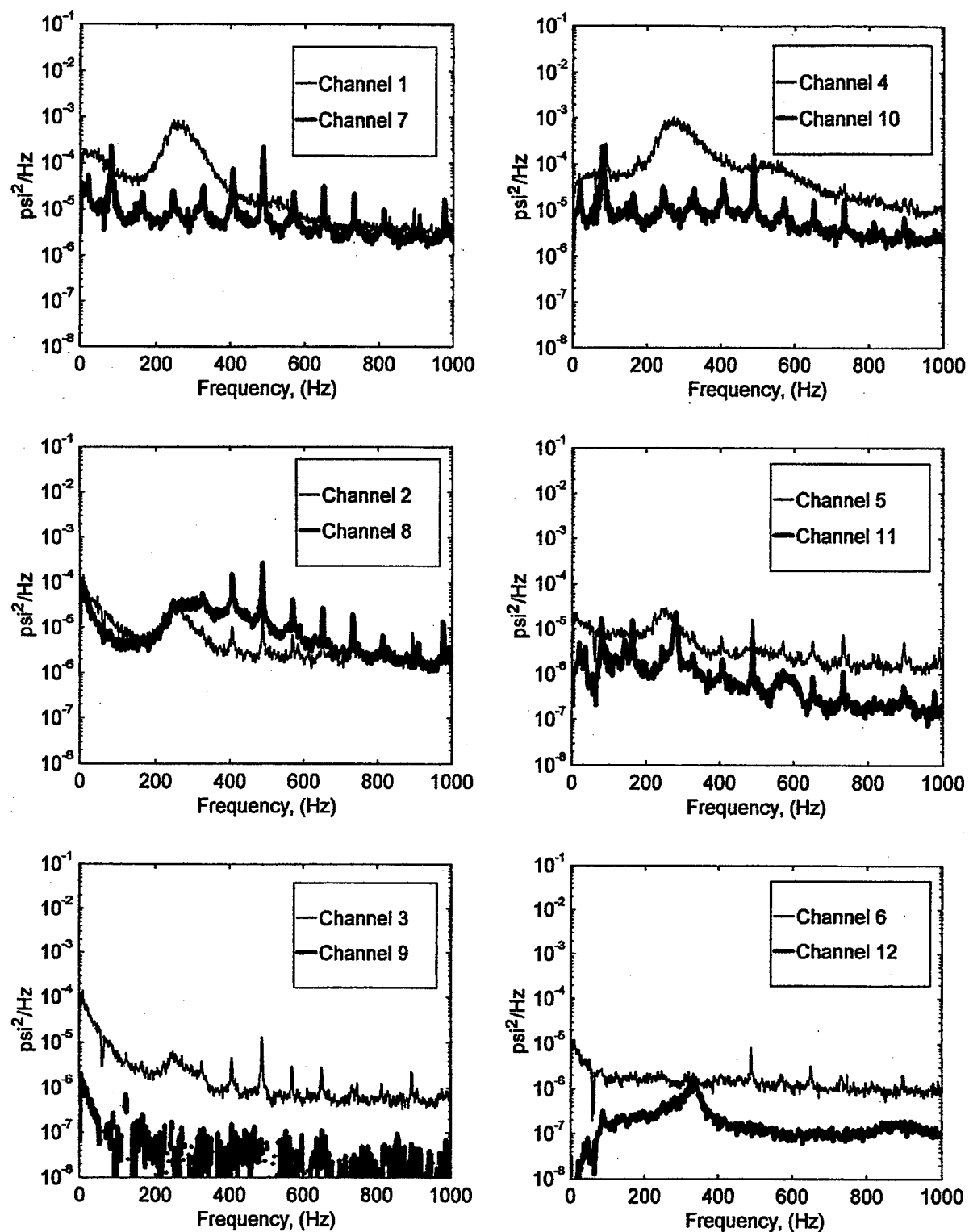
FIGURE B-33. PRESSURE POWER SPECTRAL DENSITY (RUN 10, POINT 3)
$$(\overline{q} = 45 psf, \alpha = 5^{\circ}, \psi = -10^{\circ})$$
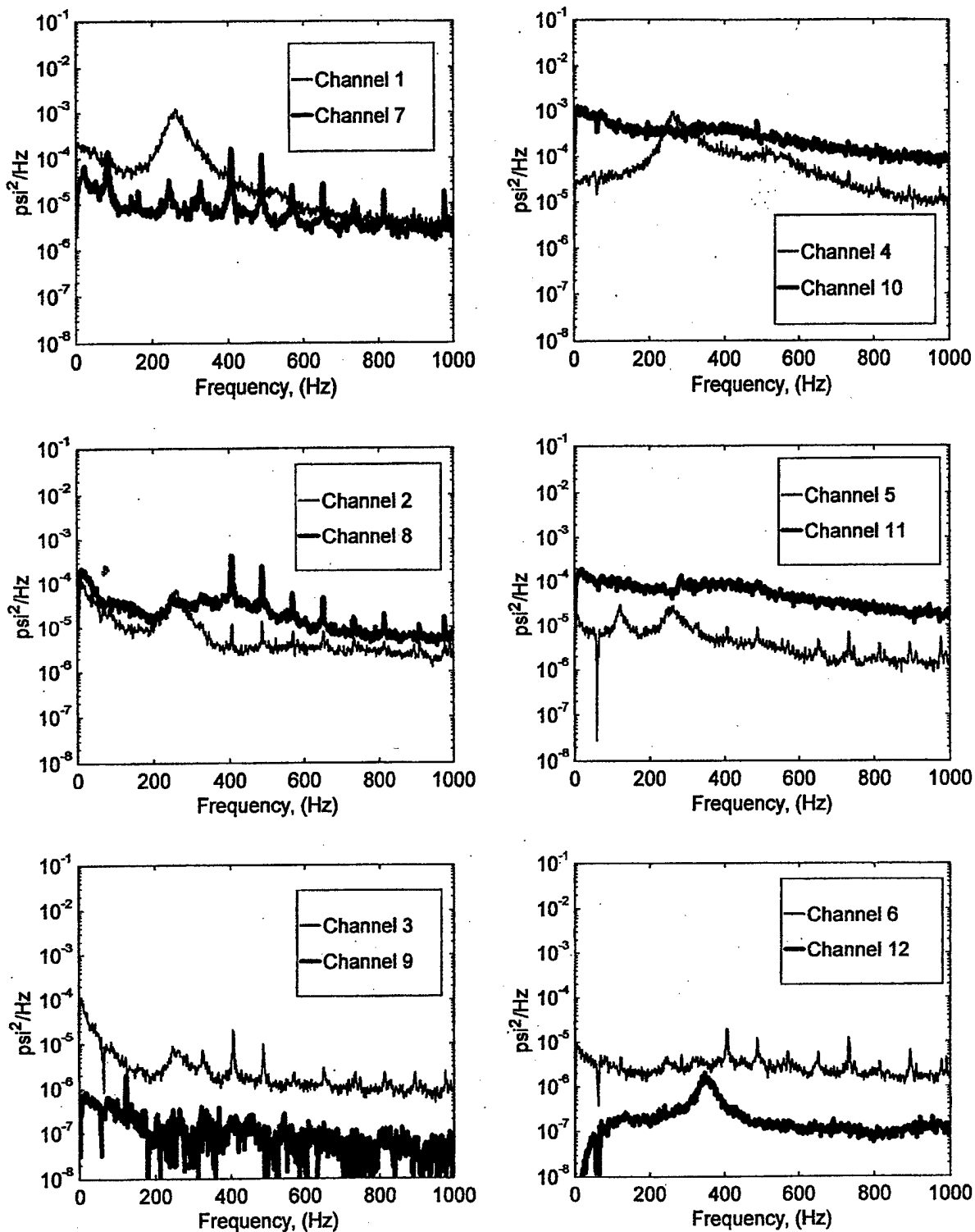
FIGURE B-34. PRESSURE POWER SPECTRAL DENSITY (RUN 10, POINT 4)

$$(\overline{q} = 45 psf, \alpha = 10^{\circ}, \psi = -10^{\circ})$$
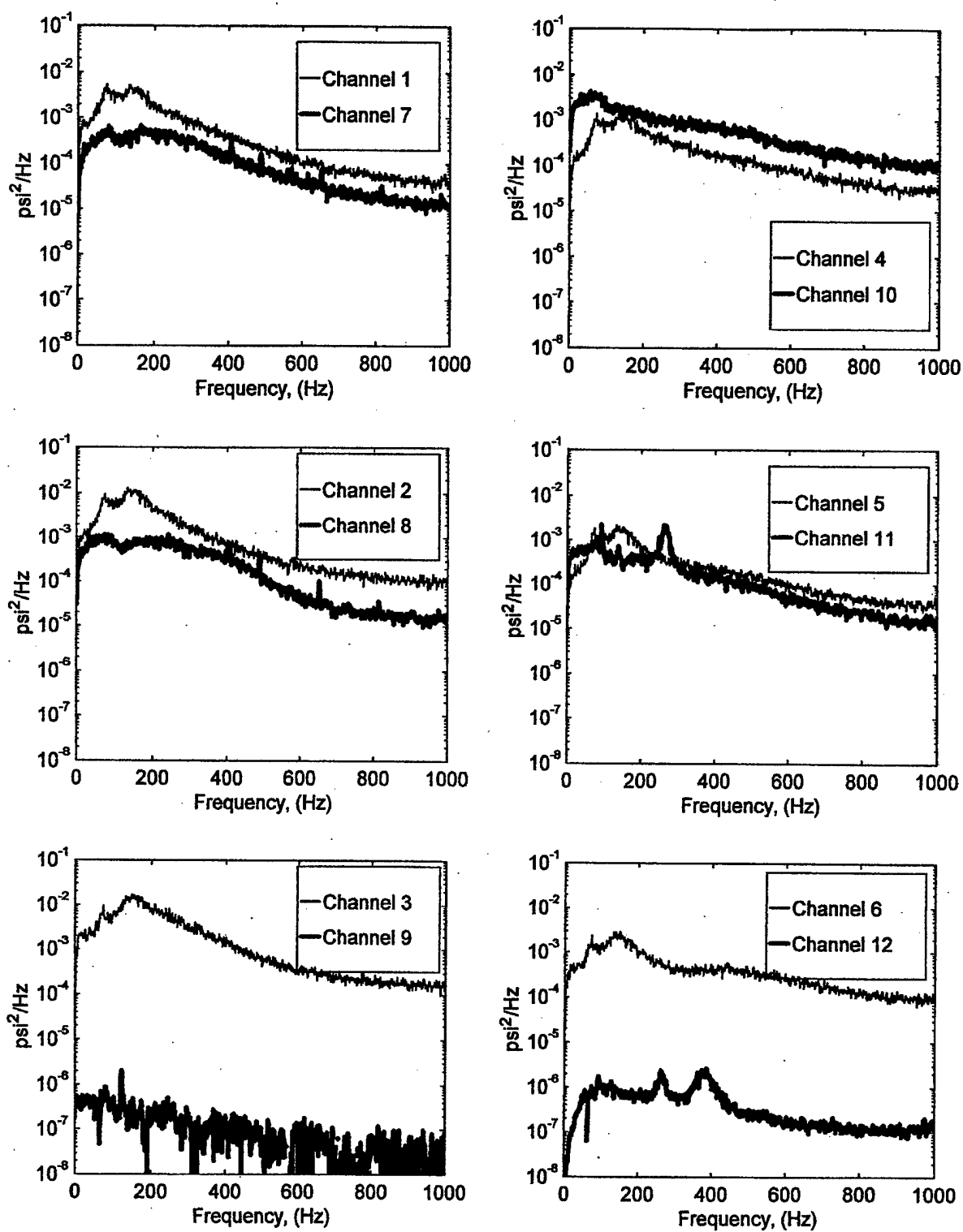
FIGURE B-35. PRESSURE POWER SPECTRAL DENSITY (RUN 10, POINT 5)

$(\overline{q} = 45\,psf, \alpha = 15°, \psi = -10°)$
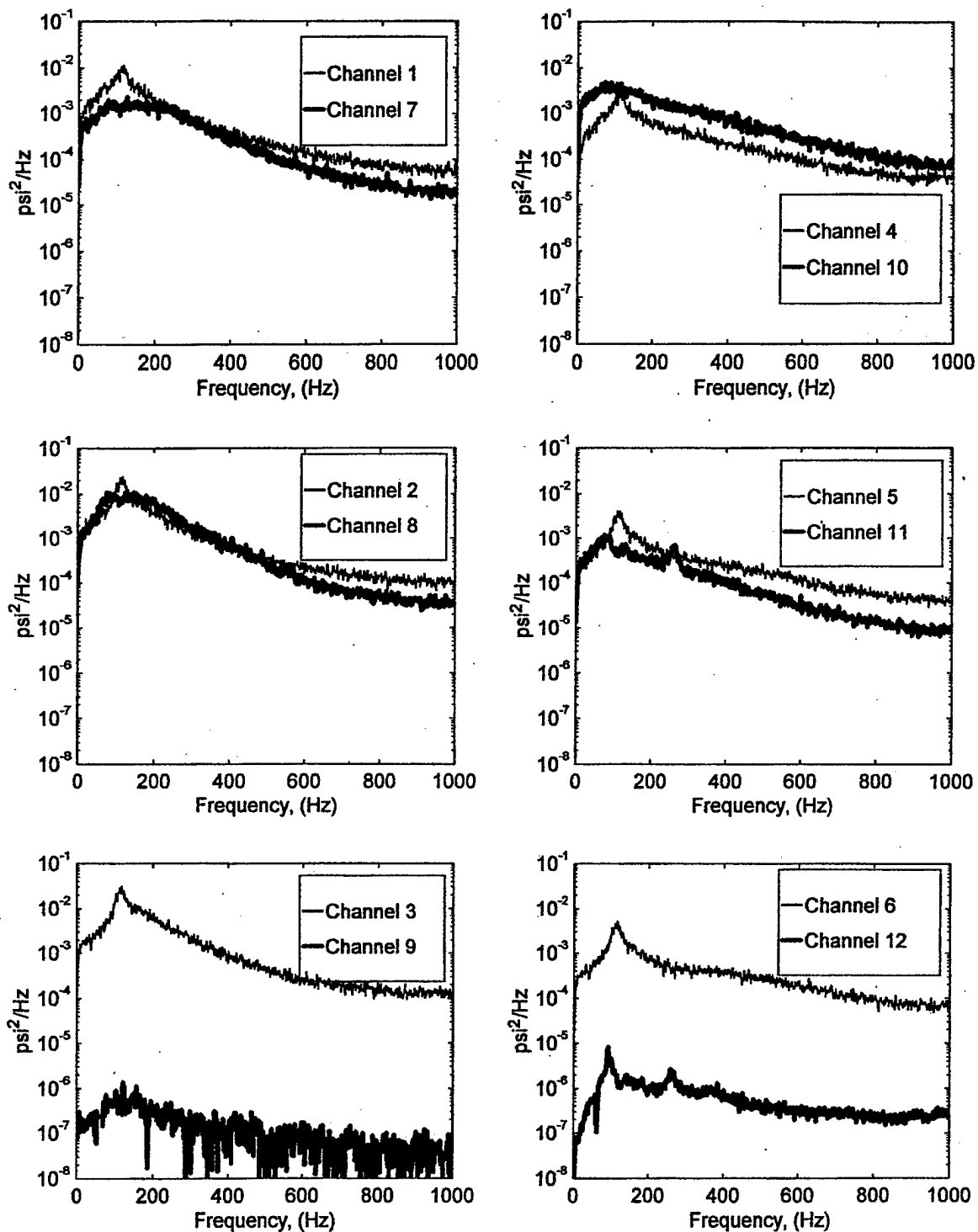
FIGURE B-36. PRESSURE POWER SPECTRAL DENSITY (RUN 10, POINT 6)
$$(\overline{q} = 45\,psf, \alpha = 20^{\circ}, \psi = -10^{\circ})$$
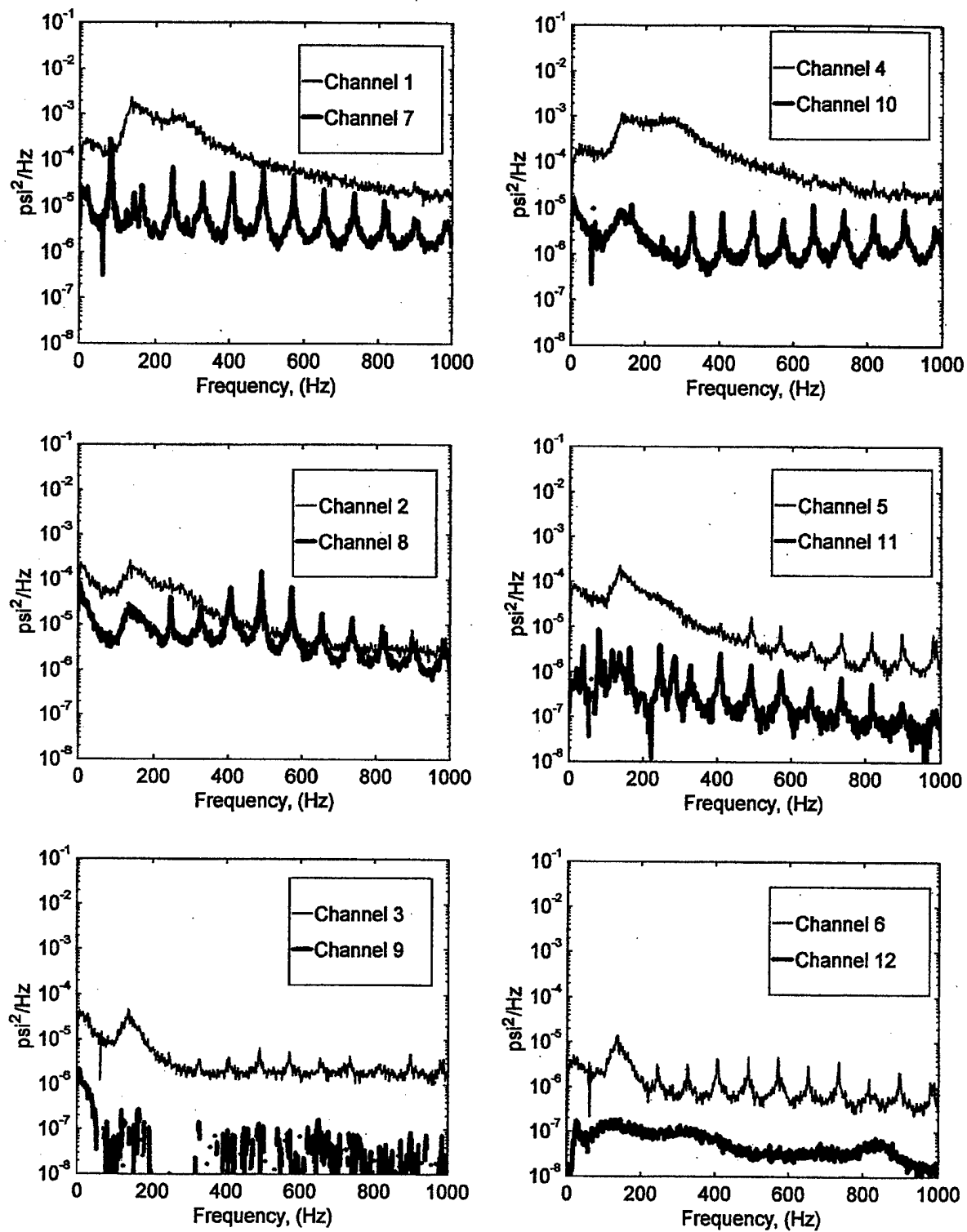
FIGURE B-37. PRESSURE POWER SPECTRAL DENSITY (RUN 11, POINT 1)
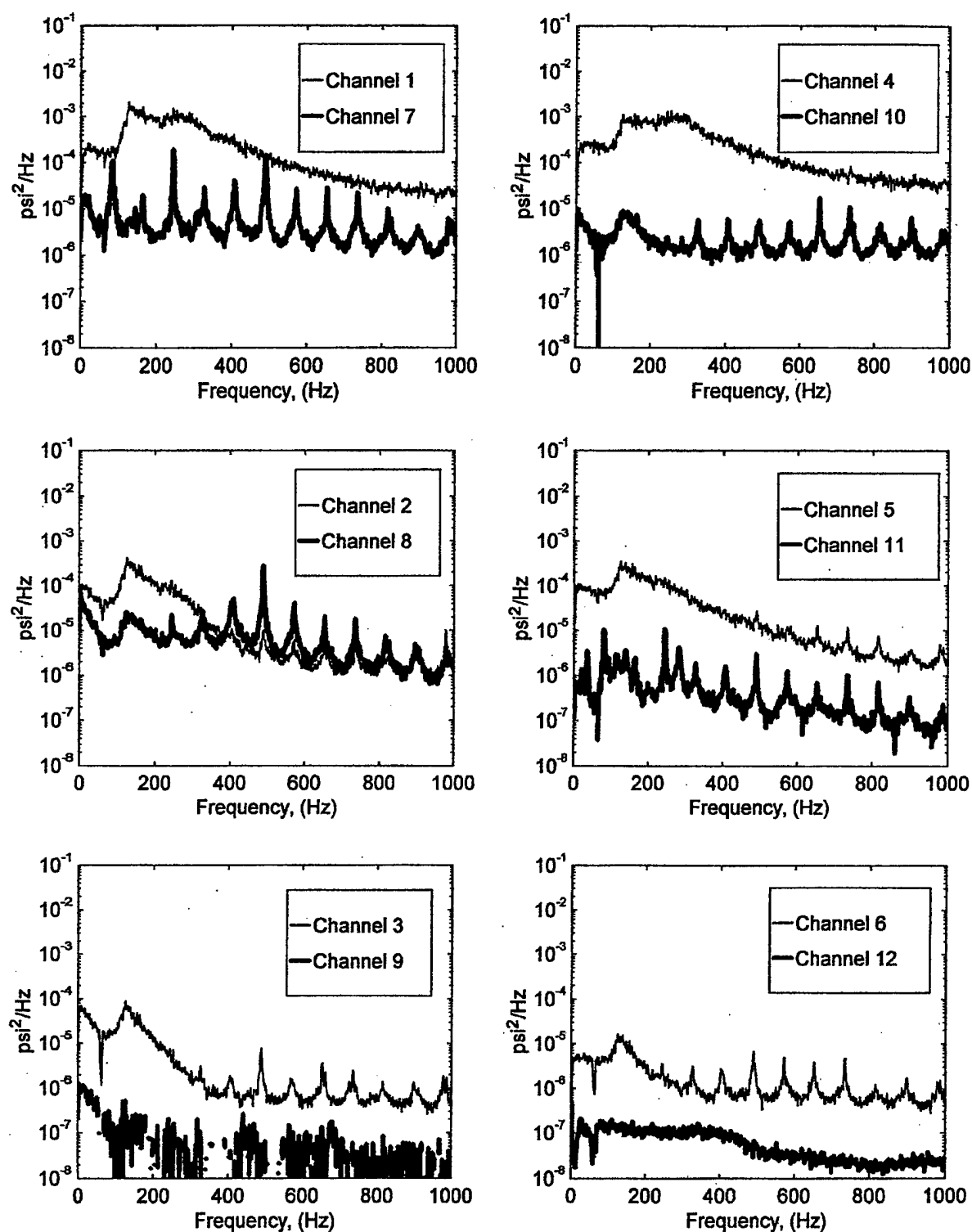
$$(\bar{q} = 25\,psf, \alpha = -5°, \psi = -20°)$$

FIGURE B-38. PRESSURE POWER SPECTRAL DENSITY (RUN 11, POINT 2)

$$(\overline{q} = 25 psf, \alpha = 0^{\circ}, \psi = -20^{\circ})$$
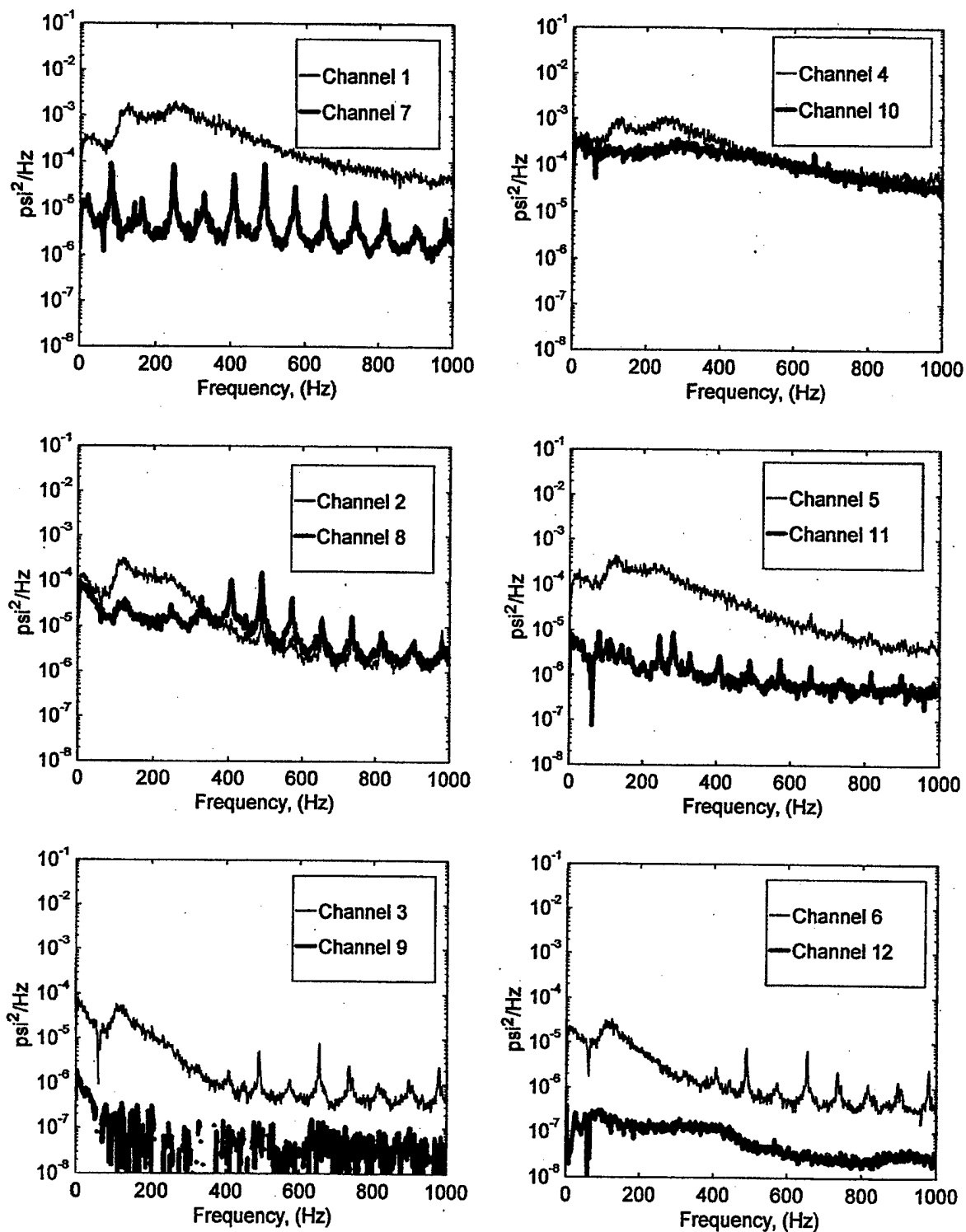
FIGURE B-39. PRESSURE POWER SPECTRAL DENSITY (RUN 11, POINT 3)
$(\overline{q} = 25psf, \alpha = 5°, \psi = -20°)$
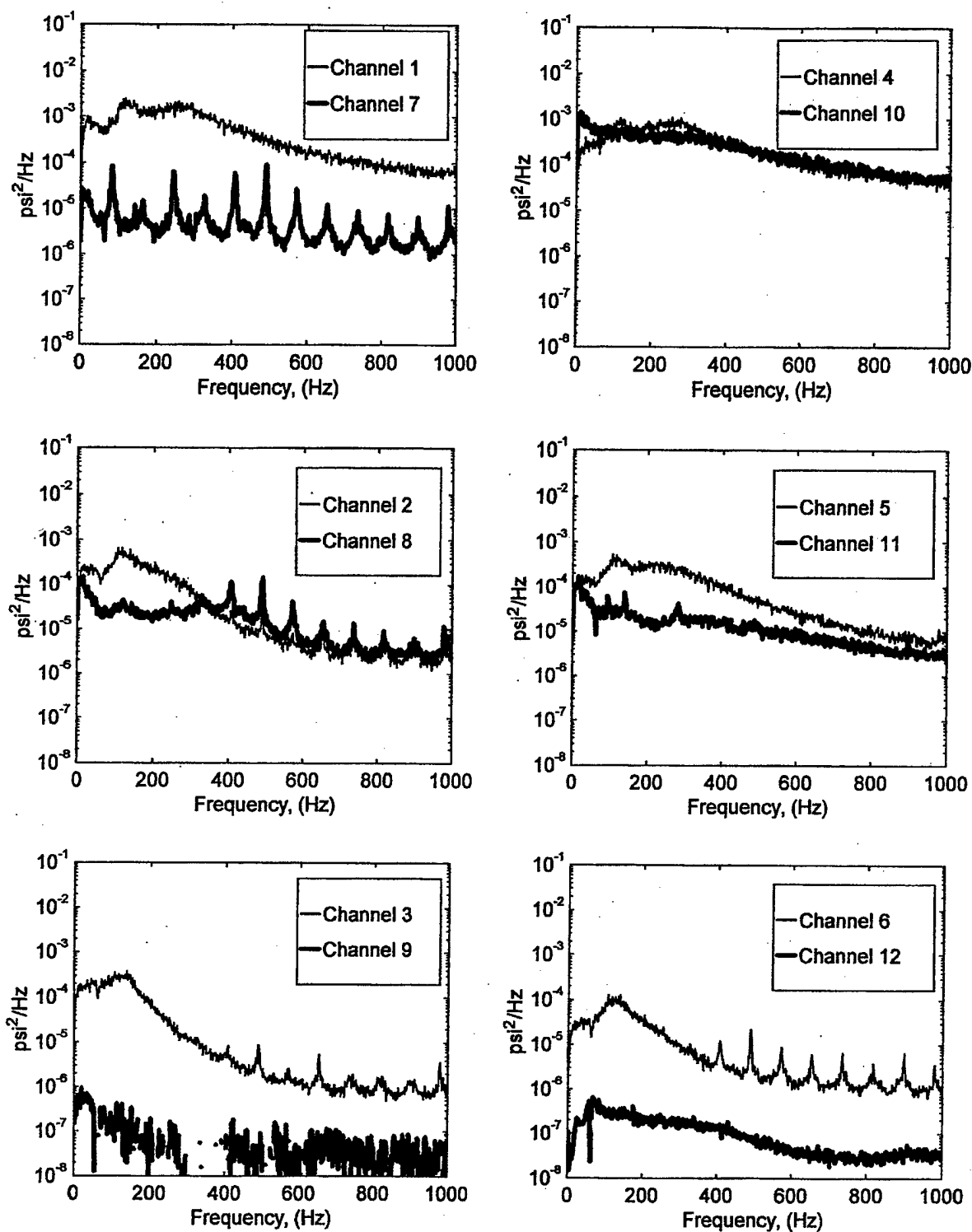
FIGURE B-40. PRESSURE POWER SPECTRAL DENSITY (RUN 11, POINT 4)
$(\overline{q} = 25\,psf, \alpha = 10°, \psi = -20°)$
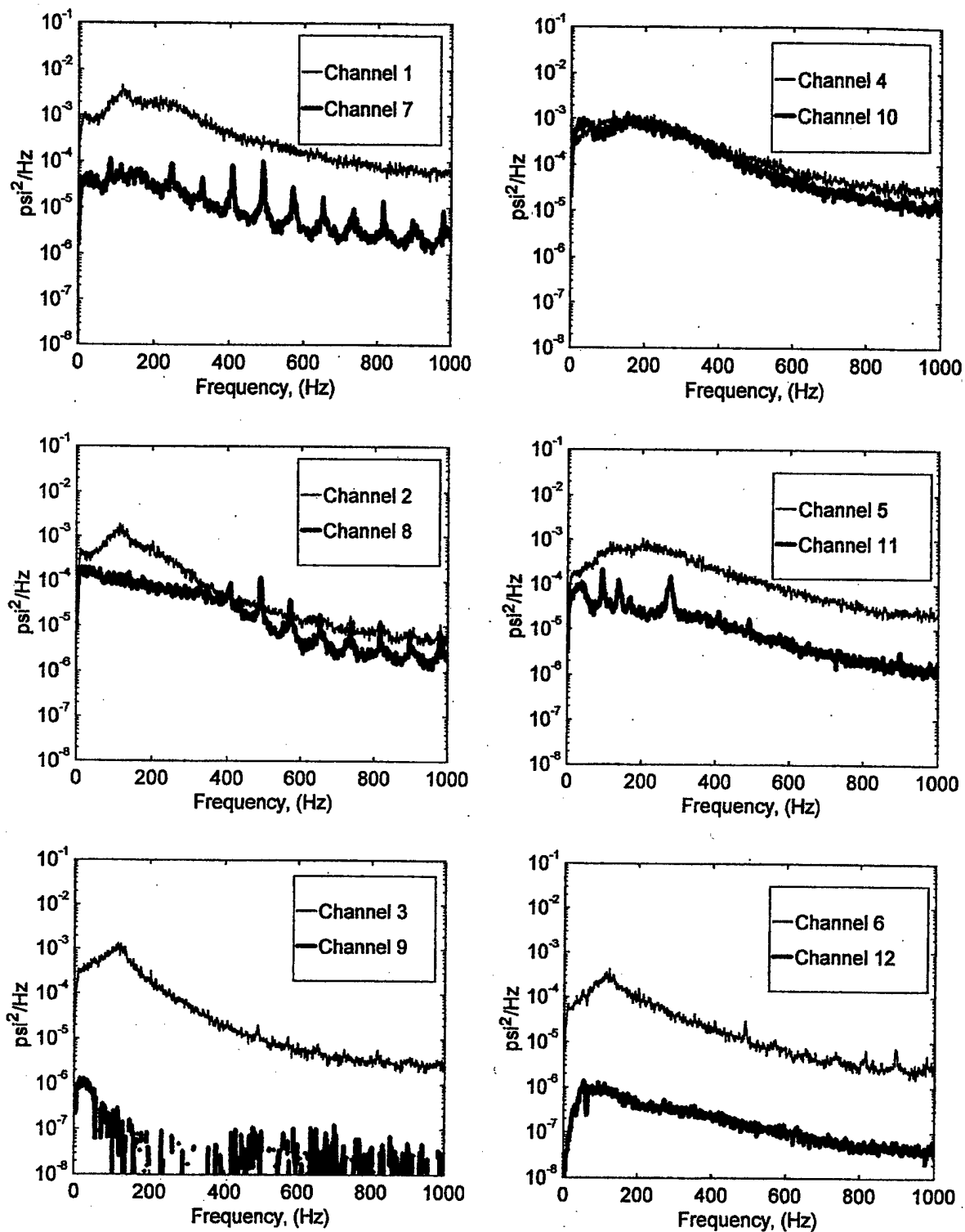
FIGURE B-41. PRESSURE POWER SPECTRAL DENSITY (RUN 11, POINT 5)
$(\overline{q} = 25\,psf, \alpha = 15°, \psi = -20°)$
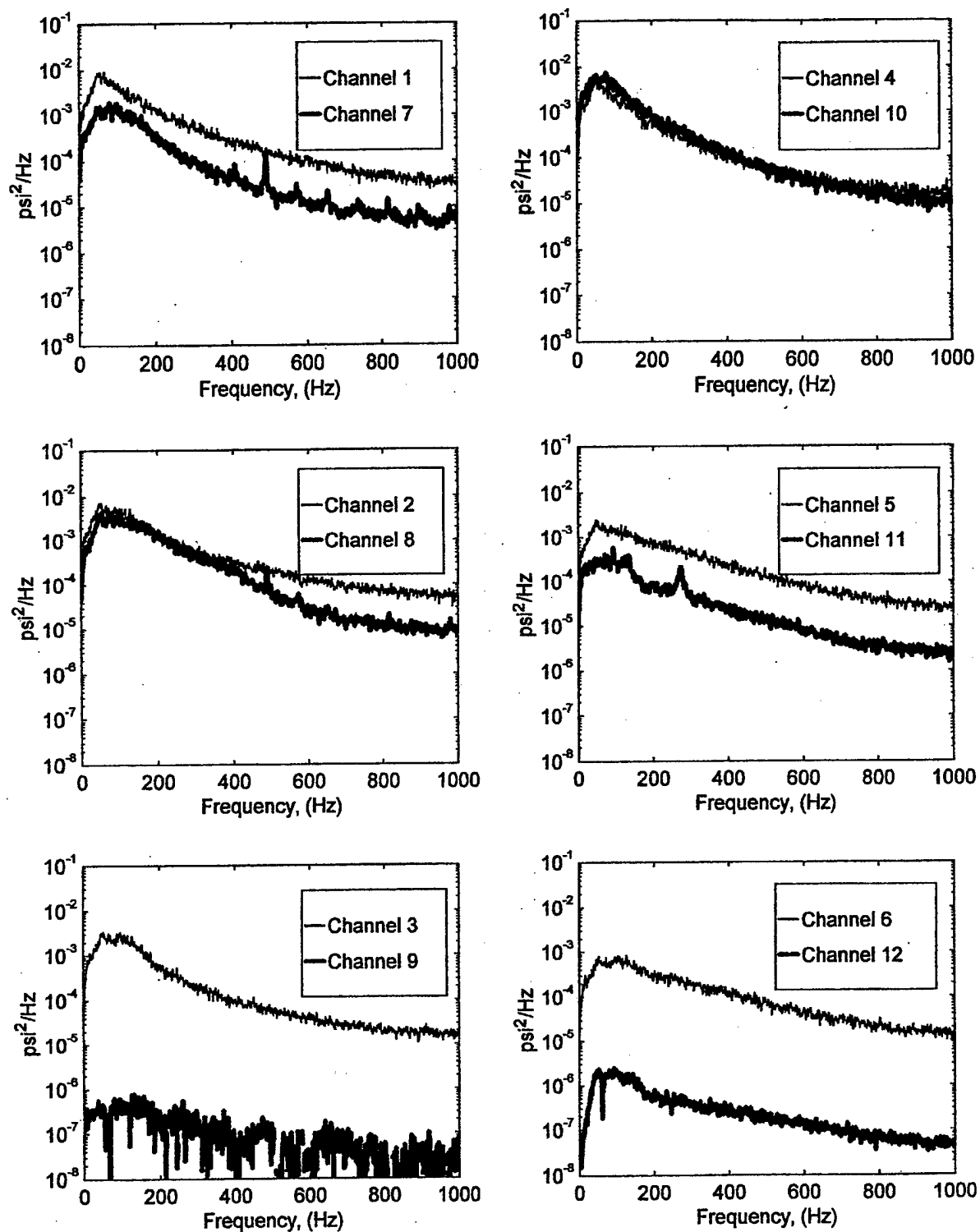
FIGURE B-42. PRESSURE POWER SPECTRAL DENSITY (RUN 11, POINT 6)
$(\overline{q} = 25\,psf, \alpha = 20^{\circ}, \psi = -20^{\circ})$
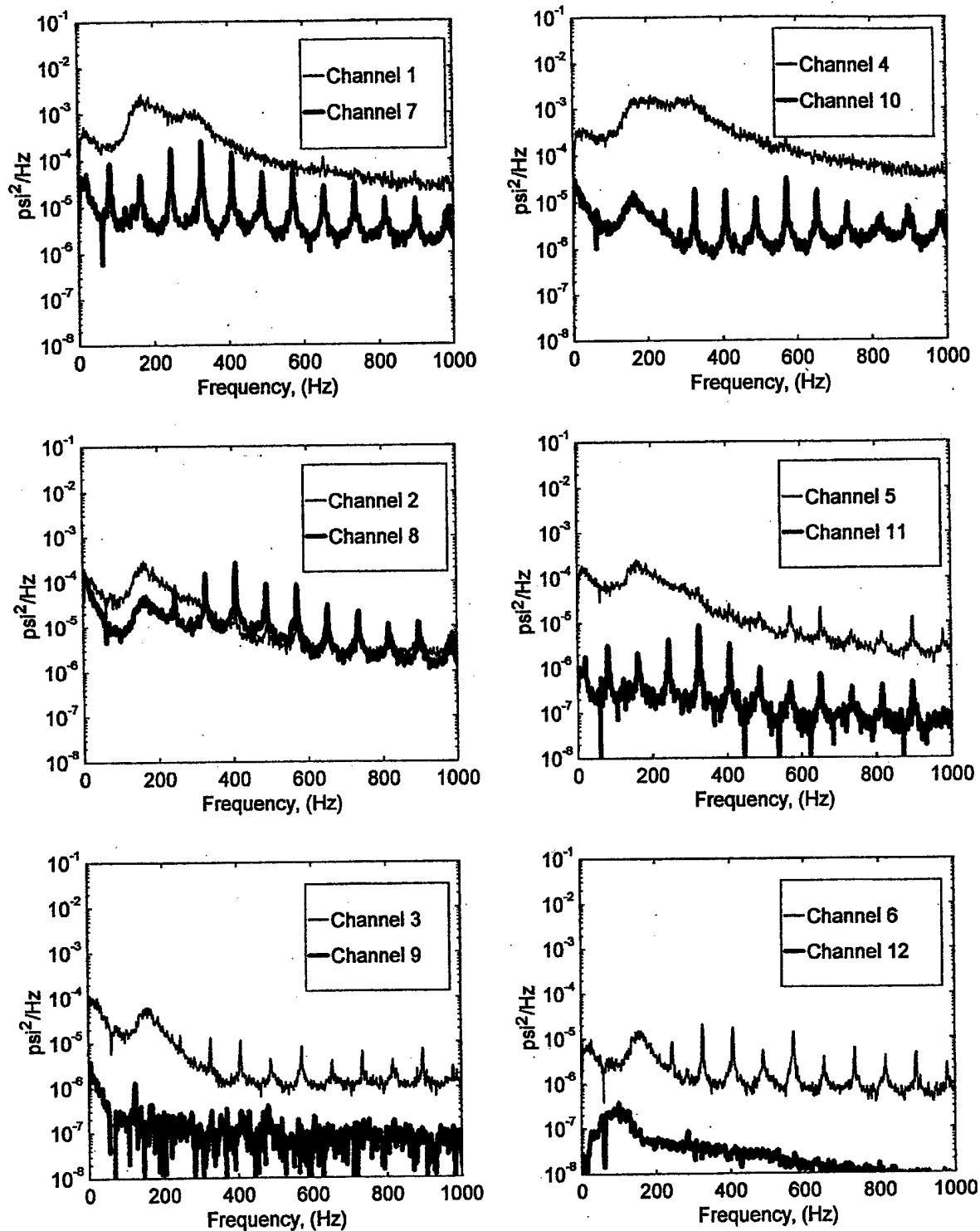
FIGURE B-43. PRESSURE POWER SPECTRAL DENSITY (RUN 12, POINT 1)
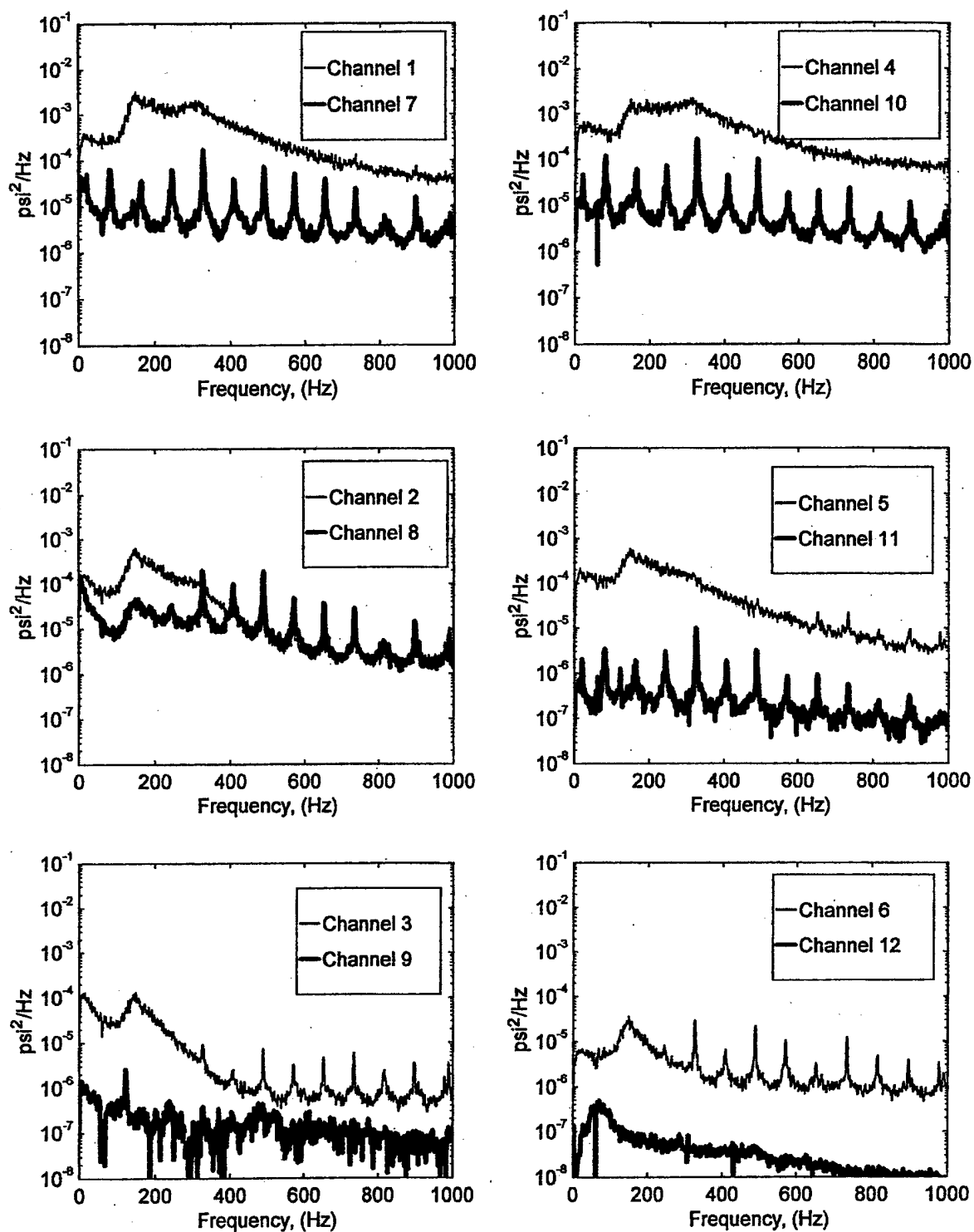
$$(\overline{q} = 35\,psf, \alpha = -5°, \psi = -20°)$$

FIGURE B-44. PRESSURE POWER SPECTRAL DENSITY (RUN 12, POINT 2)

$$(\overline{q} = 35\,psf, \alpha = 0^{\circ}, \psi = -20^{\circ})$$
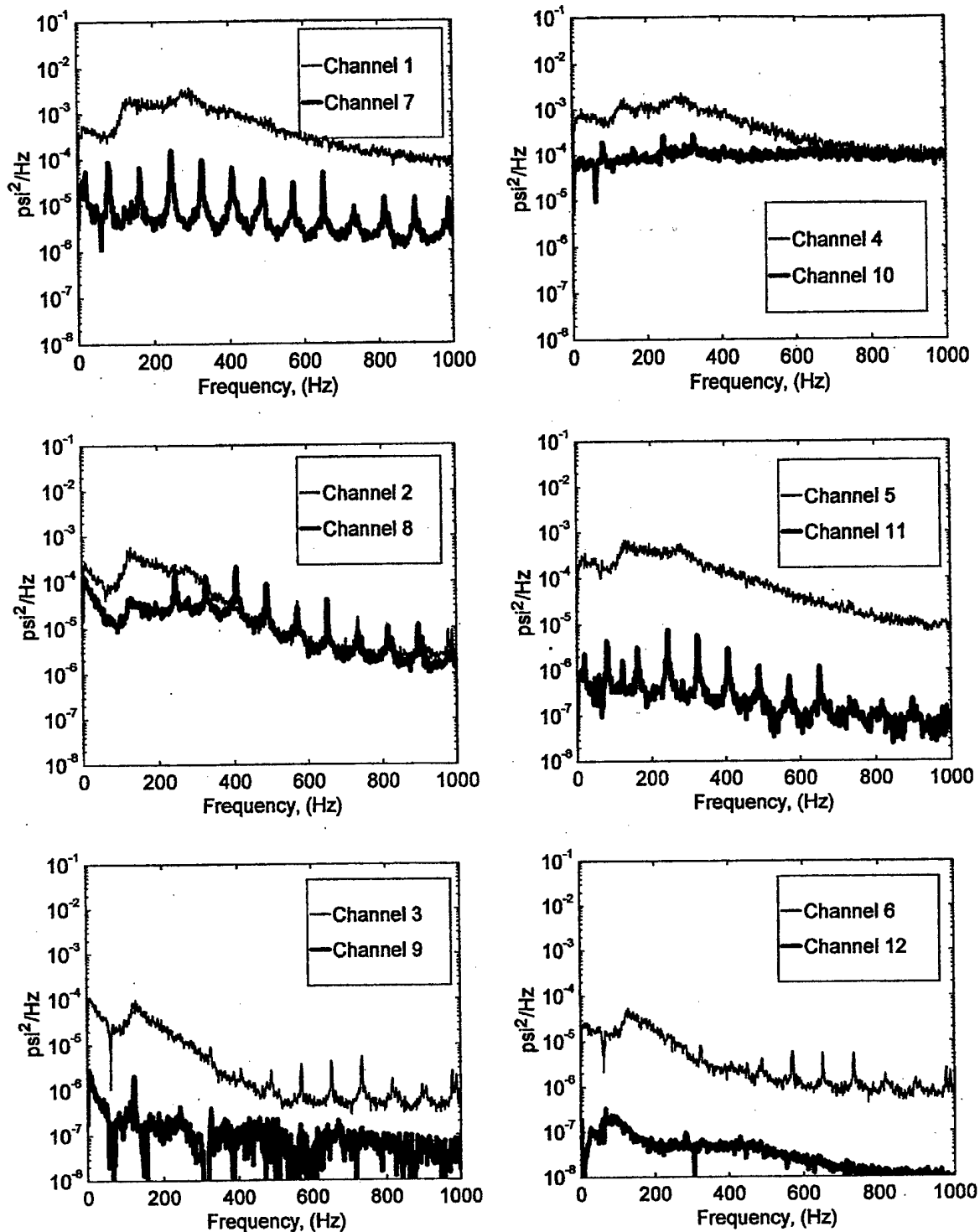
FIGURE B-45. PRESSURE POWER SPECTRAL DENSITY (RUN 12, POINT 3)
$(\overline{q} = 35\,psf, \alpha = 5^{\circ}, \psi = -20^{\circ})$
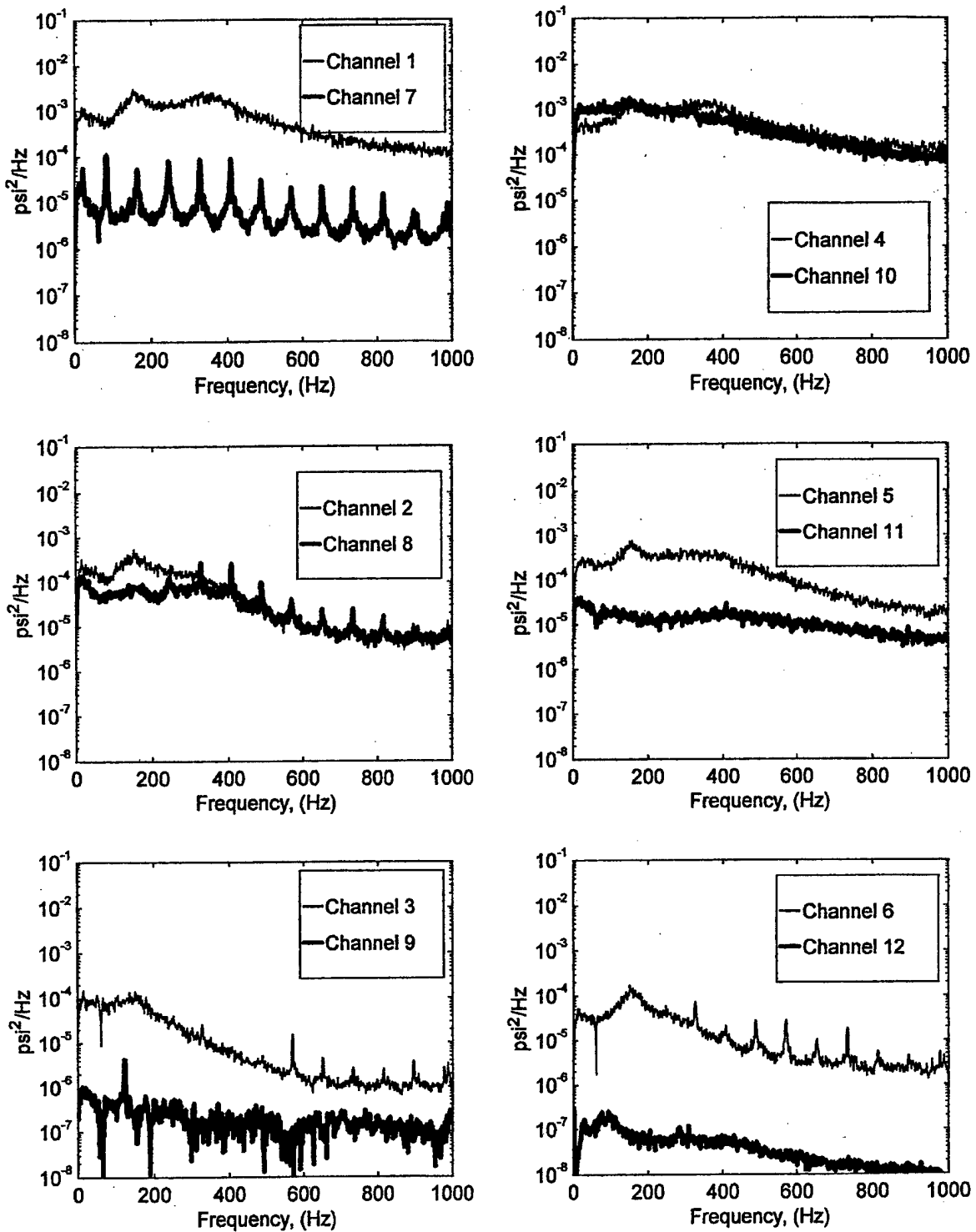
FIGURE B-46. PRESSURE POWER SPECTRAL DENSITY (RUN 12, POINT 4)
$(\overline{q} = 35\,psf, \alpha = 10^{\circ}, \psi = -20^{\circ})$
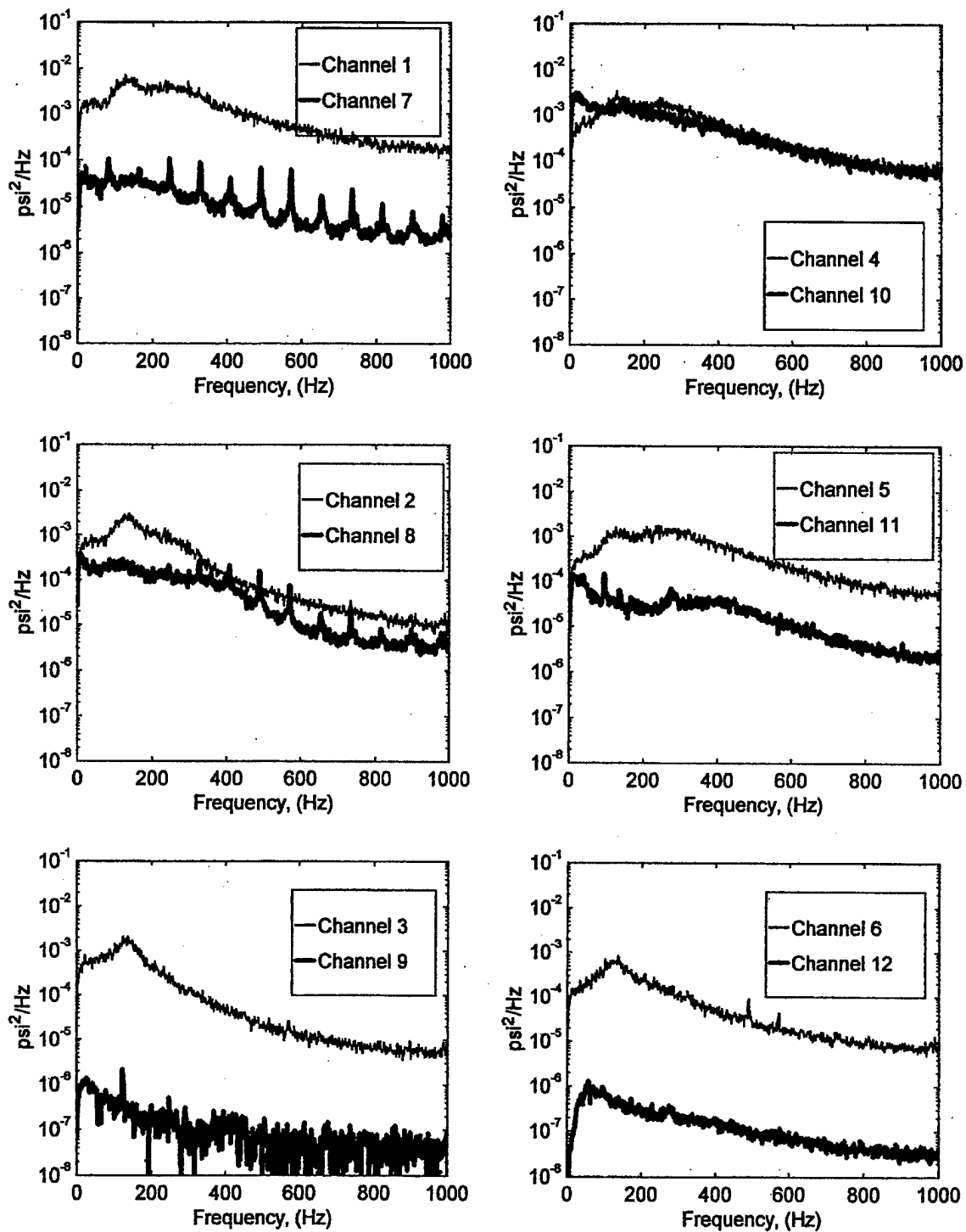
FIGURE B-47. PRESSURE POWER SPECTRAL DENSITY (RUN 12, POINT 5)
$(\bar{q} = 35\,psf, \alpha = 15^{\circ}, \psi = -20^{\circ})$
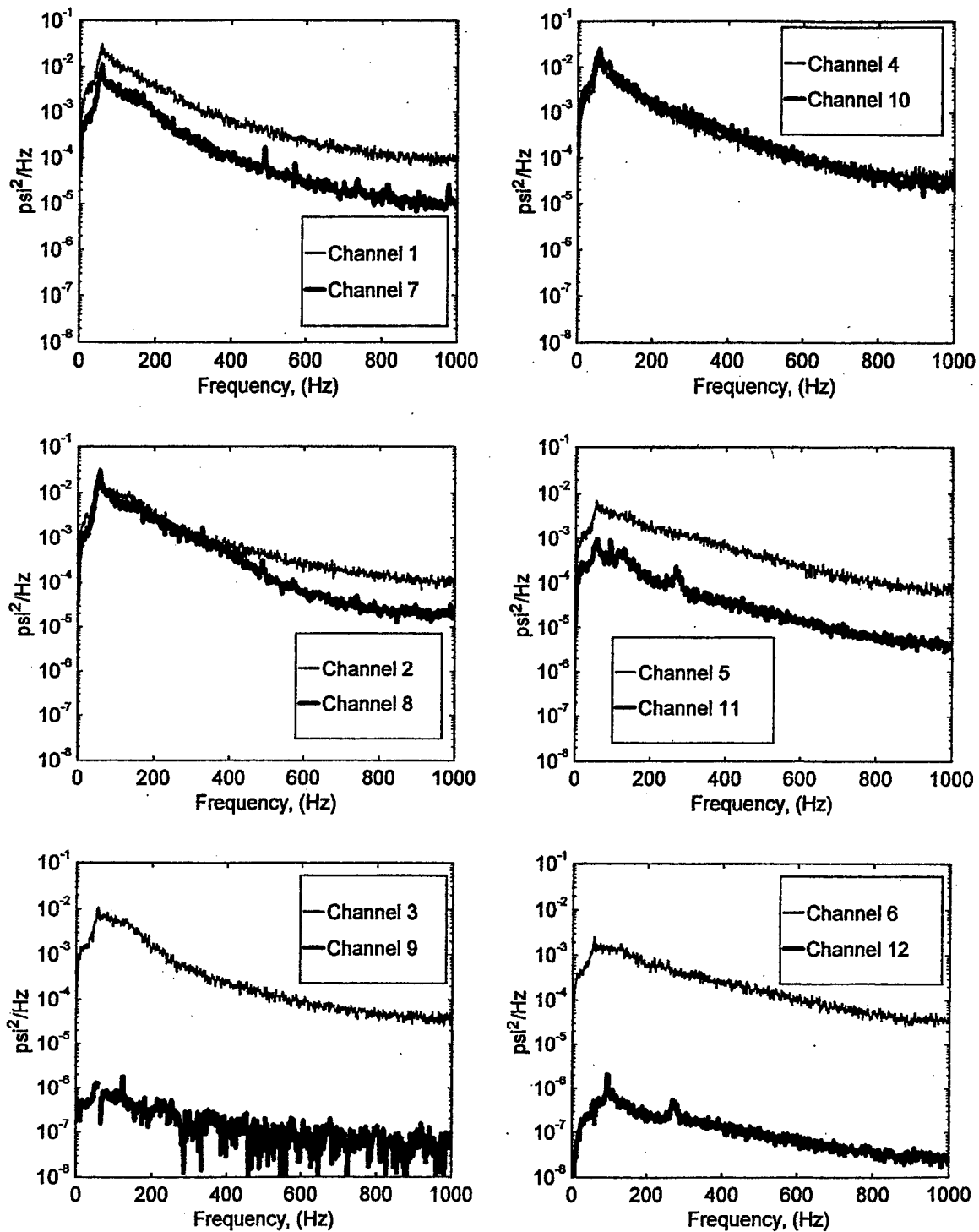
FIGURE B-48. PRESSURE POWER SPECTRAL DENSITY (RUN 12, POINT 6)
$$(\overline{q} = 35\,psf, \alpha = 20^{\circ}, \psi = -20^{\circ})$$
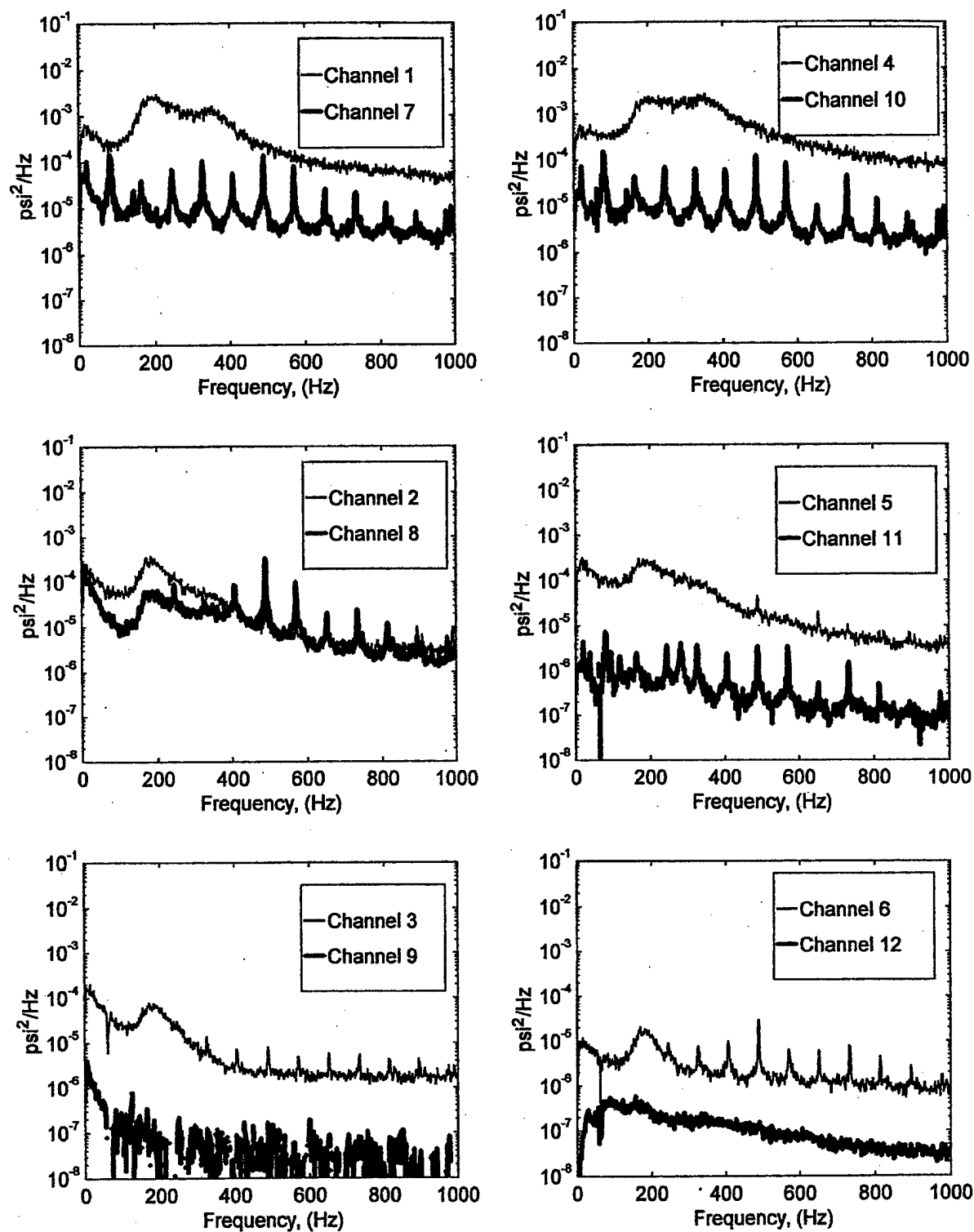
FIGURE B-49. PRESSURE POWER SPECTRAL DENSITY (RUN 13, POINT 1)
$(\overline{q} = 45 psf, \alpha = -5^\circ, \psi = -20^\circ)$

FIGURE B-50. PRESSURE POWER SPECTRAL DENSITY (RUN 13, POINT 2)

$$(\overline{q} = 45\,psf, \alpha = 0\degree, \psi = -20\degree)$$

FIGURE B-51. PRESSURE POWER SPECTRAL DENSITY (RUN 13, POINT 3)
$(\bar{q} = 45psf, \alpha = 5°, \psi = -20°)$

FIGURE B-52. PRESSURE POWER SPECTRAL DENSITY (RUN 13, POINT 4)
$(\bar{q} = 45psf, \alpha = 10^\circ, \psi = -20^\circ)$

FIGURE B-53. PRESSURE POWER SPECTRAL DENSITY (RUN 13, POINT 5)
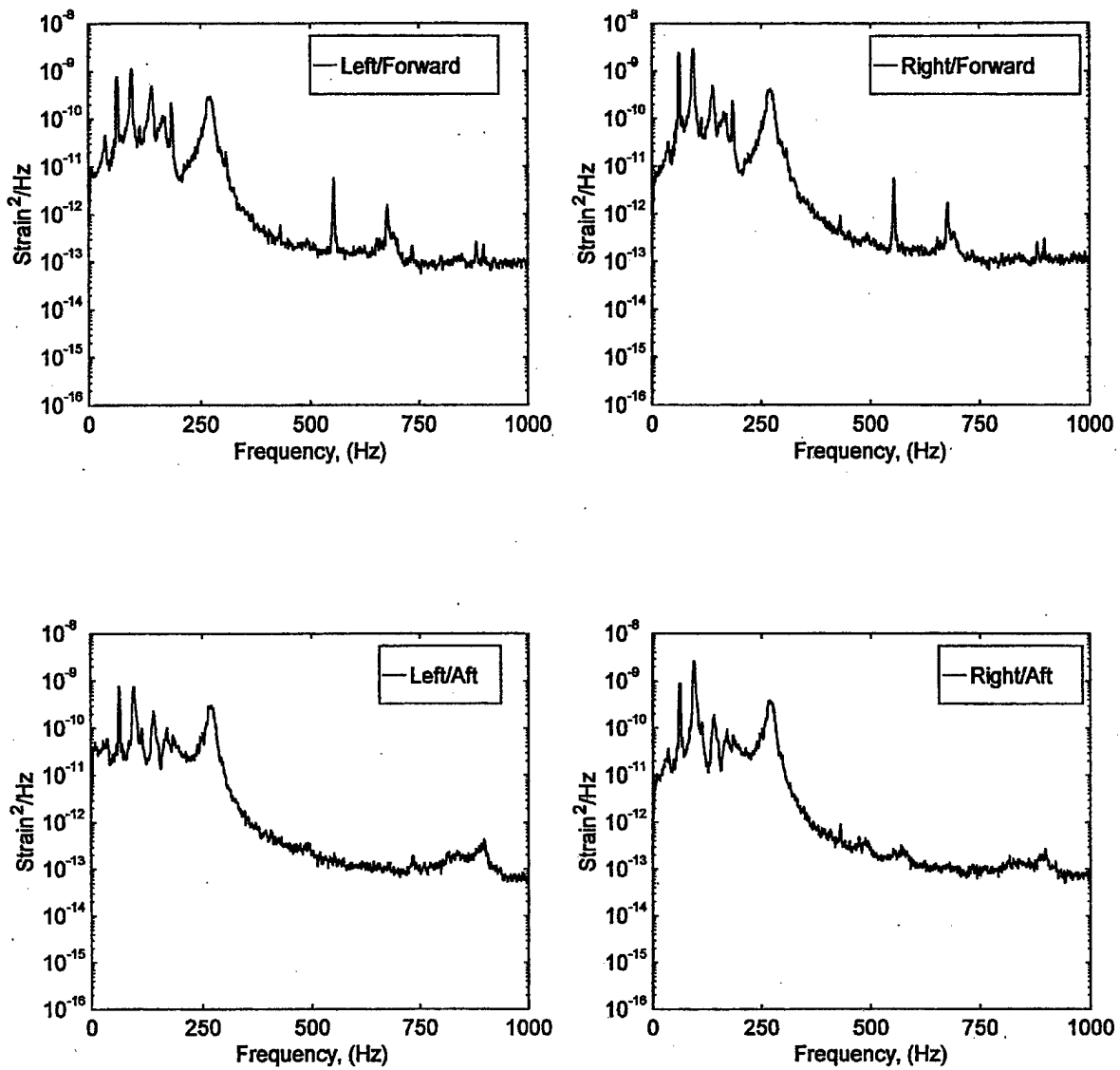$(\overline{q} = 45psf, \alpha = 15°, \psi = -20°)$
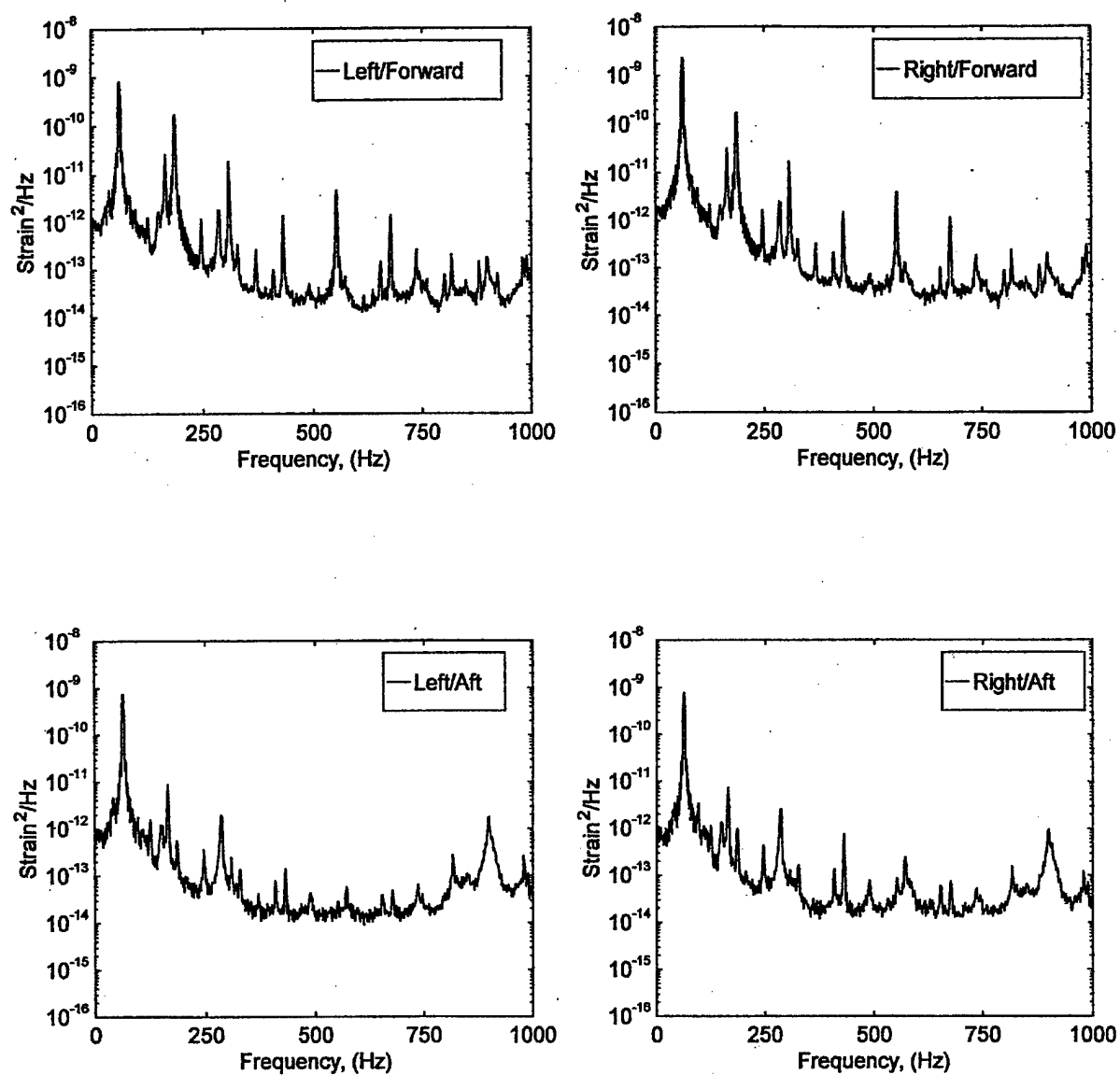
FIGURE C-1. STRAIN POWER SPECTRAL DENSITY (RUN 5, POINT 1)
$(\overline{q} = 25 psf, \alpha = -5^{\circ}, \psi = 0^{\circ})$

FIGURE C-2. STRAIN POWER SPECTRAL DENSITY (RUN 5, POINT 2)
$(\overline{q} = 25\,psf, \alpha = 0°, \psi = 0°)$
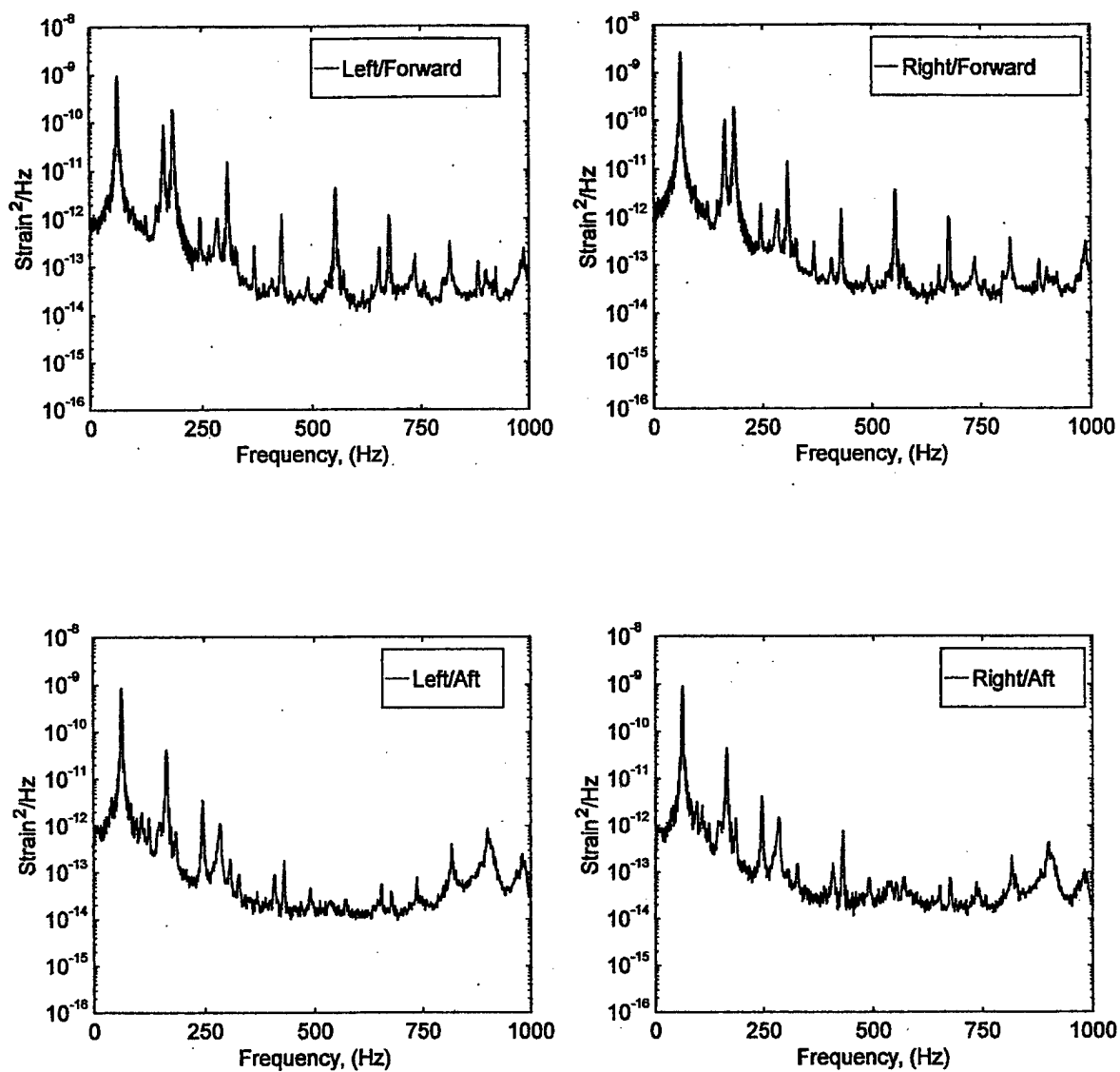
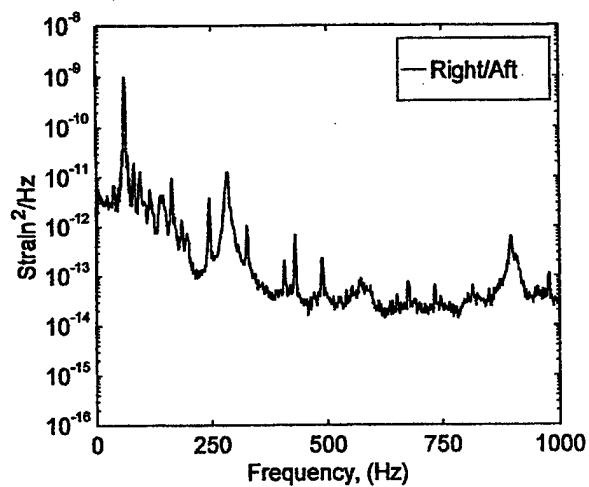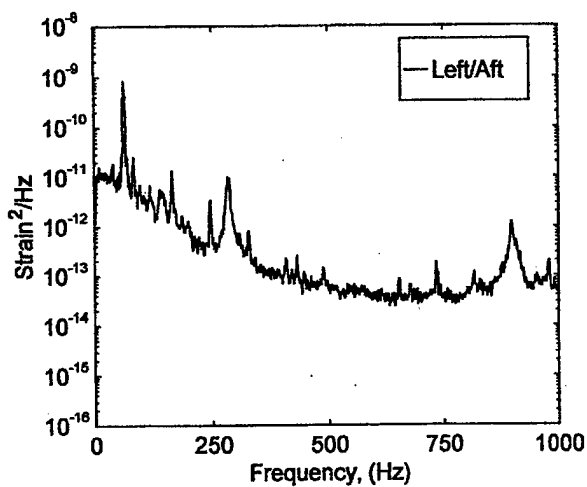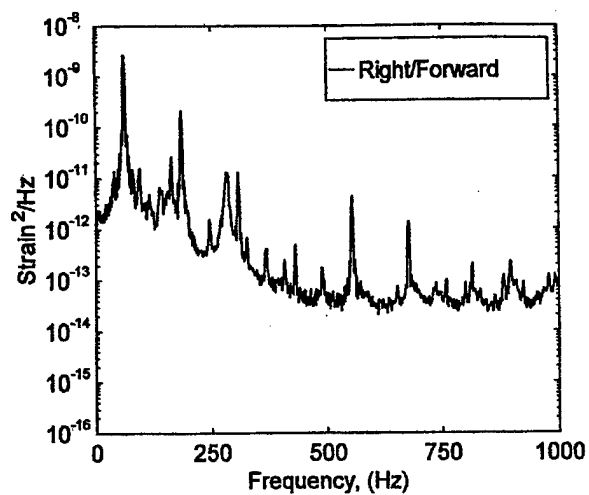FIGURE C-3. STRAIN POWER SPECTRAL DENSITY (RUN 5, POINT 3)
$$(\overline{q} = 25 psf, \alpha = 5^{\circ}, \psi = 0^{\circ})$$

FIGURE C-4. STRAIN POWER SPECTRAL DENSITY (RUN 5, POINT 4)
$(\overline{q} = 25psf, \alpha = 10^{\circ}, \psi = 0^{\circ})$
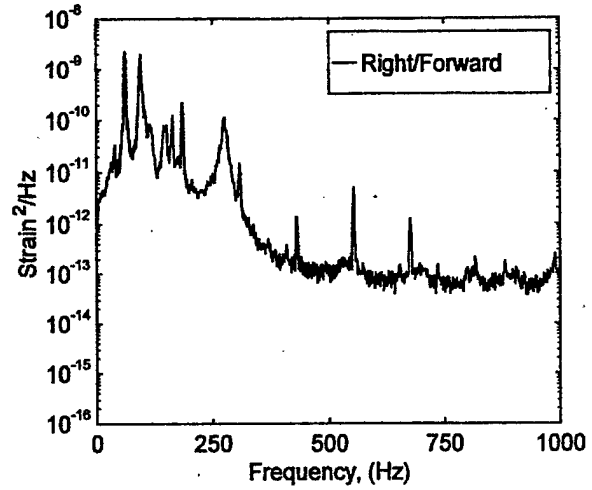
FIGURE C-5. STRAIN POWER SPECTRAL DENSITY (RUN 5, POINT 5)
$$(\overline{q} = 25psf, \alpha = 15°, \psi = 0°)$$
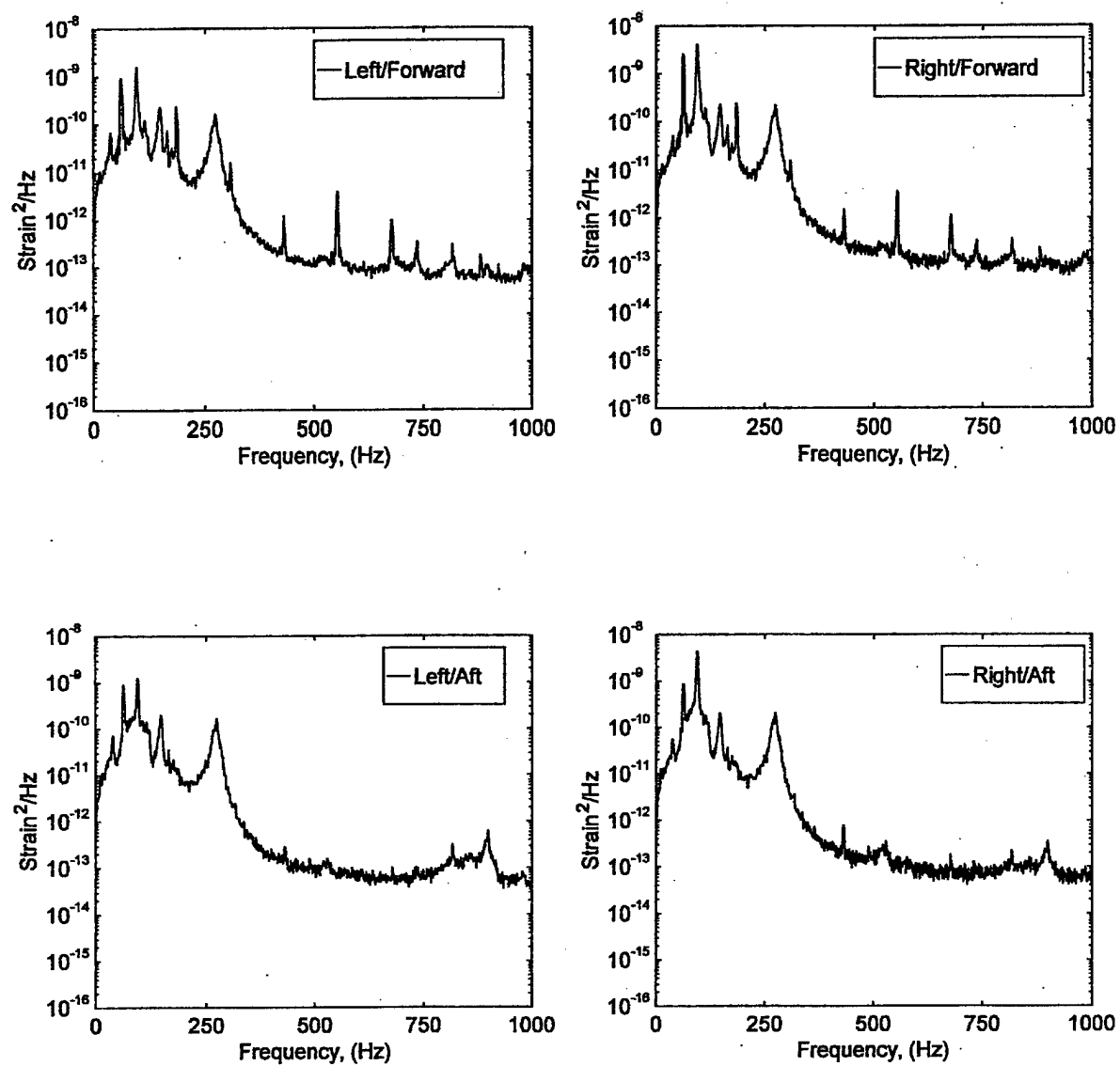
FIGURE C-6. STRAIN POWER SPECTRAL DENSITY (RUN 5, POINT 6)
$(\overline{q} = 25psf, \alpha = 20^{\circ}, \psi = 0^{\circ})$
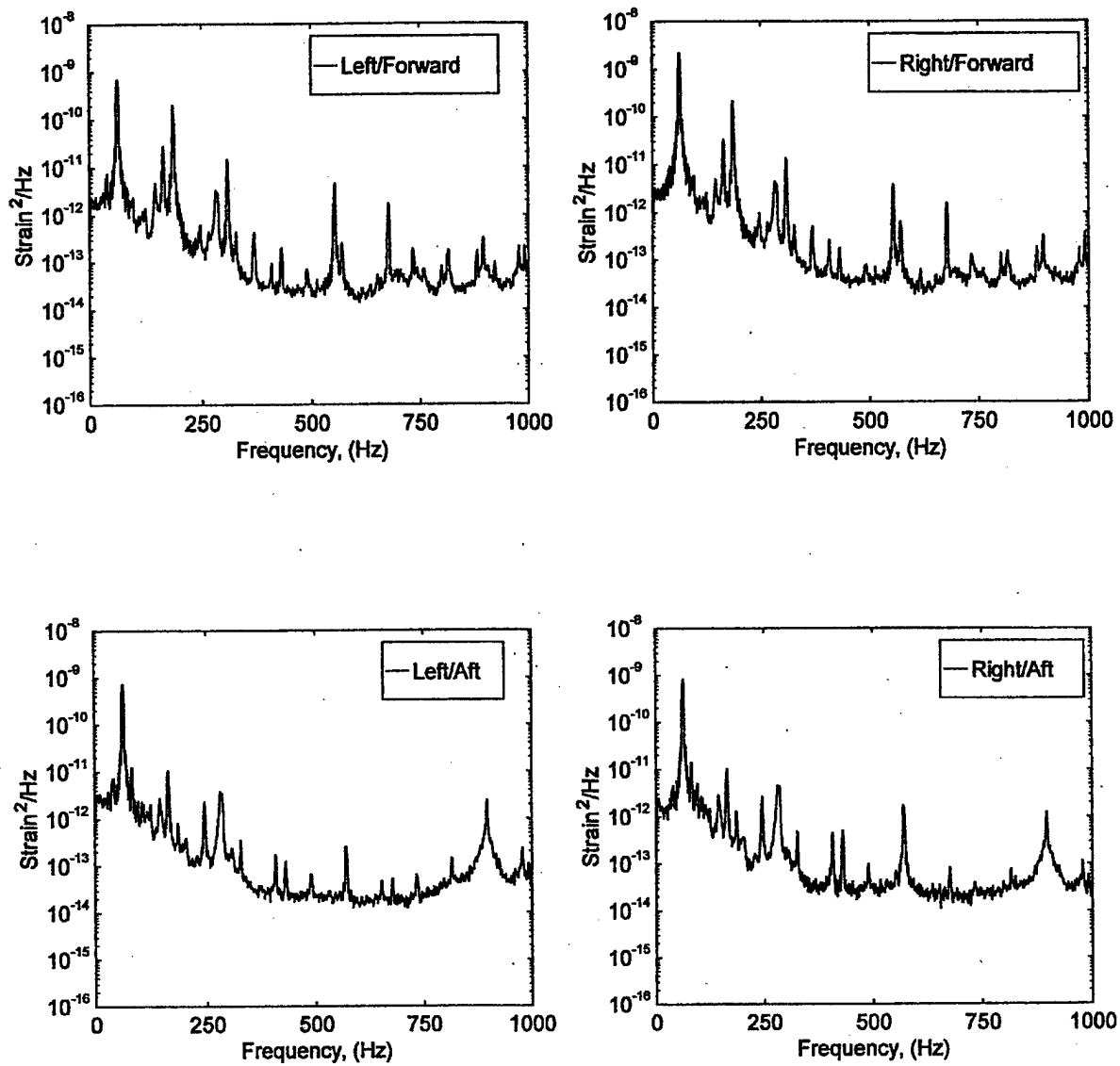
FIGURE C-7. STRAIN POWER SPECTRAL DENSITY (RUN 7, POINT 1)
$$(\overline{q} = 35\,psf, \alpha = -5^{\circ}, \psi = 0^{\circ})$$
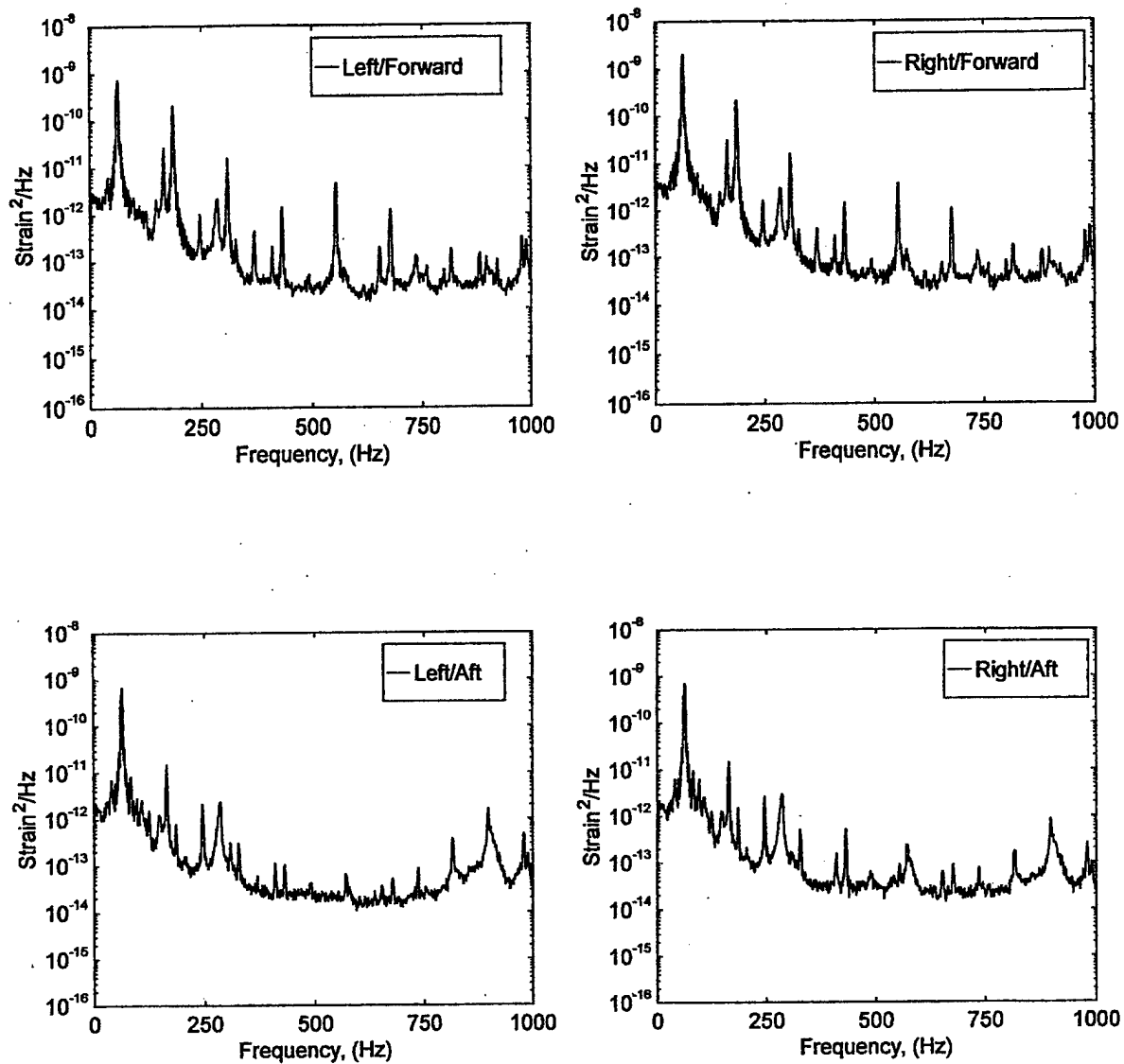
FIGURE C-8. STRAIN POWER SPECTRAL DENSITY (RUN 6, POINT 2)
$(\overline{q} = 35\,psf, \alpha = 0^{\circ}, \psi = 0^{\circ})$
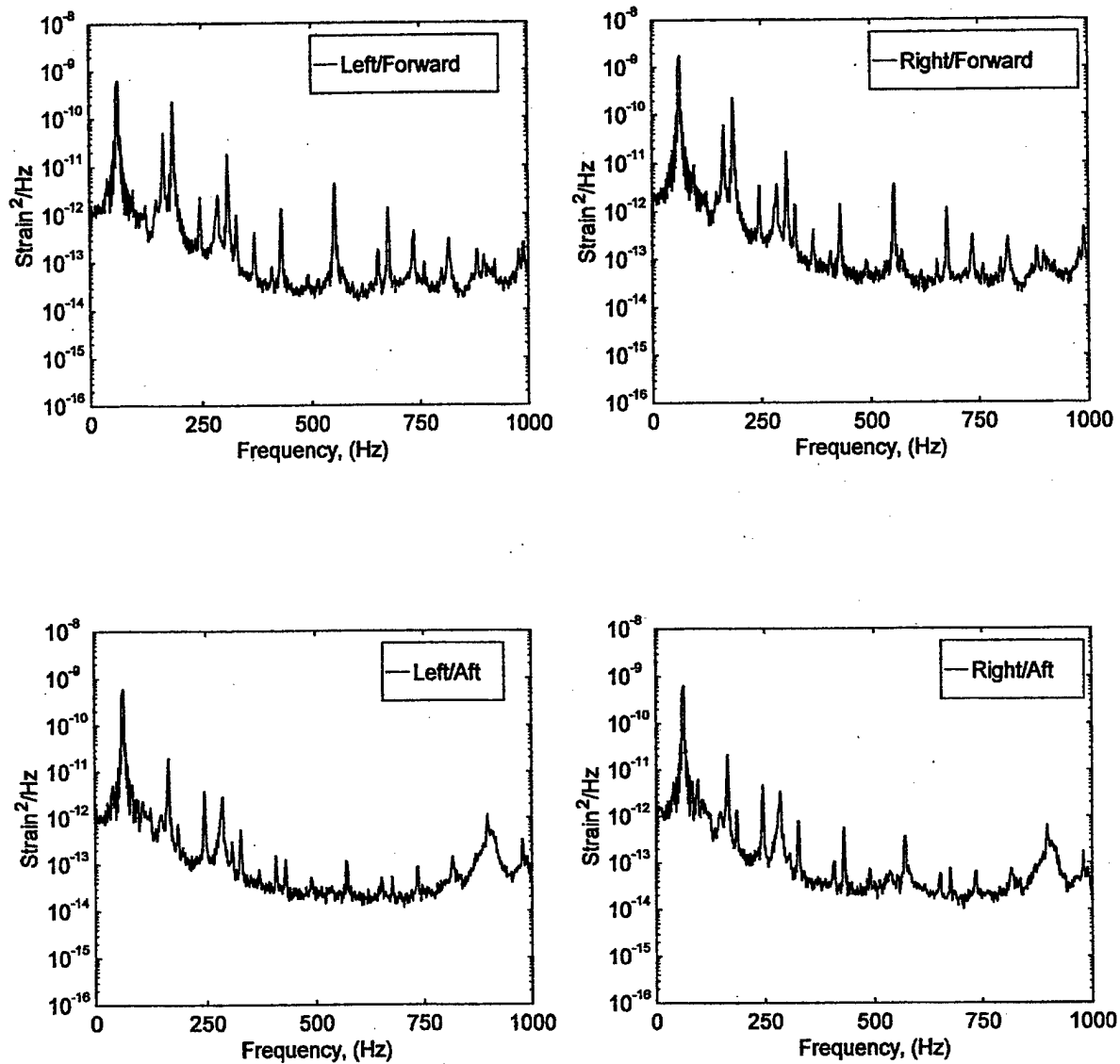
FIGURE C-9. STRAIN POWER SPECTRAL DENSITY (RUN 6, POINT 3)
$$(\bar{q} = 35\,psf, \alpha = 5^{\circ}, \psi = 0^{\circ})$$
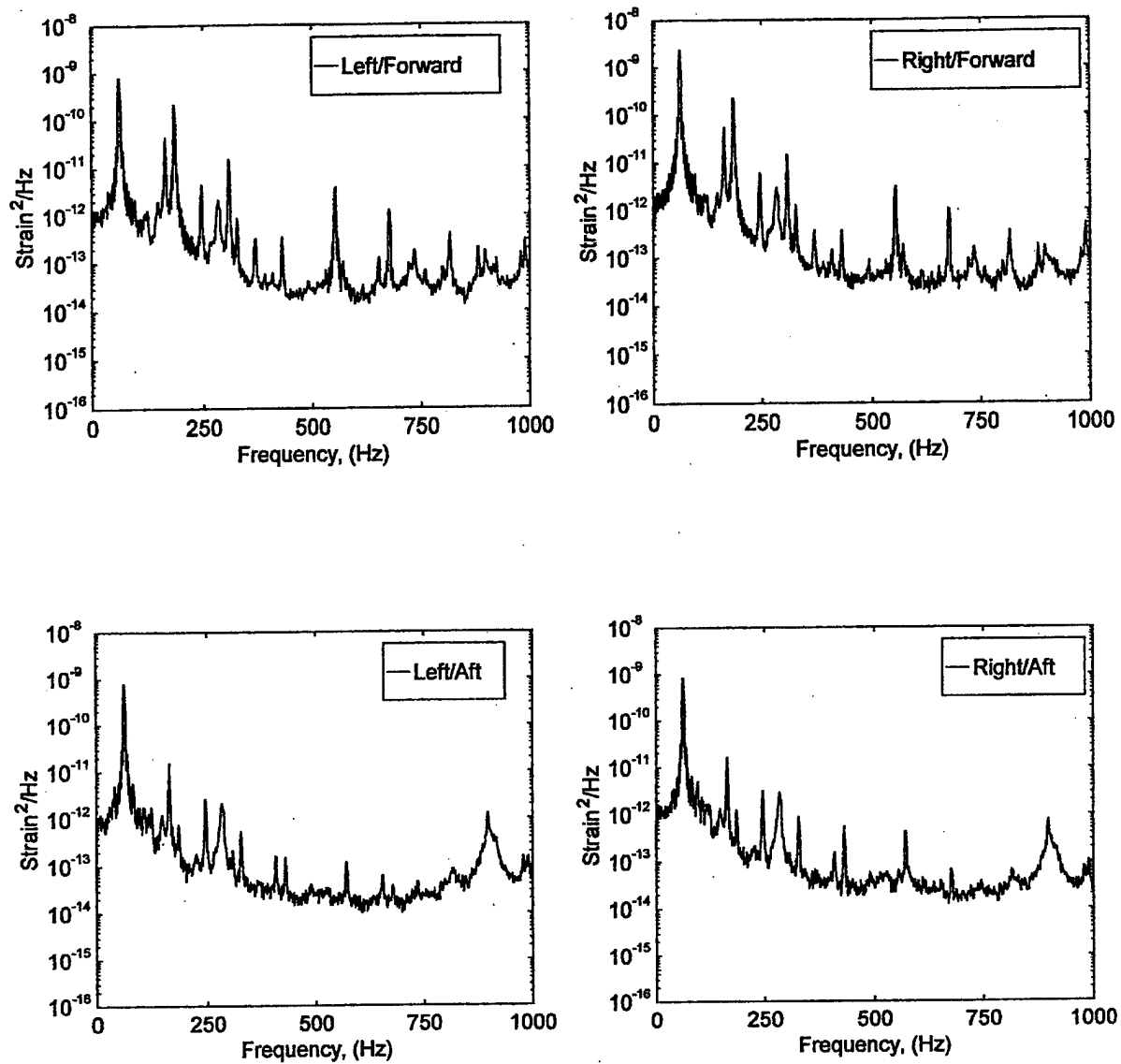
FIGURE C-10. STRAIN POWER SPECTRAL DENSITY (RUN 6, POINT 4)
$(\overline{q} = 35\,psf, \alpha = 10^\circ, \psi = 0^\circ)$
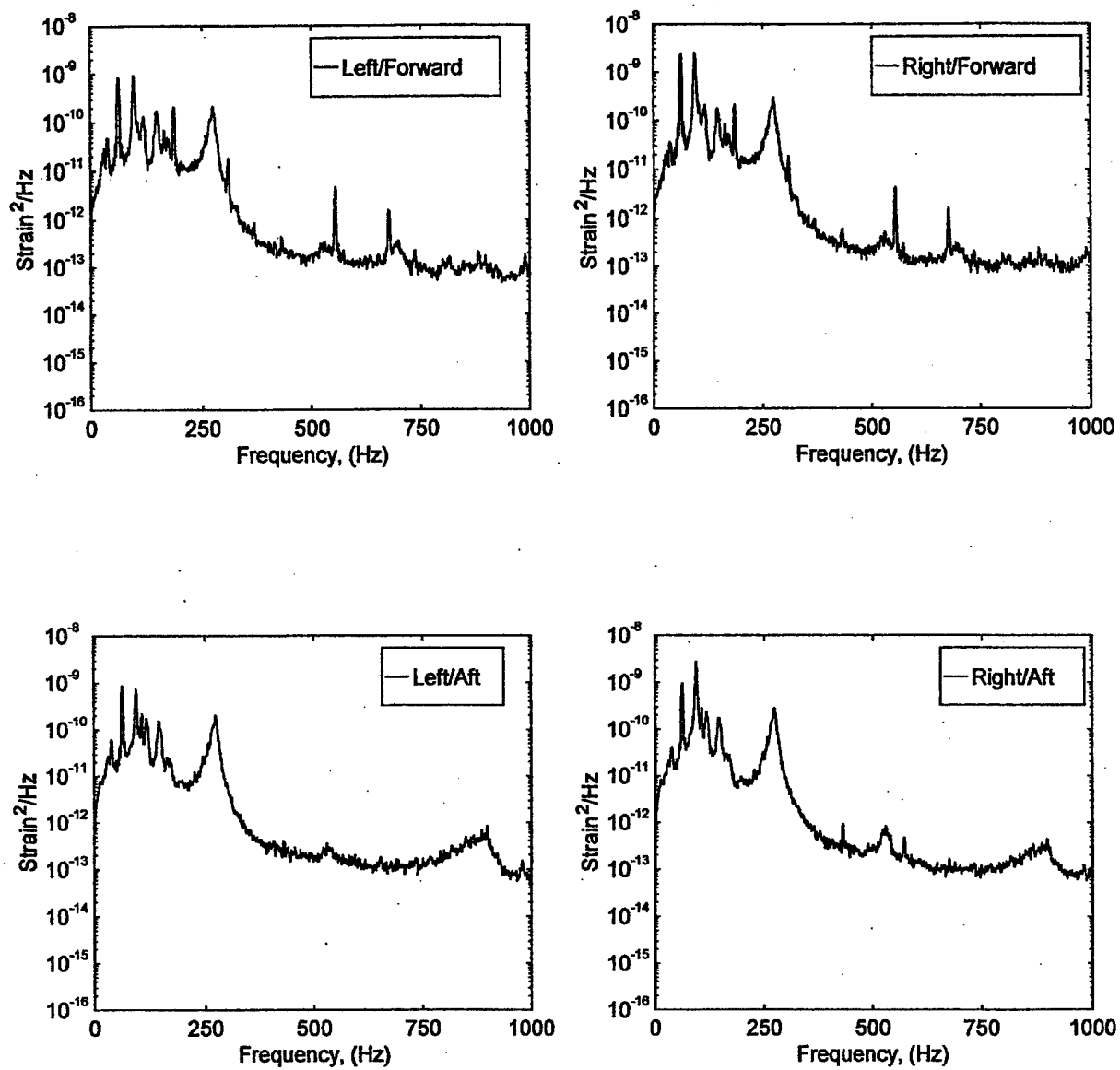
FIGURE C-11. STRAIN POWER SPECTRAL DENSITY (RUN 6, POINT 5)
$(\overline{q} = 35\,psf, \alpha = 15°, \psi = 0°)$
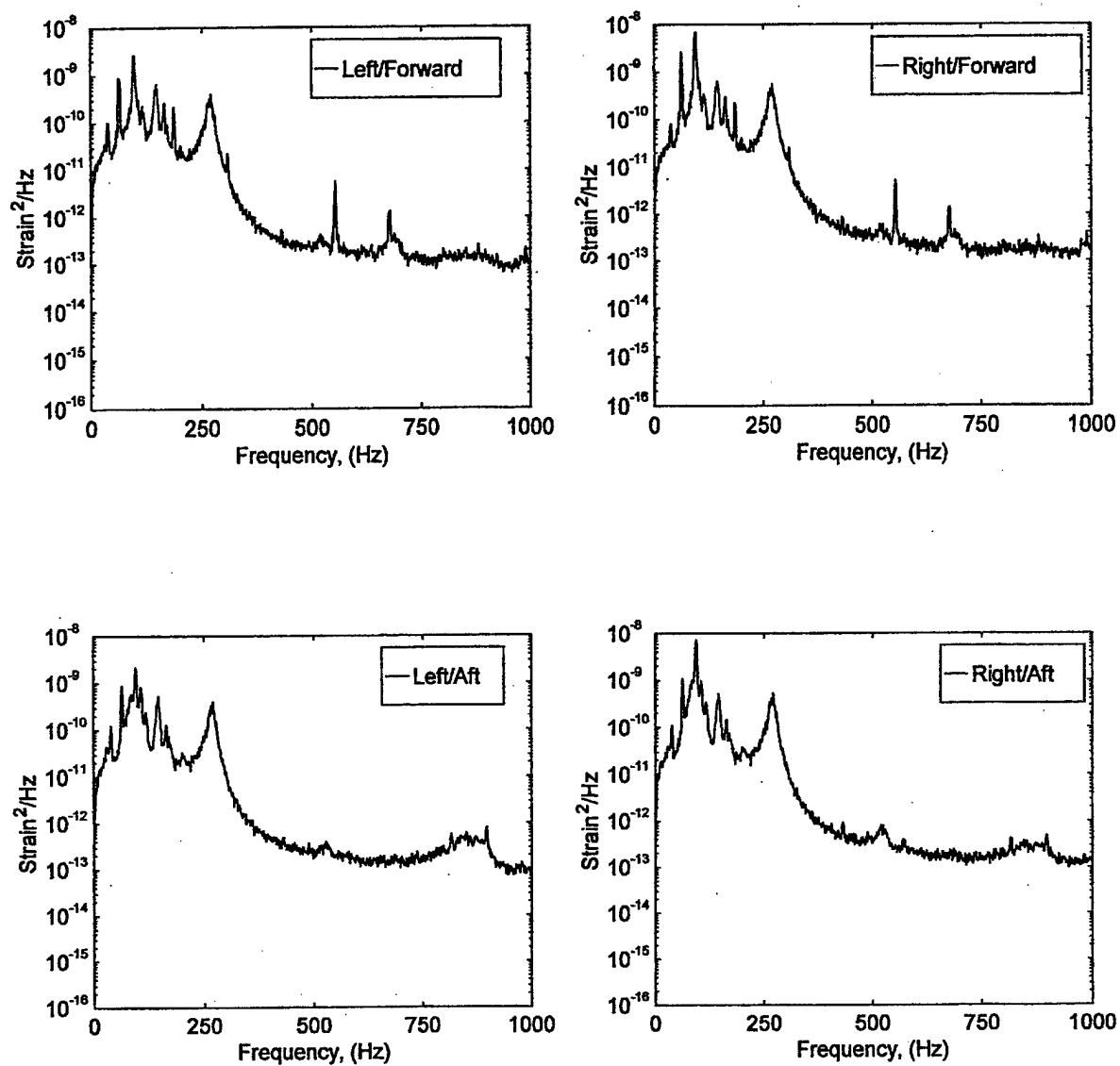
FIGURE C-12. STRAIN POWER SPECTRAL DENSITY (RUN 6, POINT 6)

$$(\overline{q} = 35\,psf, \alpha = 20^{\circ}, \psi = 0^{\circ})$$
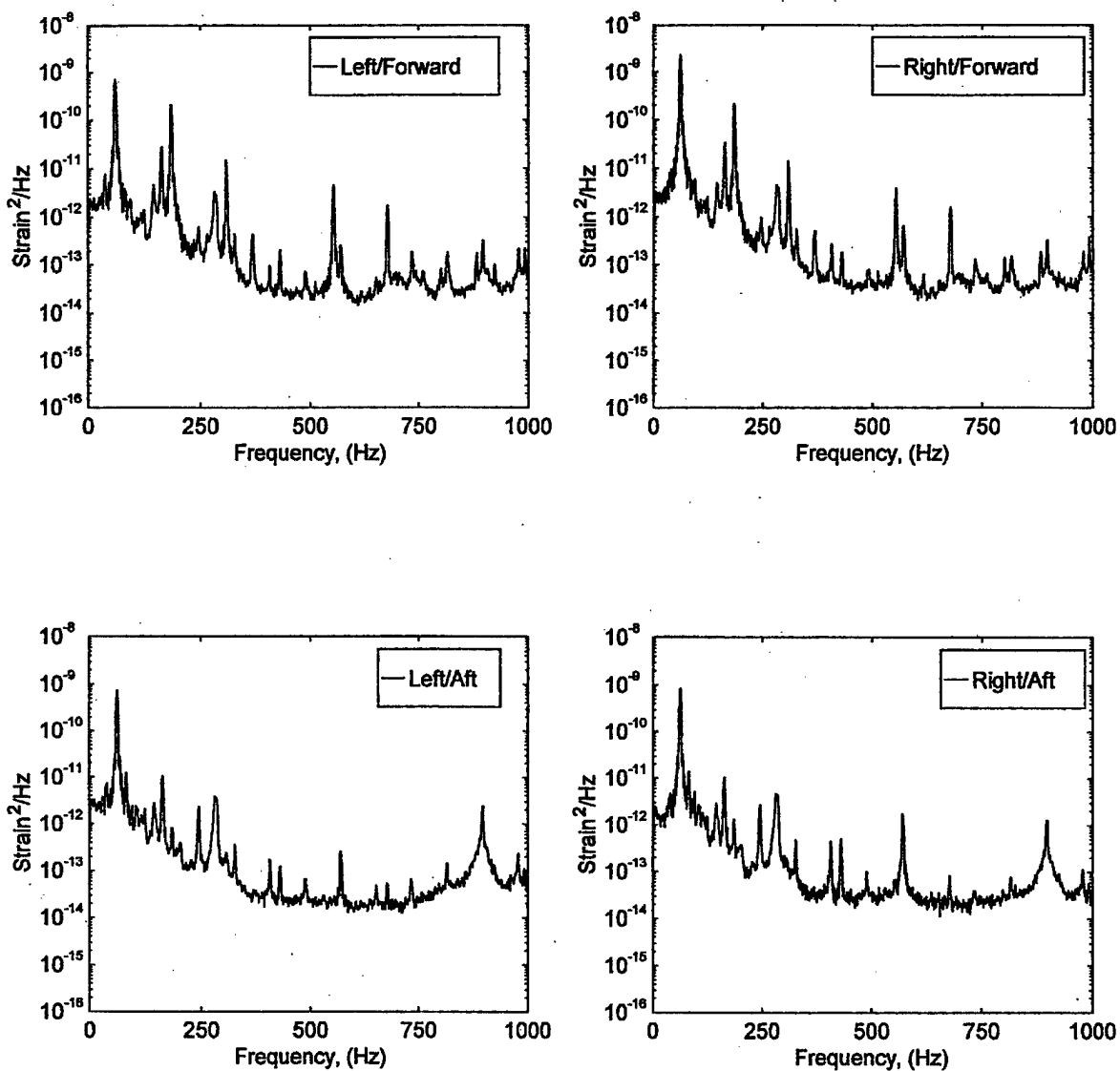
FIGURE C-13. STRAIN POWER SPECTRAL DENSITY (RUN 7, POINT 1)
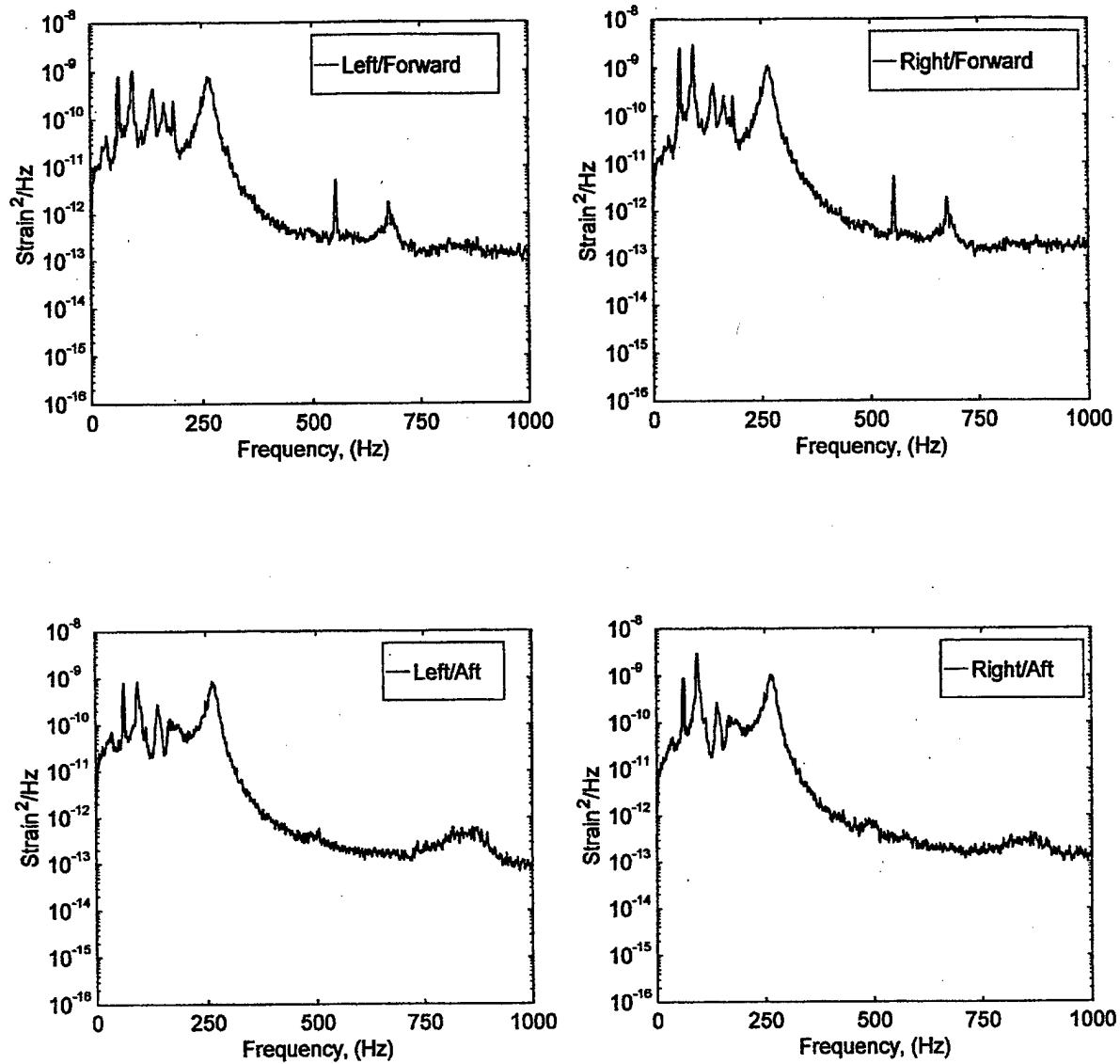$(\overline{q} = 45psf, \alpha = -5^{\circ}, \psi = 0^{\circ})$

C-13
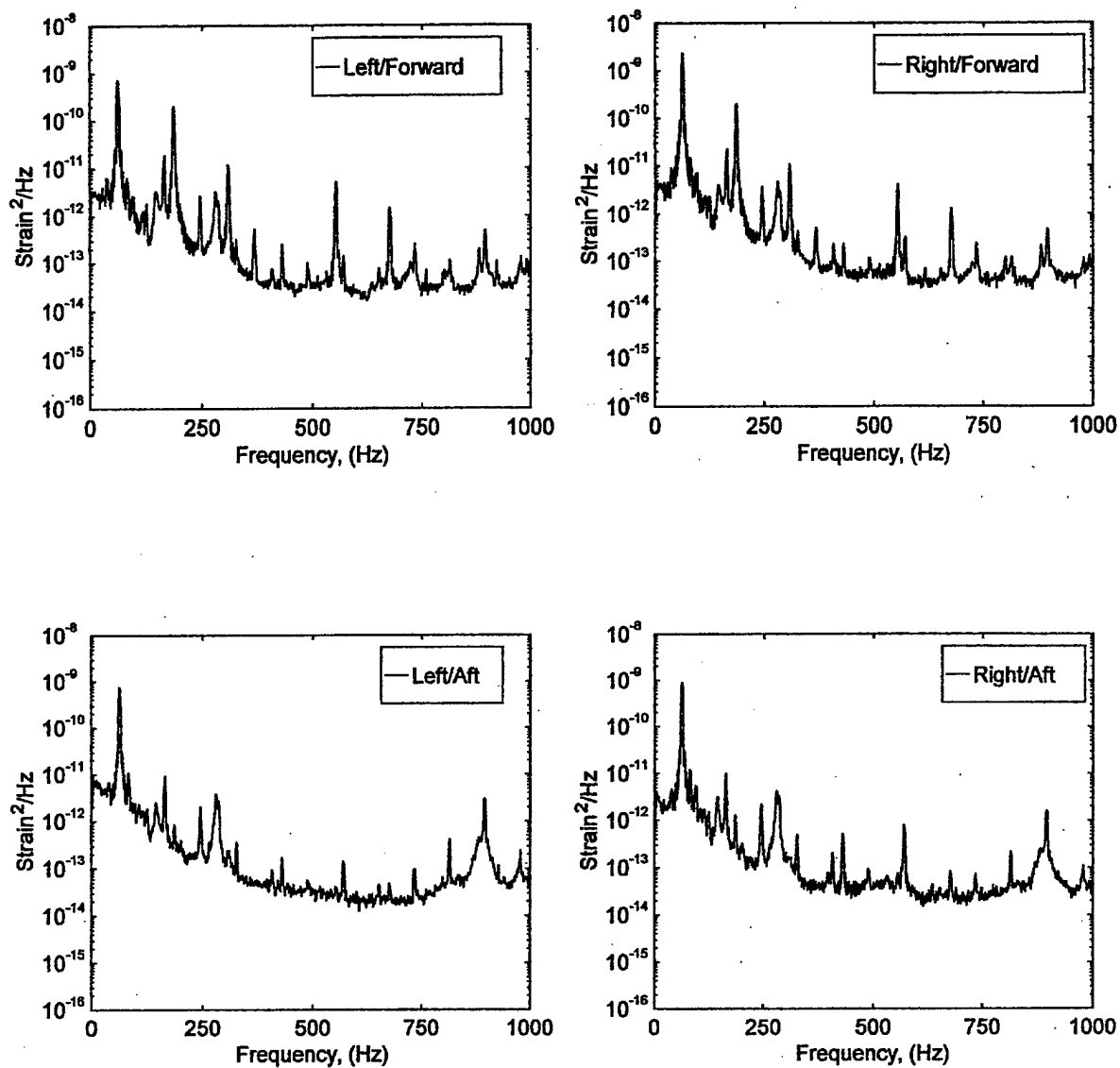
FIGURE C-14. STRAIN POWER SPECTRAL DENSITY (RUN 7, POINT 2)
$(\overline{q} = 45psf, \alpha = 0^{\circ}, \psi = 0^{\circ})$

FIGURE C-15. STRAIN POWER SPECTRAL DENSITY (RUN 7, POINT 3)
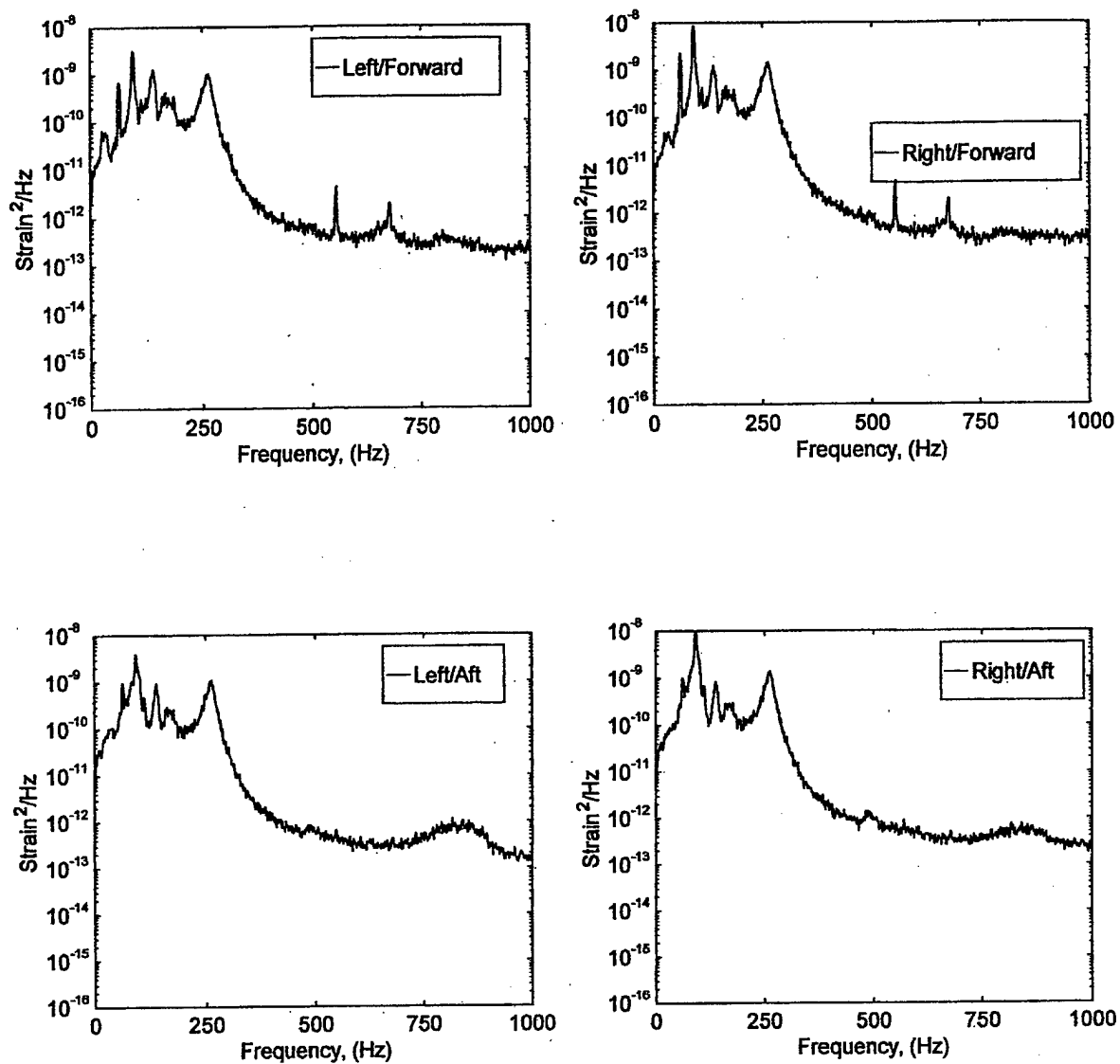$$(\overline{q} = 45psf, \alpha = 5^{\circ}, \psi = 0^{\circ})$$
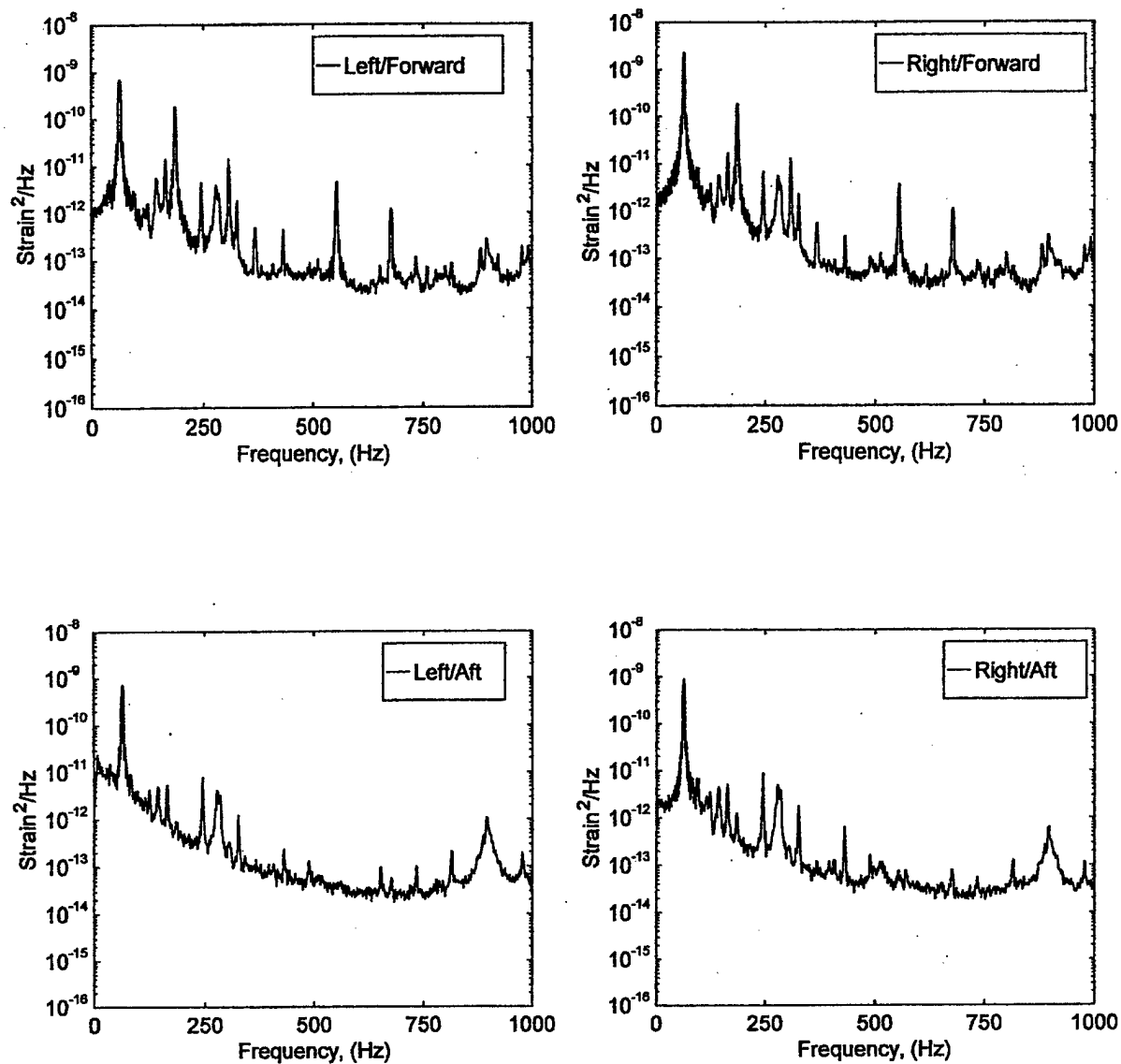
FIGURE C-16. STRAIN POWER SPECTRAL DENSITY (RUN 7, POINT 4)
$(\overline{q} = 45 psf, \alpha = 10^{\circ}, \psi = 0^{\circ})$

FIGURE C-17. STRAIN POWER SPECTRAL DENSITY (RUN 7, POINT 5)
$(\bar{q} = 45 psf, \alpha = 15^{\circ}, \psi = 0^{\circ})$

C-17
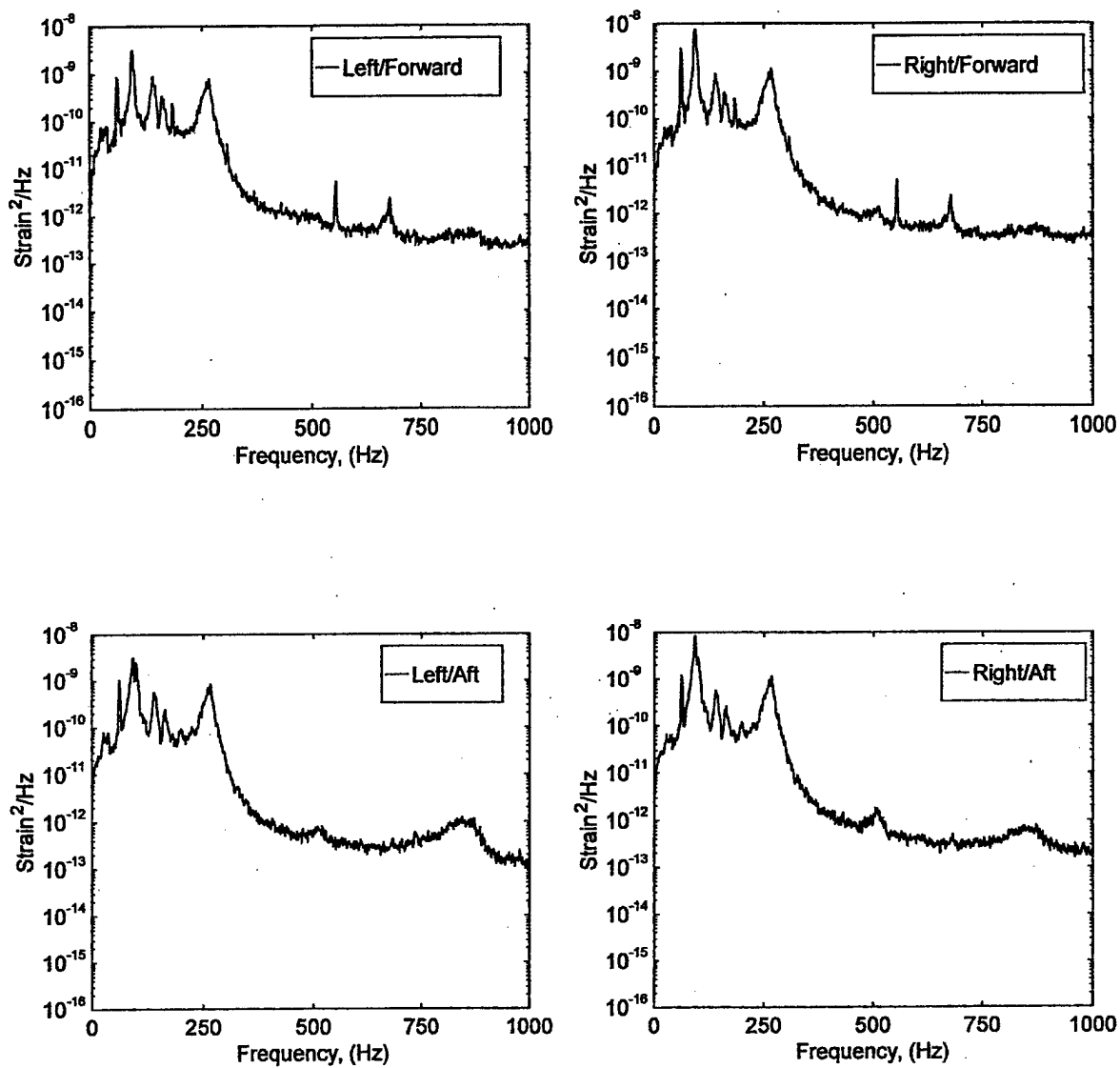
FIGURE C-18. STRAIN POWER SPECTRAL DENSITY (RUN 7, POINT 6)
$$(\bar{q} = 45psf, \alpha = 20^\circ, \psi = 0^\circ)$$
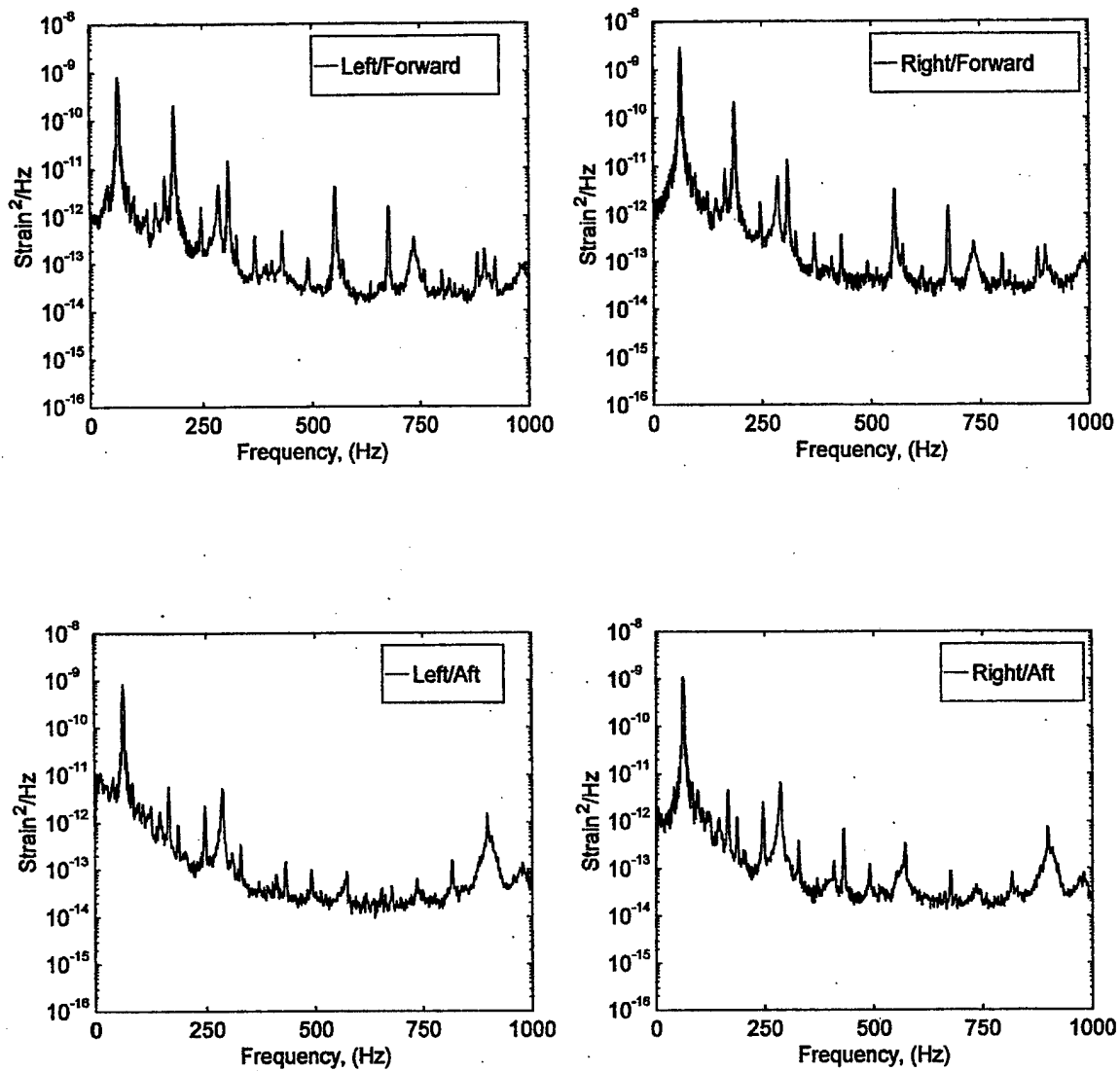
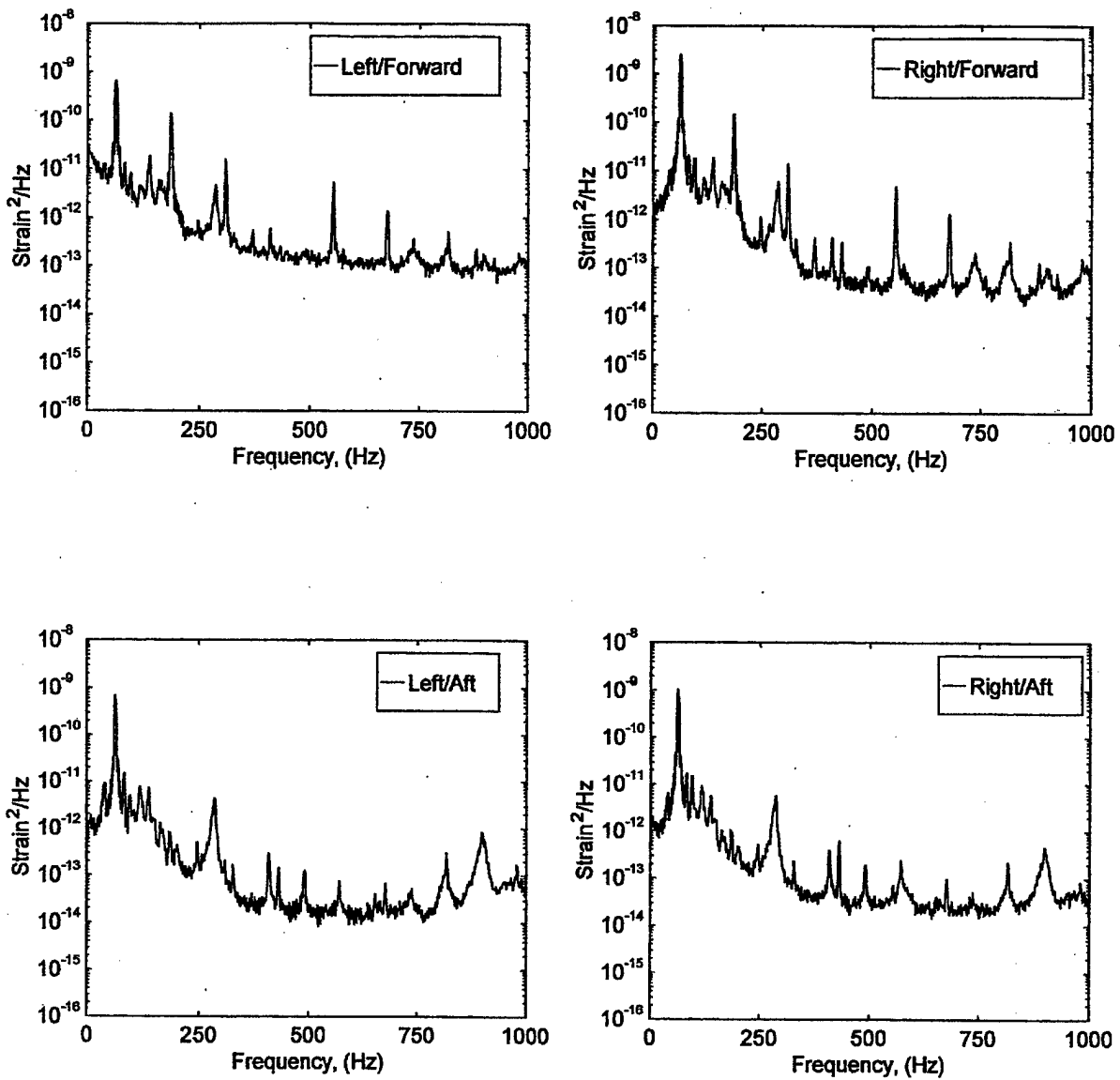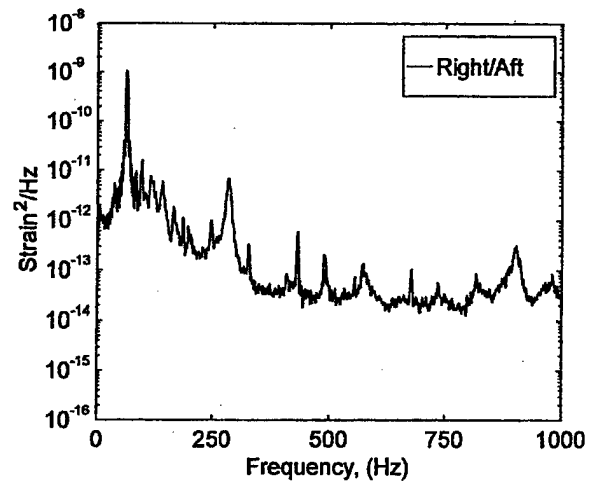FIGURE C-19. STRAIN POWER SPECTRAL DENSITY (RUN 8, POINT 1)
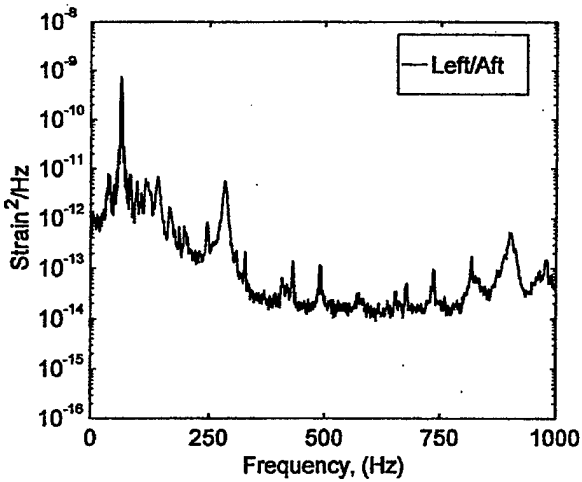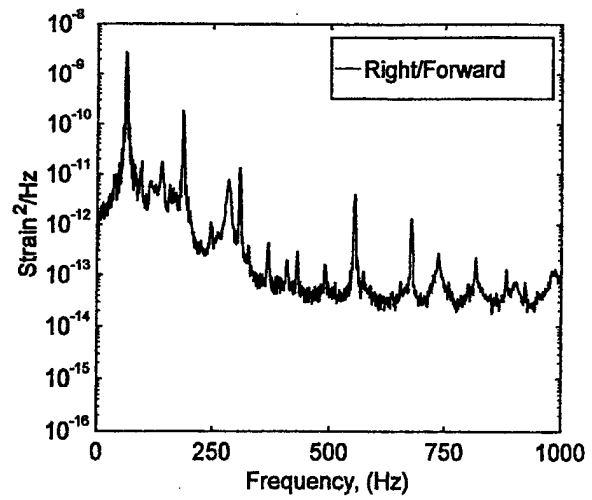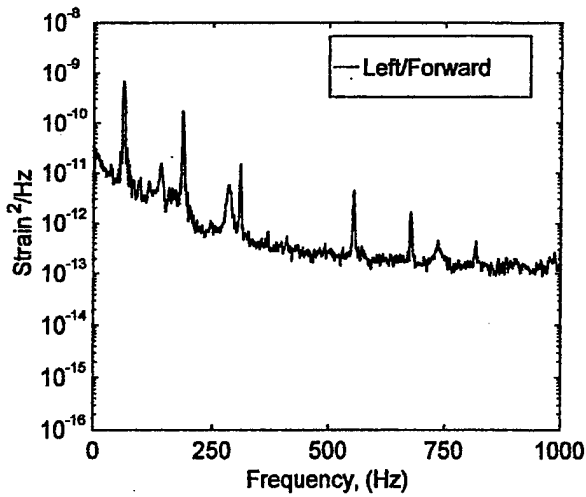$$(\overline{q} = 25 psf, \alpha = -5^{\circ}, \psi = -10^{\circ})$$
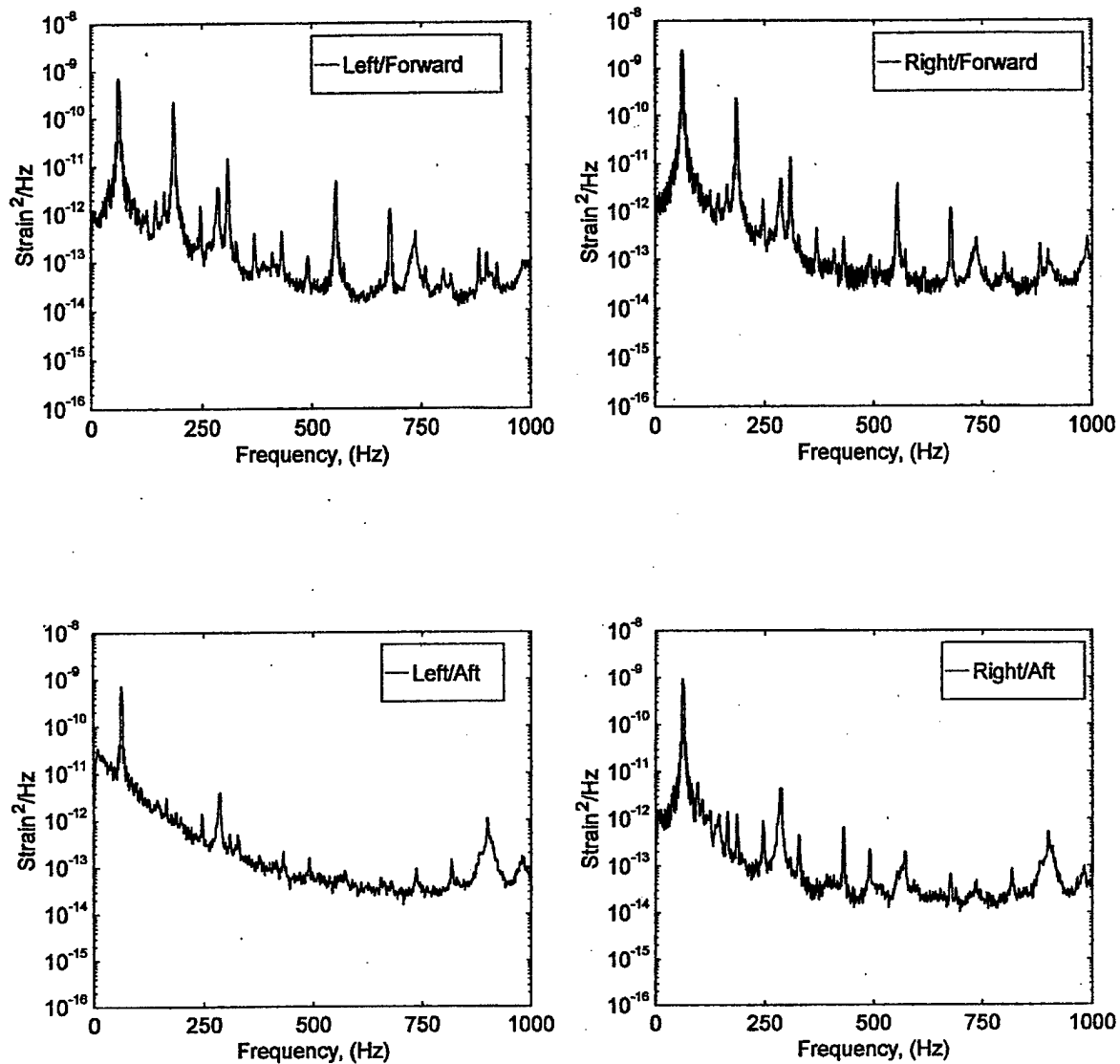
FIGURE C-20. STRAIN POWER SPECTRAL DENSITY (RUN 8, POINT 2)
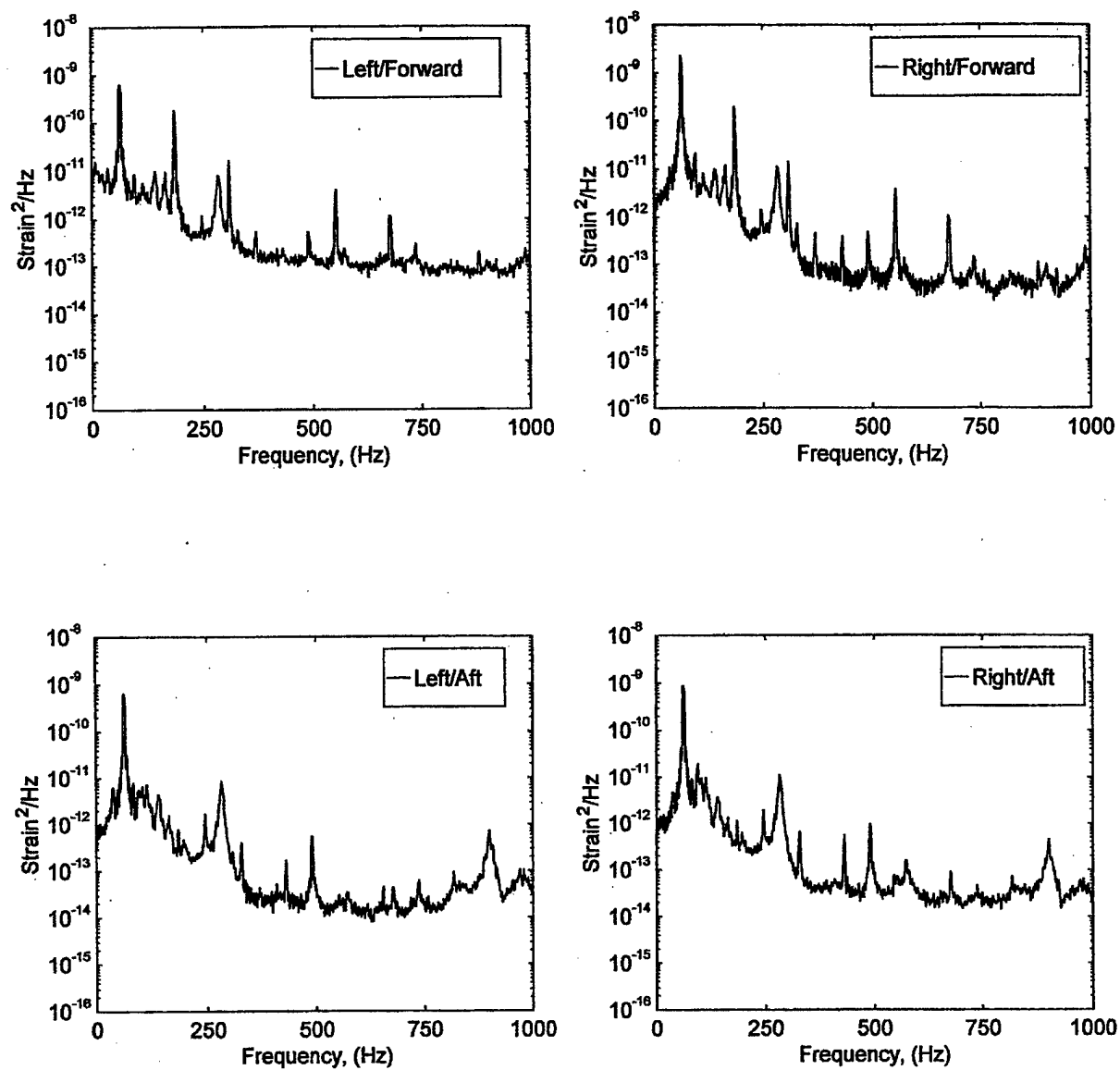$(\overline{q} = 25\,psf, \alpha = 0^{\circ}, \psi = -10^{\circ})$
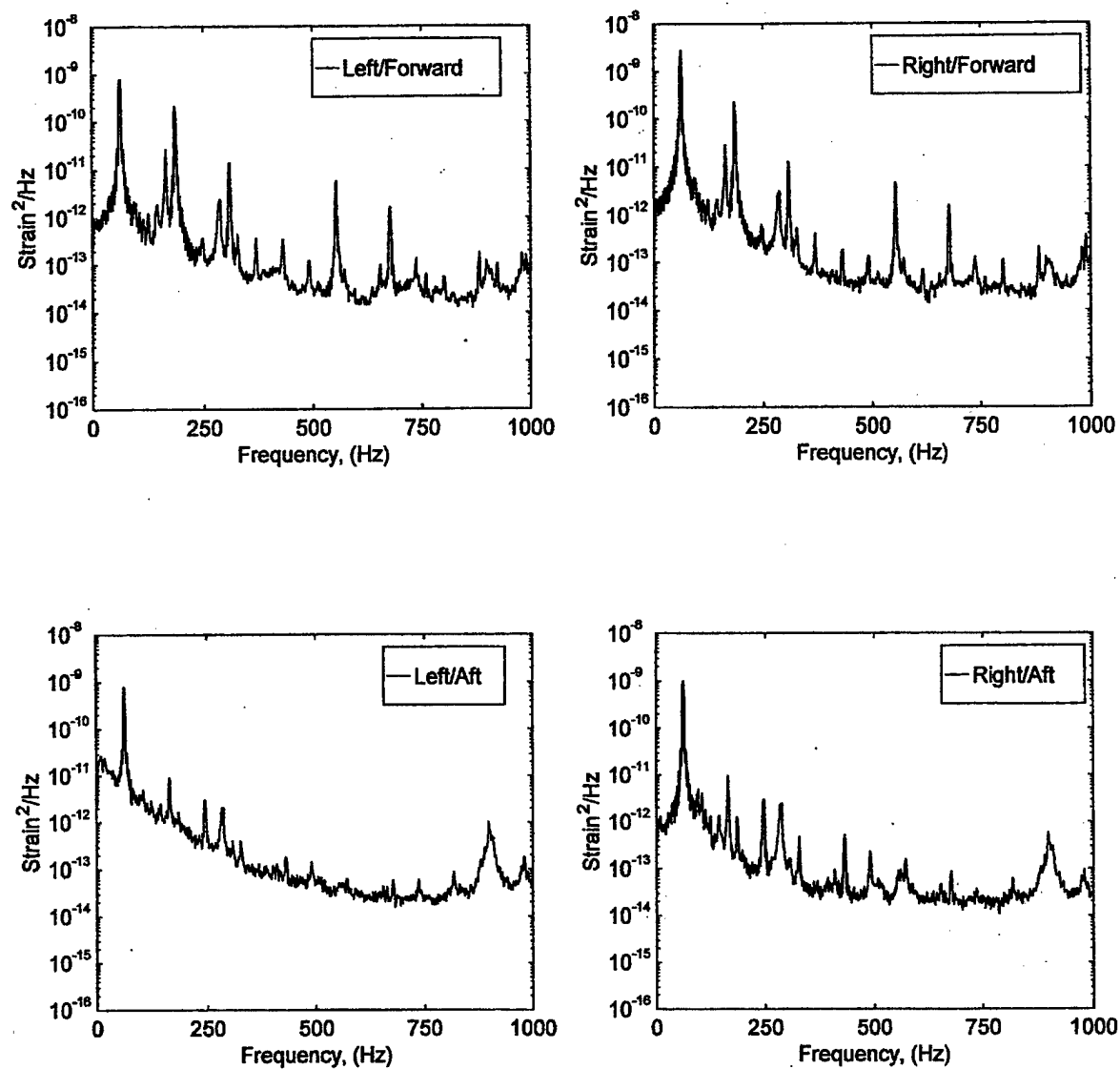
FIGURE C-21. STRAIN POWER SPECTRAL DENSITY (RUN 8, POINT 3)
$(\overline{q} = 25\,psf, \alpha = 5^{\circ}, \psi = -10^{\circ})$
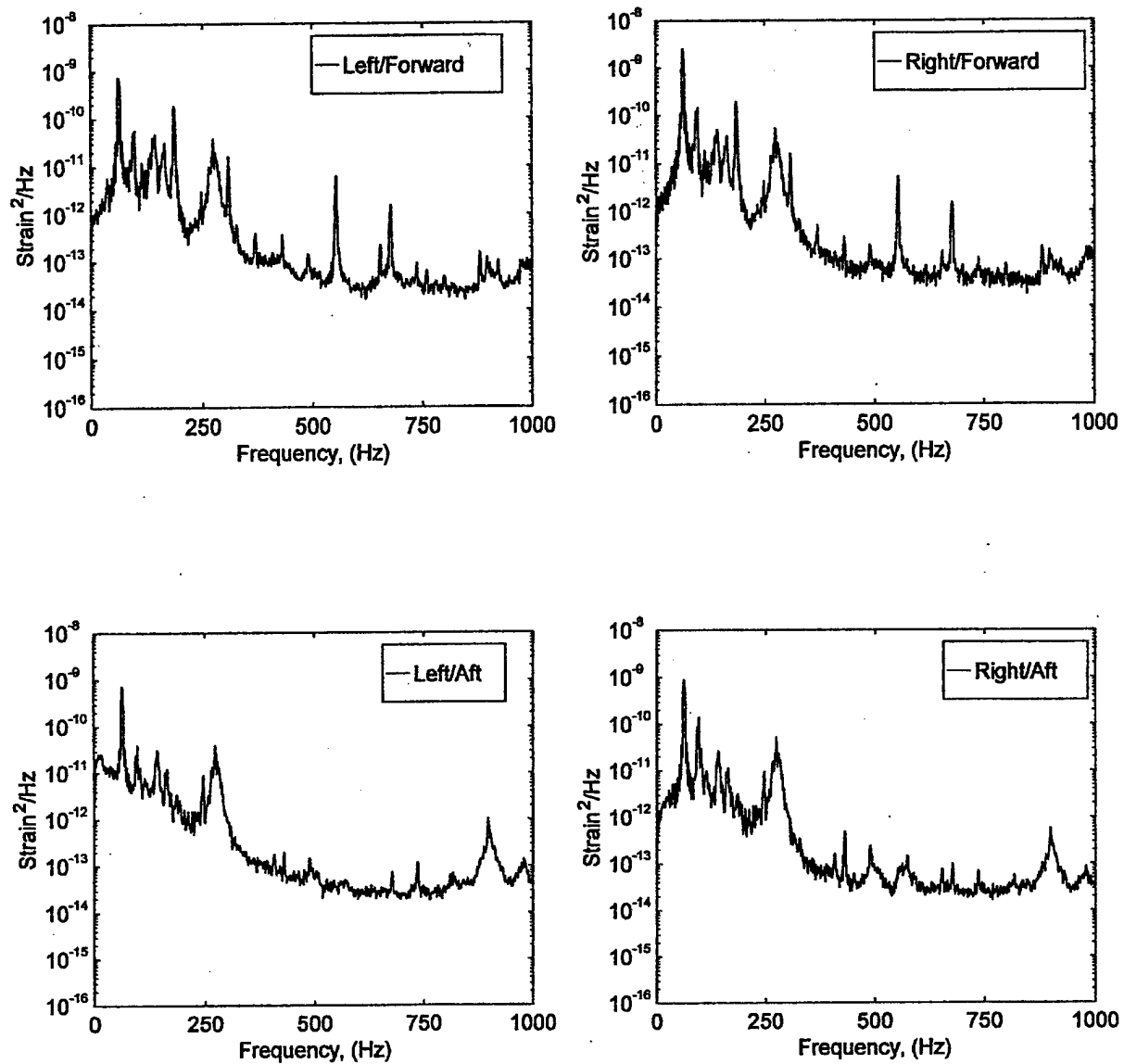
FIGURE C-22. STRAIN POWER SPECTRAL DENSITY (RUN 8, POINT 4)
$(\overline{q} = 25\,psf, \alpha = 10°, \psi = -10°)$
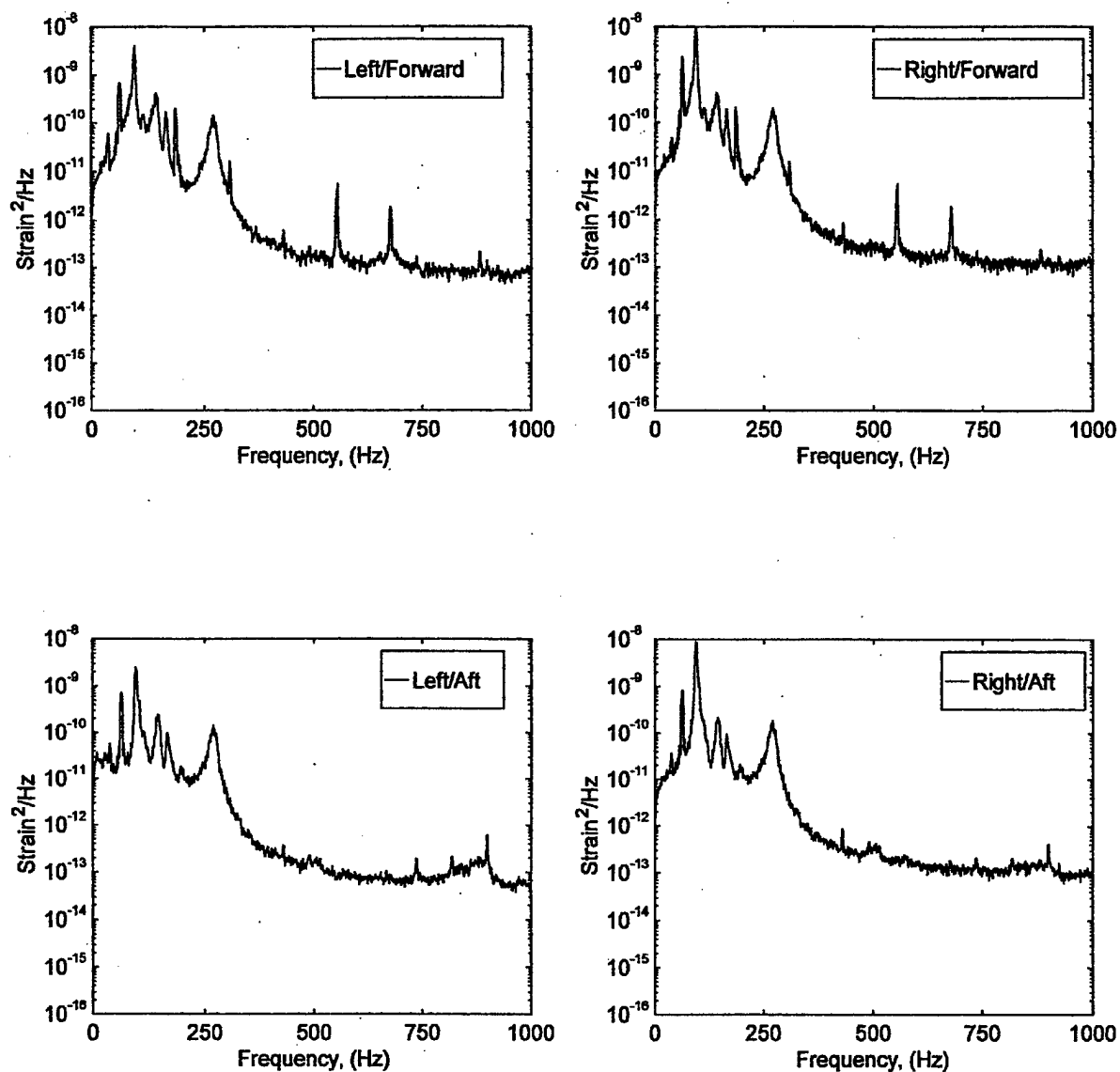
FIGURE C-23. STRAIN POWER SPECTRAL DENSITY (RUN 8, POINT 5)
$(\bar{q}=25psf, \alpha=15^{\circ}, \psi=-10^{\circ})$
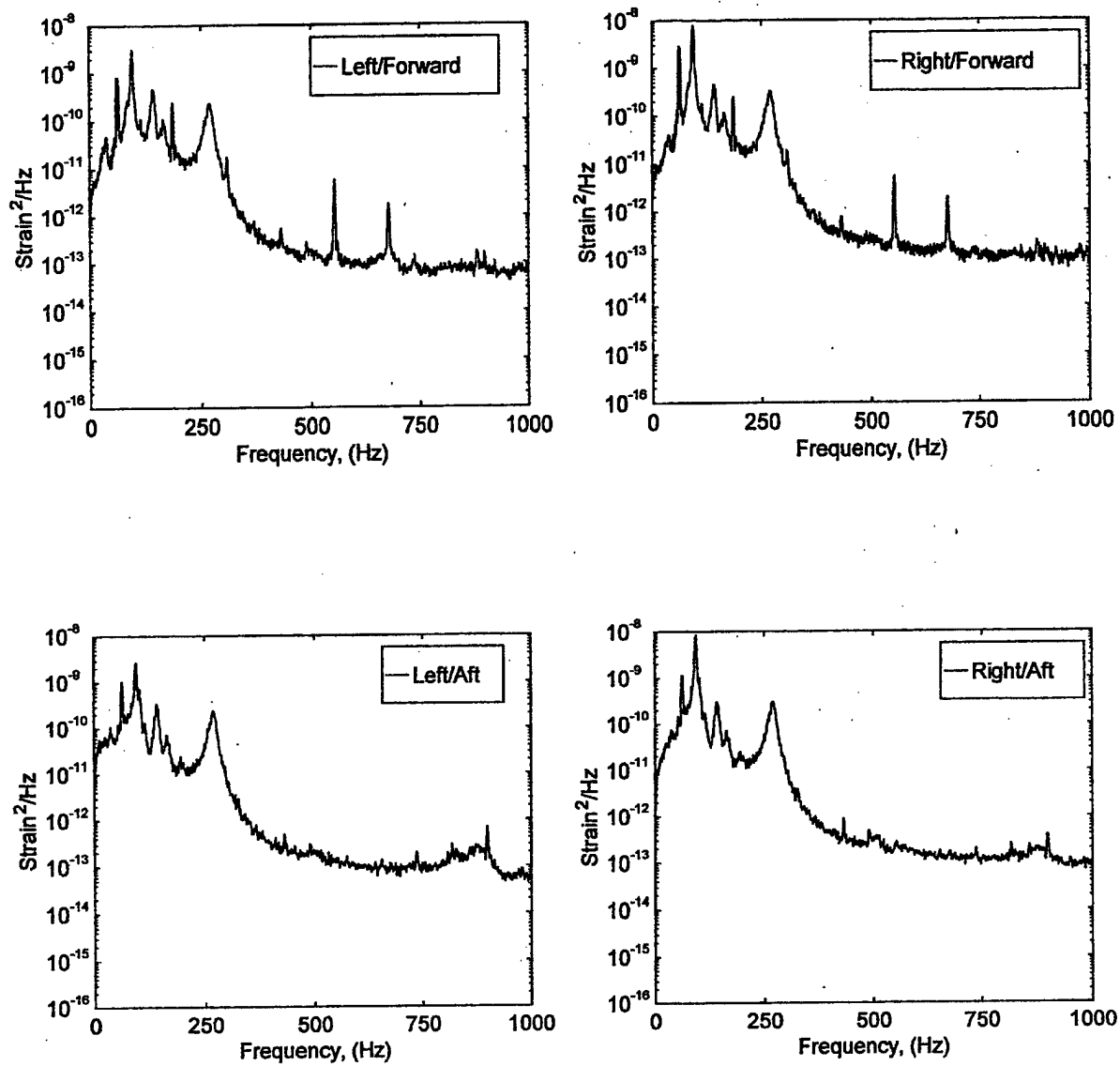
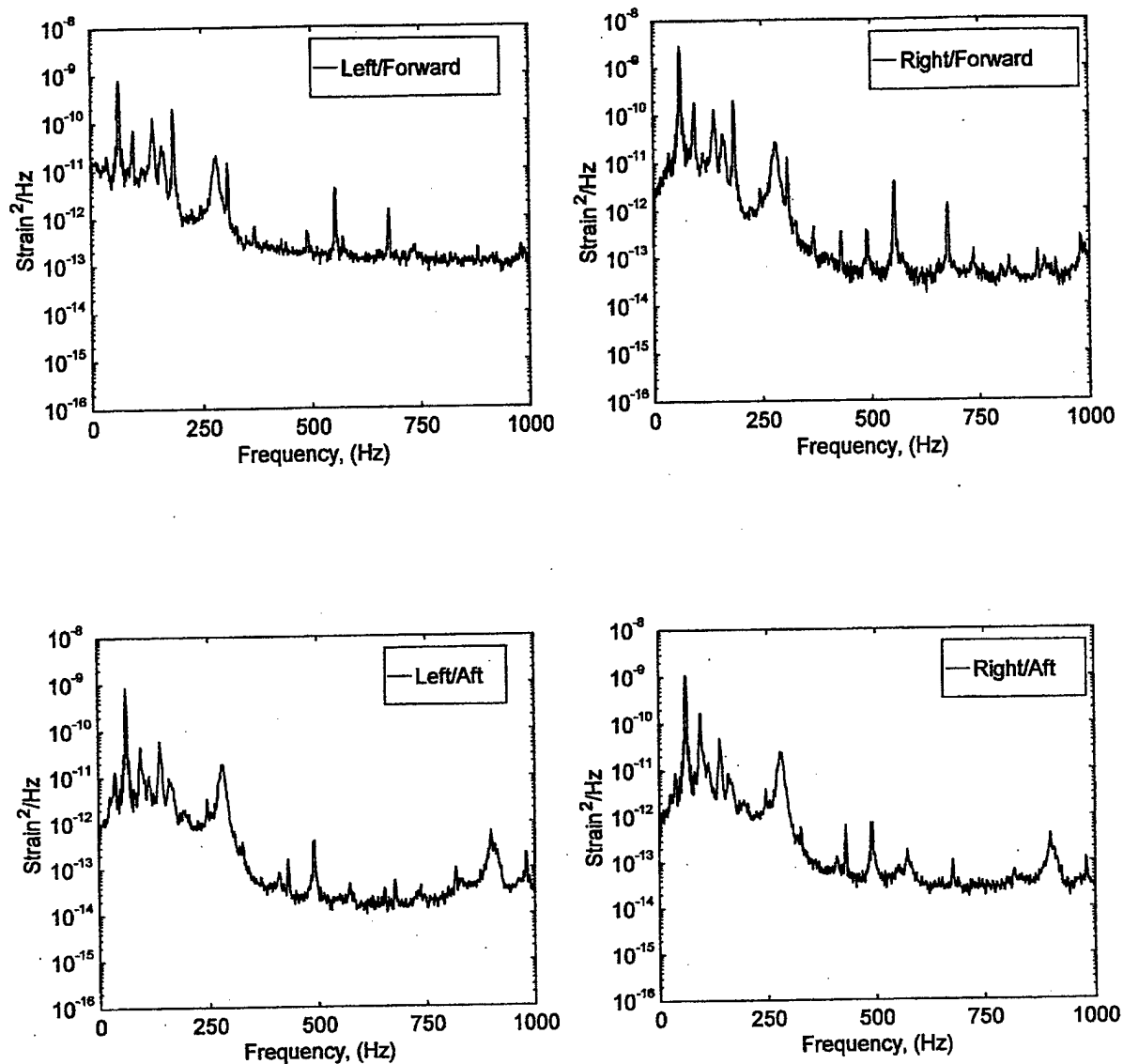FIGURE C-24. STRAIN POWER SPECTRAL DENSITY (RUN 8, POINT 6)
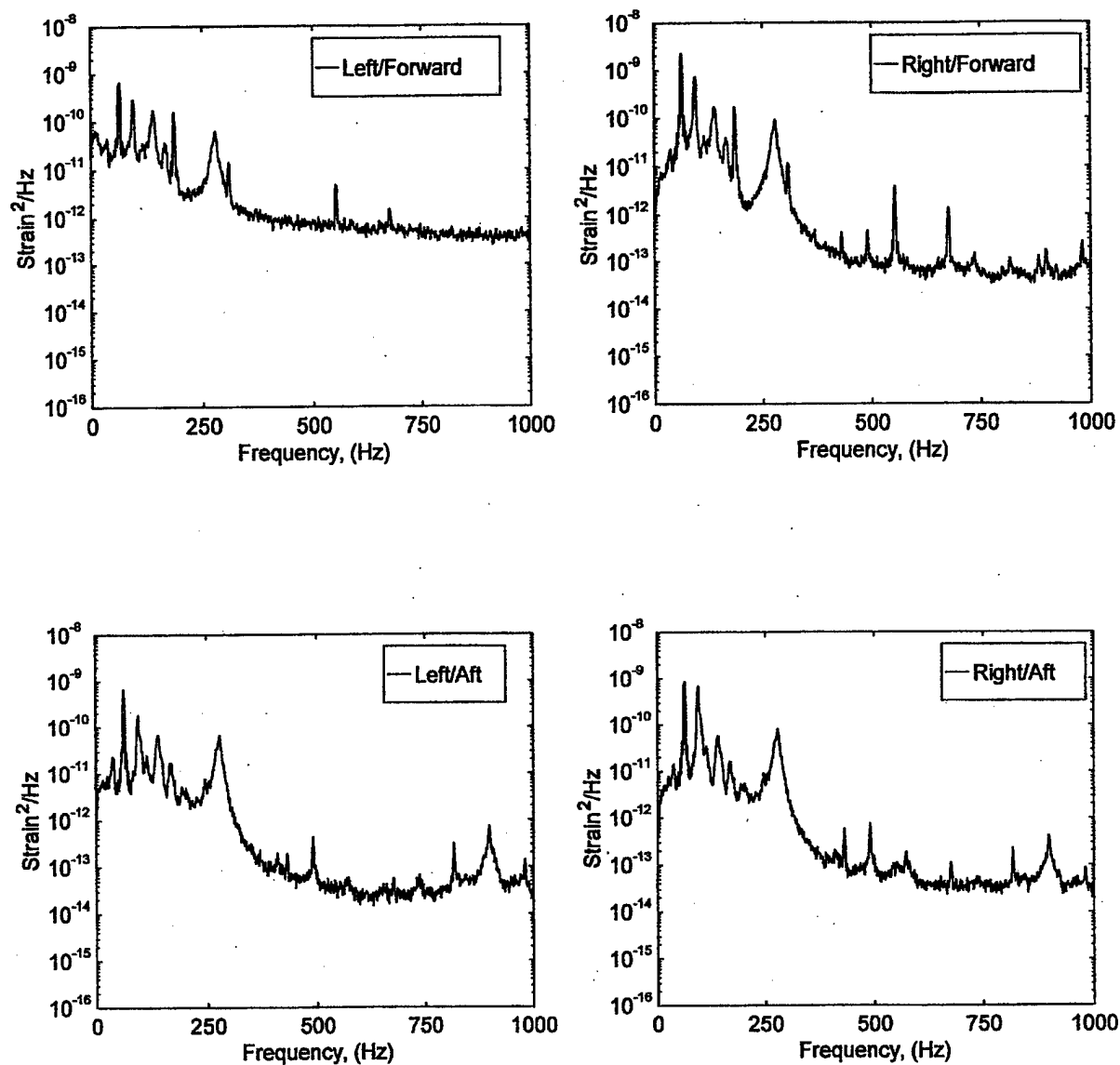$(\overline{q} = 25psf, \alpha = 20^{\circ}, \psi = -10^{\circ})$
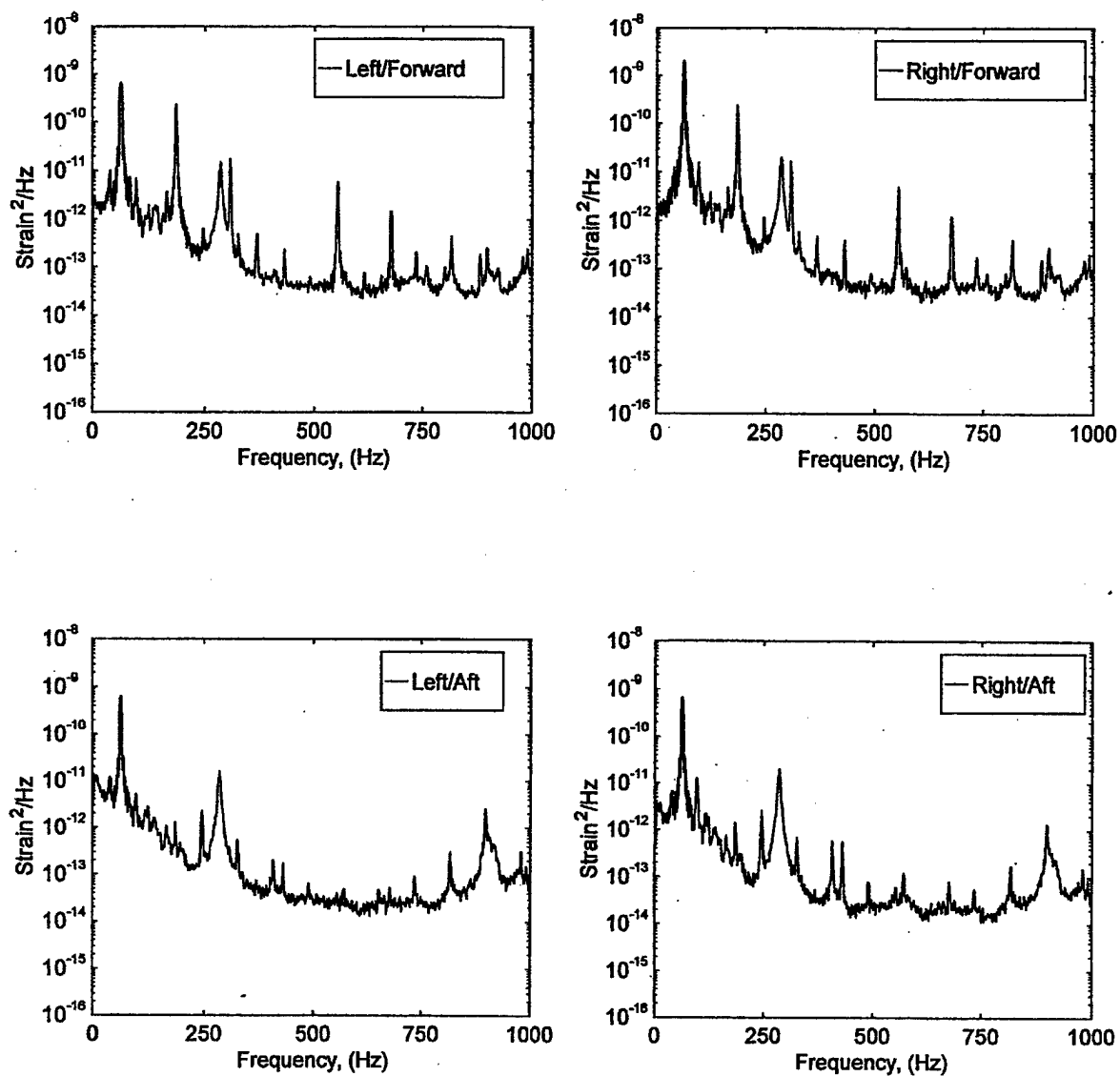
FIGURE C-25. STRAIN POWER SPECTRAL DENSITY (RUN 9, POINT 1)
$(\overline{q} = 35\,psf, \alpha = -5^{\circ}, \psi = -10^{\circ})$
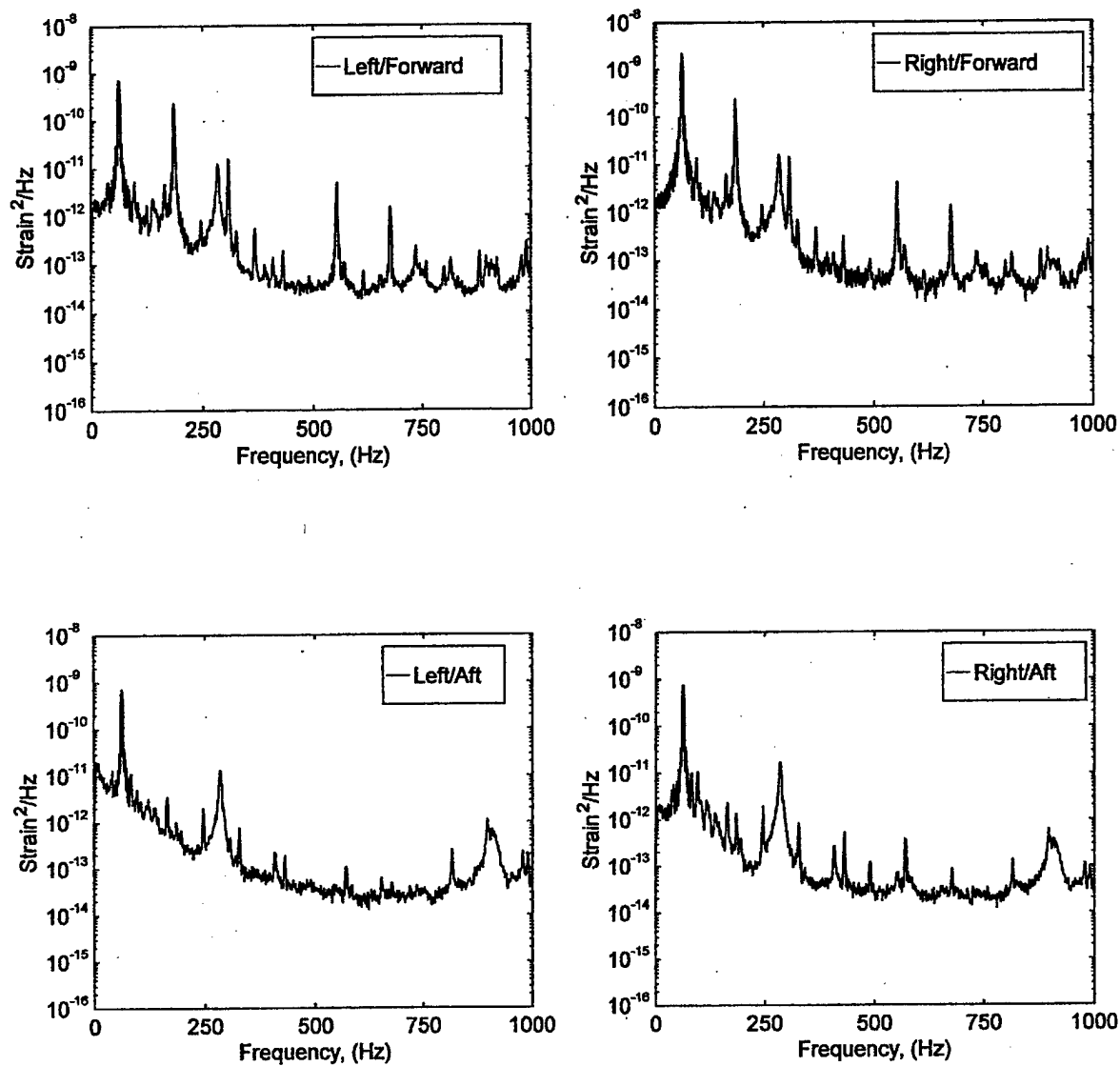
FIGURE C-26. STRAIN POWER SPECTRAL DENSITY (RUN 9, POINT 2)
$(\overline{q} = 35\,psf, \alpha = 0°, \psi = -10°)$
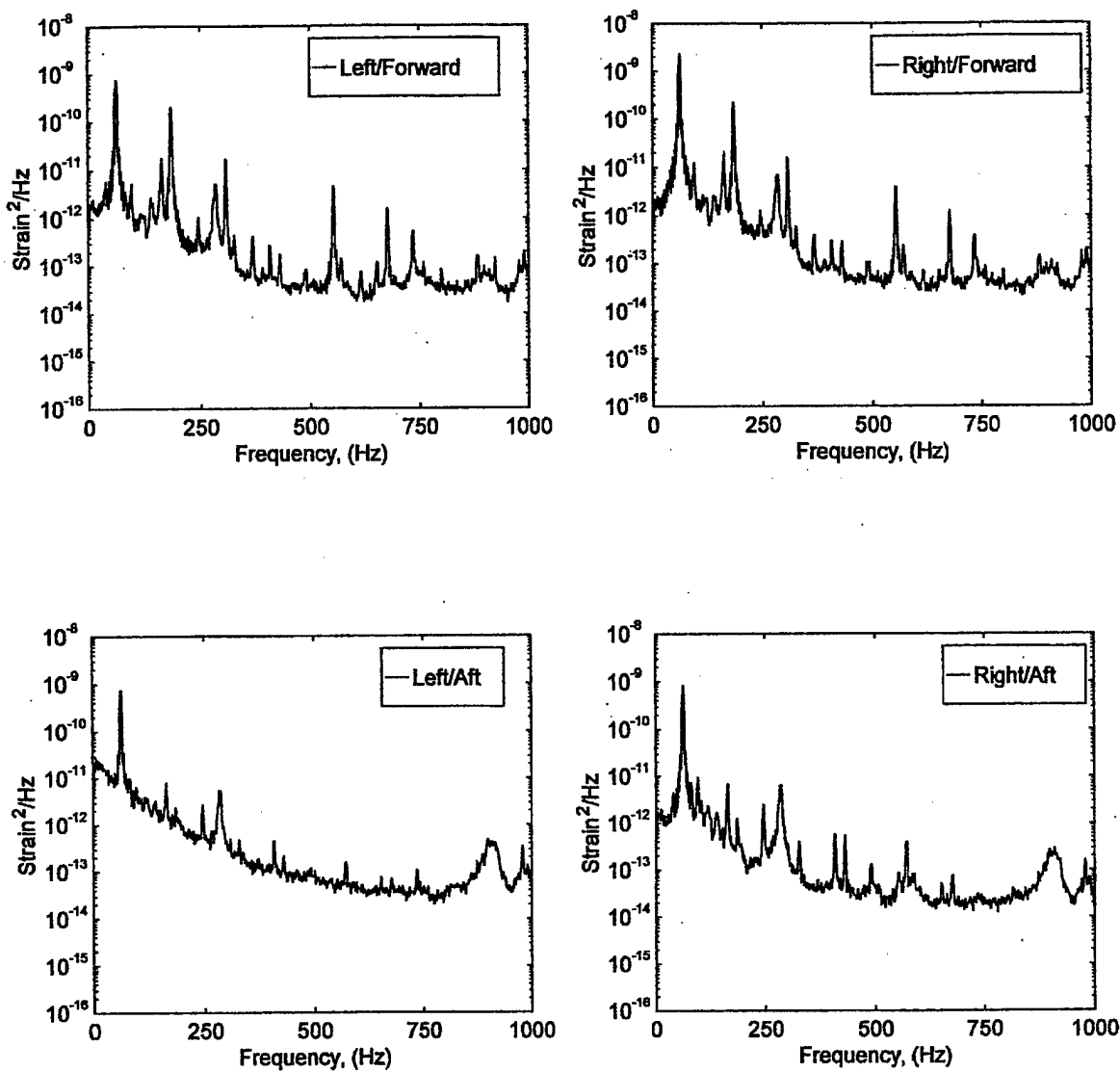
FIGURE C-27. STRAIN POWER SPECTRAL DENSITY (RUN 9, POINT 3)

$(\overline{q} = 35\,psf, \alpha = 5^{\circ}, \psi = -10^{\circ})$
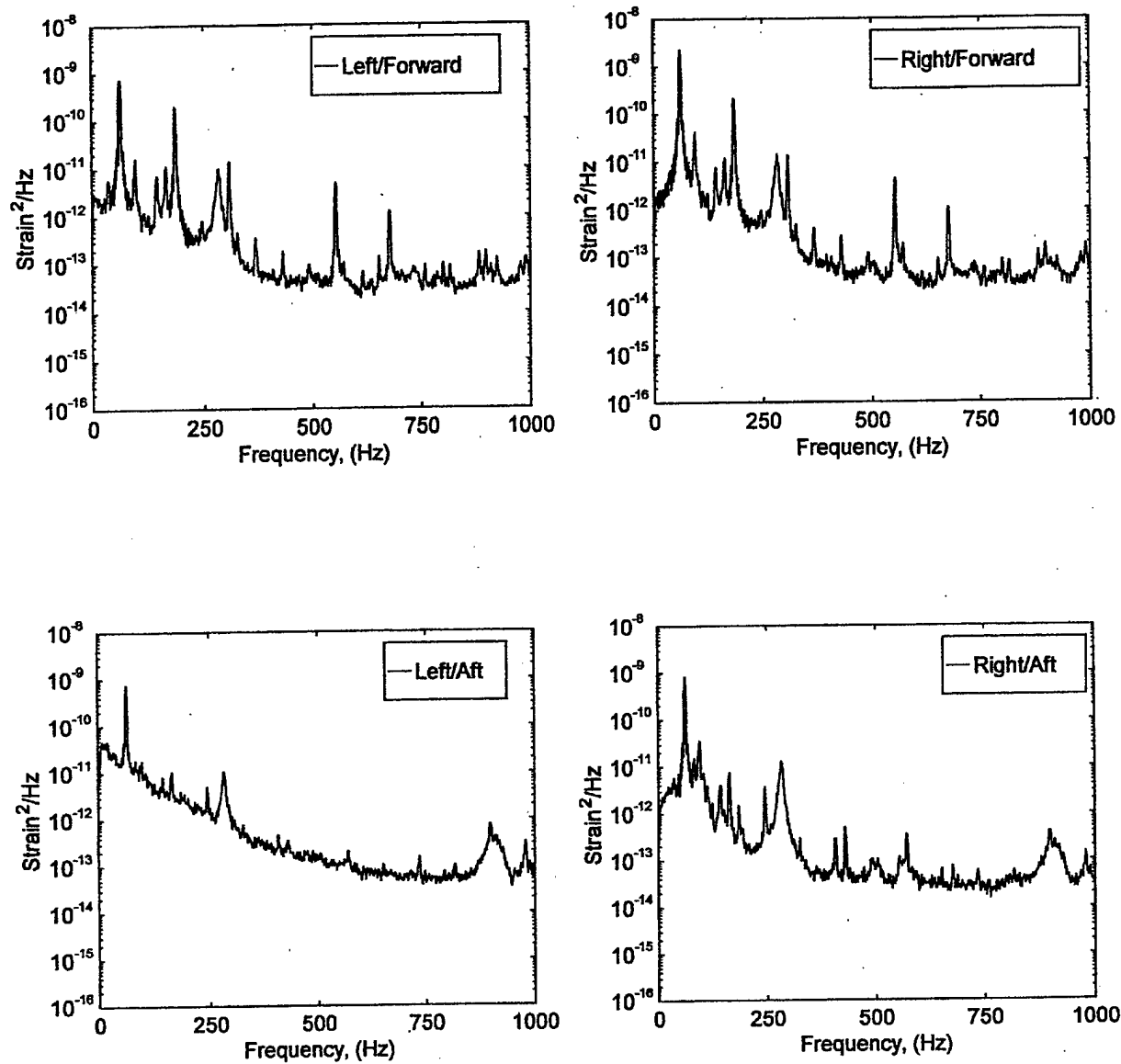
FIGURE C-28. STRAIN POWER SPECTRAL DENSITY (RUN 9, POINT 4)

$$(\overline{q} = 35\,psf, \alpha = 10^\circ, \psi = -10^\circ)$$

FIGURE C-29. STRAIN POWER SPECTRAL DENSITY (RUN 9, POINT 5)
$(\overline{q} = 35\,psf, \alpha = 15^{\circ}, \psi = -10^{\circ})$
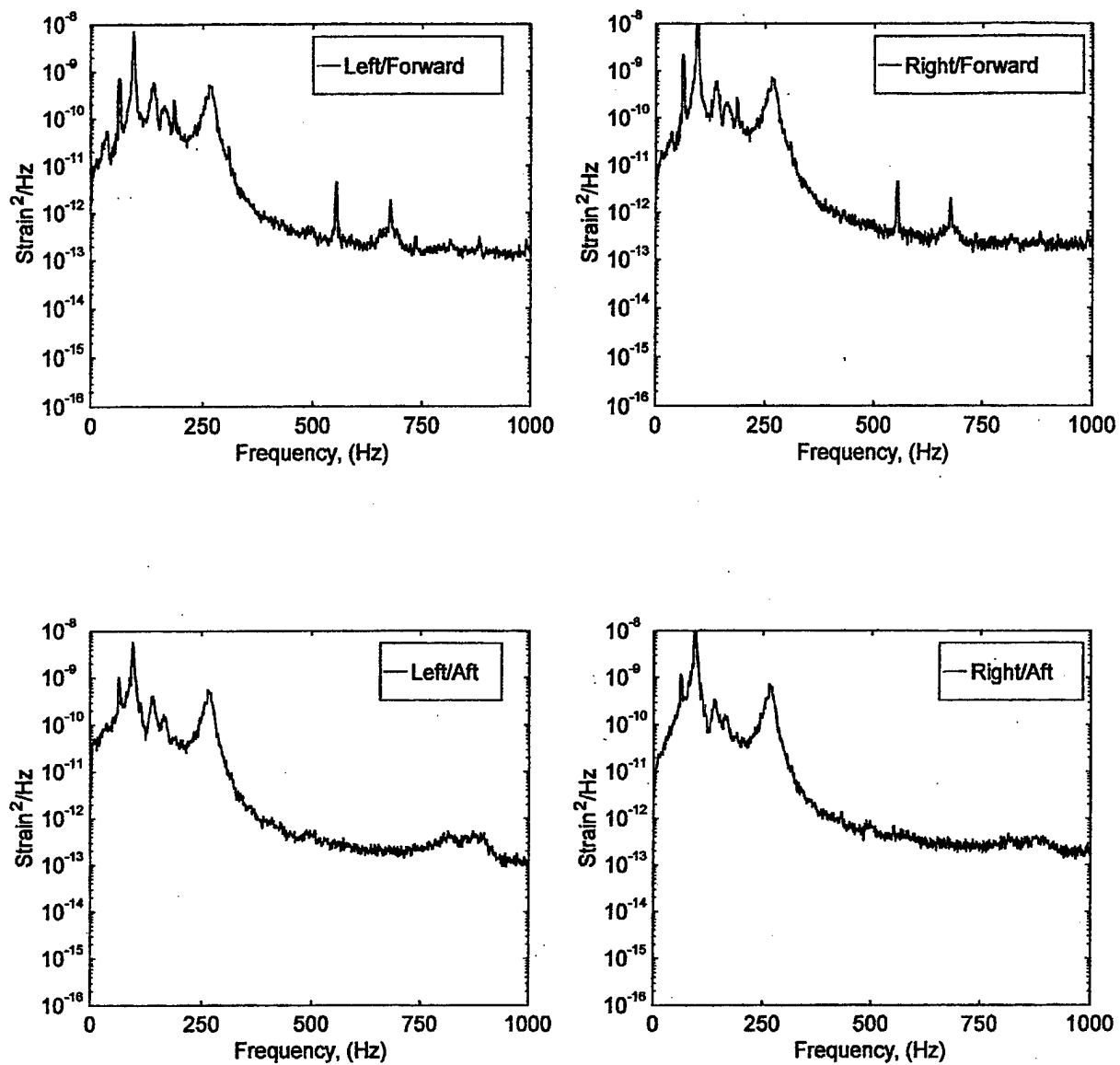
FIGURE C-30. STRAIN POWER SPECTRAL DENSITY (RUN 9, POINT 6)
$(\overline{q} = 35\,psf, \alpha = 20^{\circ}, \psi = -10^{\circ})$
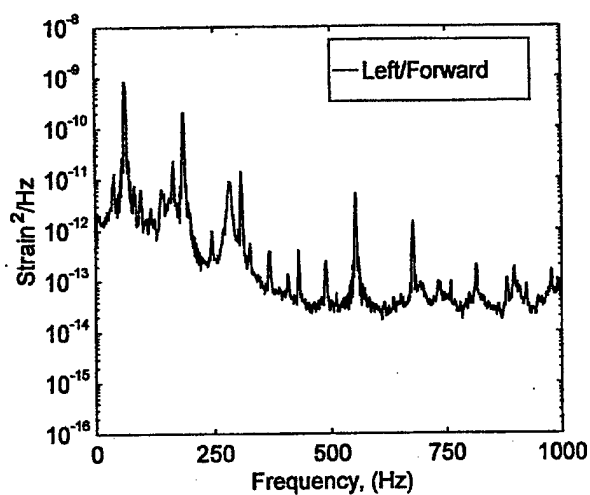
FIGURE C-31. STRAIN POWER SPECTRAL DENSITY (RUN 10, POINT 1)
$(\bar{q} = 45\,psf, \alpha = -5^{\circ}, \psi = -10^{\circ})$
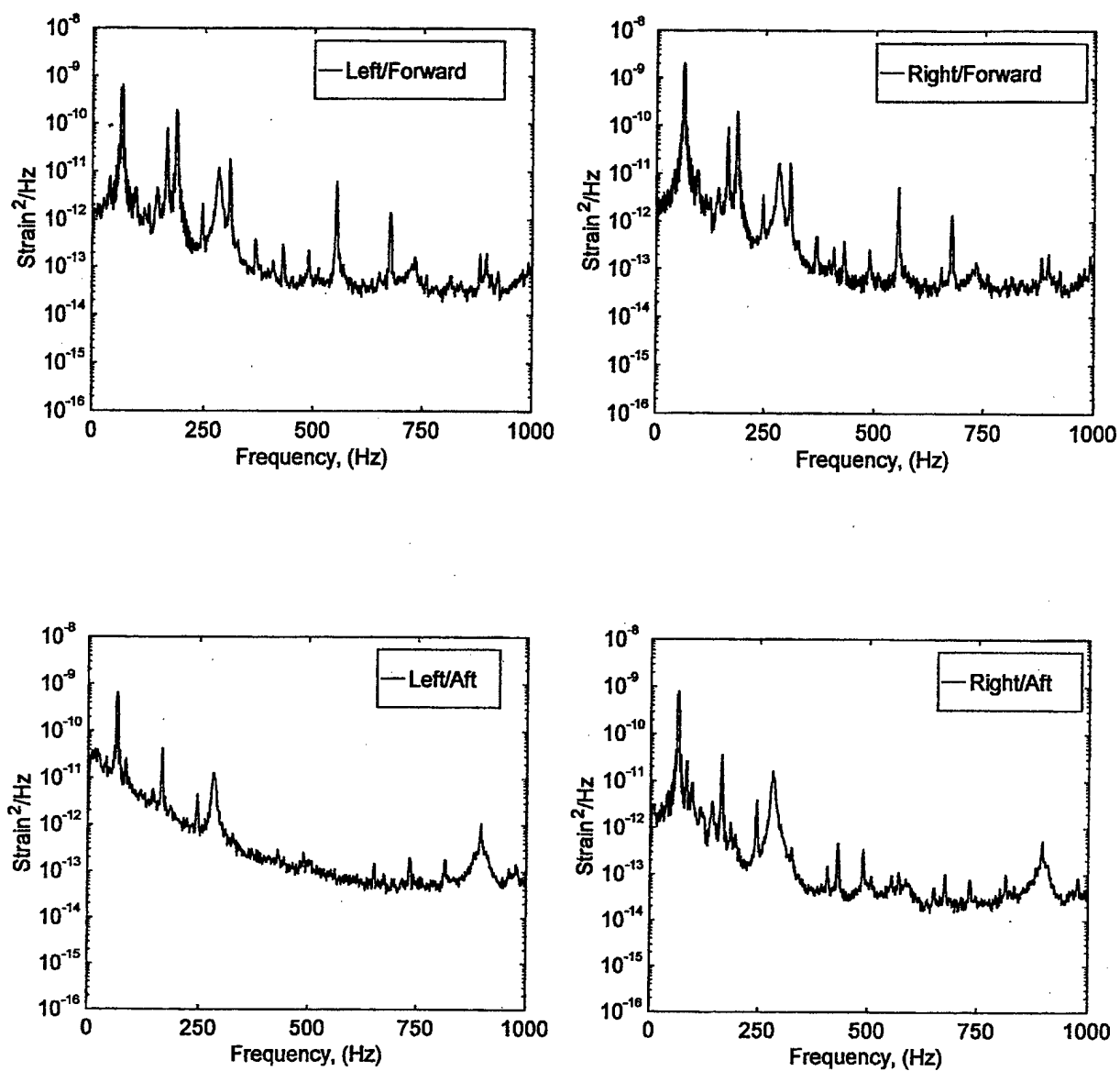
FIGURE C-32. STRAIN POWER SPECTRAL DENSITY (RUN 10, POINT 2)
$(\overline{q} = 45psf, \alpha = 0^{\circ}, \psi = -10^{\circ})$
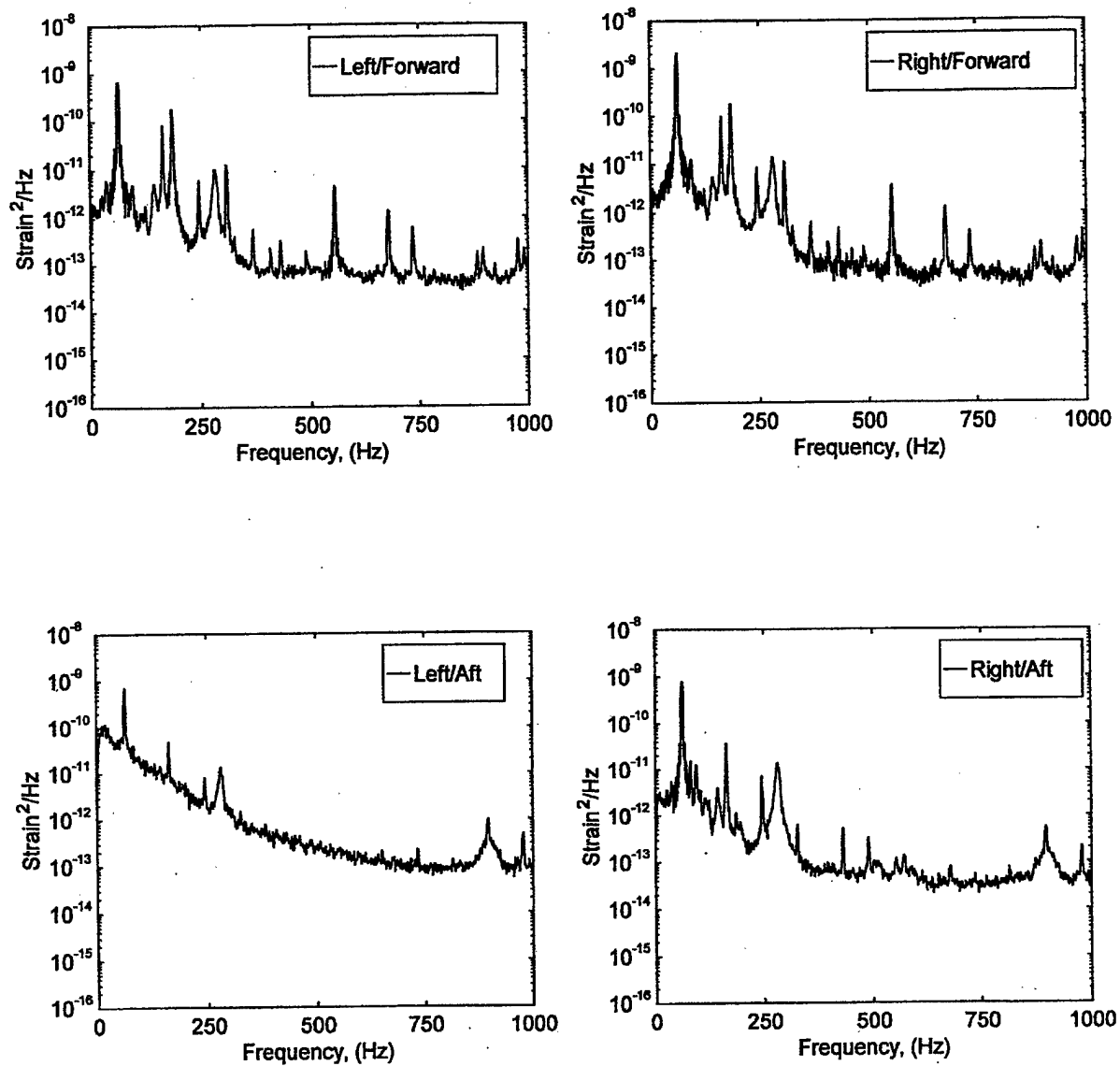
FIGURE C-33. STRAIN POWER SPECTRAL DENSITY (RUN 10, POINT 3)
$$(\overline{q} = 45psf, \alpha = 5^\circ, \psi = -10^\circ)$$
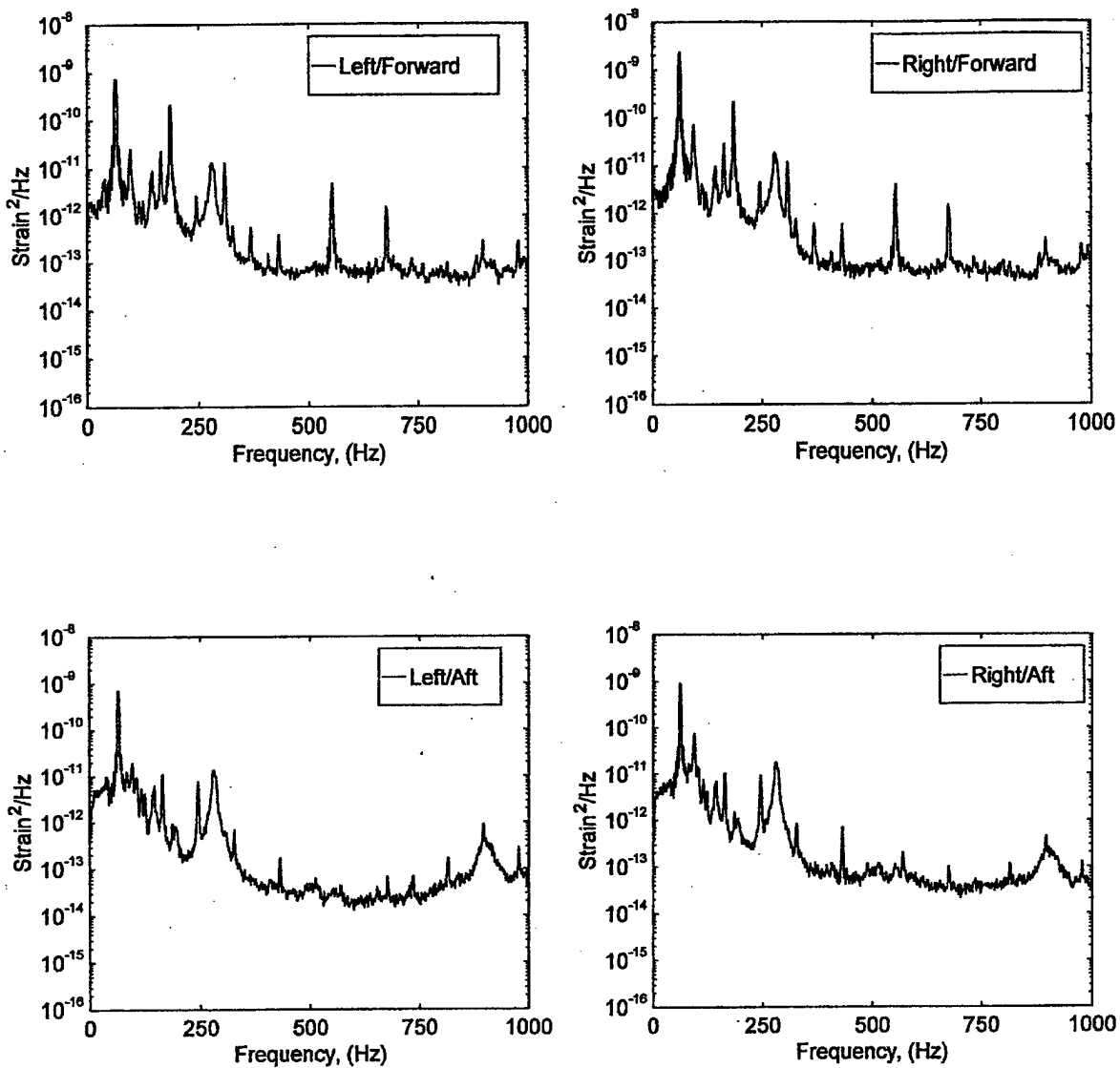
FIGURE C-34. STRAIN POWER SPECTRAL DENSITY (RUN 10, POINT 4)
$(\overline{q} = 45 psf, \alpha = 10^{\circ}, \psi = -10^{\circ})$

FIGURE C-35. STRAIN POWER SPECTRAL DENSITY (RUN 10, POINT 5)
$(\overline{q} = 45psf, \alpha = 15^{\circ}, \psi = -10^{\circ})$

FIGURE C-36. STRAIN POWER SPECTRAL DENSITY (RUN 10, POINT 6)
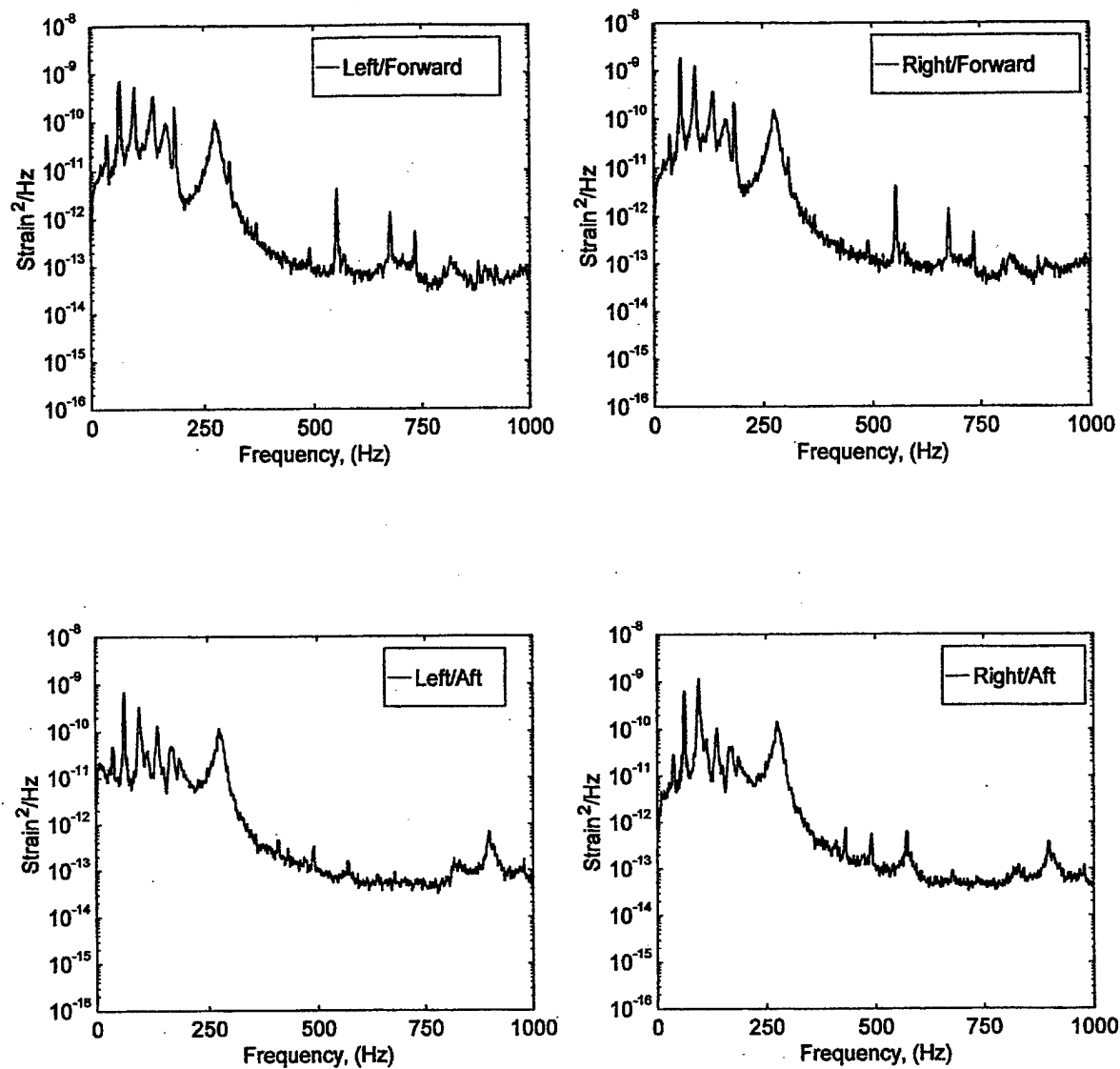$(\overline{q} = 45\,psf, \alpha = 20^\circ, \psi = -10^\circ)$

FIGURE C-37. STRAIN POWER SPECTRAL DENSITY (RUN 11, POINT 1)
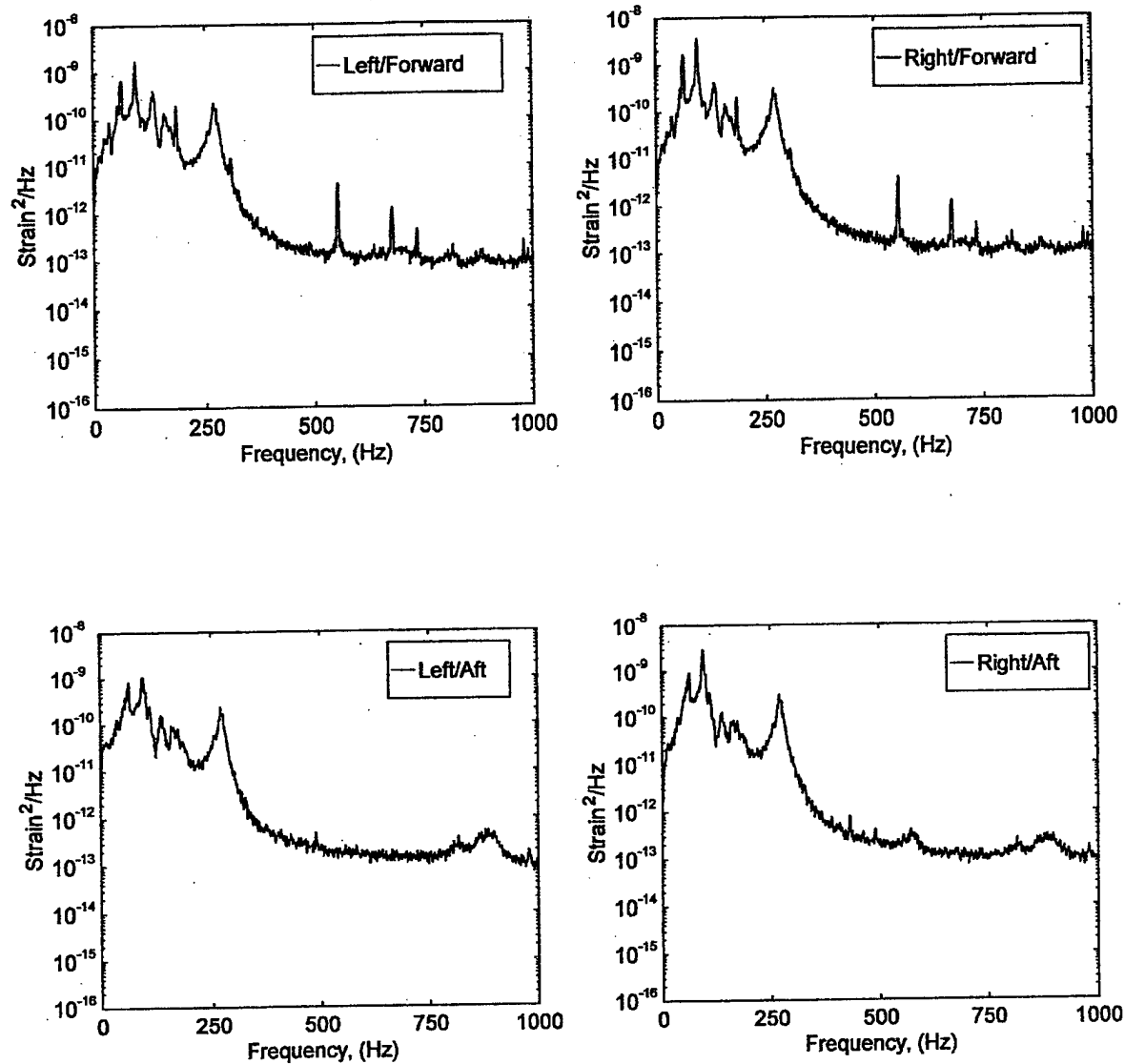$(\bar{q} = 25psf, \alpha = -5^{\circ}, \psi = -20^{\circ})$

FIGURE C-38. STRAIN POWER SPECTRAL DENSITY (RUN 11, POINT 2)
$(\overline{q} = 25psf, \alpha = 0°, \psi = -20°)$

FIGURE C-39. STRAIN POWER SPECTRAL DENSITY (RUN 11, POINT 3)

$$(\overline{q} = 25 psf, \alpha = 5\degree, \psi = -20\degree)$$

FIGURE C-40. STRAIN POWER SPECTRAL DENSITY (RUN 11, POINT 4)
$$(\overline{q} = 25\,psf, \alpha = 10°, \psi = -20°)$$

FIGURE C-41. STRAIN POWER SPECTRAL DENSITY (RUN 11, POINT 5)
$(\bar{q}=25psf,\alpha=15^{\circ},\psi=-20^{\circ})$
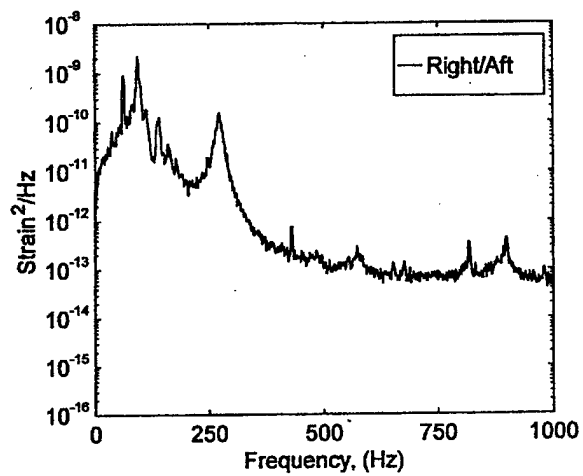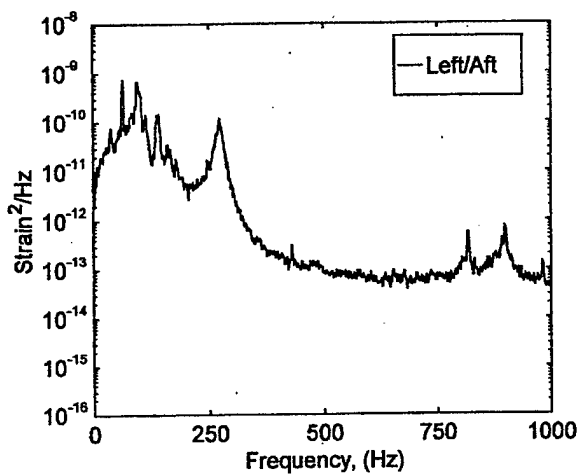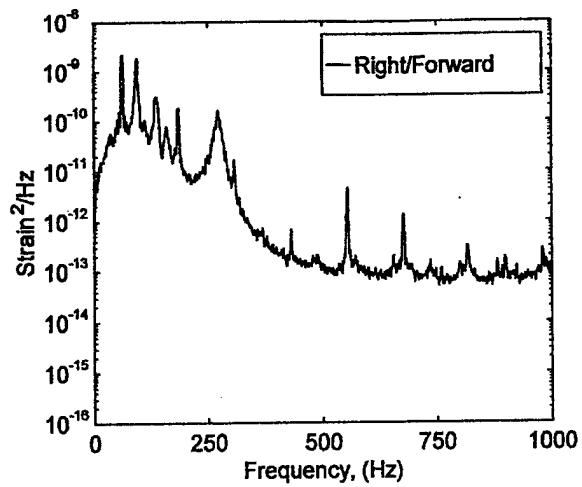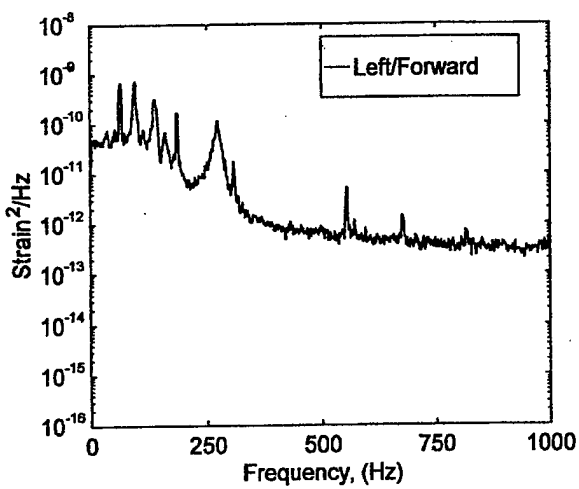
FIGURE C-42. STRAIN POWER SPECTRAL DENSITY (RUN 11, POINT 6)
$(\overline{q} = 25 psf, \alpha = 20°, \psi = -20°)$
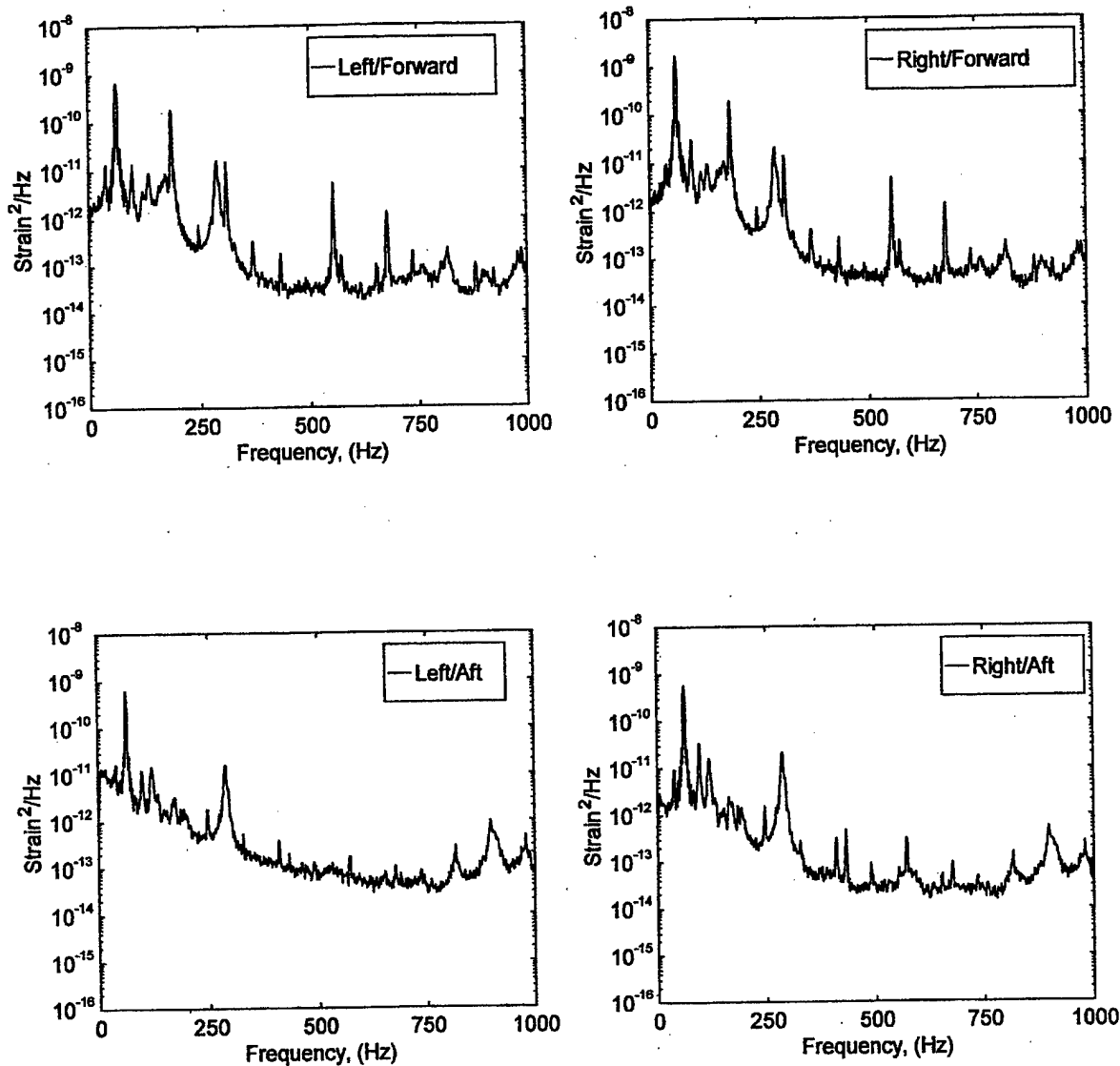
FIGURE C-43. STRAIN POWER SPECTRAL DENSITY (RUN 12, POINT 1)
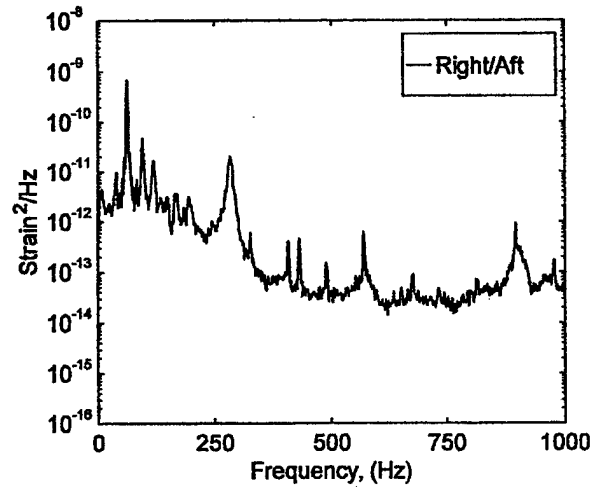$(\overline{q} = 35\,psf, \alpha = -5^{\circ}, \psi = -20^{\circ})$
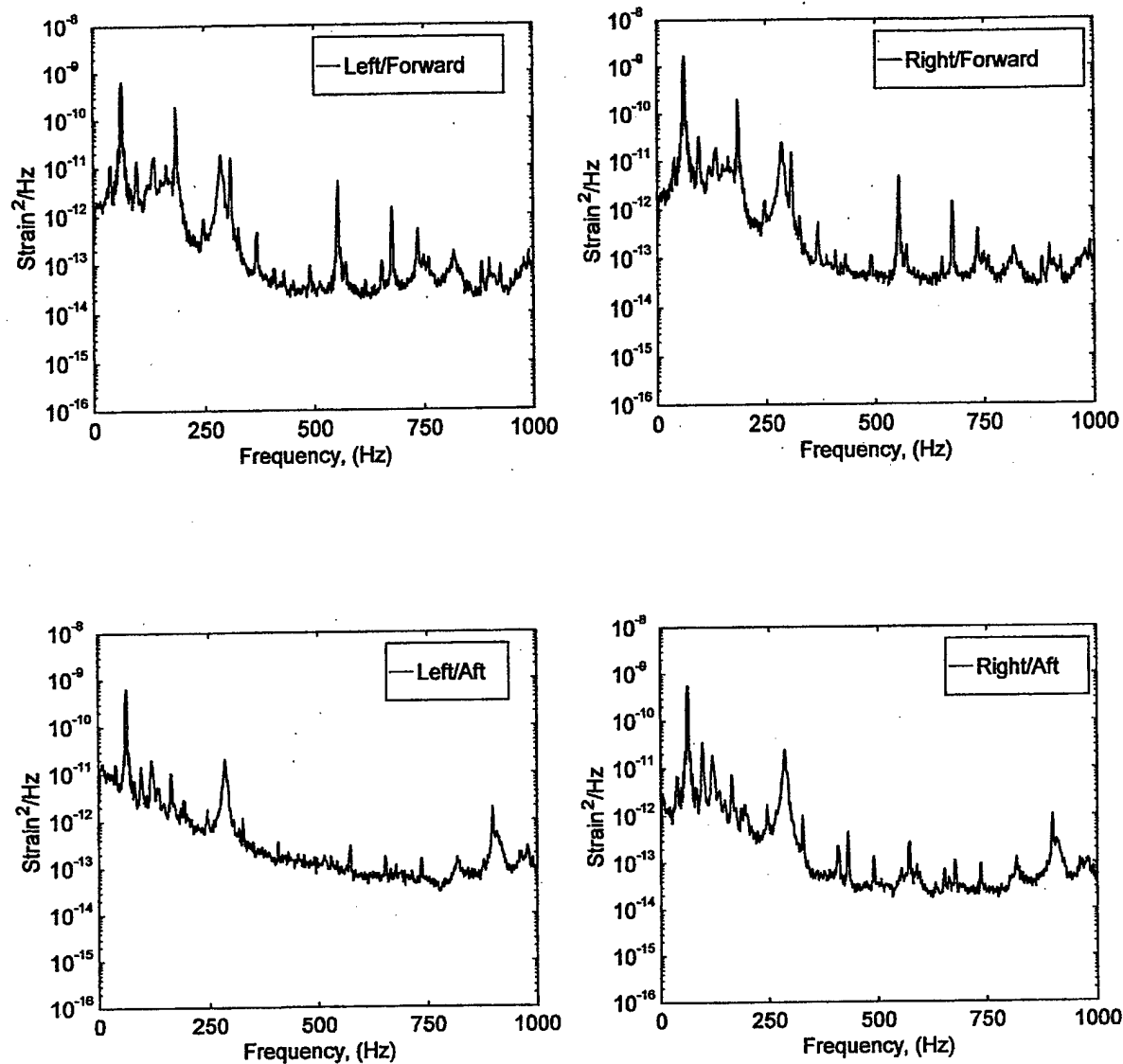
FIGURE C-44. STRAIN POWER SPECTRAL DENSITY (RUN 12, POINT 2)
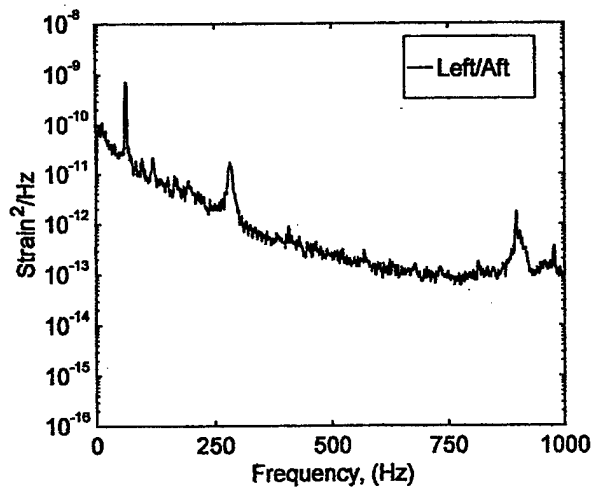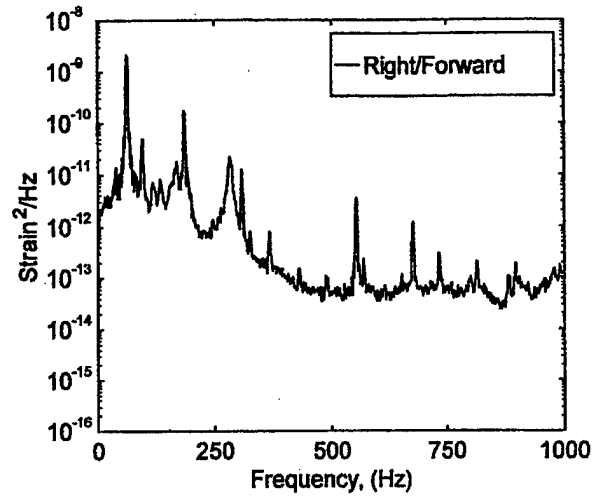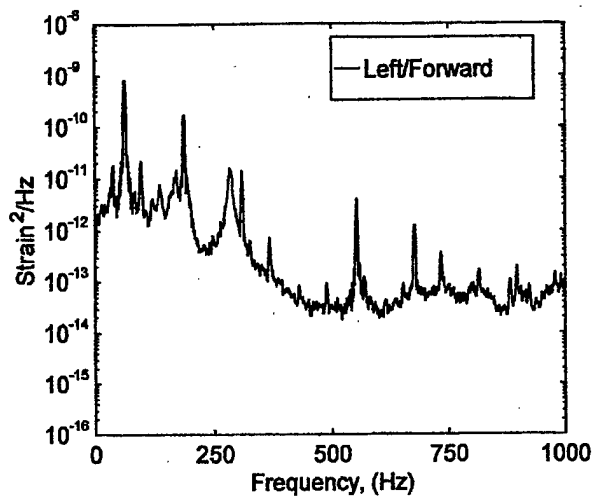$(\overline{q} = 35\,psf, \alpha = 0^{\circ}, \psi = -20^{\circ})$
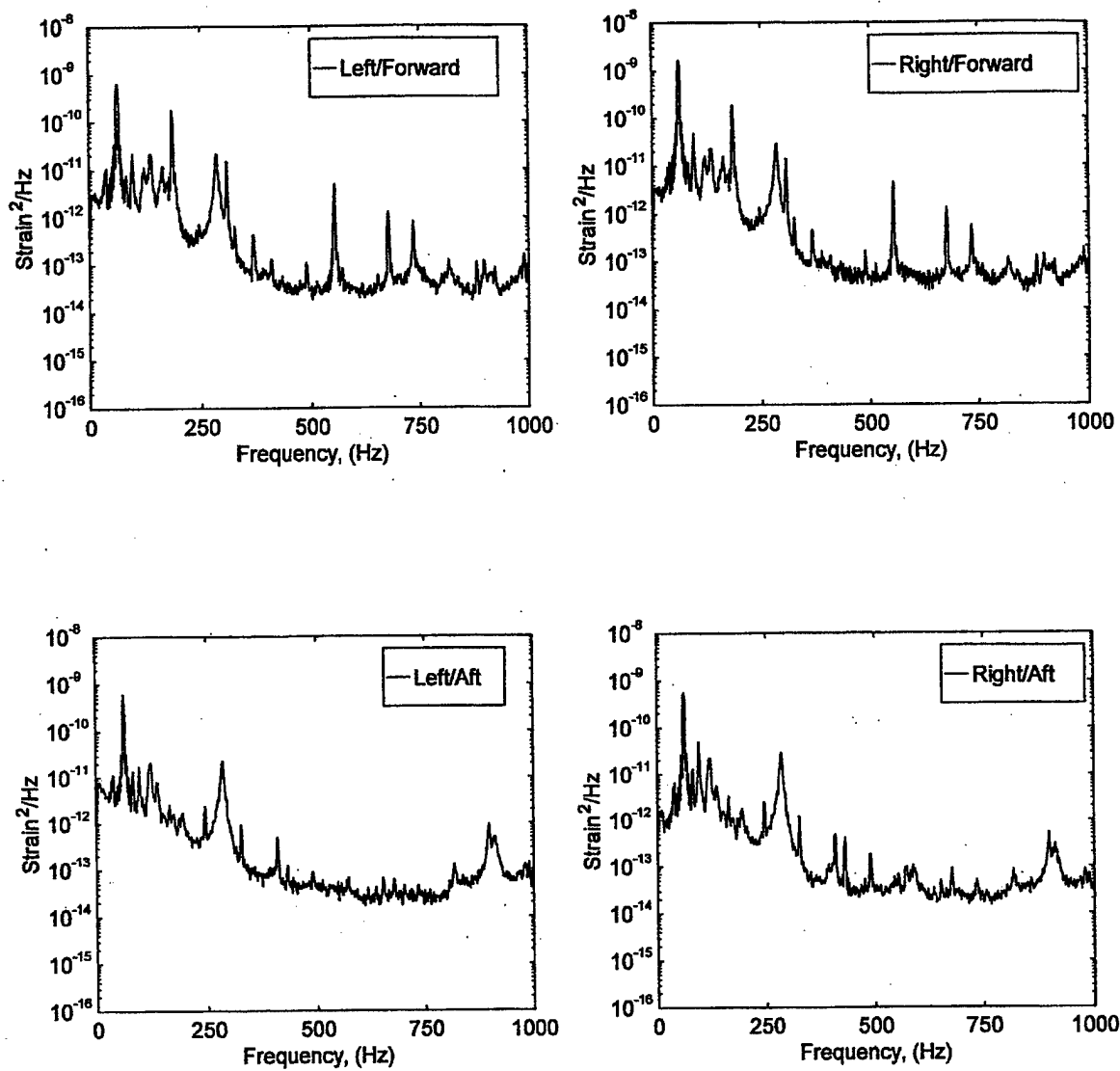
FIGURE C-45. STRAIN POWER SPECTRAL DENSITY (RUN 12, POINT 3)
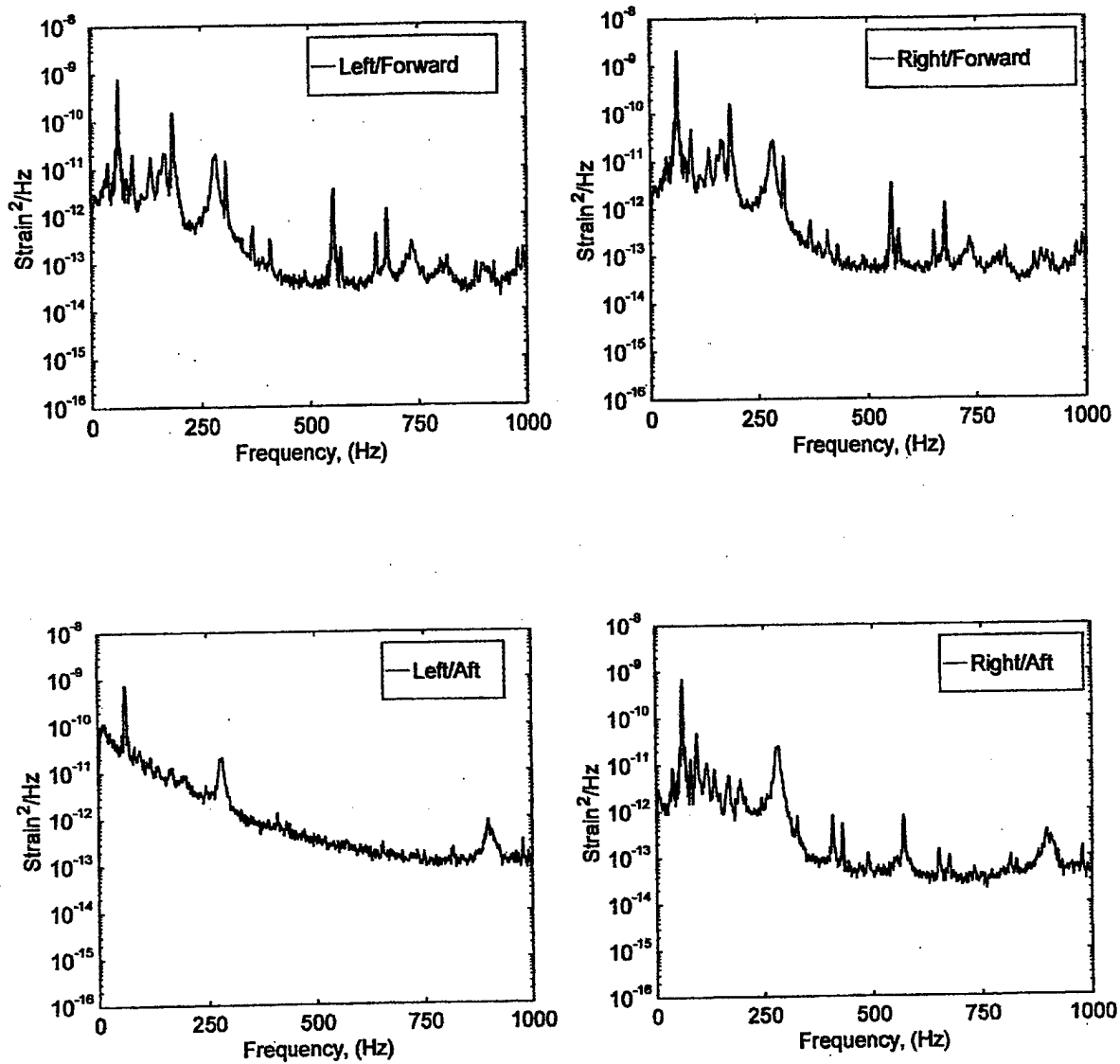$(\overline{q} = 35psf, \alpha = 5^{\circ}, \psi = -20^{\circ})$
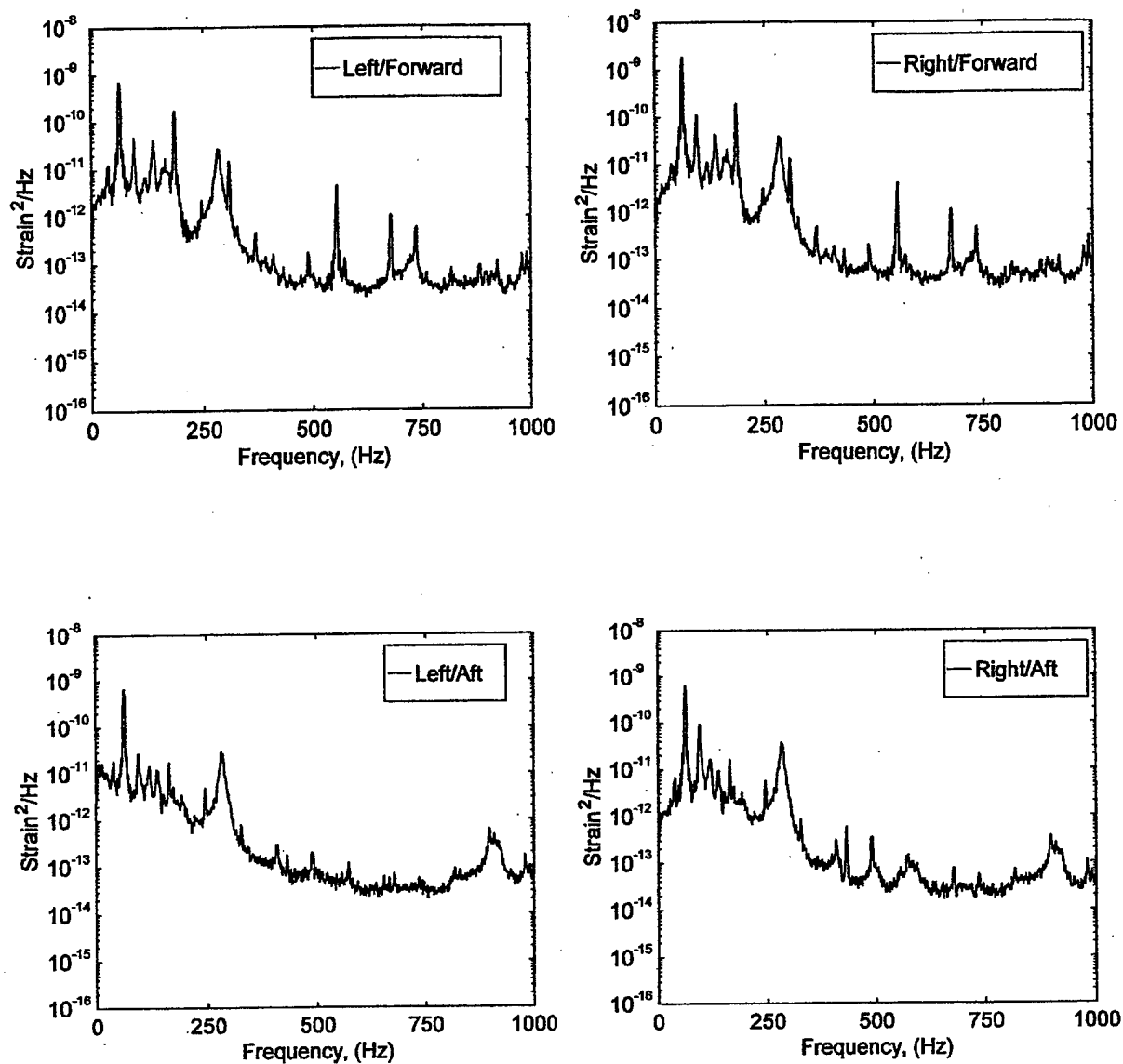
FIGURE C-46. STRAIN POWER SPECTRAL DENSITY (RUN 12, POINT 4)
$$(\bar{q} = 35psf, \alpha = 10^{\circ}, \psi = -20^{\circ})$$

FIGURE C-47. STRAIN POWER SPECTRAL DENSITY (RUN 12, POINT 5)
$(\overline{q} = 35\,psf, \alpha = 15^{\circ}, \psi = -20^{\circ})$

FIGURE C-48. STRAIN POWER SPECTRAL DENSITY (RUN 12, POINT 6)
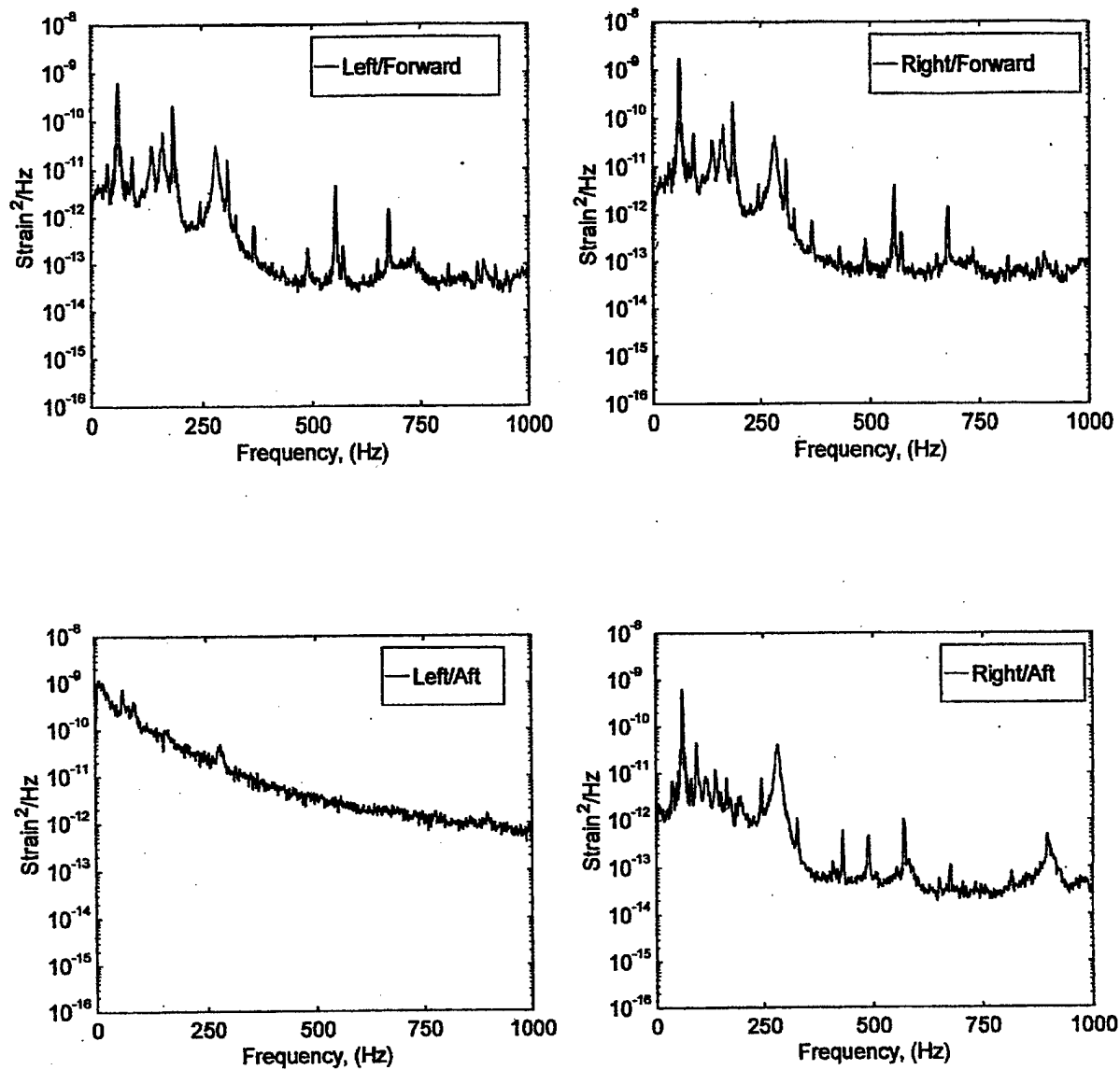$(\bar{q} = 35\,psf, \alpha = 20^{\circ}, \psi = -20^{\circ})$

FIGURE C-49. STRAIN POWER SPECTRAL DENSITY (RUN 13, POINT 1)
$(\overline{q} = 45psf, \alpha = -5^\circ, \psi = -20^\circ)$

FIGURE C-50. STRAIN POWER SPECTRAL DENSITY (RUN 13, POINT 2)
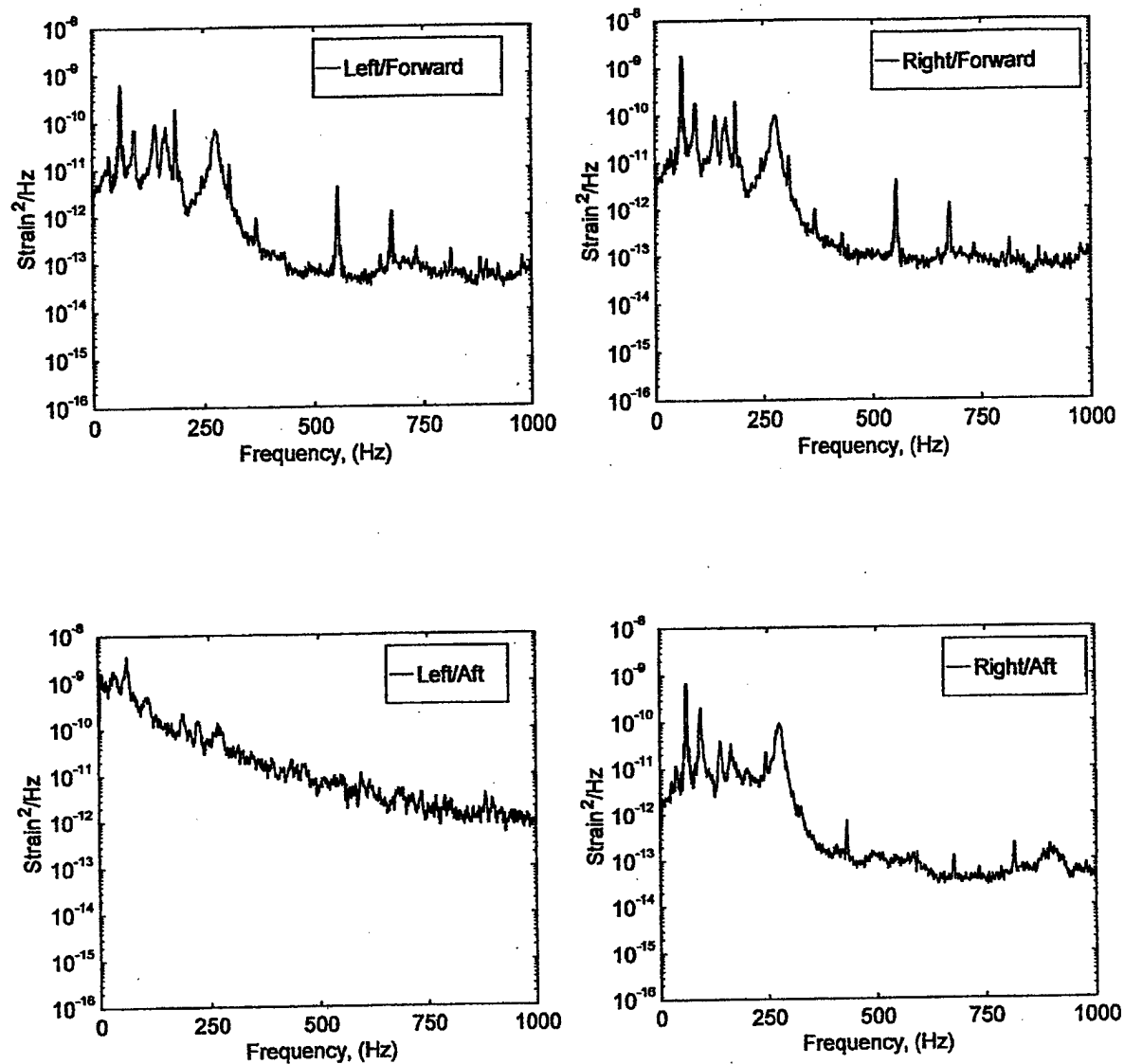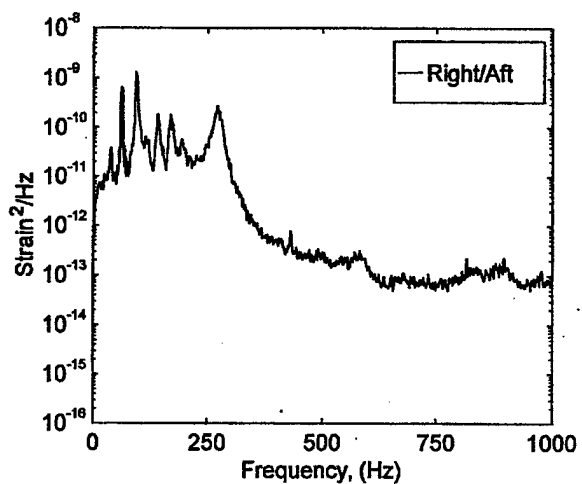$(\overline{q} = 45 psf, \alpha = 0^{\circ}, \psi = -20^{\circ})$

FIGURE C-51. STRAIN POWER SPECTRAL DENSITY (RUN 13, POINT 2)
$(\overline{q} = 45 psf, \alpha = 5^{\circ}, \psi = -20^{\circ})$

FIGURE C-52. STRAIN POWER SPECTRAL DENSITY (RUN 13, POINT 4)
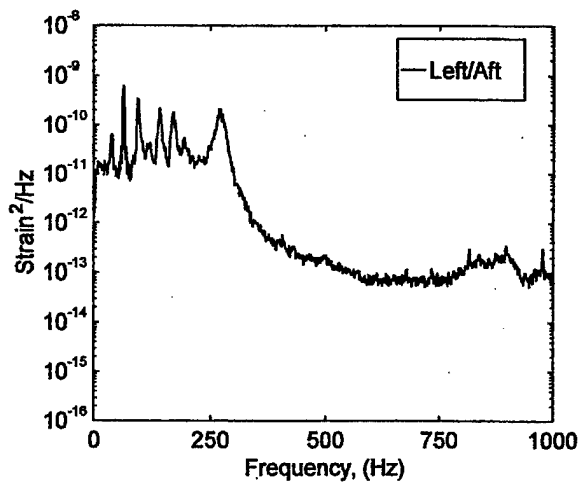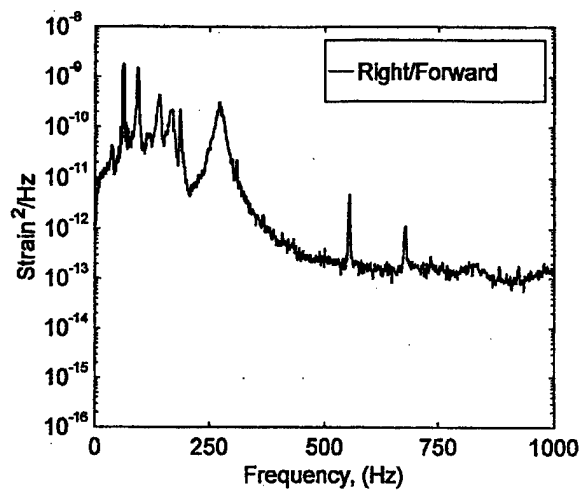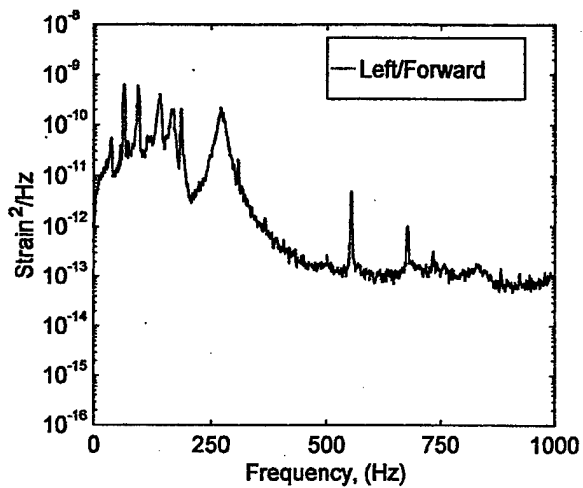$(\overline{q} = 45\,psf, \alpha = 10^{\circ}, \psi = -20^{\circ})$

FIGURE C-53. STRAIN POWER SPECTRAL DENSITY (RUN 13, POINT 5)
$(\bar{q} = 45psf, \alpha = 15^\circ, \psi = -20^\circ)$